**Springer Series in Synergetics** 



Andreas W. Liehr

# Dissipative Solitons in Reaction Diffusion Systems

Mechanisms, Dynamics, Interaction



# **Springer Complexity**

Springer Complexity is an interdisciplinary program publishing the best research and academic-level teaching on both fundamental and applied aspects of complex systems – cutting across all traditional disciplines of the natural and life sciences, engineering, economics, medicine, neuroscience, social and computer science.

Complex Systems are systems that comprise many interacting parts with the ability to generate a new quality of macroscopic collective behavior the manifestations of which are the spontaneous formation of distinctive temporal, spatial or functional structures. Models of such systems can be successfully mapped onto quite diverse "real-life" situations like the climate, the coherent emission of light from lasers, chemical reaction-diffusion systems, biological cellular networks, the dynamics of stock markets and of the internet, earthquake statistics and prediction, freeway traffic, the human brain, or the formation of opinions in social systems, to name just some of the popular applications.

Although their scope and methodologies overlap somewhat, one can distinguish the following main concepts and tools: self-organization, nonlinear dynamics, synergetics, turbulence, dynamical systems, catastrophes, instabilities, stochastic processes, chaos, graphs and networks, cellular automata, adaptive systems, genetic algorithms and computational intelligence.

The three major book publication platforms of the Springer Complexity program are the monograph series "Understanding Complex Systems" focusing on the various applications of complexity, the "Springer Series in Synergetics", which is devoted to the quantitative theoretical and methodological foundations, and the "SpringerBriefs in Complexity" which are concise and topical working reports, case-studies, surveys, essays and lecture notes of relevance to the field. In addition to the books in these two core series, the program also incorporates individual titles ranging from textbooks to major reference works.

### **Editorial and Programme Advisory Board**

Henry Abarbanel, Institute for Nonlinear Science, University of California, San Diego, USA

Dan Braha, New England Complex Systems Institute and University of Massachusetts Dartmouth, USA

Péter Érdi, Center for Complex Systems Studies, Kalamazoo College, USA and Hungarian Academy of Sciences, Budapest, Hungary

Karl Friston, Institute of Cognitive Neuroscience, University College London, London, UK

Hermann Haken, Center of Synergetics, University of Stuttgart, Stuttgart, Germany

Viktor Jirsa, Centre National de la Recherche Scientifique (CNRS), Université de la Méditerranée, Marseille, France

Janusz Kacprzyk, System Research, Polish Academy of Sciences, Warsaw, Poland

Kunihiko Kaneko, Research Center for Complex Systems Biology, The University of Tokyo, Tokyo, Japan

Scott Kelso, Center for Complex Systems and Brain Sciences, Florida Atlantic University, Boca Raton, USA

Markus Kirkilionis, Mathematics Institute and Centre for Complex Systems, University of Warwick, Coventry, UK

Jürgen Kurths, Nonlinear Dynamics Group, University of Potsdam, Potsdam, Germany

Andrzej Nowak, Department of Psychology, Warsaw University, Poland

Linda Reichl, Center for Complex Quantum Systems, University of Texas, Austin, USA

Peter Schuster, Theoretical Chemistry and Structural Biology, University of Vienna, Vienna, Austria

Frank Schweitzer, System Design, ETH Zurich, Zurich, Switzerland

Didier Sornette, Entrepreneurial Risk, ETH Zurich, Zurich, Switzerland

Stefan Thurner, Section for Science of Complex Systems, Medical University of Vienna, Vienna, Austria

# Springer Series in Synergetics

# Founding Editor: H. Haken

The Springer Series in Synergetics was founded by Herman Haken in 1977. Since then, the series has evolved into a substantial reference library for the quantitative, theoretical and methodological foundations of the science of complex systems.

Through many enduring classic texts, such as Haken's *Synergetics* and *Information and Self-Organization*, Gardiner's *Handbook of Stochastic Methods*, Risken's *The Fokker Planck-Equation* or Haake's *Quantum Signatures of Chaos*, the series has made, and continues to make, important contributions to shaping the foundations of the field.

The series publishes monographs and graduate-level textbooks of broad and general interest, with a pronounced emphasis on the physico-mathematical approach.

For further volumes: http://www.springer.com/series/712

# Andreas W. Liehr

# Dissipative Solitons in Reaction Diffusion Systems

Mechanisms, Dynamics, Interaction



Dr. Andreas W. Liehr Freiburg Materials Research Center University of Freiburg Freiburg Germany

ISSN 0172-7389 ISBN 978-3-642-31250-2 ISBN 978-3-642-31251-9 (eBook) DOI 10.1007/978-3-642-31251-9 Springer Heidelberg New York Dordrecht London

Library of Congress Control Number: 2012951921

# © Springer-Verlag Berlin Heidelberg 2013

This work is subject to copyright. All rights are reserved by the Publisher, whether the whole or part of the material is concerned, specifically the rights of translation, reprinting, reuse of illustrations, recitation, broadcasting, reproduction on microfilms or in any other physical way, and transmission or information storage and retrieval, electronic adaptation, computer software, or by similar or dissimilar methodology now known or hereafter developed. Exempted from this legal reservation are brief excerpts in connection with reviews or scholarly analysis or material supplied specifically for the purpose of being entered and executed on a computer system, for exclusive use by the purchaser of the work. Duplication of this publication or parts thereof is permitted only under the provisions of the Copyright Law of the Publisher's location, in its current version, and permission for use must always be obtained from Springer. Permissions for use may be obtained through RightsLink at the Copyright Clearance Center. Violations are liable to prosecution under the respective Copyright Law.

The use of general descriptive names, registered names, trademarks, service marks, etc. in this publication does not imply, even in the absence of a specific statement, that such names are exempt from the relevant protective laws and regulations and therefore free for general use.

While the advice and information in this book are believed to be true and accurate at the date of publication, neither the authors nor the editors nor the publisher can accept any legal responsibility for any errors or omissions that may be made. The publisher makes no warranty, express or implied, with respect to the material contained herein.

Printed on acid-free paper

Springer is part of Springer Science+Business Media (www.springer.com)

Dedicated to Dani, Yanara, Milena & Joschua

# **Preface**

This is a book about fascination. A fascination which had hit me in 1996, when I got a position as student assistant in the workgroup of Prof. Purwins and started to upgrade a numerical solver of two-dimensional reaction-diffusion systems to three spatial dimensions. We were heading for self-organized localized structures of three-component reaction-diffusion systems. Due to their particle-like characteristics, we called them quasi-particles and later on renamed them to dissipative solitons. The simulations and theoretical investigations surprised us again and again with complexity on the one hand and general mechanisms on the other, such that we were heading for detecting them experimentally, which finally succeeded.

After finishing my doctoral thesis on this topic, the fascination did not seem to falter and I was very happy that my proposition for a book on *Dissipative Solitons in Reaction-Diffusion Systems* to appear in Springer's Synergetics Series was accepted. I have always been inspired by books in this field through my studies, so it is a great honor for me to contribute to this series.

The central idea of this book is to give an overview, introduce important concepts and methods, and follow them, wherever possible, down to concrete results, both numerically and experimentally, which allows for weaving all the important details and general methods to a broad view on dissipative solitons in reaction-diffusion systems.

Therefore, this book should attract not only the experienced scientist, who is interested in self-organization phenomena and might become inspired to new research directions, but also the student, who likes to learn how to investigate complex systems. And somehow, I hope, that this book transfers my fascination to other people.

Ortenberg (Baden)

Andreas W. Liehr

# **Foreword**

This book by Andreas W. Liehr is a valuable addition to the Springer Series in Synergetics.

Indeed, the experimental and theoretical study of the spontaneous ("self-organized") formation of structures in physical, chemical, and other systems is still a lively subject in modern science. This book focuses its attention on reaction-diffusion systems, where it masters to build a bridge between basic concepts and concrete results by a combination of analytical and numerical approaches. This and its clear style make the book not only most valuable for scientists and graduate students, but at least some of its chapters may form an excellent basis for courses on physical/chemical nonequilibrium systems.

I have read this text with great pleasure, and I am sure its readers will share my impression.

Stuttgart, February 2013 Hermann Haken

# Acknowledgments

The manuscript of this book accompanied me for a couple of years. Its content was mainly researched at the Institute of Applied Physics at the University of Münster, while the book matured at the Freiburg Materials Research Center (FMF) of the University of Freiburg and at numerous train rides between Offenburg and Karlsruhe.

The one person who shared this journey with me is my wife and best friend Daniela Kempa, who has patiently encouraged the finishing of this book. Thank you so much!

I also like to thank C. Ascheron from Springer Verlag for having the confidence that this manuscript will be finished, and H.-G. Purwins and J. Honerkamp for letting me explore the fascination of research in all its width and depth. Of course, there are many other people who contributed to this book in one way or the other. There were night-long discussions, experiments explained, mathematical methods clarified, articles written, presentations prepared, software designed, creative research environments fostered, and of course many valuable reviews of this manuscript. Many thanks to A. Adamatzky, Sh. Amiranashvili, B. Anderssen, Yu. A. Astrov, M. Bär, J. Berkemeier, M. Bode, H. U. Bödeker, I. R. Epstein, T. D. Frank, R. Friedrich, E. L. Gurevich, S. V. Gurevich, H. Haken, St. Kottemer, St. Meisen, A. S. Moskalenko, Y. Nishiura, M. C. Röttger, C. P. Schenk, and A. L. Zanin.

Finally, I like to thank the steering committee of the High Performance Computing Center Stuttgart (HLRS) for the generous grants of computing time on the Cray T3E, the German Science Foundation (DFG) for a doctoral grant at graduate school Nichtlineare Kontinuierliche Systeme, and Apple Research & Technology Support (ARTS) for mobile equipment.

# **Contents**

1	Intr	oductio	on	1
	1.1	Struct	ure Formation	2
	1.2	A Ver	y Short Literature Survey	5
		1.2.1	Self-organization and Localized Structures	5
		1.2.2	Spirals	6
		1.2.3	Pattern	6
		1.2.4	Fronts	7
		1.2.5	Dissipative Solitons	7
	1.3	How t	o Read This Book	8
	Refe	erences		9
2	Exp	erimen	tal Observations	15
	2.1		ical Systems	15
		2.1.1	Overview	15
		2.1.2	Catalytic Oxidation of CO on Pt(110)	16
		2.1.3	The Belousov-Zhabotinsky Reaction	17
		2.1.4	The Belousov-Zhabotinsky-Aerosol	
			OT-Microemulsion System	19
		2.1.5	Ferrocyanide-Iodate-Sulphite (FIS) Reaction	22
	2.2	Planar	Semiconductor Gas-Discharge Systems	24
		2.2.1	Experimental Set-Up	24
		2.2.2	Observation of Current Density Filaments	25
		2.2.3	Generation and Annihilation Phenomena	26
		2.2.4	Dynamics	32
		2.2.5	Interaction Processes with Conservation of the	
			Number of Dissipative Solitons	33
	Dof	rancas	•	30

xiv Contents

3	Moc	deling .		43
	3.1	One-C	Component Systems with Symmetric Potential	43
		3.1.1	Local Bistability	43
		3.1.2	Spatial Bistability	46
		3.1.3	Spatial Bistability in Extended Systems	49
	3.2	One-C	Component Systems with Unsymmetric Potential	50
		3.2.1	Local Bistability	50
		3.2.2	Critical Nuclei and Trigger Fronts in	
			One-Dimensional Systems	53
		3.2.3	Critical Nuclei and Trigger Fronts in Two- and	
			Three-Dimensional Systems	55
		3.2.4	Stabilization of Localized Structures by Global Feedback	58
	3.3	Two-C	Component Reaction-Diffusion Systems	60
		3.3.1	Transition from Global to Local Feedback	60
		3.3.2	The Turing-Instability	62
		3.3.3	Stationary Solutions	64
		3.3.4	Delayed Inhibition	68
		3.3.5	Voronoi-Diagrams	71
		3.3.6	Critical Nuclei of Dissipative Solitons	72
	3.4	Three-	-Component Reaction-Diffusion Systems	76
		3.4.1	Propagating Dissipative Solitons	76
		3.4.2	Complex Dissipative Solitons	81
		3.4.3	Phenomenological Context	82
	Refe	erences		85
4	Dvn	amics.		91
	4.1		eations	91
	4.2		-Preserving Destabilizations	93
		4.2.1	Goldstone-Mode	93
		4.2.2	Propagator-Mode	96
		4.2.3	Complementary Modes	97
		4.2.4	Drift- and Rotational-Bifurcation	98
		4.2.5	Translational and Rotational Velocities	104
		4.4.5		
	4.3			108
	4.3		ions of Motion	108 109
	4.3	Equat		
	4.3	Equat 4.3.1	ions of Motion	109
	4.3	Equat: 4.3.1 4.3.2	ions of Motion	109 110
	4.3	Equat 4.3.1 4.3.2 4.3.3 4.3.4	ions of Motion	109 110 111
		Equat: 4.3.1 4.3.2 4.3.3 4.3.4 4.3.5	ions of Motion	109 110 111 112
5	Refe	Equat: 4.3.1 4.3.2 4.3.3 4.3.4 4.3.5 erences	ions of Motion  Transformation to Homogeneous State $u_0 = 0$ Specify Complementary Modes  Perturbation Ansatz  Projection onto Complementary Modes  Reduced Dynamics	109 110 111 112 115 116
5	Refe	Equat. 4.3.1 4.3.2 4.3.3 4.3.4 4.3.5 erences	ions of Motion  Transformation to Homogeneous State $u_0 = 0$ Specify Complementary Modes  Perturbation Ansatz  Projection onto Complementary Modes  Reduced Dynamics  of Slow Dissipative Solitudes	109 110 111 112 115
5	Refe	Equat 4.3.1 4.3.2 4.3.3 4.3.4 4.3.5 erences raction	ions of Motion  Transformation to Homogeneous State $u_0 = 0$ Specify Complementary Modes  Perturbation Ansatz  Projection onto Complementary Modes  Reduced Dynamics  of Slow Dissipative Solitudes  ation of Bound States	109 110 111 112 115 116 119 120
5	Refe Inte	Equat 4.3.1 4.3.2 4.3.3 4.3.4 4.3.5 erences raction	ions of Motion  Transformation to Homogeneous State $u_0 = 0$ Specify Complementary Modes  Perturbation Ansatz  Projection onto Complementary Modes  Reduced Dynamics  of Slow Dissipative Solitudes	109 110 111 112 115 116

Contents xv

		5.2.3	Interaction Law	128
		5.2.4	Bound States	130
		5.2.5	Checking the Reduced Dynamics	133
	5.3		ring	135
	5.4	Rotati	ng Bound States	137
		5.4.1	Formation of Rotating Bound States	137
		5.4.2	Dynamics of Rotating Bound States	140
		5.4.3	Formation of Spiralling Bound States	146
	5.5		lex Bound States	148
	5.6	Many-	-Particle Dynamics	154
	Refe	erences		157
6	Dyn	amics a	and Interaction of Experimental Dissipative Solitons	159
	6.1		astic Time Series Analysis	159
	6.2		ion to Two-Dimensional Trajectories	162
	6.3	Brown	nian and Active Brownian Motion	163
	6.4	Drift-l	Bifurcation	168
	6.5		ction	170
	Refe	erences		173
7	Gen	eration	and Annihilation	175
	7.1		olling Generation and Annihilation	176
		7.1.1	Controlling the Propagation Velocity	176
		7.1.2	Generating Clusters from Scratch	180
		7.1.3	Self-completion	183
		7.1.4	Feedback Control	185
	7.2	Annih	ilation of Dissipative Solitons	186
		7.2.1	Strong Repulsion	186
		7.2.2	Weak Repulsion	187
	7.3	Gener	ation of Dissipative Solitons	190
		7.3.1	Strong Repulsion	190
		7.3.2	Weak Repulsion	196
		7.3.3	Self-replication	198
	7.4	Mecha	anisms of Strong Interaction	199
		7.4.1	Annihilation	199
		7.4.2	Generation	201
	Refe	erences		203
8	Sun	ımarv		207
J				208
	Kere	rence.		200
In	dov			200

# **Acronyms**

# **Experiments**

$a_{\rm SC}$	Width of the semiconductor
d	Width of the reaction space
D	Diameter of the active area
$f_{\rm rep}$	Sampling frequency
$\phi = \phi(x,t)$	Luminance distribution

 $\langle \phi(x,t) \rangle_x$  Spacial average of luminance distribution  $\phi_T$  Threshold value of luminance distribution  $\phi$ 

I Global current

 $\kappa_1$  Illumination parameter  $\kappa_2$  Feedback parameter

 $L_{\rm d}$  Edge length of the displayed area p(t) Position of current density filament

 $p_X$  Partial pressure of gas X

 $R_0$  Series resistor

 $\rho_{SC}$  Specific resistivity of the semiconductor

 $\sigma_{BZ}$  Excitability of the Belousov-Zhabotinsky reaction

 $\sigma_{SC}$  Specific conductivity of the semiconductor

t Time coordinate  $t_{\rm exp}$  Exposure time

 $T_{\rm SC}$  Temperature of the semiconductor

 $egin{array}{ll} U_0 & {
m Applied \ dc \ voltage} \ U_{
m c} & {
m Ignition \ voltage} \ x & {
m Spatial \ coordinate} \ \end{array}$ 

 $[X]_0$  Concentration of substance X prior to reaction

xviii Acronyms

# **Field Equations**

u = u(x, t)	Activator
v = v(x, t)	Driving inhibitor
w = w(x, t)	Stabilizing inhibitor
u	Vector field $\boldsymbol{u}(u, v, w)^{\mathrm{T}}$ of the reaction-diffusion components
$u_0$	Homogeneous solution $(u_0, v_0, w_0)^T$ of the field equations
$\bar{u}$	Stationary solution of the field equations
$\overset{\curvearrowright}{u}$	Propagating solution of the field equations
$\tilde{u}$	Perturbation of stationary solution $\bar{u}$
$\boldsymbol{u}_{\mathrm{n}}$	Solution of the field equations with $u_{\rm n,0} = 0$
x	Vector of spatial coordinates
t	Time coordinate
$f(u)$ $\lambda$	Nonlinearity of model system
λ	Parameter of cubic nonlinearity
$D_u$	Diffusion constant of activators u
$D_v$	Diffusion constant of driving inhibitor $v$
$D_w$	Diffusion constant of stabilizing inhibitor w
$\kappa_1$	Driving constant
$\kappa_2$	Coupling constant of global activator feedback
$\kappa_3$	Coupling constant of driving inhibitor $v$ to activator $u$
$\kappa_4$	Coupling constant of stabilizing inhibitor $w$ to activator $u$
$\varkappa_1$	Offset of driving term $\kappa_{1,\text{eff}}(u)$
τ	Time scale parameter of driving inhibitor $v$
$\theta$	Time scale parameter of stabilizing inhibitor w
κ	Vector of parameters $\boldsymbol{\kappa} = (\kappa_1, \kappa_2, \kappa_3, \kappa_4, \tau, \theta, d_u, d_v, d_w, \lambda)^{\mathrm{T}}$
$\Omega$	Subset of $\mathbb{R}^n$ for which $\boldsymbol{u}$ is solved numerically
$L_x$	Length of domain $\Omega$ parallel to x-coordinate
$\Delta_x$	Spatial discretization length
$\Delta_t$	Temporal discretization length

# **Reduced Dynamics**

$F(u;\kappa)$	Vector field of spatiotemporal dynamics
$\mathcal{D}(\bar{\pmb{u}};\pmb{\kappa})$	Fréchet derivative of $F(u; \kappa)$ at $u = \bar{u}$
$\mathcal{D}^{\dagger}(ar{m{u}};m{\kappa})$	Adjoined operator of $\mathcal{D}(\bar{u}; \kappa)$
${\cal G}$	Goldstone-mode, $\mathcal{D}(\bar{\boldsymbol{u}}, \kappa)\mathcal{G} = 0$
$\mathcal{G}^{\dagger}$	Complementary Goldstone-mode, $\mathcal{D}^{\dagger}(\bar{\boldsymbol{u}}, \kappa)\mathcal{G}^{\dagger} = 0$
${\cal P}$	Propagator mode, generalized eigenmode of operator $\mathcal D$
$\mathcal{P}^{\dagger}$	Complementary propagator mode, generalized eigenmode of opera-
	tor $\mathcal{D}^{\dagger}$
$\mathcal{F}_i$	Complex eigenfunction of operator $\mathcal{D}$ with eigenvalue $v_i$ .
$\mathcal{M}$	Matrix of parameters

Acronyms xix

$\mathcal{L}$	Linear operator
$\kappa_{\rm c}$	Critical control parameter
κ <sub>c</sub>	Vector of parameters having a critical component $\kappa_c$
κ <sub>¢</sub>	Vector of parameters without critical component
$ au_{ m c}$	Drift- or rotational bifurcation point
$c_{x_i}$	Velocity parallel to axis $x_i$
$\bar{c}_{x_i}$	Equilibrium velocity parallel to axis $x_i$
$\omega = \bar{c}_{\phi}$	Angular velocity
Q	Form factor
$\kappa_1(\mathbf{x})$	Parameter inhomogeneity
$\bar{\kappa}_1$	Reference value of parameter inhomogeneity $\kappa_1(x)$
$\hat{\kappa}_1$	Amplitude of parameter inhomogeneity $\kappa_1(x)$
N(u)	Nonlinear functional without constant or linear terms
$T_m = \epsilon^m t$	Time scale
$\boldsymbol{p}(t)$	Position of localized solution
$\alpha(t)$	Amplitude of propagator mode of localized solution
d	Distance between two localized solutions
$d_0$	Binding distance with vanishing interaction
$d_{\rm r}( au)$	Binding distance of rotating bound state
$W_{\rm DS}(d)$	Vector field of distance dependent interaction
$\boldsymbol{W}_{\kappa_1}(\boldsymbol{p})$	Vector field of inhomogeneity induced interaction
F(d)	Central force
$F_{\rm Z}(d)$	Centrifugal force
$V_{\rm ww}(d)$	Interaction potential
$V_{ m v}(\dot{p})$	Kinetic potential
ξ	Scattering parameter

# **Stochastic Time Series Analysis**

$\boldsymbol{q}(t)$	Time-dependent quantity
$\acute{\boldsymbol{q}}(t)$	Solution of Langevin equation
$\boldsymbol{h}(\boldsymbol{q}(t))$	Deterministic dynamics
$\mathbf{\Gamma}(t)$	Fluctuating Langevin force
<u>R</u>	Noise amplitude matrix
$rac{\pmb{R}}{\mathbb{B}_i}$	Bin, subset of measurements
$ ilde{q}_i$	Center of bin $\mathbb{B}_i$
$\Delta_q$	With of bin
$N_i$	Number of events in bin $\mathbb{B}_i$
$\gamma_n$	Vector of normal distributed random numbers
$\hat{\gamma}$	Normal distributed pseudo random number
$v = \dot{p}$	Velocity of dissipative soliton
$v_0 = \bar{c}_x$	Equilibrium velocity
$\Delta_v$	Width of velocity bins
$F_{\rm e}(d) = \frac{1}{d}F(d)$	Interaction
$d_{\mathrm{C}}$	Critical distance with $F_{\rm e}(d) _{d>d_{\rm c}}\approx 0$

# Chapter 1 Introduction

How the leopard got its spots

Proud and handsome in his beautiful coat, the hyena went loping through the jungle. Suddenly he stopped, gazing down at the tortoise who stood in his way looking up at him plaintively. "Hyena, I am in need of your help. I cannot reach the fruit of this tree, but if you were to shake the branches. the fruit would fall down. Will you help me?"

"I'll do even more than you ask," replied the hyena. "I'll take you to the fruit!" Seizing the tortoise between his strong teeth, he jumped up into the tree and put the tortoise down in a fork of branches high above the ground. Then he leaped down again, laughing diabolically at the tortoise's plight before disappearing into the jungle.

Afraid to move, clinging to the branch, the tortoise stayed up there for hours, while the sun slowly dipped over to the west, lengthening the shadow of the tree. Every time he looked down at the ground far below, he felt dizzy and terrified, but he had to keep his eyes open for he knew that help wouldn't come from the skies. At last, with darkness falling and despair growing, the tortoise saw a leopard padding past the tree and cried for help. The leopard leaped gracefully into the tree and brought the frightened tortoise back to the ground. At his request the leopard shook the branches so that the fruit fell to the ground for the tortoise to eat.

The leopard didn't wait to be thanked and was gliding into the gathering darkness when the tortoise called him back. "Leopard, listen to me before you go. You have been very good to me, and I would like to do something for you in return. If you let me paint black spots all over your tawny coat, you will be admired throughout the jungle. Come in the morning when the sun gives us light."

The leopard's dull coat was completely transformed by the black spots that the tortoise painted in with care and artistic skill. 2 1 Introduction

And just as the artist had predicted, when the leopard swaggered through the jungle he was followed by the admiring glances of the other animals.[...]

A fairy tale of the Bantu speaking people of Africa. Retold after a version known from the South African tribes Zulu, Xhosa, Basuto, Bechuana, Herero, and Shangaan [1.1].

**Abstract** The chapter introduces the topic of structure formation, and gives a literature survey to reaction-diffusion systems. It closes with a short guideline how to read the book.

### 1.1 Structure Formation

The oldest evidence for the interest of mankind in structures and patterns in nature is given by the fairy tales of African tribes explaining the beautiful coat patterns of leopards (Fig. 1.1a) and zebras by fantastic events in the past [1.1, 1.12]. These coat patterns are fascinating because of their regular but individual structure showing the high order of a pattern, which has been organized by itself. Comparable regular structures can also be found in the inanimate world: Examples are cloud streets (Fig. 1.1d) or convection cells of heated fluid layers (the famous Rayleigh-Bérnard experiment [1.13], Fig. 1.1g). In all three cases the structures are macroscopic phenomena resulting from the cooperative interaction of many subsystems, which in case of physical systems can be identified as molecules of atmosphere or fluid generating the pattern in an ongoing process. In case of the coat patterns, the subsystems are phenomenologically connected with so-called morphogens determining the coat pattern at a time within the embryonic development of the mammal [1.14]. The phenomenon of the spontaneous development of regular structures in dynamical systems by the cooperative interaction of many subsystems is called self-organization and is investigated with the methods of synergetics [1.15, 1.16]. The rich variety of systems being treated with the methods of synergetics are also summarized as complex systems [1.17, 1.18].

Structures do not only arise close to thermodynamic equilibrium but also far away from it. In the latter case, a flux of energy or matter is essential for the development and preservation of the structure. Far away from thermodynamic equilibrium, the dynamics of a system are described by nonlinear evolution equations. Therefore, the increase of a control parameter beyond a critical value – the so-called bifurcation point – can result in symmetry breaking, which is observable as a transition from the disordered state into an ordered one. These structures are characterized by a balance between non-linearity and dissipation, which stabilizes the structures against small perturbations. Spatial temporal [1.19] and spatiotemporal structures arising far away from thermodynamic equilibrium are called *dissipative structures* [1.20].

1.1 Structure Formation 3

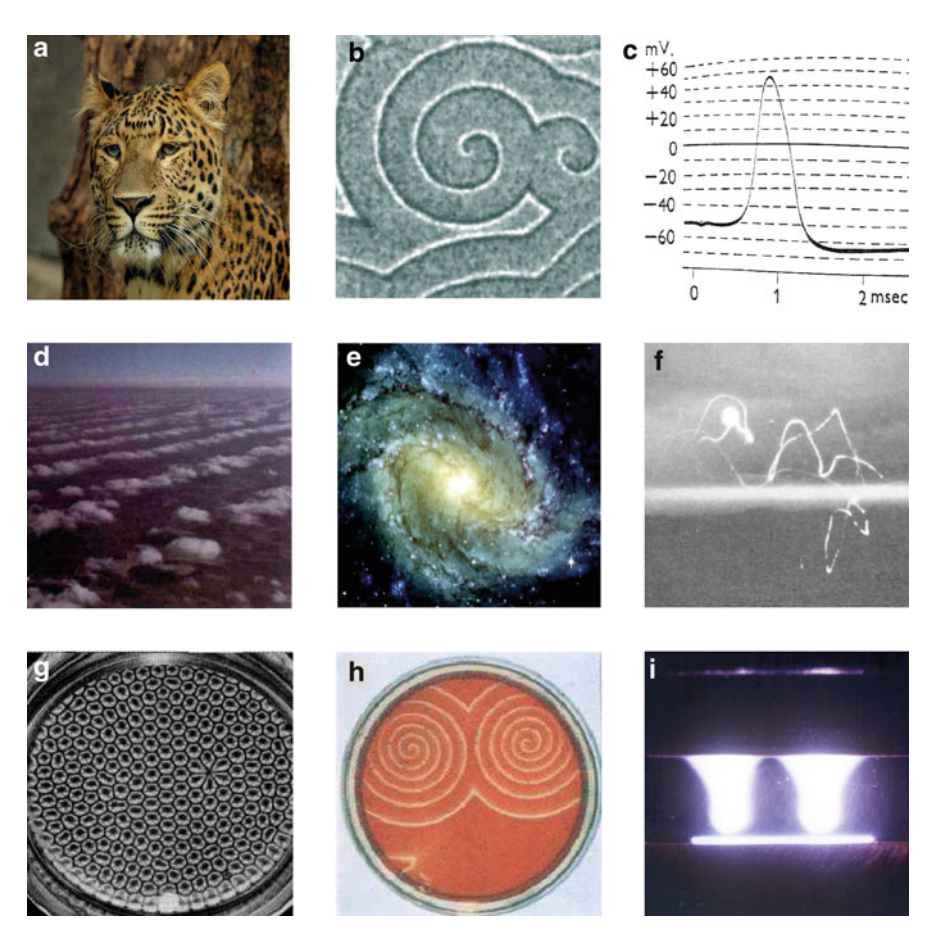


**Fig. 1.1** Examples for spatial and spatiotemporal structures. Sub-figures show patterns (*first column*), spirals (*second column*) and localized structures (*third column*) as examples from animate world (*first row*), inanimate nature (*second row*) and experiment (*third row*) (**a**) leopard [1.2], (**b**) amoeba [1.3], (**c**) nerve pulse on squid axon [1.4], (**d**) cloud streets [1.5, p. 29], (**e**) spiral galaxy M83 [1.6], (**f**) picture of unusual lightning close to the ground [1.7], which was later on identified as ball lightning [1.8, p. 57f], (**g**) convection pattern in silicon oil [1.9], (**h**) spirals in the Belousov-Zhabotinsky-Reaction [1.10], (**i**) filaments in semiconductor gas-discharge system [1.11]

Well-known examples for spatiotemporal order are spiral-like structures: formed by the amoeba of the slime mould *dictyostelium discoideum* (Fig. 1.1b), spiral galaxies (Fig. 1.1e), or spiral waves in the famous Belousov-Zhabotinsky reaction (Fig. 1.1h). Spirals are generic structures in excitable media. They can be characterized by an autocatalytic or self-enhancing process, a following refractory phase and spatial coupling by diffusion. For example, in the Oregonator-model [1.21] of the Belousov-Zhabotinsky reaction, two autocatalytic processes compete with each other, because the reaction product of one process is the reagent of the other process

4 1 Introduction

and the refractory phase starts as soon as the resources of the respective process are used up. By taking diffusion into account, which is relevant in all chemical systems, the Belousov-Zhabotinsky reaction is a typical example for a *reaction-diffusion-system*. Even for galactic dimensions the mechanisms of excitable media are applied. Here, the interstellar dust emitted from the atmosphere of earlier condensed stars enhances the probability of the condensation of new stars, whereas the heating of interstellar dust by developed stars inhibits the occurrence of further condensation processes [1.22], which might explain the formation of certain spiral galaxies of Sc-type [1.23, 1.24]. Therefore, these types of spiral galaxies can be understood as giant pendants of the spirals being observed on earth.

On Earth, the spiral-like structures of slime mould dictyostelium discoideum result from the need to survive. If food, warmth or humidity are lacking, the amoebae will exhale a cyclic adenosine monophosphate (cAMP) signal. This messenger spreads by diffusion and stimulates the receptors of neighbored amoebae which themselves exhale an increased amount of cAMP until their receptors become non-sensitive for a certain time and their cAMP output decays [1.25]. Here, we find the typical characteristics of an active medium: An autocatalytic process in the form of cAMP secretion, a rest period in the form of desensitization of receptors, and, moreover, diffusion. This yields a formation of cAMP-waves spreading from a center and results in spiral-like structures of amoebae (Fig. 1.1b), which travel against the gradient of cAMP concentration (chemotaxis). In the center of the spiral, the amoebae pile up to a fruiting body of  $10^4$ – $10^6$  amoebae whose spores can survive the disadvantageously environmental condition. As the amoebae can act completely independently of each other in more favorable conditions, the discussed aggregation process is not only a nice example for the formation of spiral-like structure in animated nature but also an example where evolution has led to self-organization processes in order to increase the survival of a species.

This slightly extensive discussion of different systems regarding self-organization illustrates the universality underlying structure formation: Systems showing structure formation are very different with respect to their interacting subsystems as well as the spatial and temporal scales on which formation occurs. However, in many cases, it is possible to identify basic principles (e.g. the mechanism of excitable (active) media) which in turn enable an elementary understanding of the observed phenomena.

In this respect, this book focuses on localized self-organized structures, which are observed in systems that are far away from thermodynamic equilibrium. The most famous and important example in this context is given by nerve pulses (Fig. 1.1c). Modelling these localized structures also leads to the concept of reaction-diffusion-systems [1.26–1.29]. A spectacular and not yet completely understood phenomenon of self-organized localized structures in inanimate nature is the occurrence of ball lightning (Fig. 1.1f), which is in contrast to the manageable current filaments in semiconductor gas-discharge-systems (Fig. 1.1i). These structures are particularly suitable for the investigation in laboratories, because the experimental setup is easy to handle and non-equilibrium states relax after changes of control parameter on

a time scale of millisecond, whereas transients (e.g. in hydrodynamic or chemical systems) decay on a time scale of minutes.

Current filaments are solitary structures with distinctive characteristics of particles, like scattering, the formation of bound states, as well as the generation and annihilation of particles [1.30]. Such objects are called *dissipative solitons* [1.31, 1.32], which resembles the analogy to localized waves in conservative systems, so-called *solitons*, occurring as surface waves on water [1.33] or solutions of Sine-Gordon or nonlinear Schrödinger equation [1.34]. However, as a unique nomenclature hasn't been accepted, different notations like *puls* [1.35], *spot* [1.36] or *autosoliton* [1.37] can be found in the literature.

This book focuses in particular on dissipative solitons in spatially extended systems, which are observed in reaction-diffusion systems with two inhibiting components. While one inhibitor reacts slowly on changes of the activator, the second one follows changes of the activator quickly. Therefore the slow inhibitor destabilizes the localized structure and triggers the propagation of the dissipative soliton and might be called the driving inhibitor. On the other hand the fast inhibitor inherently stabilizes the shape of the activator peak and is called the stabilizing inhibitor. In the course of the book the complex dynamics of dissipative solitons enabled by one activator and two inhibitors are investigated by large scale numerical computations being accomplished by theoretical and experimental investigations, which lead to a comprehensive understanding of dissipative solitons in reaction-diffusion systems.

# 1.2 A Very Short Literature Survey

# 1.2.1 Self-organization and Localized Structures

The variety of self-organization phenomena in animate and inanimate nature is reflected by the rich variety of publications on this topic. Therefore, a comprehending survey can hardly be found and I can only outline the connection between some publications, that are, at least from my point of view, important and interesting.

An excellent introduction to the topic of structure formation is given in the book of Ball [1.38], the review article of Cross and Hohenberg [1.39] and the textbooks of Nishiura [1.40] and Hoyle [1.41]. The fundamental methods of synergetics are introduced by Haken [1.15, 1.16], while the fundamentals of reaction-diffusion systems are discussed by Fife [1.42] and Smoller [1.43]. Conceptually, the application range of synergetics covers all sciences and fields of research [1.17, 1.18], such as: biology [1.14, 1.44–1.48], chemistry [1.49–1.53], sociology [1.54], optical systems [1.55–1.57], semiconductors [1.58, 1.59], hydrodynamical systems [1.60], liquid crystals [1.61], granular media [1.62], and gas discharge systems [1.63, 1.64]. This book focuses on localized structures far away from thermodynamic equilibrium [1.65]. Examples are nerve pulses [1.29, 1.66], pulses in electrical networks [1.28, 1.67],

6 1 Introduction

oscillons in granular media [1.68, 1.69], concentration drops of chemical reagents [1.70–1.73], solitary structures on parametrically driven liquid films [1.74], dissipative solitons in optical systems [1.75], filaments in semiconductors [1.76, 1.77] and gases being powered by microwaves [1.78], and current filaments in gas discharge systems [1.30, 1.79–1.83]. While the dissipative solitons of optical systems are used for real applications, e.g. to optical communication networks [1.84], applications concerning self-organized computation are in a period of development [1.85–1.87]. Examples include the computation of Voronoi diagrams [1.88, 1.89] or solving the optimal path problem [1.90,1.91]. It has also been suggested that dissipative solitons might be used for the transportation of micro-freight [1.92] or act as bits of storage elements [1.75, 1.93–1.95]. A broader overview on dissipative solitons in different kind of systems can be found in the book edited by Ankiewicz and Akhmediev [1.96, 1.97] and the review of Purwins et al. [1.65].

The investigation of dissipative solitons in reaction-diffusion systems started in the middle of the last century and was carried out simultaneously with the investigation of other dissipative structures in reaction-diffusion systems, such as fronts, patterns and spirals. At this point, it is appropriate to outline the connections and differences of these four structure categories.

# 1.2.2 Spirals

Spirals are a generic structure of excitable media [1.98], which – although being spatially extended – have an identifiable center [1.99]. From this point of view, they can be investigated in the context of localized structures [1.100, 1.101]. Thus, with patterns, spirals share the property of spatial extension, while, with dissipative solitons, they share the property of localization. Slightly curved spiral arms propagate with a velocity that is proportional to the local curvature. This shows an elementary connection to front propagation in two-dimensional media [1.102]. In the context of this book, spirals typically occur from moving dissipative solitons, which are not stabilized by a global or local feedback.

# 1.2.3 Pattern

Physical/chemical pattern typically emerge from homogeneous media that are destabilized by a spatial modulation [1.103]. Therefore, they consist of basic structure elements like spots or stripes that are uniformly distributed. If a system exhibits co-existence of two different basic structures, the transition between differently patterned domains will be interpreted in terms of a front formalism [1.104]. The same holds for the transition between a pattern and a homogeneously oscillating domain, the so-called Hopf-domain [1.105, 1.106].

Patterns can also emerge from a homogeneous system being destabilized by a critical nucleus, from which a pattern starts spreading [1.107] until the domain is completely covered by the pattern. This *pattern front* can be stopped by suitable feedback mechanisms [1.108], so that the periodic structure coexists with the homogeneous part of the domain as a stable state of the system. Frequently, one observes hexagonal ordered states being build from continuously attaching and separating single dissipative solitons [1.30, 1.80, 1.109], which indicates that such clusters can be identified as crystalline phases of dissipative solitons [1.110].

# 1.2.4 Fronts

Fronts connect two different stable states of a system and are a generic structure of bistable media. In the case of excitable bistable media, fronts can connect to each other, so that dissipative solitons [1.111] or more complicated structures like three-dimensional rings and knots are formed [1.112]. Such complex structures require the non-monotonical relaxation of fronts against the homogeneous ground states of the system [1.31]. These oscillating tails result into a distance depending interaction between fronts that is either repulsive or attractive. The alternating sign of the interaction causes well defined distances with vanishing interaction, which enable the formation of stable bound states of fronts.

Because fronts are basic localized structures in one-dimensional bistable systems, they are of special interest for investigating the dynamics of localized dissipative structures [1.113–1.123]. In this context, the ansatz of Bode [1.124] is of special importance, because, close to the onset of propagation, his approach enables the description of front dynamics on the basis of a reduced set of degrees of freedom, which can be identified as amplitudes of unstable modes and coupled neutral modes.

# 1.2.5 Dissipative Solitons

Already, in the first experimental investigations on front dynamics in bistable chemical systems, assumptions were considered that the observations could be related to the phenomenon of nerve conduction [1.125]. As a corollary to the measurements of Hodgkin and Huxley [1.26], the scientists FitzHugh [1.27] and Nagumo [1.28] developed a model in form of a two-component reaction-diffusion system explaining nerve pulses as non-equilibrium structures formed from an autocatalytic component (*activator*) and an inhibiting component (*inhibitor*). In this model, the pulse itself is generated by a finite excitation of the homogeneous ground state of the system, which relaxes to the characteristic shape of the pulse. For the first time, there was a simple mathematical model available, which was based on field equations and enables (analytically or by means of computer simulations) the investigation of the dynamics of dissipative solitons. Further extensive investigations were triggered by McKean's suggestion to simplify nonlinearities as

8 1 Introduction

piecewise linear function [1.126], which enables the exact calculation of the shape and existence of dissipative solitons as well as their instabilities [1.127, 1.128]. The larger part of investigations concerning dissipative solitons concentrates on one-dimensional reaction-diffusion systems [1.37, 1.129–1.134], because in this case the dissipative solitons can be easily stabilized by an inhibiting control field and elementary interaction phenomena like scattering [1.135, 1.136], the formation of bound states [1.137] or the generation of dissipative solitons [1.107, 1.138] can be analytically treated.

Furthermore, complex stationary structures in two- or three-dimensional systems can be investigated on the basis of an activator-inhibitor model [1.112, 1.139]. Complications will come into play if one considers a propagating dissipative soliton as solution of a two-dimensional reaction diffusion system. This happens, because the structure moves due to a relative shift of its activating and its inhibiting component. As a consequence, the localized structure is not always stabilized perpendicular to its direction of motion. Only in extreme parameter regimes, where numerical solutions are difficult to obtain, it can be analytically shown that propagating dissipative solitons exist as stable solutions of two-component, twodimensional, reaction-diffusion systems [1.140]. In order to provide a stabilization of moving pulses in higher dimensional systems, some authors prefer a global feedback [1.141, 1.142]. This approach has the disadvantage of preventing only symmetric perturbations like the simultaneous growth or shrinkage of all dissipative solitons, but cannot prevent asymmetric perturbations like the growth of one pulse and the shrinkage of another one. This problem can be solved by taking into account another inhibiting component, which has a short relaxation time and a large diffusion constant [1.143, 1.144]. This additional inhibitor acts as a local feedback mechanism. Consequently, the model system can be treated in terms of a threecomponent reaction-diffusion system. Models of this type are not only investigated with regard to localized structures [1.145-1.149] but also with regard to wave instabilities of homogeneous basic states [1.104, 1.150]. Often it is convenient to discuss the stability and dynamics of dissipative solitons on basis of numerical solutions. Specialized algorithms for solving the reaction-diffusion systems of this book are presented in [1.151] and [1.152, Chap 4].

# 1.3 How to Read This Book

There are several approaches for reading this book, which might depend on the focus or background of the reader. However, the introduction is the best starting point for all of them. The second chapter is devoted to the experimental evidence of dissipative solitons in continuously driven systems with strong dissipation. The chapter covers spatially extended chemical reactions and semiconductor-gas-discharge systems and gives an illustrative overview on the observations undertaken in the last two decades. Although the first two chapters act as a kind of motivation for the following chapters, they can be easily skipped, if the reader is more interested in a more theoretical point of view.

References 9

The third chapter discusses the basic mechanisms of reaction-diffusion systems leading to the formation of localized structures. It is written as a practical guide to the most basic mechanisms of reaction-diffusion systems obtained since Turing's revolutionary concept. Therefore, this chapter might be considered as good starting points for students becoming acquainted with the topic.

Scientists, with interests in the foundations of dynamics and interaction of dissipative solitons, will find Chaps. 4 and 5 of interest. In Chap. 6 the theoretical considerations of the foregoing chapters are related to experimental observations.

A variety of generation and annihilation phenomena is discussed in Chap. 7 on the basis of simulations, which are discussed, wherever possible, in the context of the basic mechanisms introduced in Chap. 3. The book closes with a summary on the most important findings discussed in this book.

# References

- F. Stuart, The Magic Horns. Folk Tales from Africa, 2nd edn. (Addison-Wesley, Reading, 1976)
- 1.2. M.L. Nguyen, North china leopard (panthera pardus japonensis) seen through the glass of its cage. From the zoological garden of the Jardin Des Plantes in Paris. online (2006). http://commons.wikimedia.org/wiki/File:Panthera\_pardus\_japonensis\_JdP.jpg
- 1.3. C. Weijer, in *The Self-Made Tapestry. Pattern Formation in Nature*, ed. by P. Ball (Oxford University Press, Oxford, 1999), p. 71. Published with kind permission of the author
- 1.4. A.L. Hodgkin, Biol. Rev. Camb. Philos. Soc. 26(4), 339 (1951). Figure 1.1c published with kind permission of Cambridge University Press
- R. Scorer, Clouds of the World. A Complete Colour Encyclopedia, 1st edn. (Lothian, Melbourne, 1972)
- 1.6. E.O. for Astronomical Research in the Southern Hemisphere. Vlt commissioning data now publicly available. ESO Press Release 18/99, URL: http://eso.org/outreach/press-rel/pr-1999/pr-18-99.html (1999). Figure 1.1e published with kind permission of ESO Public Affairs Department
- 1.7. R.E. Holzer, E.J. Workman, J. Appl. Phys. 10, 659 (1939). Figure 1.1f published with kind permission of American Institut of Physics. Copyright (1939)
- 1.8. S. Singer, *Nature of Ball Lightning* (Plenum, New York, 1971)
- 1.9. E.L. Koschmieder, Adv. Chem. Phys. 26, 177 (1974)
- 1.10. F. Goro, On the Nature of Things. The Scientific Photography of Fritz Goro (Aperture, New York, 1993). Figure 1.1h published with kind permission of Thomas Goreau
- 1.11. H. Willebrand, Strukturbildung in lateral ausgedehnten Gasentladungssystemen. Dissertation, Institut für Angewandte Physik, Westfälische Wilhelms-Universität Münster (1992). Figure 1.1i published with kind permission of the author.
- 1.12. W.L. Paye, M.H. Lippert, Why Leopard has Spots. Dan Stories from Liberia (Fulcrum, Colorado, 1998)
- 1.13. A.V. Getling, Rayleigh-Bénard Convection. Structures and Dynamics. Advanced Series in Nonlinear Dynamics, vol. 11 (World Scientific, Singapore, 1998)
- 1.14. J.D. Murray, *Mathematical Biology* (Springer, Berlin, 1993)
- 1.15. H. Haken, Synergetics. An Introduction. Nonequilibrium Phase Transitions and Self-Organization in Physics, Chemistry and Biology. Springer Series in Synergetics, vol. 1, 3rd edn. (Springer, Berlin, 1983)
- 1.16. H. Haken, Advanced Synergetics. Instability Hierarchies of Self-Organizing Systems and Devices. Springer Series in Synergetics, vol. 20, 2nd edn. (Springer, Berlin, 1987)

10 1 Introduction

1.17. F.T. Arecchi, Complexity in Science: Models and Metaphors, in *The Emergence of Complexity in Mathematics, Physics, Chemistry and Biology*, ed. by B. Pullman. Pontificiae Academiae Scientiarum Scripta Varia, vol. 89 (Princeton University Press, Princeton, 1996), pp. 129–160

- 1.18. S. Solomon, E. Shir, Europhys. News **34**(2), 54 (2003)
- 1.19. A.H. Nayfeh, D.T. Mook, Nonlinear Oscillations (Wiley, New York, 1995)
- 1.20. I. Prigogine, Structure, Dissipation and Life (North-Holland, Amsterdam, 1969), pp. 23-53
- 1.21. R.J. Field, R.M. Noyes, J. Chem. Phys. **60**(5), 1877 (1974)
- 1.22. D. Cartin, G. Khanna, Phys. Rev. E 65, 016120 (2001). doi: 10.1103/PhysRevE.65.016120
- 1.23. L. Smolin, Galactic disks as reaction-diffusion systems (1996), arXiv:astro-phy/9612033
- 1.24. L. Smolin, Philos. Trans. R. Soc. Lond. A 361, 1081 (2003). doi: 10.1098/rsta.2003.1185
- 1.25. A.F.M. Marée, From pattern formation to morphogenesis. Multicellular coordination in dictyostelium discoideum. Dissertation, Faculteit Biologie, Universiteit Utrecht. (2000), http://www.iam.ubc.ca/~stan/Thesis/
- 1.26. A.L. Hodgkin, A.F. Huxley, J. Physiol. 117, 500 (1952)
- 1.27. R. FitzHugh, Biophys. J. 1, 445 (1962)
- 1.28. J. Nagumo, S. Arimoto, S. Yoshizawa, Proc. IRE **50**, 2061 (1962)
- 1.29. C. Koch, Biophysics of Computation. Information Processing in Single Neurons. Computational Neuroscience (Oxford University Press, New York, 1999)
- 1.30. Yu.A. Astrov, H.-G. Purwins, Phys. Lett. A **283**, 349 (2001). doi: 10.1016/S0375-9601(01) 00257-2
- 1.31. M. Bode, H.-G. Purwins, Phys. D 86, 53 (1995)
- 1.32. C.I. Christov, M.G. Velarde, Phys. D **86**, 323 (1995)
- 1.33. J.S. Russell, in Report of the fourteenth meeting of the British Association for the Advancement of Science. York 1844, London (1845), pp. 311–390, Fig. XLVII–LVII
- 1.34. M. Remoissenet, Waves Called Solitons: Concepts and Experiments, 3rd edn. (Springer, Berlin, 1999)
- 1.35. C. Elphick, E. Meron, E.A. Spiegel, SIAM J. Appl. Math. **50**(2), 490 (1990)
- D. Haim, G. Li, Q. Ouyang, W.D. McCormick, H.L. Swinney, A. Hagberg, E. Meron, Phys. Rev. Lett. 77(1), 190 (1996)
- 1.37. B.S. Kerner, V.V. Osipov, Autosolitons. A New Approach to Problems of Self-organization and Turbulence. Fundamental Theories of Physics, vol. 61 (Kluwer, Dordrecht, 1994)
- 1.38. P. Ball, The Self-made Tapestry. Pattern Formation in Nature (Oxford University Press, Oxford, 1999)
- 1.39. M.C. Cross, P.C. Hohenberg, Rev. Mod. Phys. **65**(3), 851 (1993)
- 1.40. Y. Nishiura, Far-From-Equilibrium Dynamics, Translations of Mathematical Monographs, vol. 209 (American Mathematical Society, Providence, 2002)
- 1.41. R.C. Hoyle, Pattern Formation. Introduction to Methods, 2nd edn. (Cambridge University Press, Cambridge, 2007)
- 1.42. P.C. Fife, *Mathematical Aspects of Reacting and Diffusing Systems*. Lecture Notes in Biomathematics, vol. 28 (Springer, Berlin, 1979)
- 1.43. J. Smoller, *Shock Waves and Reaction Diffusion Equations*, 2nd edn. (Springer, New York, 1994)
- 1.44. A.T. Winfree, When Time Breaks Down: The Three-Dimensional Dynamics of Electrochemical Waves and Cardiac Arrhythmias (Princeton University Press, Princeton, 1987)
- 1.45. A.J. Koch, H. Meinhardt, Rev. Mod. Phys. **66**(4), 1481 (1994)
- 1.46. E. Mosekilde, O.G. Mouritsen (eds.), Modelling the Dynamics of Biological Systems. Nonlinear Phenomena and Pattern Formation (Springer, Berlin, 1995)
- 1.47. W. Alt, A. Deutsch, G. Dunn (eds.), *Dynamics of Cell and Tissue Motion. Mathematics and Biosciences in Interaction* (Birkhäuser, Basel, 1997)
- 1.48. H. Meinhardt, Int. J. Bifurc. Chaos 7, 1 (1997)
- 1.49. Y. Kuramoto, Chemical Oscillations, Waves and Turbulence. Springer Series in Synergetics, vol. 19 (Springer, Berlin, 1984)

References 11

1.50. R.J. Field, M. Burger (eds.), Oscillations and Traveling Waves in Chemical Systems (Wiley, New York, 1985)

- 1.51. R. Kapral, K. Showalter (eds.), *Chemical Waves and Patterns*. Understanding Chemical Reactivity, vol. 10 (Kluwer, Dordrecht, 1995)
- 1.52. A. de Wit, Adv. Chem. Phys. 109, 435 (1999)
- 1.53. G. Ertl, Adv. Catal. 45, 1 (2000)
- 1.54. W. Weidlich, G. Haag, Concepts and Models of a Quantitative Sociology. The Dynamics of Interacting Populations. Springer Series in Synergetics, vol. 14 (Springer, Berlin, 1983)
- 1.55. M.A. Vorontsov, W.B. Miller (eds.), Self-organization in Optical Systems and Application in Information Technology, 2nd edn. (Springer, Berlin, 1998)
- 1.56. F.T. Arecchi, S. Boccaletti, P. Ramazza, Phys. Rep. **328**(1–2), 1 (1999)
- 1.57. T. Ackemann, W. Lange, Appl. Phys. B **72**, 21 (2001)
- 1.58. K. Aoki, Nonlinear Dynamics and Chaos in Semiconductors (Institute of Physics Publishing, Bristol/Philadelphia, 2001)
- 1.59. E. Schöll, Nonlinear Spatio-Temporal Dynamics and Chaos in Semiconductors. Cambridge Nonlinear Science Series, vol. 10 (Cambridge University Press, Cambridge, 2001)
- 1.60. T.E. Faber, Fluid Dynamics for Physicists, 2nd edn. (Cambridge University Press, Cambridge, 1997)
- 1.61. A. Buka, L. Kramer (eds.), *Pattern Formation in Liquid Crystals*. Partially Ordered Systems (Springer, Berlin, 1996)
- 1.62. G.H. Ristow, Pattern Formation in Granular Materials. Springer Tracks in Modern Physics, vol. 164 (Springer, Berlin, 2000)
- 1.63. H. Engel, F.-J. Niedernostheide, H.-G. Purwins, E. Schöll, Self-organization in Activator-Inhibitor-Systems: Semiconductors, Gas-Discharge and Chemical Media (Wissenschaftund Technik-Verlag, Berlin, 1996)
- 1.64. H.-G. Purwins, Yu.A. Astrov, I. Brauer, in *The 5th Experimental Chaos Conference*, Orlando, 28 June 1 July 1999, ed. by M. Ding, W.L. Ditto, L.M. Pecora, M.L. Spano (World Scientific, Singapore, 2001), pp. 3–13
- 1.65. H.-G. Purwins, H.U. Bödeker, S. Amiranashvili, Adv. Phys. 59(5), 485 (2010). doi: 10. 1080/00018732.2010.498228
- 1.66. A.L. Hodgkin, Biol. Rev. Camb. Philos. Soc. 26(4), 339 (1951)
- 1.67. A. Scott, Active and Nonlinear Wave Propagation in Electronics (Wiley, New York, 1970)
- 1.68. P.B. Umbanhowar, F. Melo, H.L. Swinney, Nature **382**(6594), 793 (1996)
- 1.69. C. Crawford, H. Riecke, Phys. D **129**, 83 (1999)
- 1.70. H.H. Rotermund, S. Jakubith, A. von Oertzen, G. Ertl, Phys. Rev. Lett. 66(23), 3083 (1991). doi: 10.1103/PhysRevLett.66.3083
- 1.71. K.J. Lee, W.D. McCormick, J.E. Pearson, H.L. Swinney, Nature **369**, 215 (1994). doi: 10.1038/369215a0
- 1.72. V.K. Vanag, I.R. Epstein, Chaos 17(3), 037110 (2007). doi: 10.1063/1.2752494
- 1.73. D.G. Míguez, V.K. Vanag, I.R. Epstein, Proc. Natl. Acad. Sci. USA 104(17), 6992 (2007). doi: 10.1073/pnas.0611438104
- 1.74. O. Lioubashevski, H. Arbell, J. Fineberg, Phys. Rev. Lett. **76**(21), 3959 (1996)
- 1.75. B. Schäpers, M. Feldmann, T. Ackemann, W. Lange, Phys. Rev. Lett. 85, 748 (2000)
- 1.76. Yu.A. Astrov, Semiconductors **27**(11–12), 1084 (1993)
- 1.77. V.V. Bel'kov, J. Hirschinger, V. Novák, F.-J. Niedernostheide, S.D. Ganichev, W. Prettl, Nature 397(4), 398 (1999)
- 1.78. Y.H. Ohtsuki, H. Ofuruton, Nature **350**, 139 (1991)
- 1.79. F.-J. Niedernostheide, B.S. Kerner, H.-G. Purwins, Phys. Rev. B 46, 7559 (1992)
- 1.80. Yu.A. Astrov, Yu.A. Logvin, Phys. Rev. Lett. **79**(16), 2983 (1997)
- 1.81. I. Müller, E. Ammelt, H.-G. Purwins, Phys. Rev. Lett. 82, 3428 (1999)
- 1.82. I. Brauer, M. Bode, E. Ammelt, H.-G. Purwins, Phys. Rev. Lett. 84(18), 4104 (2000)
- 1.83. S. Nasuno, Chaos **13**(3), 1010 (2003)
- 1.84. J. Martensson, A. Berntson, IEEE Photonics Technol. Lett. 13(7), 666 (2001)

12 1 Introduction

1.85. A. Adamatzky, *Computing in Nonlinear Media and Automata Collectives* (Institute of Physics Publishing, Bristol, 2001)

- A. Adamatzky, Chaos, Solitons Fractals 21(5), 1259 (2004). doi: 10.1016/j.chaos.2003.12. 068
- 1.87. A. Adamatzky, in *Unconventional Programming Paradigms*. Lecture Notes in Computer Science, vol. 3566 (Springer, Berlin, 2005), pp. 33–46. doi: 10.1007/11527800\_3
- A.L. Zanin, A.W. Liehr, A.S. Moskalenko, H.-G. Purwins, App. Phys. Lett. 81(18), 3338 (2002). doi: 10.1063/1.1518775
- B. de Lacy Costello, A. Adamatzky, N. Ratcliffe, A.L. Zanin, A.W. Liehr, H.-G. Purwins, Int. J. Bifurc. Chaos 14(7), 2187 (2004). doi: 10.1142/S021812740401059X
- 1.90. J.A. Sepulchre, A. Babloyantz, L. Stells, in *Proceedings of the International Conference on Artificial Neural Networks*, ed. by T. Kohonen, K. Makisara, O. Simula, J. Kangas (Elsevier, Amsterdam, 1991), p. 1265
- A. Mikhailov, K. Showalter, Phys. Rep. 425(2–3), 79 (2006). doi: 10.1016/j.physrep.2005.
   11.003
- T. Ichino, T. Asahi, H. Kitahata, N. Magome, K. Agladze, K. Yoshikawa, J. Phys. Chem. C 112(8), 3032 (2008). doi: 10.1021/jp7097922
- 1.93. P. Coullet, C. Riera, C. Tresser, Chaos Interdiscip. J. Nonlinear Sci. 14(1), 193 (2004). doi: 10.1063/1.1642311
- 1.94. A. Kaminaga, V.K. Vanag, I.R. Epstein, Angew. Chem. Int. Ed. 45, 3087 (2006). doi: 10.1002/anie.200600400
- H.-G. Purwins, AIP Conf. Proc. 993(1), 67 (2008). doi: 10.1063/1.2909178. http://link.aip. org/link/?APC/993/67/1
- 1.96. A. Ankiewicz, N. Akhmediev (eds.), *Dissipative Solitons*. Lecture Notes in Physics (Springer, Berlin, 2005)
- 1.97. N. Akhmediev, A. Ankiewicz (eds.), Dissipative Solitons: From Optics to Biology and Medicine, Lecture Notes in Physics, vol. 751 (Springer, Heidelberg, 2008). doi: 10.1007/ 978-3-540-78217-9
- 1.98. E. Meron, Phys. Rep. 218(1), 1 (1992)
- 1.99. D. Barkley, Phys. Rev. Lett. 72(1), 164 (1994)
- 1.100. J. Schütze, O. Steinbock, S.C. Müller, Nature **356**(6364), 45 (1992)
- 1.101. S. Komineas, F. Heilmann, L. Kramer, Phys. Rev. E 63(011103), 1 (2000)
- 1.102. A.S. Mikhailov, Foundations of Synergetics I. Distributed Active Systems. Springer Series in Synergetics, vol. 51 (Springer, Berlin, 1990)
- 1.103. A.M. Turing, Phil. Trans. R. Soc. B 237, 37 (1952)
- 1.104. E.M. Nicola, M. Or-Guil, W. Wolf, M. Bär, Phys. Rev. E 65(055101), 1 (2002)
- 1.105. G. Heidemann, M. Bode, H.-G. Purwins, Phys. Lett. A 177, 225 (1993)
- 1.106. M. Or-Guil, M. Bode, Phys. A 249 (1998)
- 1.107. P. Coullet, C. Riera, C. Tresser, Phys. Rev. Lett. 84(14), 3069 (2000)
- 1.108. A.W. Liehr, M. Bode, H.-G. Purwins, in High Performance Computing in Science and Engineering 2000. Transactions of the High Performance Computing Center, Stuttgart (HLRS) 2000, ed. by E. Krause, W. Jäger (Springer, Berlin, 2001), pp. 425–439
- 1.109. Yu.A. Astrov, Phys. Rev. E **67**(035203(R)), 1 (2003)
- 1.110. M.C. Röttger, Numerische Untersuchungen zur reduzierten Dynamik dissipativer Solitonen in einem dreikomponentigen Reaktions-Diffusions-System. Master's thesis, Institut für Angewandte Physik, Westfälische Wilhelms-Universität Münster (2003)
- 1.111. M. Bode, Beschreibung strukturbildender Prozesse in eindimensionalen Reaktions– Diffusions–Systemen durch Reduktion auf Amplitudengleichungen und Elementarstrukturen. Dissertation, Institut für Angewandte Physik, Westfälische Wilhelms-Universität Münster (1993)
- 1.112. A. Malevanets, R. Kapral, Phys. Rev. Lett. 77(4), 767 (1996)
- 1.113. A. Hagberg, E. Meron, Chaos **4**(3), 477 (1994)
- 1.114. A. Hagberg, E. Meron, Nonlinearity 7, 805 (1994). doi: 10.1088/0951-7715/7/3/006
- 1.115. M. Bode, A. Reuter, R. Schmehling, H.-G. Purwins, Phys. Lett. A 185, 70 (1994)

References 13

- 1.116. G. Flätgen, K. Krischer, Phys. Rev. E 51, 3997 (1995)
- 1.117. G. Haas, M. Bär, I.G. Kevrekidis, P.B. Rasmussen, H.H. Rotermund, G. Ertl, Phys. Rev. Lett. 75, 3560 (1995)
- 1.118. A. Malevanets, A. Careta, R. Kapral, Phys. Rev. E 52(5), 4724 (1995)
- 1.119. P. Schütz, M. Bode, V.V. Gafiichuk, Phys. Rev. E 52, 4465 (1995)
- 1.120. R.D. Benguria, M.C. Depassier, Phys. Rev. E 77(6), 1171 (1996)
- 1.121. A. Hagberg, E. Meron, Phys. Rev. Lett. **78**(6), 1166 (1997)
- 1.122. M. Sheintuch, O. Nehkamkina, Phys. Rev. E **63**(056120), 1 (2001)
- 1.123. Y. Morita, H. Ninomiya, Sugaku Expos. 23, 213 (2010)
- 1.124. M. Bode, Phys. D 106(3-4), 270 (1997)
- 1.125. R. Luther, Zeitschrift für Elektrochemie 12, 596 (1906)
- 1.126. H.P. McKean Jr., Adv. Math. 4, 209 (1970)
- 1.127. S. Koga, Y. Kuramoto, Prog. Theor. Phys. **63**(1), 106 (1980)
- 1.128. T. Ohta, M. Mimura, R. Kobayashi, Phys. D 34, 115 (1989)
- 1.129. J. Rinzel, J.B. Keller, Biophys. J. **13**(12), 1313 (1972)
- 1.130. R. Dohmen, Entwicklung von Modellgleichungen zur Beschreibung nichtlinearer Systeme und Untersuchung der Lösungsvielfalt mit analytischen und numerischen Mitteln. Dissertation, Institut für Angewandte Physik, Westfälische Wilhelms-Universität Münster (1991)
- 1.131. C. Elphick, G.R. Ierley, O. Regev, E.A. Spiegel, Phys. Rev. A 44(2), 1110 (1991)
- 1.132. C. Elphick, A. Hagberg, B.A. Malomed, E. Meron, Phys. Lett. A 230(1-2), 33 (1997)
- 1.133. V.V. Osipov, Phys. D 93, 143 (1996)
- 1.134. H. Hempel, I. Schebesch, L. Schimansky-Geier, Eur. Phys. J. B 2, 399 (1998)
- 1.135. T. Ohta, J. Kiyose, M. Mimura, J. Phys. Soc. Jpn. **66**(5), 1551 (1997)
- 1.136. S.I. Ei, M. Mimura, M. Nagayama, Phys. D 165(3–4), 176 (2002). doi: 10.1016/ S0167-2789(02)00379-2
- 1.137. M. Or-Guil, I.G. Kevrekidis, M. Bär, Phys. D 135, 154 (2000)
- 1.138. Y. Nishiura, D. Ueyama, Phys. D 130, 73 (1999)
- 1.139. C.P. Schenk, P. Schütz, M. Bode, H.-G. Purwins, Phys. Rev. E 57(6), 6480 (1998)
- 1.140. L.M. Pismen, Phys. Rev. Lett. 86(15), 548 (2001)
- 1.141. K. Krischer, A. Mikhailov, Phys. Rev. Lett. **73**(23), 3165 (1994)
- 1.142. T. Ohta, Phys. D **151**(1), 61 (2001)
- 1.143. C.P. Schenk, M. Or-Guil, M. Bode, H.-G. Purwins, Phys. Rev. Lett. 78, 3781 (1997)
- 1.144. A. Doelman, P. van Heijster, T. Kaper, J. Dyn. Differ. Equ. 21(1), 73 (2009). doi: 10.1007/ s10884-008-9125-2
- 1.145. M. Suzuki, T. Ohta, M. Mimura, H. Sakaguchi, Phys. Rev. E **52**(4), 3645 (1995)
- 1.146. R. Woesler, P. Schütz, M. Bode, M. Or-Guil, H.-G. Purwins, Phys. D 91(4), 376 (1996)
- 1.147. M. Or-Guil, M. Bode, C.P. Schenk, H.-G. Purwins, Phys. Rev. E 57(6), 6432 (1998)
- 1.148. Y. Nishiura, T. Teramoto, K.I. Ueda, Chaos 13(3), 962 (2003)
- 1.149. Y. Nishiura, T. Teramoto, K.I. Ueda, Phys. Rev. E 67(056210) (2003)
- 1.150. A.M. Zhabotinsky, M. Dolnik, I.R. Epstein, J. Chem. Phys. 103(23), 10306 (1995)
- 1.151. A.W. Liehr, A.S. Moskalenko, M.C. Röttger, J. Berkemeier, H.-G. Purwins, in *High Performance Computing in Science and Engineering '02. Transactions of the High Performance Computing Center Struttgart (HLRS) 2002*, ed. by E. Krause, W. Jäger (Springer, Berlin, 2003), pp. 48–61
- 1.152. A.W. Liehr, Dissipative Solitonen in Reaktions-Diffusions-Systemen. Dissertation, Institut für Angewandte Physik, Westfälische Wilhelms-Universität Münster (2003)

# **Chapter 2 Experimental Observations**

An experiment is a device to make Nature speak intelligibly. After that one has only to listen.

George Wald [2.1]

**Abstract** Starting points for getting acquainted with the phenomena of dissipative solitons are chemical reaction diffusion systems and a planar semiconductor-gas-discharge system. These systems exhibit dissipative solitons in the form of self-organized localized concentration spots and current density filaments, respectively. The chapter discusses the experiments and concentrates on the phenomena being directly related to the particle-like characteristics of dissipative solitons in spatially extended systems. These are the dynamics of single dissipative solitons, their mutual interaction by scattering and formation of bound states, as well as generation and annihilation processes. Due to the focus of the book, only continuously driven experiments are considered.

# 2.1 Chemical Systems

# 2.1.1 Overview

Since the first successful experimental realization of Turing patterns in a reaction-diffusion system in the beginning of the 1990s, which was undertaken by de Kepper and coworkers in the chlorite-iodate-malonic-acid (CIMA) system [2.2], the number of systems showing stationary patterns has increased significantly and the focus of research has changed to the control of spatio-temporal structure formation [2.3,2.4]. Nearly at the same time another important experimental observation was reported, namely the self-organization of localized concentration spots in a surface reaction [2.5]. These dissipative solitons propagate in a lateral extended system and interact

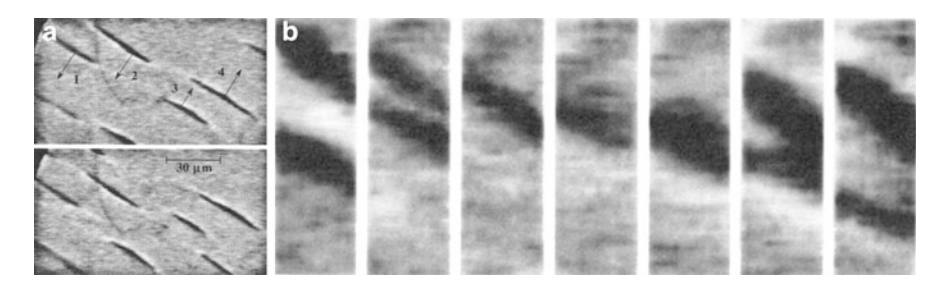


**Fig. 2.1** Propagating and interacting dissipative solitons observed as concentration peaks of atomic oxygen adsorbed on the (110) face of a platinum crystal under steady-state conditions of catalytic CO oxidation. Regions with increased oxygen concentration appear *dark*. (a) Two PEEM images recorded with a time interval of 3.0 s from a  $130 \times 70 \,\mu\text{m}^2$ -region of the crystal, (b) sequence of seven PEEM images recorded with a time interval of 1.1 s from a  $10 \times 30 \,\mu\text{m}^2$  slice showing the merging and splitting of two interacting dissipative solitons. Parameters:  $p_{\text{O2}} = 35 \,\text{mPa}$ ,  $p_{\text{CO}} = 10 \,\text{mPa}$ ,  $T = 485 \,\text{K}$ ,  $t_{\text{exp}} = 20 \,\text{ms}$  (Reprinted figure with permissions from [2.5])

in a characteristic way with each other (Sect. 2.1.2). However, although the majority of papers on structure formation in chemical systems consider spatially extended systems, reports on dissipative solitons in these systems are rarely found. The reason is twofold: In the case of the dissipative solitons observed in the ferrocyanide-iodate-sulphite reaction [2.6] some experimental details were not obvious and it took more than a decade to reproduce the original observations (Sect. 2.1.5). In the majority of other systems an external stabilization is either needed in the form of an external feedback (Sect. 2.1.3) or by boundary conditions, e.g., by constraining the active area to a ring-like geometry [2.7]. In the latter scenario the resulting dissipative solitons are comparable to nerve pulses (Fig. 1.1c), which have only one degree of freedom and therefore can only interact with each other in a very confined way. A completely different approach for stabilizing dissipative solitons in spatially extended reaction-diffusion systems has been demonstrated by the Brandeis group, which performs the Belousov-Zhabotinsky reaction in nano structured batch reactors (Sect. 2.1.4).

# 2.1.2 Catalytic Oxidation of CO on Pt(110)

The first dissipative solitons to be observed in a spatially extended reaction-diffusion system have been reported by Rotermund et al. [2.5]. They conducted experiments on the catalytic oxidation of carbon monoxide on the (110) face of a single crystal of platinum placed inside an ultra high vacuum system and monitored the experiment with a photoemission electron microscope (PEEM) [2.8]. The image contrast of this microscope results from the different dipole moments of the adsorbate complexes  $O_{ad}$  and  $CO_{ad}$ , such that oxygen covered areas appear dark, while those covered by CO are gray (Fig. 2.1). In particular, Rotermund et al. observed concentration

peaks of atomic oxygen propagating with a uniform velocity of  $3.2 \pm 0.2 \,\mu\text{m/s}$  along the crystallographic (100) direction of the Pt(110) substrate. These dissipative solitons exhibit a characteristic bell-shaped intensity profile, which is elongated perpendicular to the direction of motion (Fig. 2.1a).

Due to their parallel direction of motion only head-on collisions between dissipative solitons are observed which normally lead to the extinguishing of one of the dissipative solitons. However, one also observes the mutual annihilation of both dissipative solitons or the merging and subsequent splitting of the intermediate state (Fig. 2.1b).

Since the first reports of this phenomenon, the investigations on dissipative solitons on excitable surface reactions have been quite extended, such that a huge variety of additional phenomena like the refraction of dissipative solitons crossing the border from a domain consisting of pure platinum to a gold covered platinum domain [2.9], the merging of two dissipative solitons to a single one in the course of the catalytic reduction of NO with CO on a Pt(110) surface [2.10] or the propagation of dissipative solitons on polycrystalline platinum under atmospheric pressure [2.11] have been reported.

# 2.1.3 The Belousov-Zhabotinsky Reaction

The most important chemical reaction for the invention of self-organized spatiotemporal dynamics has been discovered in the 1950s by Belousov [2.12]. He observed that in a closed system the cerium-catalyzed bromate oxidation of citric acid undergoes a large number of oscillations before reaching thermodynamic equilibrium. Later on Zhabotinsky repeated Belousov's experiments, replacing the citric acid substrate by malonic acid and substituting the oxidation-reduction indicator ferroin (tris(1,10-phenanthroline)iron(II)) for the cerium catalyst, leading to the well-known blue-red colour changes [2.13].

Investigations of the spatio-temporal dynamics of the Belousov-Zhabotinsky (BZ) reaction started in the early 1970s of the last century with the observation of travelling concentration waves in quasi-two-dimensional layers of unstirred BZ reactant mixtures [2.14–2.16]. These waves typically appear in form of blue fronts, targets or spirals (Fig. 1.1h) embedded into the red background of the reduced catalyst. Replacing ferroin by the photosensitive catalyst Ru(bipy)<sup>2+</sup> (tris(2,2'-bipyridyl)ruthenium(II)) [2.17] opened the way towards controlling pattern formation in the BZ reaction [2.3, 2.4].

The experimental setup is straight forward [2.18, 2.19]: A thin layer of silica gel in which the light sensitive catalyst is immobilized is cast onto a microscope slide and mounted inside of a reactor that is continuously fed with fresh, catalyst-free BZ solution (Fig. 2.2a). Images  $\phi(x,t)$  of the chemical pattern are recorded by a CCD camera and are converted into a feedback signal in form of an  $30 \times 20 \,\mathrm{mm}^2$  image, which is projected through a 460 nm bandpass filter onto the gel. Because the excitability of the medium decreases with increasing light intensity the feedback

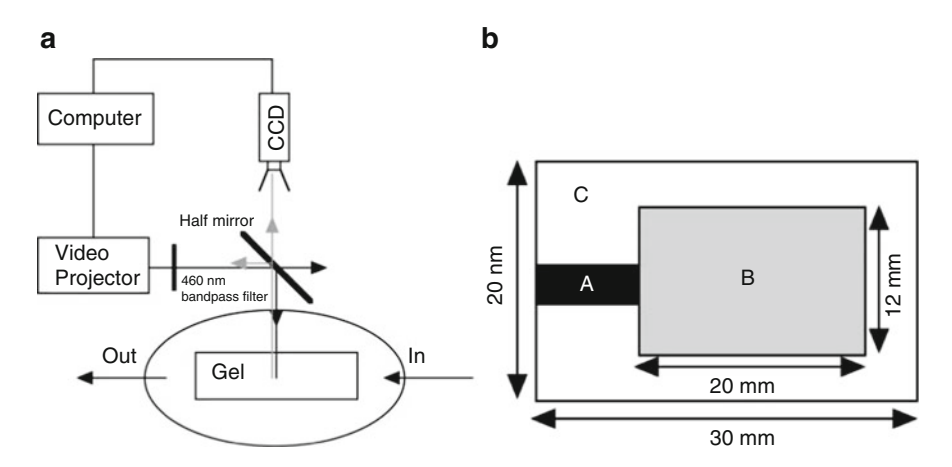


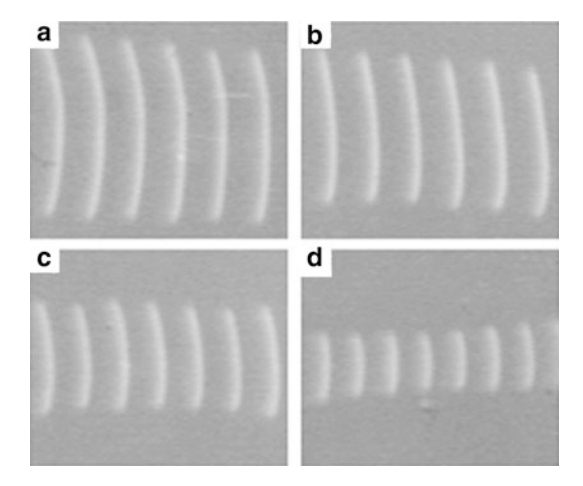
Fig. 2.2 Experimental setup for the observation of dissipative solitons in the BZ reaction [2.18]. (a) The feedback is realized as computer generated image being projected onto the reactor. (b) The feedback image consists of an initiation zone (A), a reaction zone (B) with adapted gray level, and a surrounding boundary (C) which confines the dissipative solitons. Typical parameters of the experiment are given in Fig. 2.3

image consists of three different zones (Fig. 2.2b): a dark initiation zone (label A), a reaction zone of  $20 \times 12 \, \text{mm}^2$  with adapted gray level (label B), and a boundary with high intensity (label C). The dissipative solitons are initiated in the dark zone and are allowed to propagate into the reaction zone, to which they are confined due to the high intensity of the boundary zone. The gray-level of the reaction-zone is chosen proportional to the area covered by the observed dissipative soliton, such that the illumination intensity  $\Phi(t)$  of the reaction zone is given by

$$\Phi(t + \Delta_t) = \kappa_1 + \kappa_2 \int_{\{x \mid \phi(x,t) \ge \phi_{\mathrm{T}}\}} \phi(x,t) \,\mathrm{d}x. \tag{2.1}$$

Here parameter  $\kappa_1$  determines the offset illumination within the reaction zone,  $\kappa_2$  is the feedback parameter, and  $\phi_T$  is the threshold used for separating the localized structure from the homogeneous background.

The experiments show, that self-organized localized structures form which are not confined by the boundary of the reaction zone but exhibit a well defined shape that is elongated perpendicular to the direction of motion (Fig. 2.3). Varying the feedback parameter  $\kappa_1$  reveals, that the size of the dissipative solitons decreases with increasing illumination parameter  $\kappa_1$ . This is due to the fact, that a higher illumination intensity excites a larger amount of the ruthenium catalyst, leading to an increased reaction rate of the excited catalyst with bromomalonic acid. This reaction produces bromide, which acts as inhibitor for the autocatalysis [2.17]. The same mechanism controls the size of the dissipative solitons, because a small increase of its shape would lead via the feedback loop (2.1) to an increase of the illumination



**Fig. 2.3** Propagating dissipative solitons in a photosensitive BZ-medium with optical feedback [2.18]. The images show, that the size of the dissipative solitons decrease with increasing illumination intensity (2.1) (a)  $\kappa_1 = -0.0744 \,\mathrm{mW/cm^2}$ , (b)  $\kappa_1 = -0.0248 \,\mathrm{mW/cm^2}$ , (c)  $\kappa_1 = 0.0248 \,\mathrm{mW/cm^2}$ , (d)  $\kappa_1 = 0.0744 \,\mathrm{mW/cm^2}$ . The interval between the superimposed snapshots is 40 s. Composition of catalyst free BZ-solution: [NaBrO<sub>3</sub>]<sub>0</sub> = 0.28 M, malonic acid [MA]<sub>0</sub> = 0.05 M, bromomalonic acid [BrMA]<sub>0</sub> = 0.165 M, sulfuric acid [H<sub>2</sub>SO<sub>4</sub>]<sub>0</sub> = 0.36 M. The silica gel medium  $(0.3 \times 20 \times 30 \,\mathrm{mm^3})$  was prepared by acidifying an aqueous solution of 10 % (w/w) Na<sub>2</sub>SiO<sub>3</sub> and 2.0 mM Ru(bpy)<sub>3</sub><sup>2+</sup> with H<sub>2</sub>SO<sub>4</sub>. Temperature T = 9.0 °C, displayed area 7.78 × 6.53 mm<sup>2</sup>. Feedback:  $\Delta_t = 2 \,\mathrm{s}$ ,  $\kappa_2 = 37.5 \,\mathrm{mW/cm^4}$ ,  $\phi_T = 1.1 \langle \phi(x,t) \rangle_x$ . For additional parameters see [2.18]

and a reduced excitability of the active medium. On the other hand a small decrease of its shape would lead to a decrease of the illumination and an increased excitability allowing for the growth of the dissipative soliton.

On basis of this experimental setup it has been shown, that dissipative solitons can form due to stochastic resonance [2.20], exhibit oscillatory cluster patterns [2.21], and are propelled in unexcitable BZ-media by periodic forcing [2.22]. It has also been demonstrated, that dissipative solitons can be guided on complex paths [2.23] and can interact via interaction potentials superimposed to the illumination mask [2.24, 2.25].

# 2.1.4 The Belousov-Zhabotinsky-Aerosol OT-Microemulsion System

The fact, that the BZ reaction is capable of showing spatio-temporal structure formation raises the question, whether this system is capable of developing periodic patterns. These so-called Turing patterns need two requirements: A continuous flow of matter and an inhibitor diffusing faster than the activator [2.26]. The first condition has been realized in the late 1980s by the invention of the continuously fed unstirred reactor (CFUR) [2.27]. The second condition was first realized,

not in the BZ reaction, but in the chlorite-iodide-malonic acid (CIMA) reaction [2.2, 2.28, 2.29]. These experiments were carried out in a gel CFUR allowing for a continuous supply of fresh reactants. Furthermore de Kepper et al. used starch as indicator, which forms a reversible complex with iodide, the activator for the autocatalytic reaction, and iodine, an intermediate produced in the reaction. Due to their size, these complexes stuck every now and then in the pores of the gel, which effectively reduces the diffusion rate of the activator. On the other hand the inhibitor, chlorite, can diffuse unhindered through the gel, leading to significantly larger diffusion rates compared to the activator and thus fulfilling Turing's condition [2.4].

In an aqueous solution of a typical BZ-reaction the diffusion rates of the activator, the radical BrO<sub>2</sub>, and the inhibitor, Br<sub>2</sub>, are all on the order of  $2 \cdot 10^{-5}$  cm<sup>2</sup> s<sup>-1</sup>, thus Turing patterns cannot form. An answer to this problem has been found by Vanag and Epstein, who mixed the BZ reactants with a reverse microemulsion of water, oil, and the surfactant sodium bis(2-ethyl-hexyl)sulfosuccinate, the so-called aerosol OT (AOT), realizing the BZ-AOT reaction [2.30]. The reverse microemulsion consists of droplets of water surrounded by a monolayer of AOT floating in a sea of oil. The water droplets of this ternary mixture have a diameter of several nanometers and diffuse with a rate of  $(10^{-6}-10^{-7})$  cm<sup>2</sup> s<sup>-1</sup> [2.4]. Because the polar species and thus the activator are mainly confined to the water droplets, while for certain conditions the dominant species of the oil phase is the inhibitor Br<sub>2</sub>, which diffuses with a rate of  $2 \cdot 10^{-5}$  cm<sup>2</sup> s<sup>-1</sup>, the inhibitor diffuses 10–100 times faster than the activator allowing for the formation of Turing-patterns [2.30]. Having in mind that the BZ reaction involves at least ten different reactions [2.31], which are reduced to five chemical steps in the Oregonator model [2.32], it becomes clear that the given description of the BZ-AOT reaction is quite simplified. Therefore additional mechanisms like the effect of a second fast diffusing activator are considered in order to interpret phenomena like accelerating waves [2.30]. A comprehensive overview of the phenomena observed in the BZ-AOT system can be found in [2.33].

In order to observe structure formation phenomena in the BZ-AOT system the microemulsion is prepared as a  $1.5\,\mathrm{M}$  solution of AOT in octane. One part of the microemulsion is mixed with aqueous solutions of  $\mathrm{H_2SO_4}$  and malonic acid and the second part is mixed with aqueous solutions of the catalyst and sodium bromate. Equal volumes of each microemulsion are mixed and filled into a cylindrical batch reactor of diameter 20 mm and height 0.1 mm. This reaction layer is illuminated by a 40 W tungsten lamp whose light is filtered by a 450 nm interference filter. The patterns forming in the reactive layer are observed by a CCD camera. Due to the batch configuration the pattern typically persists for  $1{\text -}3\,\mathrm{h}$ .

Two important control parameters determine the structure formation of the system: The droplet fraction and the reactivity. Both parameters cannot be tuned within a running experiment but can be varied from experiment to experiment. An overview of the experimental phenomena observed for varied droplet fraction and varied reactivity is shown in [2.30, 2.33]. The droplet fraction is directly related to the diffusion rates of the chemical species and increasing the droplet fraction basically leads to a transition from stationary to dynamic structures. On the other hand the excitability of the BZ-AOT system results from the ratio

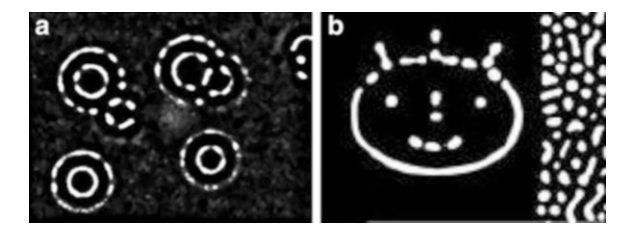


Fig. 2.4 Dissipative solitons in the BZ-AOT reaction. White areas correspond to a large concentration of the oxidized catalyst (Ru(bpy)<sub>3</sub><sup>2+</sup>). (a) Self-organized rings. (b) Structures initialized by inhomogeneous illumination. Parameters: (a) Composition of aqueous BZ-solution: [NaBrO<sub>3</sub>]<sub>0</sub> = 0.2 M, malonic acid [MA]<sub>0</sub> = 0.25 M, catalyst [Ru(bpy)<sub>3</sub><sup>2+</sup>]<sub>0</sub> = 4.2 mM, sulfuric acid [H<sub>2</sub>SO<sub>4</sub>]<sub>0</sub> = 0.25 M. Droplet fraction  $\varphi_d$  = 0.41, temperature T = 23.5 °C, displayed area 5.1 × 3.75 = mm<sup>2</sup>, for additional parameters see [2.36]. (b) Composition of aqueous BZ-solution: [NaBrO<sub>3</sub>]<sub>0</sub> = 0.25 M, malonic acid [MA]<sub>0</sub> = 0.1 M, catalyst [Ru(bpy)<sub>3</sub><sup>2+</sup>]<sub>0</sub> = 4.0 mM, sulfuric acid [H<sub>2</sub>SO<sub>4</sub>]<sub>0</sub> = 0.3 M. Droplet fraction  $\varphi_d$  = 0.45, initial illumination intensity  $I_0$  = 28 mW/cm<sup>2</sup>, illumination intensity after removing the mask  $I = I_0/5$ , temperature T = 24.0 °C, displayed area 7.7 × 5.8 = mm<sup>2</sup>, for additional parameters see [2.35]. Figures published with kind permission of I.R. Epstein

between activation and inhibition steps, which can be parameterized by the ratio  $\sigma_{BZ}$  = [H<sub>2</sub>SO<sub>4</sub>][NaBrO<sub>3</sub>]/[MA] [2.33]. While the monotonic state of the system is stable for small values of  $\sigma_{BZ}$ , one observes spontaneous formation of stationary structures for 0.01 <  $\sigma_{BZ}$  < 0.09 and complex spatio-temporal dynamics for larger values of  $\sigma_{BZ}$  [2.33, Fig. 5.3].

Dissipative solitons in form of localized stationary structures can be observed in the BZ-AOT system close to the transition from the monotonic to the periodically structured state (Fig. 2.4). They are observed as regions of locally increased concentration of the reduced catalyst taking the form of spots, concentric rings, or strings of well-defined width. In any case, the dissipative solitons have to be created by some kind of finite perturbation. This might be either dust particles [2.34] triggering the formation of concentric rings (Fig. 2.4a) or an inhomogeneous illumination. In the example shown in Fig. 2.4b the inhomogeneous illumination has been realized as a mask showing a smiley and a vertical bar [2.35]. Due to the light sensitivity of the catalyst, the masked regions exhibit a larger reactivity, leading to the spontaneous formation of a Turing-pattern in the region masked by the vertical bar as well as localized spots and strings of well-defined width in the regions shaded by the smiley mask. After removing the mask, the self-organized structures persist up to an hour, while the strings decompose into chains of localized spots still resembling an outline of the initial image. The vanishing of the localized structures is caused by consumption of the reactants due to the batch configuration of the experiment.

As mentioned above the BZ-AOT system exhibits complex spatio-temporal dynamics for larger values of  $\sigma_{BZ}$ . In contrast to the well-known phenomena of autowaves or spirals known from other reaction-diffusion systems, some of the corresponding structures observed in the BZ-AOT system are segmented. For example

one observes dash waves, segmented circular waves, segmented spirals, and fronts of bubbles [2.33]. From these observations one might suggest that the BZ-AOT system is a promising candidate for investigating the interaction of dissipative solitons in chemical reaction-diffusion systems without applying an artificial interaction by inhomogeneous illumination. In the BZ-AOT system such experiments could be prepared by initiating two or more dissipative solitons due to a transient inhomogeneous illumination similar to the example discussed in Fig. 2.4a. After removing the mask, the temperature of the system could be increased in order to increase the reactivity of system, which might lead to a drift-bifurcation of the dissipative solitons.

## 2.1.5 Ferrocyanide-Iodate-Sulphite (FIS) Reaction

From the historical point of view, the first oscillating chemical reaction showing dissipative solitons in form of localized concentration spots is the ferrocyanide-iodate sulphite (FIS) reaction [2.6]. The autocatalytic mechanism of this reaction is the hydrogen ion driven oxidation of hydrogen sulfite, which is inhibited by the hydrogen ion consuming oxidation of ferrocyanide. Therefore the spatial structures of the system can be easily visualized by using a pH indicator. Because the FIS reaction only oscillates in an open system, the continuous supply of reactants has to be provided by using a continuously stirred tank reactor (CSTR) [2.37], which was invented for generating Turing patterns in the CIMA reaction [2.38]. In the original setup of the Austin group, the reactor consists of a thin poly(acrylamide) gel layer of width d=0.2 mm and diameter D=22 mm which is fed via diffusion by the reactants from the reservoir [2.6, 2.37].

From theoretical considerations it is well known that the diffusivity of the autocatalytic species needs to be smaller than the diffusivity of the inhibitory species in order to obtain stationary self-organized patterns [2.26]. Though this topic has not been considered in the original papers of the Austin group recent investigations show that a critical concentration of weak acid functions with low mobility is needed in order to observe stationary reaction-diffusion patterns in the FIS reaction [2.39, 2.40]. Due to the fast protonation equilibrium, these functions considerable decrease the diffusivity of the hydrogen ions. In the experiments of Szalai and de Kepper this condition is realized by impregnating a disk of agarose gel with 20 mM poly(acrylate). The authors of these recent investigations assume that the same condition was realized in the original experiments of the Austin group by the hydrolysis of the poly(acrylamide) gel due to the degradation of amide functions to carboxylate functions in alkaline aqueous solutions.

In both cases the reactor is illuminated with orange light and concentrations spots of high pH are indicated by bromothymol blue, which changes from yellow to blue as the pH increases from 6.0 to 7.6. While the first report on stationary patterns in the FIS reaction discussed lamellar structures resulting from front-front interactions [2.37], a later paper [2.6] shows that increasing the concentration of ferrocyanide beyond the lamellar regime leads to the formation of concentrations spots of low pH, which undergo a subsequent process of replication by division (self-replication) and

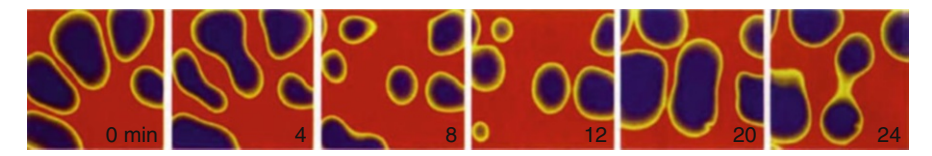


**Fig. 2.5** Self-replication of dissipative solitons observed in the ferrocyanide-iodate-sulphite reaction. *Blue* and *red* regions represent states of high and low pH, respectively. The false colour representation has been created from grayscale images recorded in reflected light with a CCD camera. Concentrations of reagents fed in the reservoir of the reactor:  $[NaIO_3]_0 = 75.0 \, \text{mM}$ ,  $[Na_2SO_3]_0 = 89.0 \, \text{mM}$ , sulfuric acid  $[H_2SO_4]_0 = 3.6 \, \text{mM}$ ,  $[NaOH]_0 = 0.25 \, \text{mM}$ ,  $[K_4Fe(CN)_6 \cdot H_2O]_0 = 36.4 \, \text{mM}$ . Input flow rate  $86.4 \, \text{ml/h}$ , temperature of the reactor  $30 \, ^{\circ}\text{C}$ , edge length of the displayed area  $L_d = 7 \, \text{mm}$ , diameter of the reaction volume  $D = 22 \, \text{mm}$ , height of the reaction volume  $d = 0.4 \, \text{mm}$ , sampling frequency  $f_{\text{rep}} = 4 \, \text{min}$  (Reprinted by permission from Macmillan Publishers Ltd: Nature [2.42], copyright 1994)

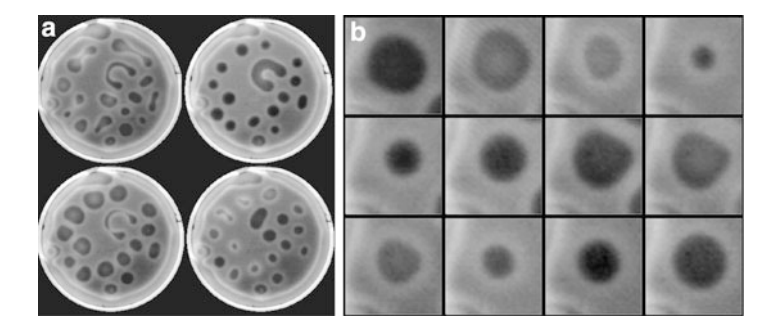


**Fig. 2.6** Breathing dissipative solitons in the FIS reaction. *Dark* and *light* regions represent states of high and low pH, respectively. The images have been recorded by a CCD camera from the light transmitted through the reactor. Concentrations of reagents fed in the reservoir of the reactor:  $[KIO_3]_0 = 75.0 \,\mathrm{mM}$ ,  $[Na_2SO_3]_0 = 89.0 \,\mathrm{mM}$ , sulfuric acid  $[H_2SO_4]_0 = 3.09 \,\mathrm{mM}$ ,  $[K_4Fe(CN)_6 \cdot H_2O]_0 = 20.0 \,\mathrm{mM}$ ,  $[poly(acrylate)]_0 = 2.0 \,\mathrm{mM}$ . Temperature of the reactor 30 °C, diameter of the reaction volume  $D = 18 \,\mathrm{mm}$ , height of the reaction volume  $d = 0.75 \,\mathrm{mm}$ , (a) sampling frequency  $f_{rep} = 8 \,\mathrm{min}$ , (b) sampling frequency  $f_{rep} = 4 \,\mathrm{min}$ , edge length of the displayed area  $L_d = 3.5 \,\mathrm{mm}$  (Reprinted with permission from [2.40])

annihilation due to overcrowding (Fig. 2.5). A similar phenomenon is observed for the semiconductor-gas-discharge system (Fig. 2.12) which has been characterized by Astrov and Purwins as spatio-temporal chaos [2.41].

In a subsequent paper the Austin group investigated the spatial bistability of the system systematically by varying the flow rate, the gel thickness, and the concentration of ferrocyanide and reported the observation of breathing domains of low pH concentration and breathing dissipative solitons in the form of high pH concentration spots embedded in a low pH concentration domain [2.43]. After realizing the crucial role of charged polymers for the differentiation between the diffusivity of the activating and the inhibiting species the Bordeaux group investigated the bistability of the spatially extended FIS reactor and repeated the original experiments of breathing dissipative solitons (Fig. 2.6). Furthermore

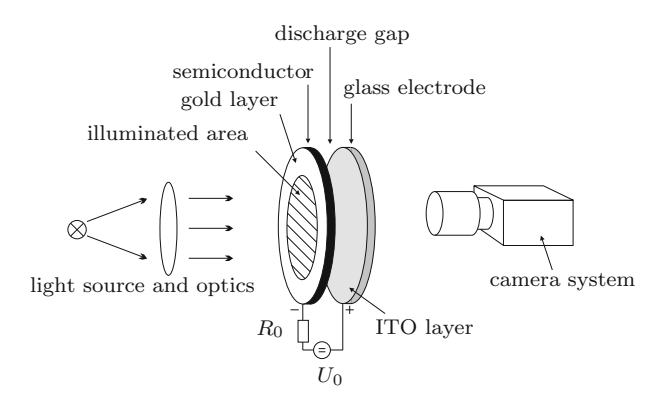


**Fig. 2.7** Experimental setup of the semiconductor gas-discharge system [2.52]. The graphics does not show the cryostat, in which the semiconductor electrode is located. Typical parameters of the system are documented in Figs. 2.8–2.20

they investigated the three-dimensional structure of the observed structures and documented the formation of one-dimensional dissipative solitons due to the interaction of reaction fronts [2.40].

It can be expected that after clarifying the experimental details of the FIS reaction, this system will lead to many new experiments on the dynamics of dissipative solitons in chemical reaction-diffusion systems.

# 2.2 Planar Semiconductor Gas-Discharge Systems

# 2.2.1 Experimental Set-Up

The experimental system discussed in this section is a variant of the device, which has originally been developed for the fast conversion of infrared light into the visible spectrum [2.44–2.51]. The heard of the experiment is a discharge gap, which is build from two planar electrodes (Fig. 2.7). For the experiments discussed in this book the discharge gap is typically filled with nitrogen at pressure  $p_{\rm g}=100-500\,{\rm hPa}$ . One of the electrodes consists of a high ohmic semiconductor like GaAs $\langle {\rm Cr} \rangle$ , Si $\langle {\rm Zn} \rangle$ , Si $\langle {\rm Pt} \rangle$  or Si $\langle {\rm Au} \rangle$  of width  $a_{\rm SC}=0.25-1.0\,{\rm mm}$ . The other electrode is a glass substrate coated with indium tin oxide (ITO), which is transparent for visible light. The high ohmic electrode is contacted by a gold layer. Typically the high and low ohmic electrodes are wired as cathode and anode, respectively. In some experiments the semiconductor electrode is located inside of a cryostat and is cooled down to  $T_{\rm SC}=100\,{\rm K}$ . In contrast to the infrared converter, which typically has a discharge gap of width  $d=0.1\,{\rm mm}$ , the pattern forming system has a discharge gap of width  $d=0.4-1.4\,{\rm mm}$ . The gas discharge system is driven by a DC voltage  $U_0$ . In some experiments the current I in the discharge gap is limited by a series resistor  $R_0$ .

The specific conductivity  $\sigma_{SC}$  of the semiconductor can be controlled by an external light source via the internal photo effect. The diameter of the illuminated semiconductor area is typically  $D \approx 20$  mm.

If the applied DC voltage  $U_0$  exceeds a critical value  $U_c$  the discharge ignites. Therefore the critical value is called ignition voltage. The emitted light is proportional to the local current density [2.53] and can be observed as luminance distribution  $\phi(x,t)$  through the transparent electrode. Of course the luminance can also be recorded by camera systems. Depending on the investigated phenomena the exposure time  $t_{\rm exp}$  varies between 0.4 and 20 ms and the sample frequency  $f_{\rm rep}$  varies between 50 Hz and 2 kHz. Typical control parameters of the experiment are the supply voltage  $U_0$  and the specific conductivity  $\sigma_{\rm SC}$  of the semiconductor.

This experiment shows a huge variety of different structure formation phenomena, which range from Turing-patterns [2.53–2.55], spirals [2.56], and zigzag destabilized structures [2.57, 2.58] to current density filaments [2.59–2.62] and filament chains [2.63]. Thereby the observed current density filaments exhibit pronounced particle-like properties like their mutual interaction (Sect. 2.2.5) and the generation and annihilation of particles (Sect. 2.2.3). Under certain experimental conditions one can observe an oscillation of the homogeneous background discharge, which triggers an oscillation of the current density filaments [2.64]. However, the following portrayal concentrates on experimental configurations with stationary background discharges.

# 2.2.2 Observation of Current Density Filaments

Dissipative solitons in form of current density filaments as observed in semiconductor gas-discharge systems are localized three-dimensional structures with two dimensions being given by the lateral expansion of the electrodes and a vertical dimension being given by the finite width of the discharge gap (Fig. 2.7). The structuring of the filaments in the vertical direction becomes more and more complex with increasing discharge gap [2.65, S. 56ff]. The increase of complexity can be explained by the formation of the positive discharge column and Faraday's dark space. However, for most experimental setups the discharge gap d is small compared to the diameter D of the active area  $(d/D \approx 10^{-2})$ , such that the current density filaments can be regarded as two-dimensional structures. In this case the emitted luminance is integrated over the vertical dimension thus becoming a two-dimensional luminance distribution. Therefore current density filaments are recognized as areas of locally increased luminance typically exhibiting a bell-shaped profile. These solitary objects only exist due to a continuous flow of energy and are classified as *dissipative solitons*.

Because the discharge is disturbed by thermal fluctuations and discharge noise [2.49] the shape of the filaments is noisy, too. However, for experiments without oscillatory instabilities and spatiotemporal uncorrelated noise the fluctuations can be averaged out from a series of snapshots as described by Gurevich et al. [2.66].

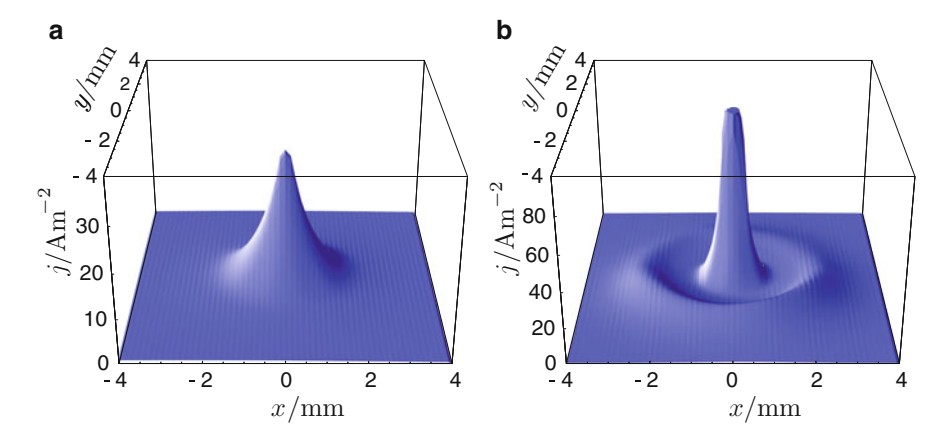


**Fig. 2.8** Averaged luminance distribution of dissipative solitons in form of current density filaments [2.52]. (a) Current density filament with bell-shaped profile averaged from 1,000 snapshots. (b) Current density filament with oscillatory tails averaged from 1,000 snapshots. Parameters: (a)  $U_0 = 2.74 \,\mathrm{kV}$ ,  $\rho_{SC} = 4.95 \,\mathrm{M}\Omega \cdot \mathrm{cm}$ ,  $R_0 = 20 \,\mathrm{M}\Omega$ ,  $I = 46 \,\mathrm{\mu}\mathrm{A}$ , semiconductor GaAs $\langle \mathrm{Cr} \rangle$ ,  $p_{\mathrm{N}_2} = 280 \,\mathrm{hPa}$ ,  $T_{\mathrm{SC}} = 105 \,\mathrm{K}$ ,  $D = 17 \,\mathrm{mm}$ ,  $d = 250 \,\mathrm{\mu m}$ ,  $a_{\mathrm{SC}} = 1.0 \,\mathrm{mm}$ ,  $t_{\mathrm{exp}} = 20 \,\mathrm{ms}$ ,  $f_{\mathrm{rep}} = 50 \,\mathrm{Hz}$ . (b)  $U_0 = 3.9 \,\mathrm{kV}$ ,  $\rho_{SC} = 3.05 \,\mathrm{M}\Omega \cdot \mathrm{cm}$ ,  $R_0 = 4.4 \,\mathrm{M}\Omega$ ,  $I = 200 \,\mathrm{\mu}\mathrm{A}$ , semiconductor GaAs $\langle \mathrm{Cr} \rangle$ ,  $p_{\mathrm{N}_2} = 280 \,\mathrm{hPa}$ ,  $T_{\mathrm{SC}} = 100 \,\mathrm{K}$ ,  $D = 17 \,\mathrm{mm}$ ,  $d = 500 \,\mathrm{\mu m}$ ,  $a_{\mathrm{SC}} = 1.0 \,\mathrm{mm}$ ,  $t_{\mathrm{exp}} = 20 \,\mathrm{ms}$ ,  $f_{\mathrm{rep}} = 50 \,\mathrm{Hz}$ 

An example of a bell-shaped luminance distribution of an experimentally observed filament is shown in Fig. 2.8a. For some experiments this method is also capable of visualizing the oscillatory tails of current density filaments [2.52], which usually are not visible within the background noise. A corresponding example is given in Fig. 2.8b.

#### 2.2.3 Generation and Annihilation Phenomena

The particle-like character of dissipative solitons becomes obvious from the fact, that they are generated or annihilated as a whole. Therefore current density filaments are the smallest elementary building block from which more complex bound or unbound states are formed. In general generation and annihilation phenomena occur either due to a variation of control parameters or due to interaction processes with other dissipative solitons or the domain boundary. In the following sections both scenarios are discussed by means of representative experimental examples.

#### 2.2.3.1 Controlling the Specific Conductivity of the Semiconductor

An important mechanism for generating dissipative solitons is the Turingmechanism, which is a spatial instability leading to the spontaneous structuring of

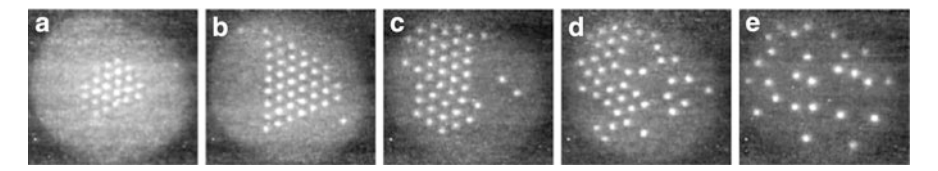


**Fig. 2.9** Evolution of a Turing-pattern to an assemble of particle-like structures due to an increase of the specific conductivity of the semiconductor [2.59]. Subfigures (a) and (b) show Turing-patterns with small and large amplitude, respectively. Subfigures (c)–(e) show the dissolving of the hexagonal structure and the transition to a liquid-like state, which is characterized by the mutual interaction of the current density filaments, while a certain short-range order is preserved. In order to realize a high specific resistivity of the Si(Zn)-semiconductor, the system has been cooled down to a temperature of  $T_{SC} = 90$  K. The series of images (a)–(e) corresponds to an increase of the specific conductivity of the semiconductor from  $\sigma_H = 0.8 \cdot 10^{-8}$  to  $4.0 \cdot 10^{-8}$  (Ω cm)<sup>-1</sup>,  $U_0 = 2.9$  kV,  $R_0 = 41$  MΩ,  $p_{N_2} = 260$  hPa, D = 20 mm, d = 500 μm

the domain (Sect. 3.3.2). In the semiconductor gas-discharge system the Turing-instability can be triggered by a variation of the specific conductivity of the semiconductor as shown by Astrov and Purwins [2.59]. In this experiment the increase of the conductivity destabilizes a homogeneous gas discharge into a hexagonal Turing-pattern with small amplitude (Fig. 2.9a), which evolves into a hexagonal pattern with large amplitude if the specific conductivity of the semiconductor is increased even further (Fig. 2.9b). With ongoing stepwise increase of the control parameter the rigid arrangement of the cluster dissolves, which is accompanied by more and more localized structures dissolving from the cluster (Fig. 2.9c–e). Thereby single current density filaments behave like individual, mutually interacting particles of a liquid state. For example *elastic* scattering between two current density filaments or the formation of transient bound states can be observed [2.59, p. 352], which indicates the existence of a certain short range order between the current density filaments.

The experiment also shows, that the number of current density filaments fluctuates. For example single filaments vanish after collisions with the boundary of the active (illuminated) area of the semiconductor. At the same time the reduction of the number of filaments boosts the generation of new filaments by two- or many-particle-processes (cf. Fig. 2.13).

A completely different phenomena is observed, if the experiment is performed without a series resistor [2.41, Fig. 5]. In this case the global current is not restricted, such that increasing the specific conductivity while keeping the supply voltage fixed leads to an increase of the amplitude of the current density filament. Therefore the spatial period of the pattern grows until the filaments finally become unstable and start to split and merge spontaneously which is characterized as spatio-temporal chaos [2.41].

#### 2.2.3.2 Controlling the Supply Voltage

An important feature of the semiconductor gas-discharge system is its multistability, which is reflected by an hysteresis of the current-voltage-characteristics.

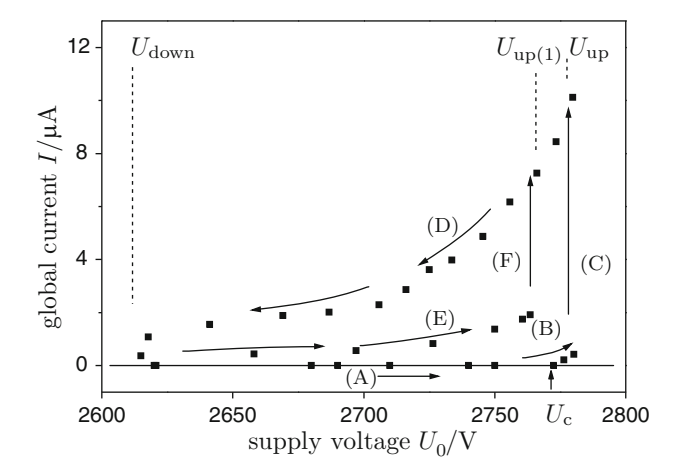


**Fig. 2.10** Current-voltage-characteristic of the self-completion scenario [2.55]. Parameters: No series resistor,  $p_{\rm N_2}=168\,{\rm hPa}$ ,  $D=20\,{\rm mm}$ ,  $d=1.0\,{\rm mm}$ ,  $a_{\rm SC}=1.0\,{\rm mm}$ 

Such kind of hysteresis is e.g. reported by Astrov and Logvin [2.55], who observe the generation of new current-density filaments due to a self-completion scenario. From the theoretical point of view this observation is very important, because it is the experimental evidence of an effect predicted by Gierer and Meinhardt [2.67], which can be regarded as one of the generic mechanisms for generating dissipative solitons (cf. Sect. 7.1.3).

In order to summarize the observation of Astrov and Logvin [2.55] their recorded current-voltage-characteristics is reprinted in Fig. 2.10. Its *tags* (A)–(F) refer to the six phases of the experiment:

- (A) If the supply voltage  $U_0$  is below the ignition voltage  $U_c$  the gas discharge will not ignite. In this phase the gas is in a dielectric state.
- (B) If the supply voltage  $U_0$  is increased above the ignition voltage  $U_c$  a self-sustained homogeneous discharge will evolve, which is reflected by an nearly linearly increasing global current I.
- (C) At the critical voltage  $U_{\rm up}$  the homogeneous discharge is spontaneously destabilized to a hexagonal Turing-pattern composed of current density filaments. This pattern formation is accompanied by a switch of the current-voltage-characteristic to its high-current branch.
- (D) Decreasing the supply voltage  $U_0$  leads to the successive extinguishing of single current density filaments which is accompanied by a decrease of the discharge current I. Tuning the supply voltage even below the critical value  $U_{\rm down}$  leads to the vanishing of the last current density filament and the system returns to its zero current branch (A).
- (E) If the supply voltage is not decreased below the critical value  $U_{\text{down}}$ , such that one current density filament (Fig. 2.11a) still remains, and the supply voltage is increased, the global current increases, too.

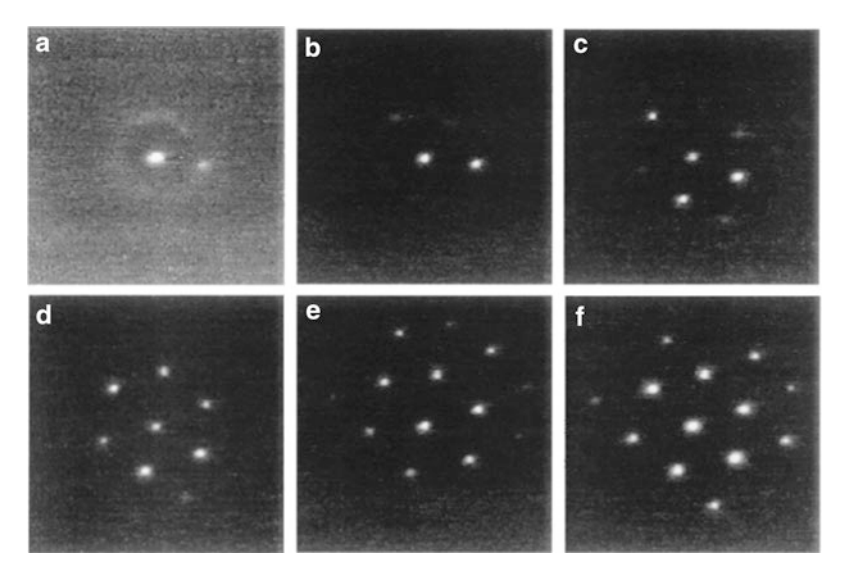
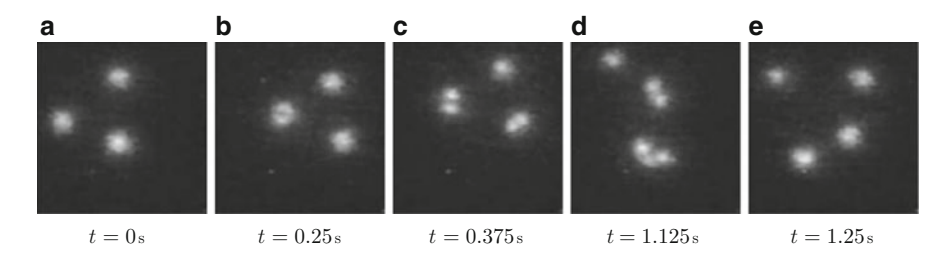


Fig. 2.11 The self-completion scenario observed from Astrov and Logvin [2.55]. (a)–(f) Luminance distribution emitted from the discharge gap for step-wise increased supply voltage  $U_0$  at branch (F) of the current-voltage-characteristic shown in Fig. 2.10. The width of the depicted luminance distribution is 14 mm. Parameters:  $U_0 \approx 3.2\,\mathrm{kV}$ , no series resistor,  $p_{\mathrm{N}_2} = 150\,\mathrm{hPa}$ ,  $d = 1.4\,\mathrm{mm}$ ,  $a_{\mathrm{SC}} = 450\,\mathrm{\mu m}$ ,  $t_{\mathrm{exp}} = 40\,\mathrm{ms}$ . For additional parameters see [2.55]

(F) Further increase of the control parameter above the critical value of  $U_{\rm up(1)}$  leads to the generation of new current density filaments, which is reflected by a switch of the characteristic to the high current branch. Note, that the remaining current density filament acts as a kind of seed, because the newly generated filaments ignite on its oscillating tail forming a hexagon of one central and six surrounding filaments (Fig. 2.11b–d). Additional filaments ignite on the edges of the hexagonal grid (Fig. 2.11e, f), such that a cluster of hexagonally ordered current density filaments evolves.

A similar generation process of current density filaments due to the measurement of a current-density-characteristic has been reported by Becker and Ammelt [2.65, 2.68, 2.69]. Though, it does not show the spontaneous formation of a Turing-pattern or a hexagonal cluster, but the successive ignition of current density filaments on rather arbitrary locations on the gas discharge plane, which most likely is caused by inhomogeneities of the semiconductor [2.65, S. 44]. Therefore the related current-voltage-characteristic cannot be regarded as generic. However, simulations of the self-completion scenario on isotropic domains (Sect. 7.1.3) indicate, that the experiment performed by Astrov and Logvin also had some kind of inhomogeneities e.g. due to an inhomogeneous illumination of the semiconductor. Otherwise it would not be possible to observe the successive ignition of current density filaments.

The increase of the supply voltage can also trigger a completely different generation phenomenon, the so-called self-replication, which is reported by Strümpel



**Fig. 2.12** Generation of current density filaments due to self-replication, which has been triggered by an increase of the supply voltage [2.41]. In order to realize a high specific resistivity of the Si(Pt)-semiconductor, the system has been cooled down to a temperature of  $T_{\rm SC}=77~{\rm K}$ .  $U_0=1.9~{\rm kV}$ ,  $R_0=41~{\rm M}\Omega$ ,  $p_{\rm N_2}=210~{\rm h}{\rm Pa}$ ,  $D=22~{\rm mm}$ ,  $d=350~{\rm \mu m}$ ,  $L_{\rm d}=4.25~{\rm mm}$ ,  $t_{\rm exp}=500~{\rm \mu s}$ 

[2.70, p. 99], Astrov and Purwins [2.41]. It is characterized by the spontaneous division of a dissipative soliton as depicted in Fig. 2.12. The series of snapshots shows the transition from three to four current density filaments due to a splitting process. The division obviously results from an intrinsic instability of the dissipative solitons, which becomes visible as lateral contraction of the localized structures. In simulations a similar effect is induced by a spatial inhomogeneity (Sect. 7.3.3). However, the fact that self-replication of dissipative solitons has also been observed in other self-organizing semiconductor gas discharge systems [2.70, 2.71] and chemical systems (Fig. 2.5) reflects the generic nature of the phenomenon.

#### 2.2.3.3 Generation by Interaction

Interaction processes between dissipative solitons can also trigger the ignition of new particle-like structures. This effect is e.g. observed for ensembles of propagating dissipative solitons, which have been created by an increase of the specific conductivity of the semiconductor, if the global current is restricted due to a series resistor (cf. Fig. 2.9). For such configuration Astrov and Purwins report [2.59], that two or three current density filaments are able to generate another filament, if their distance drops below a characteristic critical value (Fig. 2.13). The newly generated dissipative soliton is also a stable entity and instantly starts to interact with its neighboured dissipative solitons. However, this interaction does not trigger a chain reaction due to the series resistor which restricts the global current. On the other hand the ignition of new dissipative solitons due to interaction processes becomes more likely, if other current density filaments have been annihilated, e.g. due to an interaction process with the boundary of the active area.

Obviously this so-called *replication* process bears some similarity to the later state of the self-completion phenomena (Fig. 2.11c–f) at which the additional filaments ignite in a characteristic distance to the already existing ones. Indeed both phenomena can be related to the same mechanism, viz. the superposition of oscillating tails of the localized structures (Sect. 7.4.2).

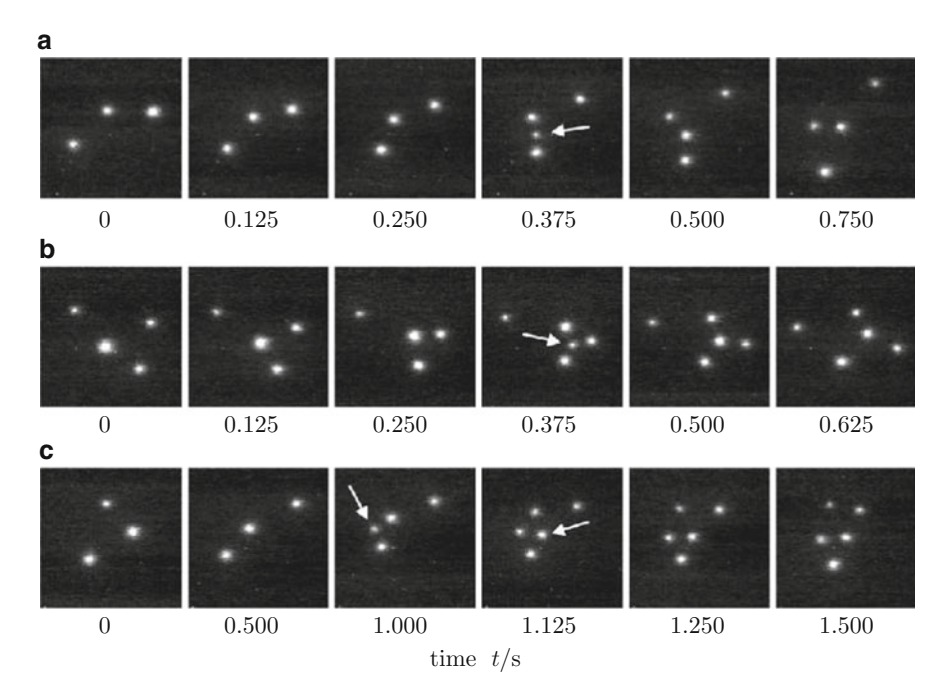


**Fig. 2.13** The replication of current density filaments due to the interaction of two (a) or three (b) and (c) dissipative solitons [2.59]. The *arrow* indicates the generated filament. Parameters correspond to Fig. 2.9e

#### 2.2.3.4 Annihilation by Interaction

Complementary to the generation of current density filaments is their annihilation, which is observed in two different variants: Annihilation by fading and annihilation by merging. While the latter is clearly identified as a two-particle process the fading of filaments occurs typically in significant distance to other filaments [2.70, S. 102], such that mutual interaction with other dissipative solitons can be neglected. If the fading occurs close to the boundary of the active area a collision with the boundary is most likely the cause of the annihilation.

In order to give an illustrative example of the rarely observed merging of current density filaments, Fig. 2.14 visualizes an experimental observation of Bödeker [2.72, 2.73]. The subfigures shows negatives of the luminance distribution in order to present the details of the process with optimal contrast. Two current density filaments approach each other (Fig. 2.14a) and merge to a transient state with high local current density (Fig. 2.14b, c). This transient state decays to a single dissipative soliton in the range of milliseconds (Fig. 2.14d), such that the number of dissipative solitons effectively has been reduced by one.

Note, that the system is not stable in the presented scenario, if only one current density filaments exists. Therefore a new filament will shortly ignite after

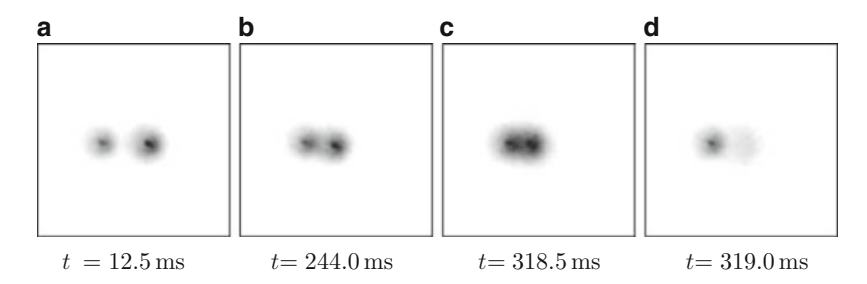


**Fig. 2.14** Annihilation by merging. The snapshots are negatives of the luminance distribution recorded by Bödeker [2.72, p. 38]. (a) Approaching current density filaments. (b) and (c) Merging of current density filaments to transient state. (d) Reconfiguration to single current density filament. Parameters:  $L_{\rm d}=8\,{\rm mm},\ U_0=3.8\,{\rm kV},\ \rho_{SC}=4.14\,{\rm M}\Omega\cdot{\rm cm},\ R_0=20\,{\rm M}\Omega,\ {\rm semiconductor}$  GaAs ${\rm Cr}$ ,  $p_{\rm N_2}=290\,{\rm hPa},\ T_{\rm SC}=100\,{\rm K},\ D=17\,{\rm mm},\ d=500\,{\rm \mu m},\ a_{\rm SC}=1.0\,{\rm mm},\ t_{\rm exp}=0.4\,{\rm ms},\ f_{\rm rep}=2\,{\rm kHz}$ 

an annihilation has occurred. A similar interplay between generation and annihilation has been observed in the many-particle system presented in Fig. 2.9e. Here annihilation is mainly caused by collisions with the boundary of the active area and therefore can be regarded as annihilation by fading.

## 2.2.4 Dynamics

For certain experimental parameters only a single or a few current density filaments exist within the active area of the semiconductor gas-discharge-system. If the electrodes have been prepared with sufficient homogeneity, the current density filaments will move on irregular paths indicating a significant influence of noise. However, the experimenter will quickly observe, that for some experimental parameters the filaments seem to be less influenced by noise than for other parameter sets.

In order to visualize these differences the position p(t) of the current density filaments has to be extracted from a set of recorded luminance distributions  $\phi(x,t_j)$ . For this purpose a threshold  $\phi_T$  is chosen, which separates the luminance distribution  $\phi(x,t)$  into a subarea  $\{\phi(x,t)|\phi(x,t)\geq\phi_T\}$  of increased luminosity, which indicates the existence of a current density filament, and the embedding background discharge [2.74]. Having this threshold  $\phi_T$  at hand the position p(t) of the dissipative soliton can be computed from

$$p(t) = \frac{\int\limits_{\{x \mid \phi(x,t) \ge \phi_T\}} x \,\phi(x,t) \,\mathrm{d}x}{\int\limits_{\{x \mid \phi(x,t) \ge \phi_T\}} \phi(x,t) \,\mathrm{d}x}.$$
 (2.2)

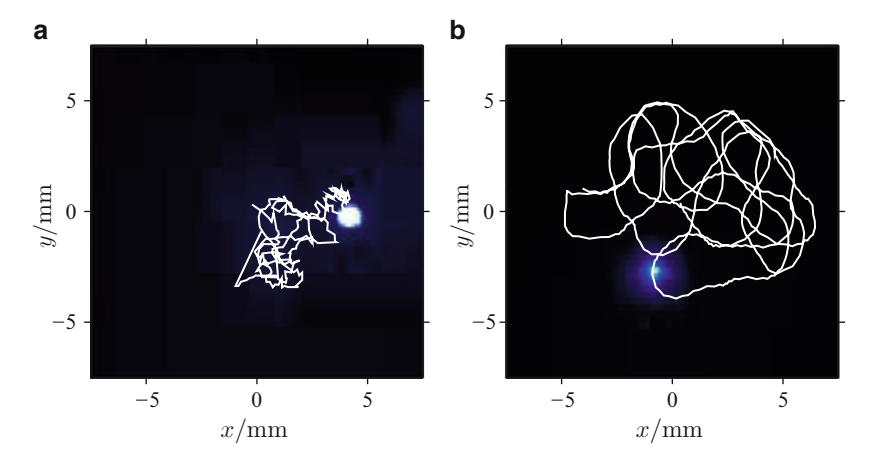


**Fig. 2.15** Dynamics of current density filaments [2.61]. The subfigures show a snapshot of the luminosity emitted from the discharge gap. Superimposed to the false colour representation of the luminosity are trajectories of the localized structures. (a) Trajectory of the current density filament for 31 s. Parameters:  $U_0 = 3.60 \,\mathrm{kV}$ ,  $\rho_{SC} = 2.02 \,\mathrm{M}\Omega \cdot \mathrm{cm}$ ,  $R_0 = 10 \,\mathrm{M}\Omega$ ,  $I = 116 \,\mu\mathrm{A}$ , semiconductor GaAs(Cr),  $p_{\mathrm{N}_2} = 280 \,\mathrm{hPa}$ ,  $T_{\mathrm{SC}} = 100 \,\mathrm{K}$ ,  $D = 17 \,\mathrm{mm}$ ,  $d = 550 \,\mu\mathrm{m}$ ,  $a_{\mathrm{SC}} = 1.0 \,\mathrm{mm}$ ,  $t_{\mathrm{exp}} = 20 \,\mathrm{ms}$ ,  $f_{\mathrm{rep}} = 50 \,\mathrm{Hz}$ . (b) Trajectory of the current density filament for 39 s. Parameters from Fig. 2.8a

If several dissipative solitons exist simultaneously on the active area the threshold has to assure, that each localized structure i can be assigned a unique position  $p_i(t)$ . For the experimentally recorded trajectories presented in this work the analysis has been performed by the programs FilaCount and FilaTrace [2.75].

Two typical filament trajectories p(t) are visualized in Fig. 2.15a, b. Each subfigure shows a snapshot of the luminance distribution  $\phi(x, y)$  with the corresponding filament trajectory. They visualize the different types of motion observed experimentally. While the trajectory of Fig. 2.15a is characterized by frequent random changes of the direction of motion, the trajectory of Fig. 2.15b represents a relative smooth motion with less frequent changes of the direction of motion.

These observations lead to the question, whether the qualitative differences of the dynamics of current density filaments are caused by an intrinsic property of the self-organized structures. This question is considered in Sect. 6 by introducing a stochastic time series analysis, which is capable of separating the deterministic and the stochastic part of the dynamics.

# 2.2.5 Interaction Processes with Conservation of the Number of Dissipative Solitons

Up to now the particle-like character of dissipative solitons has been discussed on basis of experimental results, which show the generation or annihilation of these self-organized entities as a whole in the course of two- or many-particle

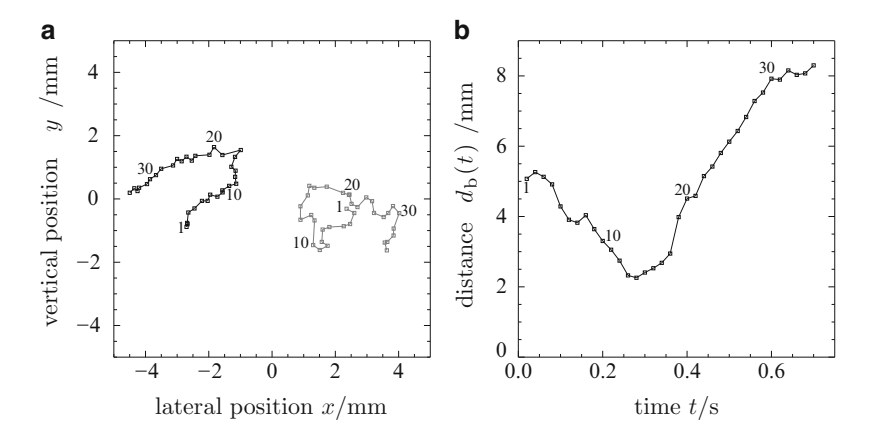


**Fig. 2.16** Scattering of two dissipative solitons [2.52]. *Numbers* reference the respective snapshots. (a) Trajectories  $p_i(t)$  extracted from the recorded luminance distribution. The symbols are enumerated with respect to the snapshot from which the positions have been extracted. (b) Time series of particle distance  $d_b(t) = |p_2(t) - p_1(t)|$ . Parameters:  $U_0 = 3.7 \,\mathrm{kV}$ ,  $\rho_{SC} = 1.52 \,\mathrm{M}\Omega$ ·cm,  $R_0 = 4.4 \,\mathrm{M}\Omega$ ,  $I = 300 \,\mathrm{\mu}A$ , semiconductor GaAs $\langle \mathrm{Cr} \rangle$ ,  $p_{\mathrm{N}_2} = 270 \,\mathrm{hPa}$ ,  $T_{\mathrm{SC}} = 100 \,\mathrm{K}$ ,  $D = 20 \,\mathrm{mm}$ ,  $d = 500 \,\mathrm{\mu}m$ ,  $a_{\mathrm{SC}} = 1.0 \,\mathrm{mm}$ ,  $t_{\mathrm{exp}} = 20 \,\mathrm{ms}$ ,  $t_{\mathrm{rep}} = 50 \,\mathrm{Hz}$ 

interactions. Another important aspect of their particle-like properties is the ability to interact with each other while the number of interacting dissipative solitons is preserved. The following sections document this ability on basis of experimentally observed scattering events (Sect. 2.2.5.1), the formation of transient bound states (Sect. 2.2.5.2), the dynamics of rotating bound states (Sect. 2.2.5.3), and many particle phenomena (Sect. 2.2.5.4). These observations act as motivation for the theoretical considerations conducted in Chap. 5.

#### 2.2.5.1 Scattering

A good example for demonstrating the particle-like character of dissipative solitons are scattering processes, where the motion of individual dissipative solitons is affected by the attractive or repulsive interaction of other dissipative solitons without being captured in transient bound states. In such scenarios the dissipative solitons approach each other up to a distinct distance, such that the merging of dissipative solitons cannot occur. Note, that the scattering distance is a typical characteristic of interaction processes for a chosen set of experimental parameters. Such kind of interaction is shown in Fig. 2.16 as trajectories  $p_1(t)$  and  $p_2(t)$  of their luminance distribution (Fig. 2.16a), which have been computed from (2.2). Additionally Fig. 2.16b shows the distance  $d_b(t) = |p_2(t) - p_1(t)|$  of the interacting dissipative solitons. The symbols of both plots are enumerated with respect to the number of the recorded luminance distribution, from which the positions have been extracted. Despite the fluctuations it can be seen from the plots, that the dissipative

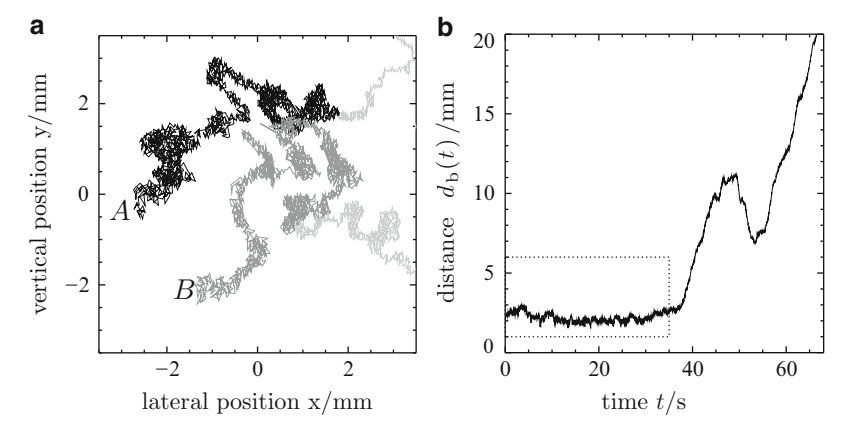


**Fig. 2.17** Transient bound state of two dissipative solitons [2.52]. (a) Trajectories  $p_i(t)$  computed from the respective luminance distributions. *Black* and *dark gray* lines indicate trajectories of the first 35 s, where the dissipative solitons are considered as being bound. *Light gray* lines indicate trajectories for t > 35 s. (b) Distance  $d_b(t)$  of the dissipative solitons. Parameters:  $U_0 = 3.1 \,\text{kV}$ ,  $\rho_{SC} = 4.19 \,\text{M}\Omega \cdot \text{cm}$ ,  $R_0 = 4.4 \,\text{M}\Omega$ ,  $I = 170 \,\mu\text{A}$ , semiconductor GaAs $\langle \text{Cr} \rangle$ ,  $p_{N_2} = 280 \,\text{hPa}$ ,  $T_{SC} = 100 \,\text{K}$ ,  $D = 20 \,\text{mm}$ ,  $d = 450 \,\mu\text{m}$ ,  $a_{SC} = 1.0 \,\text{mm}$ ,  $t_{\text{exp}} = 50 \,\text{ms}$ 

solitons approach each other up to a closest distance at the 14th snapshot, when the mutual repulsion enforces a change of direction, such that the dissipative solitons veer away from each other.

#### 2.2.5.2 Transient Bound States

One of the most astonishing property of current density filaments is the fact, that they are able to build bound states. These are characterized by a distinct binding distance between the bound filaments. In most cases the bound state decays within a short time interval after its formation into two independent filaments due to external fluctuations. A typical example for such kind of bound state is shown in Fig. 2.17 on basis of two particle trajectories (Fig. 2.17a) and the evolution of the distance between these solitary objects (Fig. 2.17b). The plotted trajectories start at positions A and B corresponding to t = 0 in Fig. 2.17b, when the bound state already has formed. Obviously the dynamics act on two different time scales: A fast time scale reflecting the stochastic dynamics of the individual dissipative soliton and a slow time scale on which the bound state propagates. Fluctuations of the fast time scale become visible in Fig. 2.17b as short term fluctuations of the distance between the dissipative solitons. Within the first 37 s of the recording the binding distance fluctuates around a mean value of  $(2.2 \pm 0.3)$  mm. Contrary to this obviously stabilized binding is the break-up of the bound state at  $t \approx 37$  s, which leads to a rapid separation of the filaments (Fig. 2.17b). Only the beginning of this separation is shown in Fig. 2.17a, which covers approximately the first 40 s of the distance plot.

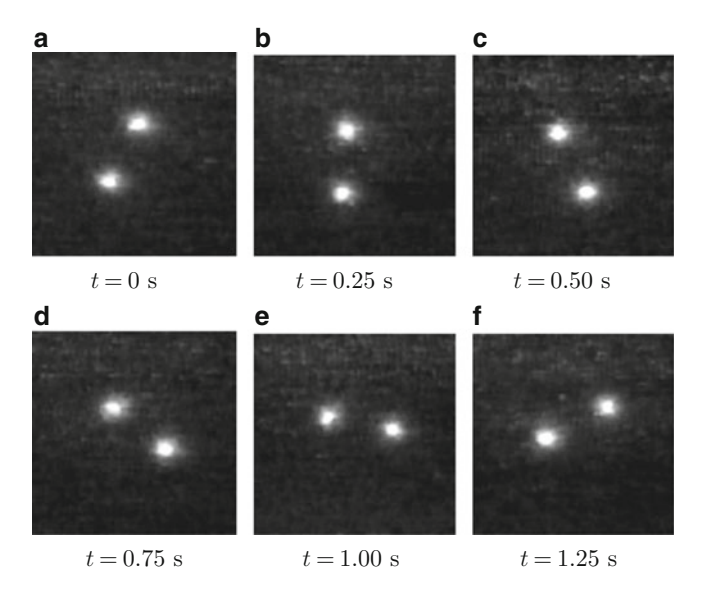


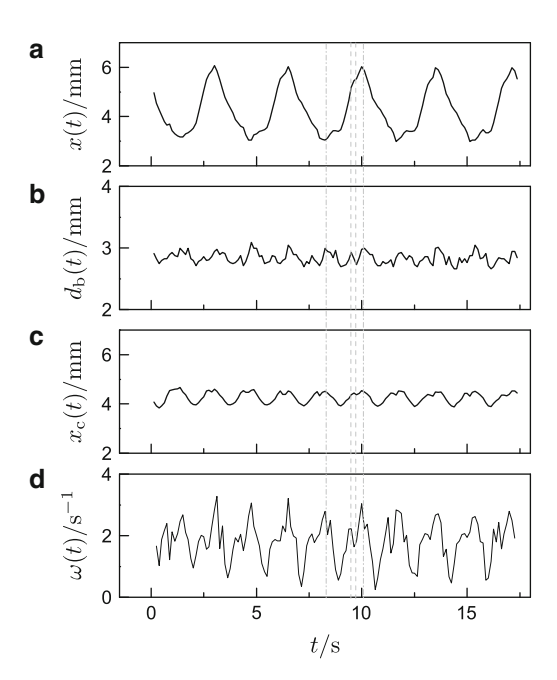
Fig. 2.18 Rotating bound state of two dissipative solitons observed in the semiconductor gas-discharge system [2.62]. The images show the luminance distributions of the counterclockwise rotating structure covering approximately a rotation of 180°. Parameters:  $L_{\rm d}=9\,{\rm mm},\ U_0=1.9\,{\rm kV},\ \rho_{SC}=22.2\,{\rm M}\Omega\cdot{\rm cm},\ R_0=5\,{\rm M}\Omega,\ I=3.2\,{\rm \mu A},\ {\rm semiconductor}\ {\rm Si}\langle{\rm Zn}\rangle,\ p_{\rm N_2}=200\ {\rm hPa},\ T_{\rm SC}=90\,{\rm K},\ d=0.8\,{\rm mm},\ a_{\rm SC}=1.0\,{\rm mm},\ D=20\,{\rm mm},\ t_{\rm exp}<0.01\,{\rm s}$ 

The stabilized binding on the one hand and the rapid increase of distance on the other hand indicate a special kind of interaction, which changes from attraction to repulsion in dependency of the interaction distance. Historically such kind of interaction had been an important attempt for explaining the complex structures found in inanimate nature since the eighteenth century [2.76, 2.77], which had only been discarded due to the success of modern physics at the beginning of the twentieth century. However, in dissipative systems this is the most important type of interaction between self-organized structures, which is discussed in detail in Chap. 5.

#### 2.2.5.3 Rotating Structures

In Sect. 2.2.3 the self-completion scenario has been introduced, which is suitable for generating small clusters of dissipative solitons. This mechanism has been applied for generating a rotating cluster of two dissipative solitons by starting with a propagating current density filament and increasing the supply voltage until a second filaments ignites in direct neighbourhood to the first one. The resulting structure is shown in Fig. 2.18. Obviously the two current density filaments form a bound state, which rotates counterclockwise. Further increase of the supply voltage results in

Fig. 2.19 Dynamics of the rotating bound state depicted in Fig. 2.18 [2.62]. Gray vertical lines indicate the correlations between the different time series. They mark significant discontinuities of the dynamics within one half period of rotation. (a) Projection of position p(t)of the upper right dissipative soliton depicted in Fig. 2.18a on the x-axis. (**b**) Distance  $d_{\rm b}(t)$  between the rotating dissipative solitons. (c) Projection of the center  $p_c(t)$ of the bound state on the x-axis. (d) Angular velocity  $\omega(t)$  of the bound state



the ignition of additional current density filaments and a much more complicated dynamics of the resulting cluster, which should not be discussed here. The detailed examination of the observed dynamics is visualized in Fig. 2.19. The discussion starts with the time series of the *x*-coordinate of the upper right dissipative soliton depicted in Fig. 2.18a. In Fig. 2.19a its *x*-coordinate has been plotted for five rotations. The curve shows a repeated pattern with significant deviations from the sinusoidal form. Notably, the deviations are replicated for each rotation, which indicates the influence of spatial inhomogeneities.

The time series of the distance  $d_b(t)$  between the dissipative solitons is shown in Fig. 2.19b for the same time interval. The distance  $d_b(t)$  fluctuates characteristically around the mean distance of  $(2.836 \pm 0.093)$  mm with half the period observed for x(t). This is caused by the fact, that both dissipative solitons are identical and are identically influenced by the spatial inhomogeneities.

Defining the center  $p_c(t) = (x_c(t), y_c(t))^T$  of the bound state as the midpoint of the connecting line between the centers of both luminosity distributions, another characteristic time series  $x_c(t)$  can be examined (Fig. 2.19c). Its curve shows the same periodicity as the distance  $d_b(t)$  and a fine structure, which is obviously correlated to the fine structure of x(t). Additionally one observes, that the fluctuations of the center of the cluster are accompanied by strong fluctuations of the angular velocity  $\omega(t)$  of the cluster (Fig. 2.19d).

The observation indicates, that bound states of dissipative solitons do not need to be transient (Sect. 2.2.5.2) but also exist as stable states. However, in the presented scenario the dynamics of the rotating bound state is strongly influenced

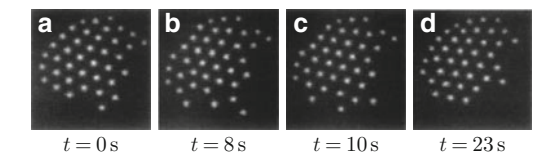


Fig. 2.20 Many particle system with constant number of dissipative solitons [2.55]. (a)–(d) Snapshots of the luminance distribution for constant parameters:  $U_0 = 1,900 \text{ V}$ ,  $p_{\text{N}_2} = 130 \text{ hPa}$ ,  $T_{\text{SC}} \approx 90 \text{ K}$ , d = 0.8 mm,  $a_{\text{SC}} = 1.0 \text{ mm}$ , D = 20 mm, for additional parameters see [2.55]

by spatial inhomogeneities, which are presumably located at the semiconductor. The inhomogeneities excite internal degrees of freedom such that the binding distance is not constant.

Note, that the distance between both dissipative solitons is small compared to the distance of the filaments to the boundary of the active area, such that the boundary does not stabilize the structure or influences its dynamics. This is in contrast to the observation of rotating hexagonal patterns on circular domains as reported for combustion experiments [2.78, 2.79] or ac-driven gas-discharge systems [2.80], for which the rotational dynamics is determined by the circular shape of the domain and the related breaking of symmetry. However, rotating bound states of dissipative solitons, which are not stabilized by the boundary of the system, are for example observed for oil droplets on a bath of silicon oil which is oscillated vertically [2.81–2.83].

#### 2.2.5.4 Many Particle Phenomena

In Sect. 2.2.3.1 a many particle phenomena has been introduced, where the number of dissipative solitons varies due to repeated generation and annihilation processes. Comparable results are also obtained for experimental parameters without generation and annihilation processes of dissipative solitons. In these cases the number of dissipative solitons is constant, but the ordering of the clusters varies due to the stochastic dynamics of the system.

An example for such kind of phenomena is show in Fig. 2.20. The figure shows four snapshots of the luminosity distribution emitted from 39 current density filaments, which have been generated due to a self-completion scenario (Sect. 2.2.3). However, the number of dissipative solitons is constant, because the system parameters are not changed and does not permit the annihilation or generation of particles due to interaction processes.

The series of snapshots shows a cluster of hexagonally ordered current density filaments, which is not rigid but allows for the relocation of single dissipative solitons at the boundaries of the cluster. On the time scale of several seconds the consecutive process of detaching and reconnecting of single dissipative solitons leads to the restructuring of the cluster. Astroy and Logvin interpret this observation

References 39

as noise induced evaporation and condensation of individual dissipative solitons [2.55], at which the hexagonally ordered state is identified as condensed phase.

#### References

- 2.1. G. Wald, Nobel Lect. Physiol. Med. 4, 255 (1967)
- V. Castets, E. Dulos, J. Boissonade, P. De Kepper, Phys. Rev. Lett. 64(24), 2953 (1990). doi:10.1103/PhysRevLett.64.2953
- A. Mikhailov, K. Showalter, Phys. Rep. 425(2–3), 79 (2006). doi:10.1016/j.physrep.2005.
   11.003
- 2.4. V.K. Vanag, I.R. Epstein, Chaos 18(2), 026107 (2008). doi:10.1063/1.2900555
- 2.5. H.H. Rotermund, S. Jakubith, A. von Oertzen, G. Ertl, Phys. Rev. Lett. 66(23), 3083 (1991). doi:10.1103/PhysRevLett.66.3083. Copyright 1991 by the American Physical Society
- K.J. Lee, W.D. McCormick, J.E. Pearson, H.L. Swinney, Nature 369, 215 (1994). doi:10. 1038/369215a0
- D.G. Míguez, V.K. Vanag, I.R. Epstein, Proc. Natl. Acad. Sci. USA 104(17), 6992 (2007). doi:10.1073/pnas.0611438104
- W. Engel, M. Kordesch, H. Rotermund, S. Kubala, A. von Oertzen, Ultramicroscopy 36(1–3), 148 (1991). doi:10.1016/0304-3991(91)90146-W
- K. Asakura, J. Lauterbach, H.H. Rotermund, G. Ertl, J. Chem. Phys. 102(20), 8175 (1995). doi:10.1063/1.469229
- J. Christoph, M. Eiswirth, N. Hartmann, R. Imbihl, I. Kevrekidis, M. Bär, Phys. Rev. Lett. 82(7), 1586 (1999). doi:10.1103/PhysRevLett.82.1586
- S.Y. Yamamoto, C.M. Surko, M.B. Maple, R.K. Pina, Phys. Rev. Lett. 74(20), 4071 (1995). doi:10.1103/PhysRevLett.74.4071
- 2.12. B.P. Belousov, in Compilation of Abstracts on Radiation Medicine (Medgiz, Moscow, 1959), pp. 145–152. In Russian
- 2.13. A.M. Zhabotinsky, Biofizika 9, 306 (1964). In Russian
- 2.14. A.N. Zaikin, A.M. Zhabotinsky, Nature 225, 535 (1970). doi:10.1038/225535b0
- 2.15. A.T. Winfree, Science 175, 634 (1972)
- 2.16. A.M. Zhabotinsky, A.N. Zaikin, J. Theor. Biol. 40(1), 45 (1973). doi:10.1016/0022-5193(73) 90164-1
- 2.17. L. Kuhnert, Nature 319, 393 (1986). doi:10.1038/319393a0
- 2.18. E. Mihaliuk, T. Sakurai, F. Chirila, K. Showalter, Faraday Discuss. 120, 383 (2002). doi:10.1039/b103431f. Reproduced by permission of The Royal Society of Chemistry.
- 2.19. E. Mihaliuk, T. Sakurai, F. Chirila, K. Showalter, Phys. Rev. E 65(6), 065602 (2002). doi:10.1103/PhysRevE.65.065602
- 2.20. S. Kádár, J. Wang, K. Showalter, Nature 391, 770 (1998). doi:10.1038/35814
- V.K. Vanag, L. Yang, M. Dolnik, A.M. Zhabotinsky, I.R. Epstein, Nature 406, 389 (2000). doi:10.1038/35019038
- 2.22. I. Sendina-Nadal, E. Mihaliuk, J. Wang, V. Perez-Munuzuri, K. Showalter, Phys. Rev. Lett. 86(8), 1646 (2001)
- 2.23. T. Sakurai, E. Mihaliuk, F. Chirila, K. Showalter, Science 296(5575), 2009 (2002). doi:10.1126/science.1071265
- 2.24. A.J. Steele, M. Tinsley, K. Showalter, Chaos 18(2), 026108 (2008). doi:10.1063/1.2900386
- 2.25. M.R. Tinsley, A.J. Steele, K. Showalter, Eur. Phys. J. 165, 161 (2008). doi:10.1140/epjst/e2008-00859-7
- 2.26. A.M. Turing, Philos. Trans. R. Soc. B 237, 37 (1952)
- Z. Zoszticzius, W. Hosrthemke, W.D. McCormick, H.L. Swinney, W.Y. Tam, Nature 329, 619 (1987). doi:10.1038/329619a0

- Q. Ouyang, V. Castets, J. Boissonade, J.C. Roux, P.D. Kepper, H.L. Swinney, J. Chem. Phys. 95(1), 351 (1991)
- 2.29. Q. Ouyang, H.L. Swinney, Nature 352, 610 (1991). doi:10.1038/352610a0
- V.K. Vanag, I.R. Epstein, Phys. Rev. Lett. 87(22), 228301 (2001). doi:10.1103/PhysRevLett. 87.228301
- 2.31. R.J. Field, E. Körös, R.M. Noyes, J. Am. Chem. Soc. 94(25), 8649 (1972). doi:10.1021/ja00780a001
- 2.32. R.J. Field, R.M. Noyes, J. Chem. Phys. **60**(5), 1877 (1974)
- 2.33. V.K. Vanag, I.R. Epstein, Patterns of nanodroplets: the Belousov-Zhabotinsky-aerosol OT-microemulsion system, in *Self-Organized Morphology in Nanostructured Materials*. Springer Series in Materials Science, vol. 99 (Springer, Heidelberg, 2008), pp. 89–113. doi: 10.1007/978-3-540-72675-3\\_5
- 2.34. A. Kaminaga, V.K. Vanag, I.R. Epstein, J. Chem. Phys. **122**, 174706 (2005). doi:10.1063/1. 1888386
- 2.35. A. Kaminaga, V.K. Vanag, I.R. Epstein, Angew. Chem. Int. Ed. 45, 3087 (2006). doi:10. 1002/anie.200600400
- V.K. Vanag, I.R. Epstein, Phys. Rev. Lett. 92(12), 128301 (2004). doi:10.1103/PhysRevLett. 92.128301
- K.J. Lee, W.D. McCormick, Q. Ouyang, H.L. Swinney, Science 261(5118), 192 (1993). doi: 10.1126/science.261.5118.192
- 2.38. R.D. Vigil, Q. Ouyang, H.L. Swinney, Phys. A 188, 17 (1992)
- 2.39. I. Szalai, P.D. Kepper, J. Phys. Chem. A 112(5), 783 (2008). doi:10.1021/jp711849m
- 2.40. I. Szalai, P.D. Kepper, Chaos Interdiscip. J. Nonlinear Sci. 18(2), 026105 (2008). doi: 10.1063/1.2912719. http://link.aip.org/link/?CHA/18/026105/1. Copyright 2008, American Institute of Physics
- 2.41. Yu.A. Astrov, H.-G. Purwins, Phys. Lett. A **358**, 404 (2006). doi:10.1016/j.physleta.2006.05. 047. Fig. 2.12 published with kind permission of Elsevier. Copyright (2006)
- 2.42. K.J. Lee, W.D. McCormick, J.E. Pearson, H.L. Swinney, Nature 369, 215 (1994). doi:10. 1038/369215a0
- 2.43. G. Li, Q. Ouyang, H.L. Swinney, J. Chem. Phys. 105(24), 10830 (1996). doi:10.1063/1. 472891
- 2.44. T.C. Lengnick, Discharge tube. Patent 1,936,514, United States Patent Office (1933)
- 2.45. S.S. Kasimov, L.G. Paritskii, S.M. Rivkin, Investigation of the ionization-type image converter. VINITI N2693-74 (1974). In Russian
- 2.46. Yu.A. Astrov, L.M. Portsel, S.P. Teperick, H. Willebrand, H.-G. Purwins, J. Appl. Phys. **74**(4), 2159 (1993)
- 2.47. L.M. Portsel, Yu.A. Astrov, I. Reimann, E. Ammelt, H.-G. Purwins, J. Appl. Phys. **85**, 3960 (1999)
- 2.48. J.H.R. Kim, H. Maurer, Yu.A. Astrov, M. Bode, H.-G. Purwins, J. Comput. Phys. 170, 395 (2001)
- 2.49. V.M. Marchenko, S. Matern, Yu.A. Astrov, L.M. Portsel, H.-G. Purwins, Proc. SPIE 4669, 1 (2002)
- S. Matern, V.M. Marchenko, Yu.A. Astrov, L.M. Portsel, H.-G. Purwins, Proc. SPIE 4669, 13 (2002)
- S. Matern, V.M. Marchenko, Yu.A. Astrov, L.M. Portsel, H.-G. Purwins, Photonik 3, 84 (2002)
- 2.52. H. Bödeker, A.W. Liehr, T.D. Frank, R. Friedrich, H.-G. Purwins, New J. Phys. 6(62), 1 (2004). Published with kind permission of IOP Publishing Ltd
- 2.53. E. Ammelt, Yu.A. Astrov, H.-G. Purwins, Phys. Rev. E **58**(6), 7109 (1998)
- 2.54. Yu.A. Astroy, E. Ammelt, S. Teperick, H.-G. Purwins, Phys. Lett. A **211**(3), 184 (1996)
- 2.55. Yu.A. Astrov, Yu.A. Logvin, Phys. Rev. Lett. **79**(16), 2983 (1997). Figs. 2.10, 2.11, and 2.20 published with kind permission of the American Physical Society. Copyright (1997)
- E.L. Gurevich, A.S. Moskalenko, A.L. Zanin, Yu.A. Astrov, H.-G. Purwins, Phys. Lett. A 307(5–6), 299 (2003)

References 41

- 2.57. Yu.A. Astrov, E. Ammelt, H.-G. Purwins, Phys. Rev. Lett. 78(16), 3129 (1997)
- 2.58. Yu.A. Astroy, I. Müller, E. Ammelt, H.-G. Purwins, Phys. Rev. Lett. 24(15), 5341 (1998)
- 2.59. Yu.A. Astrov, H.-G. Purwins, Phys. Lett. A 283, 349 (2001). Figs. 2.9 and 2.13 published with kind permission of Elsevier. Copyright (2001)
- 2.60. H. Bödeker, M.C. Röttger, A.W. Liehr, T. Frank, R. Friedrich, H.-G. Purwins, Phys. Rev. E **67**(056220), 1 (2003), doi:10.1103/PhysRevE.67.056220
- 2.61. A.W. Liehr, H.U. Bödeker, M.C. Röttger, T.D. Frank, R. Friedrich, H.-G. Purwins, New J. Phys. 5(89), 1 (2003). http://stacks.iop.org/1367-2630/5/89. Published with kind permission of IOP Publishing Ltd
- 2.62. A.W. Liehr, A.S. Moskalenko, Yu.A. Astrov, M. Bode, H.-G. Purwins, Eur. Phys. J. B 37, 199 (2004). Figs. published with kind permission of EDP Sciences
- 2.63. C. Strümpel, H.-G. Purwins, Yu.A. Astrov, Phys. Rev. E 63(2), 026409/1 (2001)
- 2.64. C. Strümpel, Yu.A. Astrov, H.-G. Purwins, Phys. Rev. E **65**(066210), 1 (2002)
- 2.65. D. Becker, Frontausbreitung und Filamentstrukturen in einem zweidimensionalen gleichspannungsbetriebenen Gasentladungssystem. Master's thesis, Institut für Angewandte Physik, Westfälische Wilhelms-Universität Münster, 1994
- S.V. Gurevich, H.U. Bödeker, A.S. Moskalenko, A.W. Liehr, H.-G. Purwins, Phys. D 199(1–2), 115 (2004). doi:10.1016/j.physd.2004.08.020
- 2.67. H. Meinhardt, A. Gierer, J. Cell Sci. 15, 321 (1974)
- 2.68. E. Ammelt, Untersuchungen zur Strukturbildung in planaren Gasentladungssystemen mit bildverarbeitenden Methoden. Dissertation, Institut für Angewandte Physik, Westfälische Wilhelms-Universität Münster, 1995
- 2.69. H.-G. Purwins, AIP Conf. Proc. 993(1), 67 (2008). doi:10.1063/1.2909178. http://link.aip.org/link/?APC/993/67/1
- 2.70. J.C. Strümpel, Experimentelle Untersuchung der raumzeitlichen Strukturierung in einem planaren Halbleiter-Gasentladungssystem. Dissertation, Institut für Angewandte Physik, Westfälische Wilhelms-Universität Münster, 2001
- 2.71. H. Willebrand, F.-J. Niedernostheide, E. Ammelt, R. Dohmen, H.-G. Purwins, Phys. Lett. A 153(8), 437 (1991)
- 2.72. H.U. Bödeker, Dynamik und Wechselwirkung dissipativer Solitonen in einer planaren Gleichspannungs-Gasentladung. Master's thesis, Institut für Angewandte Physik, Westfälische Wilhelms–Universität Münster, 2003
- 2.73. H.-G. Purwins, H.U. Bödeker, A.W. Liehr, in *Dissipative Solitons*, ed. by N. Akhmediev, A. Ankiewicz (Springer, Berlin, 2005), pp. 267–308
- 2.74. J.C. Russ, *The Image Processing Handbook*, 4th edn. (CRC, Boca Raton, 2002)
- 2.75. S. Flothkötter, Untersuchung laufender Stromfilamente in einem Si(ZN)-Hybrid-Gasentl-adungssystem. Master's thesis, Institut für Angewandte Physik, Westfälische Wilhelms-Universität Münster, 2001
- 2.76. P.R.J. Boscovich, Theoria philosophiae naturalis. Redacta ad unicam legem virium in natura existentium (Remondiniana, Venedig, 1763)
- 2.77. R.J. Boscovich, A Theory of Natural Philosophy. English Edition from the Text of the First Venetian Edition Published Under the Personal Superintendence of the Author in 1763 (MIT, Cambridge, 1966)
- 2.78. G.H. Gunaratne, M. El-Hamdi, M. Gorman, Mod. Phys. Lett. B 10(28), 1379 (1996)
- 2.79. A. Palacios, G.H. Gunaratne, M. Gorman, K.A. Robbins, Chaos 7(3), 463 (1997)
- 2.80. A.L. Zanin, E.L. Gurevich, A.S. Moskalenko, H.U. Bödeker, H.-G. Purwins, Phys. Rev. E **70**(3), 036202 (2004). doi:10.1103/PhysRevE.70.036202
- Y. Couder, S. Protiere, E. Fort, A. Boudaoud, Nature 437(7056), 208 (2005). doi:10.1038/ 437208a
- S. Protiere, Y. Couder, E. Fort, A. Boudaoud, J. Phys. Condens. Matter 17(45), S3529 (2005). doi:10.1088/0953-8984/17/45/044
- S. Protiere, A. Boudaoud, Y. Couder, J. Fluid Mech. 554(7056), 85 (2006). doi:10.1017/ S0022112006009190

# Chapter 3 Modeling

The discreteness just results as a structure from the laws ruling the reality. By no means these laws are completely understood, but a probably correct analogy from physics of rigid bodies might be the occurrence of partial tones – e.g. of a bell – from the finite size of the bell and the laws of elasticity not at all being discontinuous.

Erwin Schrödinger, 1952, translated from a voice recording [3.1].

**Abstract** The goal of this chapter is the exploration of fundamental aspects for structure formation in reaction-diffusion systems. In other words: What is the minimal requirement for structure formation? Therefore the considerations start with discussing the dynamics resulting from a cubic non-linearity which leads to the concept of bifurcations and bistability. Taking spatial coupling into account one finds periodic structures and stationary fronts. Extending the nonlinearity by means of a driving term new phenomena like trigger fronts and critical nuclei are explored. The stabilization of critical nuclei by global feedback leads to the introduction of a second component and the well-known phenomena of extended activator-inhibitor systems: Turing-patterns, localized solutions with exponentially and oscillatory decaying tails as well as the formation of Voronoi-diagrams. Finally, a second inhibitor is introduced and simple dissipative soliton solutions are discussed.

# 3.1 One-Component Systems with Symmetric Potential

# 3.1.1 Local Bistability

A typical property of nonlinear systems is the parameter dependent occurrence of bi- and multi-stability. In this context bistability means, that a dynamic system has got two attractors [3.2, p. 28]. In the most simple case these attractors correspond

44 3 Modeling

to stable stationary states of the system, which can be switched in between by sufficient large perturbations. Multi-stability occurs, if more than two attractors exist. These phenomena are observed in a broad variety of nonlinear systems: e.g. rest positions of nonlinear torsional oscillators [3.3], membrane activity of olfactory bulb mitral cells [3.4], concentration density of reagents, [3.5,3.6], optical properties of nonlinear media [3.7], current density characteristics of gas-discharge-systems [3.8] and semiconductor devices [3.9–3.12].

The extensive experimental observations show, that the combination of local bistability and spatial coupling leads to spatiotemporal structures, such that bistable systems are hopeful candidates for structure formation phenomena. However, it will be shown that bistability is not stringently necessary for structure formation, if the structures are stabilized by competing processes (e.g. Sect. 3.3).

Because the bistability of a system, first of all, is determined by its inherent nonlinearity, we are starting with the following local dynamics:

$$\dot{u} = \lambda u - u^3. \tag{3.1}$$

Here,  $\dot{u}$  is the derivative with respect to time t. The local dynamics defined by this cubic nonlinearity is visualized in Fig. 3.1a as phase space portrait. In this diagram the change  $\dot{u}$  of quantity u is plotted as function of the respective state u of the system. Thus the quantity u increases for  $\dot{u} > 0$ , which is implied by *horizontal right arrows* and will decrease for  $\dot{u} < 0$  (*horizontal left arrows*). Between these regions ( $\dot{u} = 0$ ), the system is stationary such that the undisturbed system will stay in these states for all times. Therefore these states are called *fixed points* of the dynamics. The phase space portrait (Fig. 3.1a) visualizes that for  $\lambda \leq 0$  one stationary state exists at  $u_0^* = 0$ , while for  $\lambda > 0$  two additional stationary states appear.

The stability of these stationary states can be considered in terms of classical mechanics if the dynamics are interpreted as over-damped motion of a particle which is located at *u* and moves according to potential

$$V_{\ell}(u) = -\int_{u_0^*}^{u} f(u_h) du_h = -\int_{0}^{u} f(u_h) du_h = -\frac{\lambda}{2} u^2 + \frac{1}{4} u^4$$
 (3.2)

(Fig. 3.1b). For this approach it is assumed that the inertia of the particle is small compared to the friction force and to the force related to the potential [3.13, p. 30]. For  $\lambda \leq 0$  the potential has a global minimum at  $u_0^* = 0$  and therefore is a stable fixed point of the dynamics (gray curve in Fig. 3.1b). On the other hand the potential exhibits a local maximum at  $u_0^*$  for  $\lambda > 0$  corresponding to an unstable fixed point (black curve in Fig. 3.1b). According to this considerations small perturbations  $\tilde{u}$  of fixed point  $u_0^*$  will increase for  $\lambda > 0$ . For  $\lambda \leq 0$  perturbations will decrease such that the fixed point  $u_0^*$  will be approached asymptotically for  $t \to \infty$ . It is said that the stationary state  $u_0^*$  is asymptotically stable for  $\lambda \leq 0$  and unstable for  $\lambda > 0$ . Note, that the maximum of the potential at  $u_0^* = 0$  for  $\lambda > 0$  is flanked by two local minima  $u_0^{\pm} = \pm \sqrt{\lambda}$ , which denote two asymptotically stable fixed points

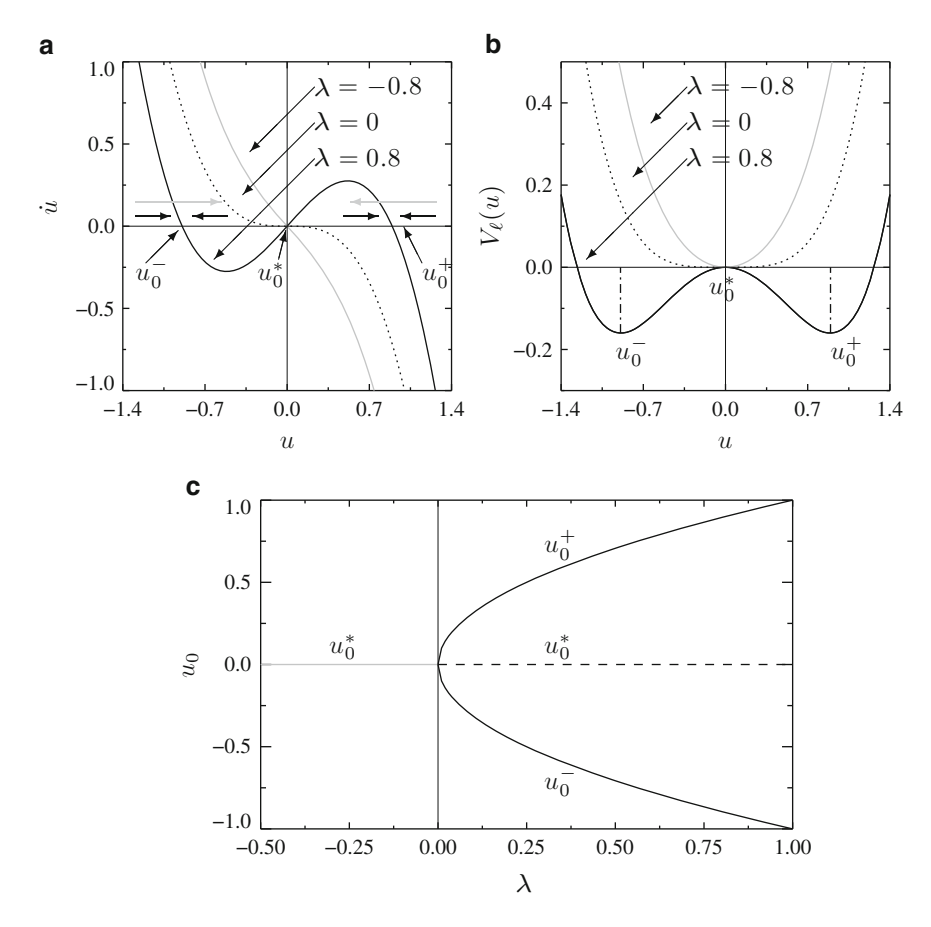


Fig. 3.1 Local dynamics exhibiting supercritical pitchfork bifurcation. *Gray* and *black curves* refer to the mono-stable and bistable case, respectively, while the separatrix is plotted by *dotted curves*. (a) Cubic characteristic f(u) (3.1) with *horizontal vectors* indicating the direction of phase flow for the mono-stable (*gray vectors*) and the bistable case (*black vectors*). (b) Potential  $V_{\ell}(u)$  (3.2) of the local dynamics. Local minima and maxima refer to stable and unstable states, respectively. (c) Bifurcation diagram showing the stationary state as function of the control parameter  $\lambda$ . The *vertical line* separates qualitatively different solutions in parameter space. *Solid* and *broken curves* refer to stable and unstable solutions of f(u) (3.1)

such that the system can be switched between these stable states by sufficient large perturbations. Thus depending on parameter  $\lambda$  the discussed system is mono-stable  $(\lambda \leq 0)$  or bistable  $(\lambda > 0)$ .

The transition of a system with one stationary state to a system with three stationary states is a qualitative change of its dynamics. Close to the stationary solution  $u_0^*=0$  this qualitative change becomes most obvious. While the phase flow drives the system towards the fixed point  $u_0^*=0$  for  $\lambda \leq 0$ , it veers away from the vicinity of  $u_0^*=0$  for  $\lambda>0$  and is driven towards one of the evolved stationary states  $u_0^{\pm}=\pm\sqrt{\lambda}$ . Such a change of phase space topology is called bifurcation.

46 3 Modeling

The special case discussed here is called supercritical pitchfork bifurcation due to the pitchfork-like bifurcation diagram depicted in Fig. 3.1c. This graph shows the stationary states of the system as function of control parameter  $\lambda$ . The critical parameter  $\lambda_c = 0$  at which the newly evolved solutions  $u_0^{\pm}$  branch is called bifurcation point. It divides the different phase space topologies in parameter space.

At the beginning of this section it has been mentioned that bistability of the local dynamics is a sufficient prerequisite for observing structure formation phenomena in spatially extended systems. Therefore we are setting  $\lambda=0.8$  for the examples of the following sections.

# 3.1.2 Spatial Bistability

In order to investigate the influence of local bistability on spatially extended systems we are taking diffusive processes into account. Diffusion is one of the most basic mechanisms of spatial coupling, which has been investigated in the in the eighteenth century in the context of heat transfer and therefore had played a crucial role in developing the theory of partial differential equations [3.14]. For this purpose we are complementing (3.1) with the term  $D_u \Delta u$ . Here parameter  $D_u$  denotes a diffusion constant and  $\Delta$  the Laplacian in  $\mathbb{R}^n$ :

$$\dot{u} = D_u \Delta u + \lambda u - u^3 \tag{3.3}$$

with u=u(x,t) and  $x\in\mathbb{R}^n$ . The homogeneous solutions of (3.3) are derived from the solutions of the local dynamics as  $u_0^*(x)=u_0^*=0$  and  $u_0^\pm(x)=u_0^\pm=\pm\sqrt{\lambda}$ . Now, we are seeking stationary solutions  $\bar{u}(x)=0$  of (3.3) and assume that the gradient  $\nabla \bar{u}(x)$  vanishes in all directions despite of  $e_x$ . This leaves us with one spatial dimension:  $\bar{u}(x)=\bar{u}(x)$ . Thus (3.3) reduces to the differential equation of an undamped oscillator

$$D_u \bar{u}'' = -\lambda \bar{u} + \bar{u}^3. \tag{3.4}$$

The mechanical equivalent of this model is a chain of nonlinear torsional oscillators having an unbalanced mass at their top and being coupled by torque springs, which is a variation of the experimental setup reported by B. Denardo et al. [3.15]. If the weight of the unbalanced mass exceeds a critical value the oscillators won't reside at their top position anymore but are held by the torque springs at the left or right hand side of the top position.

Interpreting the x-coordinate as time the solutions of (3.4) can be interpreted as dynamics of a particle with mass  $D_u$  moving in potential

$$V_{\rm r}(\bar{u}) = \frac{\lambda}{2}\bar{u}^2 - \frac{1}{4}\bar{u}^4. \tag{3.5}$$

An example of this potential for  $\lambda=0.8$  and  $D_u=5\cdot 10^{-5}$  is depicted in Fig. 3.2a. The oscillator equation (3.4) has a continuous family of solutions with energy eigenvalues  $0< E_{\rm G}<\frac{\lambda^2}{4}$  resembling periodic structures. These structures

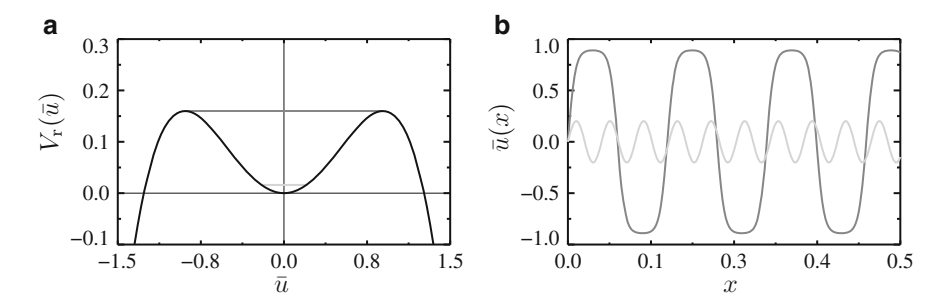


Fig. 3.2 Stationary periodic solutions of the one-dimensional oscillator (3.3). (a) Potential  $V_{\rm r}(\bar{u})$  (3.5) (black curve) and total energy  $E_{\rm G}$  of periodic structures in the harmonic limit  $E_{\rm G,h}=0.1\frac{\lambda^2}{4}$  (light gray line) and in the non-harmonic limit  $E_{\rm G,n}=0.9999\frac{\lambda^2}{4}$  (dark gray line). (b) Numerical solutions of oscillator (3.3) for the initial conditions  $\bar{u}(0)=0$  and  $\bar{u}'(0)=\sqrt{2E_{\rm G}/D_u}$ . The light gray curve corresponds to the harmonic limit with total energy  $E_{\rm G,h}$  and the dark gray curve to the non-harmonic limit with total energy  $E_{\rm G,n}$ . Parameters:  $\lambda=0.8$ ,  $D_u=5\cdot 10^{-5}$ 

can be interpreted as undamped oscillations being harmonic for  $E \to 0$  (*light gray* curve in Fig. 3.2b). However, these periodic structures are not stable against small perturbations neither in the harmonic nor in the non-harmonic limit [3.16, p. 84ff].

Let's take a closer look at the amplitude and frequency characteristics of the oscillating solutions. The total energy  $E_G$  of these solutions are the sum of the potential energy  $V_r(\bar{u})$  (3.5) and a gradient dependent part  $E_{Grad} = \frac{D_u}{2}(\bar{u}')^2$ . The amplitude  $\hat{u}$  of these solutions is given by the total energy  $E_G$ :

$$\hat{u} = \hat{u}(E_{\rm G}) = 2\sqrt{\lambda - \sqrt{\lambda^2 - 4E_{\rm G}}}.$$
 (3.6)

The spatial period  $\nu$  of the structures can be computed analytically by Baumann's approach [3.17, p. 35ff] as function of the amplitude  $\hat{u}$  respectively the total energy  $E_{\rm G}$  to

$$\nu(E_{\rm G}) = \frac{4\sqrt{D_u \frac{\hat{u}(E_{\rm G})^2 - 4\lambda}{\hat{u}(E_{\rm G})^2 - 8\lambda}} K\left(\frac{\hat{u}(E_{\rm G})}{8\lambda - \hat{u}(E_{\rm G})}\right)}{\sqrt{\frac{\lambda}{2} - \frac{\hat{u}(E_{\rm G})^2}{8}}}$$
(3.7)

with K(x) denoting the complete elliptic integral of first kind [3.18]. By plotting the spatial period  $\nu$  as function of the total energy (Fig. 3.3a) it becomes obvious that the spatial period  $\nu(E_{\rm G})$  diverges for a certain value of  $E_{\rm G}>0$  while it converges for  $E_{\rm G}\to 0$ . From the nominator of (3.7) and amplitude (3.6) follows that the spatial period diverges for  $E_{\rm G}\to \frac{\lambda^2}{4}$ . The limit  $E_{\rm G}\to 0$  of the opposite direction can be calculated from  $\hat{u}\to 0$  and  $K(x)|_{x\to 0}=\frac{\pi}{2}$  to the value of  $\nu(E_{\rm G})|_{E_{\rm G}\to 0}=2\pi\sqrt{D_u/\lambda}$  which corresponds to the period of a torsional oscillator with moment of inertia  $D_u$  and torsion coefficient  $\lambda$ .

The divergence of the spatial period  $\nu(E_{\rm G})$  in the limit  $E_{\rm G} \to \frac{\lambda^2}{4}$  leads to an infinitely extended transition  $\sqrt{\lambda} \to -\sqrt{\lambda}$  respectively  $-\sqrt{\lambda} \to \sqrt{\lambda}$ .

48 3 Modeling

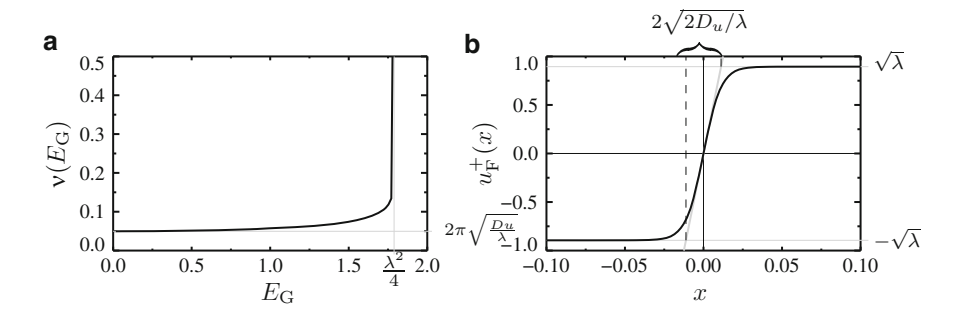


Fig. 3.3 Stationary solutions of the nonlinear equation of motion (3.4) in one-dimensional systems. (a) Spatial period  $\nu$  (3.7) plotted as function of total energy  $E_{\rm G}$ . The harmonic limit is given for  $E_{\rm G} \to 0$ . (b) Analytical solution  $u_{\rm F}(x)$  (3.8) of (3.4) for  $E_{\rm G} \to \frac{\lambda^2}{4}$ . Parameters:  $\lambda = 0.8$ ,  $D_u = 5 \cdot 10^{-5}$ 

The corresponding structure is a so-called front resembling a continuous transition in space between the two fixpoints  $u_0^{\pm}$  which are reached asymptotically for  $x \to \pm \infty$ . Concerning this limit the nonlinear equation of motion (3.4) can be solved analytically

$$u_{\rm F}^{\pm}(x) = \pm \sqrt{\lambda} \tanh\left(x\sqrt{\frac{\lambda}{2D_u}}\right)$$
 (3.8)

(cf. [3.19, 3.20]). Note, that due to the translational invariance of the system an infinite family of solutions  $\{u_{\rm F}(x-x_0)|x_0\in\mathbb{R}\}$  exists. An example of a front located at  $x_0=0$  is shown in Fig. 3.3b. The spatial region covering most of the transition from  $\pm\sqrt{\lambda}\to\mp\sqrt{\lambda}$  can be calculated from the intersection of tangent  $g(x)=x\,u_{\rm F}'(0)$  with the asymptotes  $\pm\sqrt{\lambda}$  at  $x_{1,2}=\pm\sqrt{2D_u/\lambda}$ . The distance between these intersection points is  $2\sqrt{2D_u/\lambda}$  which can be considered as length scale of the front.

In indefinitely large systems of type (3.3) fronts are quite robust against perturbations, which most likely will lead to a shift of the front. This effect is more thoroughly discussed in Sect. 4.2.1. However, due to their stability fronts respectively their analytical solution (3.8) are quite useful for checking the correctness of numerical simulations. For example consider (3.3) on a indefinitely one-dimensional domain being parameterized by spatial variable x, then the position  $x_0$  and the initial condition

$$u(x,0) = \begin{cases} \pm \sqrt{\lambda}, & \text{for } x < x_0 \\ \mp \sqrt{\lambda}, & \text{for } x \ge x_0 \end{cases}$$

$$\text{for } x \in \mathbb{R}$$
(3.9)

can be chosen, such that the numerical solution of (3.3) should relax to the front  $\bar{u}_{\rm F}(x-x_0)$  (3.8) located at  $x_0$ .

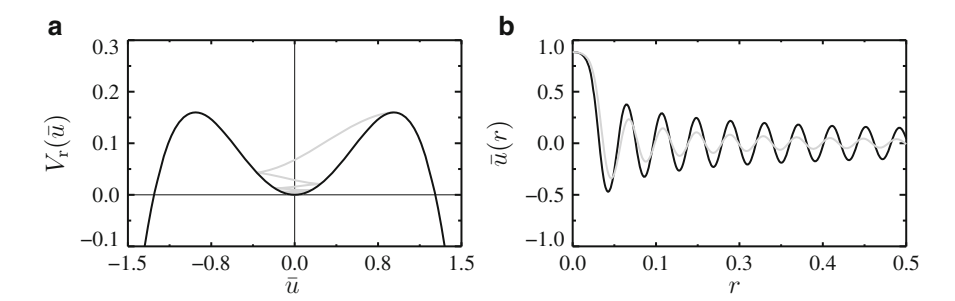


Fig. 3.4 Radial-symmetric stationary solutions of the one-component reaction-diffusion equation (3.10). (a) Potential  $V_{\rm r}(\bar{u})$  (3.5) (black curve) and total energy  $E_{\rm G} = V_{\rm r}(\bar{u}) + D_u(\bar{u}')^2/2$  (light gray curve) of the damped three-dimensional oscillation depicted in (b). The latter shows numeric approximations of two stationary radially symmetric solutions in  $\mathbb{R}^2$  (black) and in  $\mathbb{R}^3$  (light gray). Both solutions of (3.10) were computed with a Runge-Kutta scheme [3.22, p. 1095] for the interval  $r \in [\frac{1}{1,000}, \frac{1}{2}]$  and initial conditions  $u(\frac{1}{1,000}) = \sqrt{\lambda} - \frac{1}{100}, u'(\frac{1}{1,000}) = 0$ . Parameters:  $\lambda = 0.8$ ,  $D_u = 5 \cdot 10^{-5}$ 

## 3.1.3 Spatial Bistability in Extended Systems

Solutions of the one-component reaction-diffusion-system (3.3) discussed in the previous section also represent solutions on n-dimensional domains if the gradient of these solutions vanishes in (n-1) spatial directions and therefore are quasi one-dimensional. Non-trivial stationary solutions of (3.3) on two- and three-dimensional domains are discussed under the assumption of certain boundary conditions by Alfimov et al. [3.21]. They show that the stabilizing effect of the domain boundaries enables localized solutions. Here, we are not limiting the domain size and are focusing on radial symmetric solutions in  $\mathbb{R}^n$ . Therefore the one-component n-dimensional reaction-diffusion-system (3.3) is transformed to a polar (n=2) respectively a spherical coordinate system (n=3):

$$D_u\left(\bar{u}''(r) + \frac{n-1}{r}\bar{u}'(r)\right) + \lambda\bar{u}(r) - \bar{u}(r)^3 = 0$$
(3.10)

with  $u'(r)|_{r=0} = 0$ . Due to the radial symmetry of the considered solutions the angular dependency vanishes and the coordinate r parameterizes the distance to the origin of the coordinate system. The resulting ordinary differential equation (3.10) can be interpreted as oscillatory equation of a particle having mass  $D_u$  which moves in potential  $V_r(\bar{u})$  (3.5). The friction  $\frac{n-1}{r}\bar{u}'(r)$  vanishes for the one-dimensional case (n=1), such that (3.10) becomes (3.4).

Solutions of the damped oscillator equation (3.10) can be calculated numerically for finite domains with  $r \in ]0, \infty[$  (Fig. 3.4b). Starting from initial conditions  $u(r_0) \in ]-\sqrt{\lambda}, \sqrt{\lambda}[\setminus\{0\}]$  and  $u'(r_0) = 0$  these solutions exhibit damped oscillations due to energy dissipation. For  $r \to \infty$  the oscillations relax against 0 (Fig. 3.4a). Because the friction depends on the dimension of the system the oscillations decay in three-dimensional systems twice the fast than in two-dimensional

50 3 Modeling

systems (Fig. 3.4b). Concerning the spatiotemporal dynamics of (3.3) nor the two-dimensional stationary solutions neither the three-dimensional stationary solutions (Fig. 3.4) are stable, because both relax for  $r \to \infty$  against the unstable fixed point  $u_0^* = 0$  of the local dynamics (3.1).

#### 3.2 One-Component Systems with Unsymmetric Potential

## 3.2.1 Local Bistability

In the foregoing section we have seen, that there are no stable localized solutions of the one-component reaction-diffusion (3.3) with symmetric potential (Fig. 3.4) which are embedded into one of the stable homogeneous ground states  $u_0^{\pm}$ . On the other hand such types of solutions can be regarded as prototypes of dissipative solitons in reaction-diffusion systems. Therefore we are seeking prerequisites of the field equations enabling localized solutions being embedded into a stable homogeneous state.

A hint is given by the localized solutions of the two- and three-dimensional systems (Fig. 3.4) which decay to the unstable homogeneous state  $u_0^*$ . In order to enable a relaxation of localized solutions to a stable ground state  $u_0^{\pm}$  the dissipation of energy resulting from the dimension depending friction (cf. Fig. 3.4a) has to be balanced by a potential difference.

The postulation of an unsymmetric potential can be fulfilled by adding a real constant  $\kappa_1$  to (3.3) breaking the point symmetry of the cubic nonlinearity (cf. Fig. 3.5a, b):

$$\dot{u} = D_u \Delta u + \lambda u - u^3 + \kappa_1 \tag{3.11}$$

with u = u(x, t) and  $x \in \mathbb{R}^n$ . This equation describes according to Schlögl a simple chemical reaction mechanism [3.23]. Its local dynamics

$$\dot{u}(t) = \lambda u(t) - u(t)^3 + \kappa_1 \tag{3.12}$$

has a co-dimension-2-bifurcation point at  $(\lambda_C, \kappa_{1,C})^T = \mathbf{0}$  which can be visualized by the nullcline  $\{u_0(\lambda, \kappa_1) | (\lambda, \kappa_1)^T \in \mathbb{R}^2\}$  (Fig. 3.6) defined by

$$\lambda u_0 - u_0^3 + \kappa_1 = 0 \tag{3.13}$$

as stationary states of the local dynamics (3.12). The special case  $\kappa_1 = 0$  is a pitchfork bifurcation. Its branches are indicated in Fig. 3.6 as solid and broken curves with the unstable branch being masked in parts by the folded nullcline. For  $\kappa_1 \neq 0$  one finds disturbed pitchfork bifurcations, an example of which is plotted in Fig. 3.6 for  $\kappa_1 = -1$ . Note, that the pair of stable-unstable solutions branch for  $\lambda > 0$  at

$$\kappa_{1,c} = \pm 2 \left(\frac{\lambda}{3}\right)^{\frac{3}{2}} \tag{3.14}$$

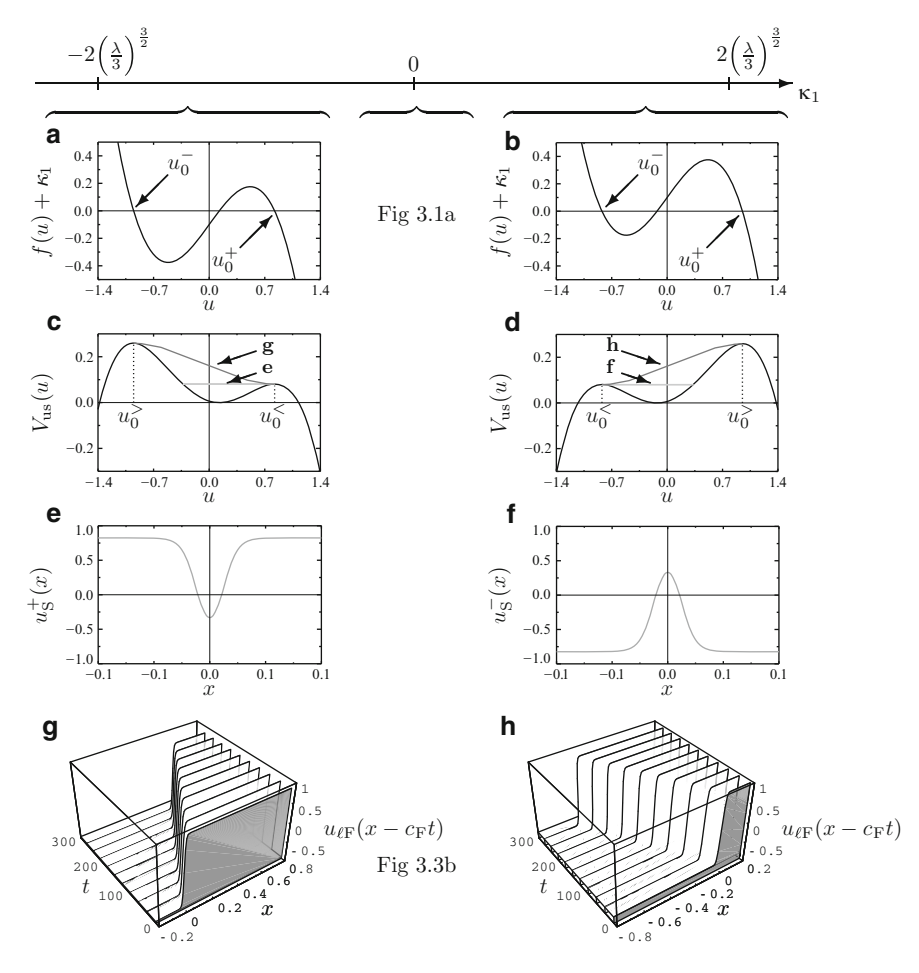


Fig. 3.5 One-dimensional solutions of the one-component reaction-diffusion-system (3.11) with unsymmetric potential (3.17). The diagrams on the *left hand side* characterize the system for  $-\kappa_{1,c} < \kappa_1 < 0$  (3.14), while the *right hand side* shows characteristic solutions for  $0 < \kappa_1 < \kappa_{1,c}$  (3.14). The column in between refers to the figures of the special case  $\kappa_1 = 0$  of the symmetric potential  $V_r(u)$  (3.5). (a) and (b) Shifted characteristic  $f(u) + \kappa_1$ . (c) and (d) Potential  $V_{us}(u)$  (3.17) of the spatially extended system (3.16) (*black curve*) with total energy  $V_{us}(u_S^{\pm}) + D_u \left(\frac{d}{dx}u_S^{\pm}\right)^2/2$  (*light gray lines*) of the critical nuclei  $u_S^{\pm}$  (3.19) depicted in subfigures (e) and (f). (c) and (d) Also show the total energy  $V_{us}(u_{\ell F}) + D_u \left(\frac{d}{dx}u_{\ell F}\right)^2/2$  (*dark gray lines*) of the moving fronts (3.25) depicted in subfigures (g) and (h). Parameters:  $\lambda = 0.8$ ,  $D_u = 5 \cdot 10^{-5}$ ,  $\kappa_1 = -0.1$  (*left column*),  $\kappa_1 = 0.1$  (*right column*)

due to saddle-node-bifurcations. Figure 3.6 also shows the projection of the saddle-node bifurcation points onto the  $u_0 = 3$  plane which reveals the characteristic cusp-like shape pointing to the co-dimensions-2-bifurcation point  $(\lambda_C, \kappa_{1,C})^T = \mathbf{0}$ . Due to its shape the co-dimension-2 bifurcation is called cusp-bifurcation.

52 3 Modeling

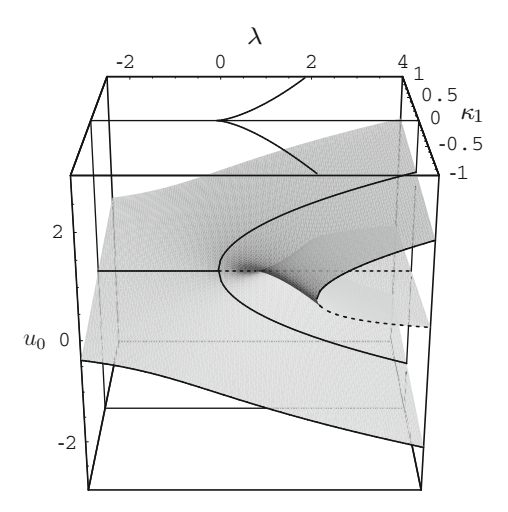


Fig. 3.6 Nullcline of the cusp-bifurcation visualized as set of solutions  $\{u_0\}_{\{(\lambda,\kappa_1)^T\}\in\mathbb{R}^2}$  for the local dynamics (3.12) of the Schlögl-model. For the special case  $\kappa_1=0$  the branches of the pitchfork-bifurcation are indicated as *solid* and *broken curves* (cf. Fig. 3.1c). The intersection at  $\kappa_1=-1$  shows a disturbed pitchfork-bifurcation with its characteristic saddle-node-bifurcation occurring at  $(\lambda,\kappa_1)^T=(3\cdot 2^{-2/3},-1)^T$  (3.14). The set of all saddle-node-bifurcation points (3.14) is the so-called cusp curve. Its projection on the  $u_0=3$  plane visualizes the characteristic cusp-shape of the curve with the co-dimension-2-bifurcation point at  $(\lambda_C,\kappa_{1,C})^T=\mathbf{0}$ 

In parameter space the cusp curve (3.14) separates the monostable parameter interval  $|\kappa_{1,m}| > |\kappa_{1,c}|$  from the bistable parameter interval  $|\kappa_{1,b}| \le |\kappa_{1,c}|$ . In this parameter interval Eq. (3.12) exhibits three stationary solutions  $u_0^- < u_0^+ < u_0^+$ . The fixed points

$$u_0^{\pm} = u_0^{\pm}(\lambda, \kappa_1) = \pm \frac{6(\mp 2)^{\frac{1}{3}}\lambda \mp (\mp 2)^{\frac{2}{3}}R(\lambda, \kappa_1)^{\frac{2}{3}}}{6R(\lambda, \kappa_1)^{\frac{1}{3}}}$$
with  $R(\lambda, \kappa_1) = \sqrt{729\kappa_1^2 - 108\lambda^3} - 27\kappa_1$  (3.15a)

are stable and the fixed point

$$u_0^* = u_0^*(\lambda, \kappa_1) = \frac{12\lambda + (1 + i\sqrt{3})R(\lambda, \kappa_1)^{\frac{2}{3}}}{(2R(\lambda, \kappa_1))^{\frac{1}{3}}}$$
(3.15b)

is unstable. The stable state of the saddle-node bifurcation is  $u_0^+$  for  $\kappa_1 > 0$  and  $u_0^-$  for  $\kappa_1 < 0$ . If a variation of parameters crosses the cusp curve and therefore changes the dynamics from bistability to monostability the system will suddenly switch to the only remaining state, which is called cusp catastrophe [3.24, 3.25]. The same scenario holds for the spatially extended system (3.11) because the fixed

points  $u_0^{\pm}$  and  $u_0^*$  (3.15) of the local dynamics (3.12) are stable  $u_0^{\pm}(x) = u_0^{\pm}$  respectively unstable  $u_0^*(x) = u_0^*$  homogeneous solutions of the one-component reaction diffusion system (3.11).

# 3.2.2 Critical Nuclei and Trigger Fronts in One-Dimensional Systems

The section starts with considering stationary solutions of the spatially extended system (3.11) which exhibit vanishing gradients in all but one spatial direction. For these solutions the one-component reaction-diffusion system reduces to a nonlinear oscillator equation

$$D_u \bar{u}'' = -\lambda \bar{u} + \bar{u}^3 - \kappa_1 \tag{3.16}$$

with  $\bar{u} = \bar{u}(x)$ . In analogy to (3.4) solutions of (3.16) describe stationary states of a chain of coupled nonlinear torque oscillators. However, this time the rest position is not located vertically above the axis of rotation ( $\kappa_1 = 0$ ) but deviates slightly from the top position ( $\kappa_1 \neq 0$ ) even if no unbalanced mass is attached ( $\lambda = 0$ , Fig. 3.6).

Interpreting the spatial coordinate as time coordinate Eq. (3.16) can be interpreted as undamped motion of a particle with mass  $D_u$  moving in the unsymmetric potential

$$V_{\rm us}(u) = \int_{u_0^*}^{u} (\lambda u_{\rm h} - u_{\rm h}^3 + \kappa_1) \, du_{\rm h} = \frac{\lambda}{2} u^2 - \frac{1}{4} u^4 + \kappa_1 u \tag{3.17}$$

(Fig. 3.5c, d). Note, that for the special case  $\kappa_1 = 0$  the potential  $V_{\rm us}(u)$  (3.17) simplifies to the symmetric potential  $V_{\rm r}(u)$  (3.5) (Figs. 3.2a and 3.4a).

In case of bistability  $0 < |\kappa_1| \le |\kappa_{1,c}|$  (3.14) the unsymmetric potential  $V_{\rm us}(u)$  has got two relative maxima  $V_{\rm us}(u_0^+) \ne V_{\rm us}(u_0^-)$  (Fig. 3.5c, d). From the foregoing section it is known, that solutions of (3.16) with total energy

$$0 < E_{G} < \min V_{us}(u_{0}^{\pm}) = \min\{V_{us}(u_{0}^{+}), V_{us}(u_{0}^{-})\}$$
(3.18)

are unstable periodic structures. Divergence of the spatial period occurs for  $E_G \to \min V_{\rm us}(u_0^\pm)$  which leads to the solution

$$u_{\rm S}^{\pm}(x) = u_0^{\pm} - \frac{3(u_0^{\pm})^2 - \lambda}{u_0^{\pm} \pm \sqrt{\frac{1}{2}(\lambda - (u_0^{\pm})^2)} \cosh\sqrt{\frac{3(u_0^{\pm})^2 - \lambda}{D_u}}x}$$
(3.19)

representing a localized stationary structure (Fig. 3.5e, f) of the one-dimensional one-component reaction-diffusion system (3.11) [3.26, 3.27]. This solution corresponds to a homoclinic orbit  $\left(u_S^{\pm}, \frac{\mathrm{d}}{\mathrm{d}x} u_S^{\pm}\right)^{\mathrm{T}}$  in phase space. Due to the translational invariance of the system (3.19) defines an indefinitely large family of localized solutions  $\{u_S^{\pm}(x-x_0)\}_{\{x_0 \in \mathbb{R}\}}$ .

54 3 Modeling

Concerning the one-dimensional time-dependent solutions u = u(x,t) of the one-component reaction-diffusion system

$$\dot{u} = D_u u'' + \lambda u - u^3 + \kappa_1 \tag{3.20}$$

the localized solution  $u_S^{\pm}(x)$  (3.19) is unstable, because it resembles a separatrix in solution space [3.28]. It separates the attractor of the stationary homogeneous state

$$u_0^{<} = \arg\min V_{\rm us}(u_0^{\pm})$$
 (3.21)

from the attractor of trigger fronts (Fig. 3.5g, h) switching the system dynamically into the dominating homogeneous state

$$u_0^> = \arg\max V_{\rm us}(u_0^{\pm}).$$
 (3.22)

The latter is determined by the largest relative maximum  $V_{\rm us}(u_0^>)$  of the potential  $V_{\rm us}(u)$  (3.17). Depending on parameter  $\kappa_1$  the following relation holds:

$$u_0^{\gtrless} = \begin{cases} u_0^{\pm} & : \kappa_1 > 0, \\ u_0^{\mp} & : \kappa_1 < 0. \end{cases}$$
 (3.23)

The instability of the homoclinic orbit  $u_S^{\pm}(x)$  (3.19) is also confirmed by Bode [3.29, p. 79ff], who investigated the interaction of fronts by a perturbation approach and found an unstable locking state such that the resulting two-front-structure can be interpreted as critical nucleus.

Trigger front solutions of (3.20) can be calculated analytically by considering solutions  $\widetilde{u} = \widetilde{u}(x',t)$ , which propagate with relative velocity c in a co-moving frame  $x' = x - c_F t$ . For  $c = c_F$  the moving solutions  $\widetilde{u}$  become stationary solutions  $u_{\ell F} = u_{\ell F}(x')$  of

$$D_{u}u_{\ell F}^{"} = -c_{F}u_{\ell F}^{'} - V_{us}^{'}(u_{\ell F}). \tag{3.24}$$

By adapting a standard front  $u_F^+(x)$  (Fig. 3.3b) to the respective  $\kappa_1$ -dependent homogeneous states  $u_0^\pm$  and  $u_0^*$  (3.15) and inserting this ansatz into (3.24) the following solution is deduced:

$$u_{\ell F}(x - c_{F}t) = \frac{u_{0}^{+} + u_{0}^{-}}{2} + \frac{u_{0}^{+} - u_{0}^{-}}{2} \tanh \left[ \frac{u_{0}^{+} - u_{0}^{-}}{2\sqrt{2D_{u}}} (x - c_{F}t) \right]$$
(3.25a)

[3.29, p. 60]. Here velocity  $c_{\rm F}$  is determined by the loss of energy

$$\int_{u_0^-}^{u_0^+} c_F u'_{\ell F} du_{\ell F} = c_F \int_{-\infty}^{+\infty} (u'_{\ell F})^2 dx = V_{us}(u_0^+) - V_{us}(u_0^-)$$
 (3.25b)

resulting from the asymptotic movement (Fig. 3.5c, d) from the higher relative potential maximum to the lower one:

$$c_{\rm F} = \frac{V_{\rm us}(u_0^+) - V_{\rm us}(u_0^-)}{\int_{-\infty}^{+\infty} (u_{\ell \rm F}')^2 \, \mathrm{d}x} = \frac{3}{2} \sqrt{2D_u} u_0^*. \tag{3.25c}$$

Therefore the direction of movement is determined for a standard front  $u_F^+$  by the sign of the unstable homogeneous stationary solution  $u_0^*$ .

For further reading on the dynamics and interaction of fronts, consider the literature on entire solutions [3.30–3.34].

# 3.2.3 Critical Nuclei and Trigger Fronts in Two- and Three-Dimensional Systems

In contrast to the solutions of the one-dimensional field equation (3.20) trigger fronts and critical nuclei cannot be computed analytically for two- or three-dimensional systems (3.11) in generic cases. They can only be determined if the problem reduces to a quasi one-dimensional systems for gradients vanishing in all but in one direction of the Cartesian coordinate system. However, formally it can be shown that stable structures cannot exist on convex domains with no-flux boundary conditions [3.35]. Hassan and Zanette [3.36] confirm this result for a three-dimensional Schlögl-model with piecewise linear characteristic. The authors also show that localized structures can be stabilized by Albedo- or Dirichlet-boundary conditions if the domain is large enough. On more complex domains with partially concave boundaries, e.g. on barbell shaped domains, fronts can be stabilized if the channel connecting the half domains is considerably thin [3.27, p. 35ff], such that the field equations can be reduced to a one-dimensional system with inhomogeneous diffusion.

Numerical solutions show that for two- and three-dimensional systems a critical nucleus exists [3.37] which separates in phase space the attractors of the non-dominant homogeneous state and a radial-symmetric trigger front. An example of which is shown in Fig. 3.7.

From a geometrical point of view the propagation velocity of weakly curved trigger fronts in two- and three-dimensional systems is not constant, but depends on their local curvature  $K_{\rm F}$ . Therefore the propagation velocity sums up to the velocity of planar fronts  $c_{\rm F}$  (3.25c) and a curvature dependent term [3.38, p. 27f]:

$$c(K_{\rm F}) = c_{\rm F} + D_u K_{\rm F} = c_{\rm F} + \frac{n-1}{R_{\rm F}} D_u. \tag{3.26}$$

Here variable  $R_F$  denotes the radius of curvature of the *n*-dimensional radial symmetric trigger front. Experimentally this effect has been observed in 1951 by Markstein for the propagation of two-dimensional flame fronts [3.39].

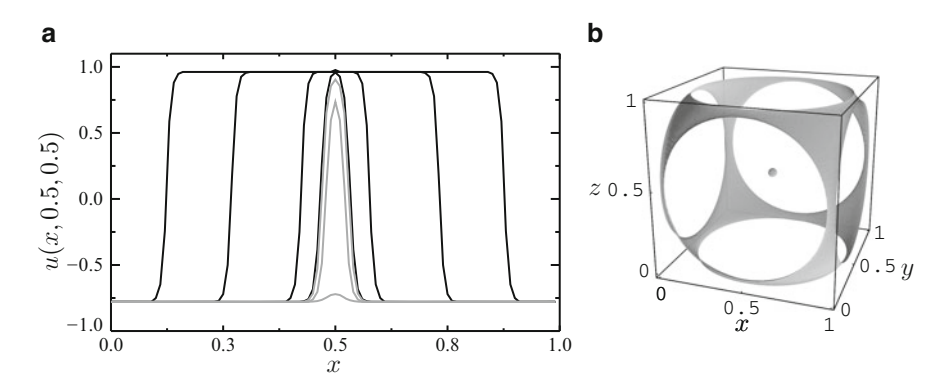


Fig. 3.7 The critical nucleus in Schlögl's model solved on a three-dimensional domain. (a) Intersection u(x, 0.5, 0.5) of two different three-dimensional solutions (black and gray curves) of the field equation (3.11) plotted for the snapshots  $t \in \{0, 60, 135, 195\}$  (black curves) and  $t \in \{15, 120, 165\}$  (gray curves). Black curves visualize a simulation, for which the initial conditions have been chosen slightly larger and broader than the critical nucleus. Therefore the snapshots show a trigger front extending uniformly into all spatial directions. Gray curves are snapshots of a simulation starting from an initial condition which has been chosen to be slightly smaller and thinner than the critical nucleus. In this case the localized excitation relaxes to the non-dominant state  $u_0^<$  (3.21). (b) Isosurfaces u(x, y, z) = 0 of the extending trigger front at t = 300 and the respective initial condition, which is visible as sphere in the center of the domain. At t = 300 the trigger front has already reached the boundaries of the domain and where it has been partly relaxed to the dominant state  $u_0^>$  (3.22). Parameters:  $\lambda = 0.8$ ,  $D_u = 5 \cdot 10^{-5}$ ,  $\kappa_1 = 0.15$ ,  $\Omega = [0, 1]^3$ ,  $\Delta_x = 0.01$ ,  $\Delta_t = 1$ 

In order to investigate the parameter regime enabling the existence of critical nuclei in two- and three-dimensional systems of Schlögl's model the respective field equation (3.11) is transformed into a polar respectively a spherical coordinate system. Considering stationary radial symmetric solutions the partial differential equation reduces to an ordinary differential equation:

$$D_u\left(u''(r) + \frac{n-1}{r}u'(r)\right) + \lambda u(r) - u(r)^3 + \kappa_1 = 0$$
(3.27)

with  $u'(r)|_{r=0} = 0$ . Here the independent variable r denotes the radial coordinate and parameter n the dimension of the considered domain. The friction term  $\frac{n-1}{r}u'(r)$  of (3.27) leads to a stable focus  $(u_0^*,0)^{\rm T}$  in phase space  $e_u \times e_{u'}$  of radially symmetric solutions [3.27, p. 42]. Therefore stationary localized solutions exist, which asymptotically reach the intermediate ground state  $u_0^*$  as damped spatial modulations for  $r \to \infty$  (cf. Fig. 3.4b). Because the ground state  $u_0^*$  is not stable with respect to the local dynamics, all stationary solutions converging for  $r \to \infty$  against  $u_0^*$  are unstable, too.

The stability range of the stable focus is confined by a separatrix in phase space, which starts close to the highest local maximum of the potential and reaches asymptotically the lower local maximum min  $V_{\rm us}(u_0^\pm)$  for  $r \to \infty$  (Fig. 3.8b–e). From the considerations of the previous section it is known, that the separatrix

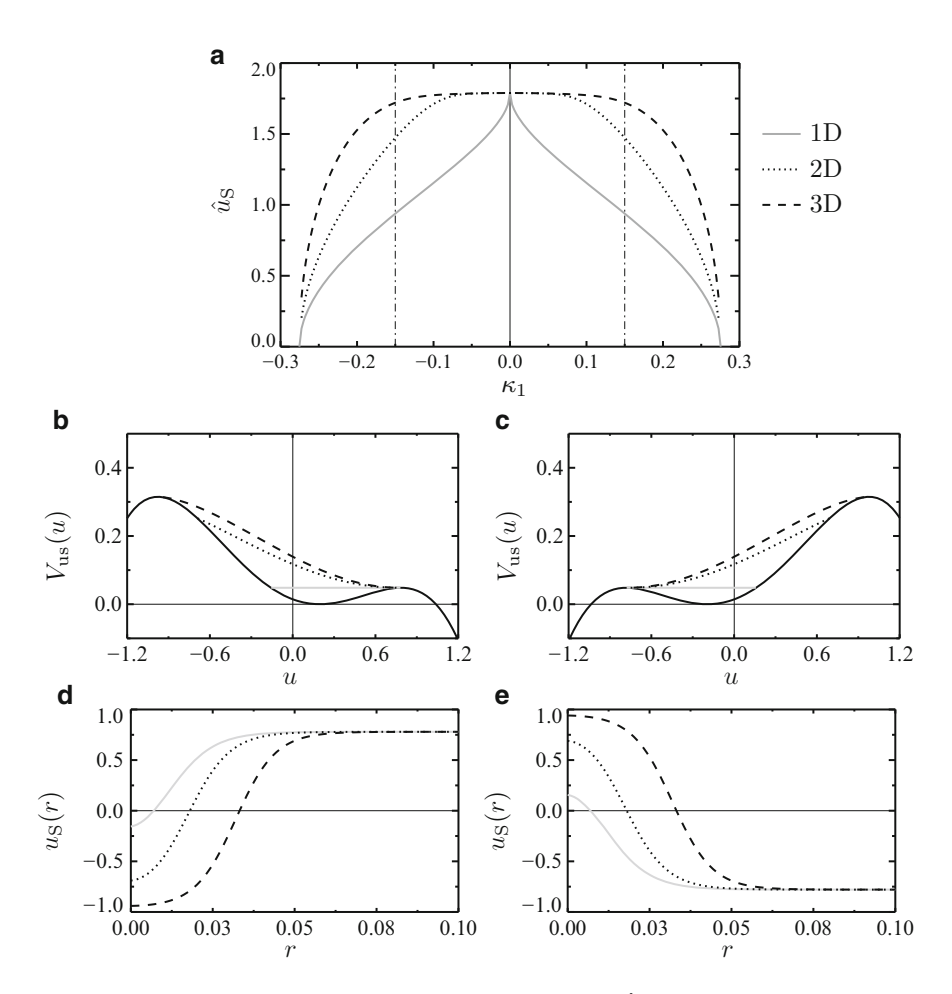


Fig. 3.8 The critical nucleus in Schlögl's model. (a) Amplitude  $\hat{u}_S = \max u_S(r) - \min u_S(r)$  of the critical nucleus  $u_S(r)$  plotted as function of parameter  $\kappa_1$ . (b) and (c) Potential  $V_{us}(u)$  (3.17) with total energy  $V_{us}(u_S) + D_u(u_S')^2/2$  of the critical nuclei depicted in (d) and (e), which have been computed as numerical solutions of the one-component field equation (3.27). *Gray curves* in subfigures (a)–(e) denote solutions on one-dimensional domains n=1, dotted curves the case n=2, and dashed curves the case n=3. Parameters:  $\lambda=0.8$ ,  $D_u=5\cdot 10^{-5}$ ,  $\kappa_1=-0.15$  (left column),  $\kappa_1=0.15$  (right column),  $\Omega=[0.01,0.1]$ ,  $\Delta_t=0.01$ , no-flux boundary condition

does only exist if the system is bistable  $0 < |\kappa_1| \le \kappa_{1,c}$  (3.14). In the respective parameter regime the amplitude  $\hat{u}_S = (\max u_S - \min u_S)$  of the one-dimensional critical nucleus increases monotonically for decreasing  $|\kappa_1|$  (gray curve in Fig. 3.8a), because the friction term of (3.27) vanishes for n=1 and the change of amplitude directly depends on the shift of the potential maxima. Note, that in phase space of one-dimensions solutions the homoclinic orbit of the separatrix transforms into a heteroclinic orbit for  $|\kappa_1| \to 0$ , which represents a stationary front in state space (Fig. 3.3).

In contrast, the amplitudes of two- and three-dimensional separatrixes are nearly constant for small absolute values of parameter  $\kappa_1$  (Fig. 3.8a). The cause of this effect becomes apparent if the total energy  $V_{\rm us}(u_{\rm S}) + D_u(u_{\rm S}')^2/2$  of the separatrixes is related to the potential (Fig. 3.8b, c): Increasing  $|\kappa_1|$  leads to minor changes of  $|V_{\rm us}(u_0^+) - V_{\rm us}(u_0^-)|$  which in two- and three-dimensional systems is balanced by friction  $D_u \frac{n-1}{r} u_{\rm S}'(r)$ . Therefore the amplitude of the separatrixes changes only negligible. In state space this effect is balanced by diverging diameters of the critical nuclei.

Figure 3.8a also shows that the three-dimensional critical nuclei are broader than their two-dimensional counterparts. Furthermore they exhibit larger amplitudes close to the critical control parameter  $\kappa_{1,c}$  (3.14) of the bistable regime. Both effects relate to the friction which is twice as large in three-dimensional systems than in two-dimensional systems.

#### 3.2.4 Stabilization of Localized Structures by Global Feedback

The critical nuclei discussed in the previous sections are typical examples for localized structures with a parameter dependent size (Fig. 3.8) which are not stabilized by a control mechanism. Therefore small perturbations lead either to the extinction or the expansion of the structure (Fig. 3.7).

Consequently, a mechanism, which controls the size of a localized structure, has to regulate the front propagation. In case of the discussed one-component field equation (3.11) the propagation is caused by a potential difference leading to a finite front velocity  $c_F$  (3.25c) respectively  $c(K_F)$  (3.26). Because the difference of the local maxima is determined by driving parameter  $\kappa_1$  it is convenient to control this parameter with respect to the size of the stabilized structure. On a finite domain  $\Omega$  this suggest the substitution of parameter  $\kappa_1$  by an effective control parameter  $\kappa_{1,\text{eff}}(u)$  with

$$\kappa_{1,\text{eff}}(u) = \varkappa_1 - \frac{\kappa_2}{\|\Omega\|} \int_{\Omega} u \, d\Omega$$
(3.28)

and  $\kappa_1$ ,  $\kappa_2$  being positive real feedback constants. Note, that the feedback integral  $\int_{\Omega} u \ d\Omega$  is normalized to the size of the domain  $\|\Omega\|$ . In experimental systems respectively electrical networks such type of feedback is realized as global series resistor (Fig. 3.23). By substituting parameter  $\kappa_1$  in field equation (3.11) with  $\kappa_{1,\text{eff}}(u)$  a field equation with global feedback is deduced:

$$\dot{u} = D_u \Delta u + \lambda u - u^3 + \kappa_1 - \frac{\kappa_2}{\|\Omega\|} \int_{\Omega} u \, d\Omega$$
 (3.29)

with u = u(x, t) and  $x \in \Omega \subset \mathbb{R}^n$  for n = 1, 2, 3. Concerning one- and twodimensional domains this equation describes phenomenologically a lateral extended gas discharge system with metallic electrodes and global series resistor, which is used as device for voltage stabilization [3.40, p. 173f].

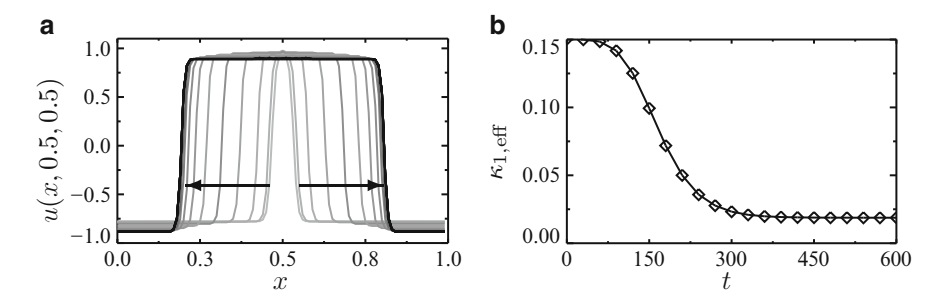


Fig. 3.9 Formation of a stationary localized structure from a critical nucleus. The numerical solution of the one-component field equation with global feedback (3.29) is obtained for the same initial condition which has been used for demonstrating the front propagation on a three-dimensional domain (Fig. 3.7). (a) Snapshots of intersection  $u(x, 0.5, 0.5, t_i)$  of field u(x, t) at  $t_i = 0, 30, \ldots, 600$ . The curves are *darkened* for increasing time  $t_i$ . The latest snapshot shows a stationary structure exhibiting a diameter of 0.72 length units. (b) Time series of the effective control parameter  $\kappa_{1,\text{eff}}(u)$  (3.28) with *diamonds* indicating the snapshots of subfigure (a). Parameters:  $\lambda = 0.8$ ,  $D_u = 5 \cdot 10^{-5}$ ,  $\kappa_1 = 0.15 + \frac{\kappa_2}{\|\Omega\|} \int_{\Omega} u(x, 0) d\Omega = -0.629$ ,  $\kappa_2 = 1.0$ ,  $\Omega = [0, 1]^3$ ,  $\Delta_x = 0.01$ ,  $\Delta_t = 1$ 

In order to understand the effect of global feedback (3.28) on the dynamics of front propagation it is useful to choose suitable initial conditions and compare a simulation of (3.29) with a respective solution obtained from (3.11). Therefore the simulation depicted in Fig. 3.7 is repeated with identical initial conditions u(x, 0) but modified field equation (3.29). Therefore we have to adapt the parameters documented in Fig. 3.7 to the new field equation. For a given initial condition u(x, 0) we claim  $\kappa_1 = \kappa_{1,\text{eff}} (u(x, 0))$  and get

$$\varkappa_1 = \kappa_1 + \frac{\kappa_2}{\|\Omega\|} \int_{\Omega} u(\mathbf{x}, 0) \, \mathrm{d}\Omega. \tag{3.30}$$

The respective simulation is documented in Fig. 3.9a as set of consecutive snapshots showing the intersection of field u at  $x = (x, 0.5, 0.5)^{T}$ . The diagram reveals that the front comes to a standstill and a stationary localized structure is formed. We also observe that the homogeneous ground state which surrounds the localized structure decreases with advancing simulation time.

This effect is related to the increasing size of the structure which decreases control parameter  $\kappa_{1,\text{eff}}$  (Fig. 3.9b). While the effective control parameter would have relaxed to zero in a one-dimensional system, it approaches  $\kappa_{1,\text{eff}}(u,600) = 0.01875$  in the present three-dimensional system. This is due to the fact that the propagation velocity  $c(K_F)$  (3.26) of weakly curved trigger fronts is the sum of the propagation velocity  $c_F$  (3.25c) of planar fronts and a curvature correction  $2D_u/R_F$ . Thus the stationary structure (Fig. 3.9a) forms due to an equilibrium between intrinsic and curvature induced front propagation. Perturbations increasing or decreasing the size of the localized structure would induce a positive respectively a negative front

propagation such that the perturbations decline. Note, that the direction of front propagation respectively the sign of the propagation velocity depends on the front type, that is  $u_F^-$  (3.8) in the presented three-dimensional simulation (Fig. 3.9a) and  $u_F^+$  in the one-dimensional scenario as discussed by Bode [3.29, p. 72f].

While the discussed global feedback mechanism is able to stabilize single localized structures, it fails in stabilizing several localized structures. For example an anti-symmetric perturbation decreasing the size of one structure while increasing the size of another one without changing the feedback term  $\kappa_{1,\rm eff}$  (3.28) cannot be compensated because it is not perceived by the control mechanism. Consequently, the shrinking structure would vanish after dropping below a critical size [3.41].

#### 3.3 Two-Component Reaction-Diffusion Systems

#### 3.3.1 Transition from Global to Local Feedback

Because the global feedback mechanism of the one-component field equation (3.29) is not suitable for the stabilization of several stationary structures [3.41] we are looking for a mechanism acting individually on every localized structure. This can be achieved by replacing the global feedback mechanism by a local one. Following this idea we consider solutions u = u(x, t) of (3.29) on a one-dimensional domain  $\Omega \subset \mathbb{R}$  of length  $L_x$ :

$$\dot{u} = D_u u'' + \lambda u - u^3 + \kappa_1 - \frac{\kappa_2}{L_x} \int_{-L_x/2}^{L_x/2} u \, dx$$
(3.31)

with  $x \in \Omega = \left[-\frac{L_x}{2}, \frac{L_x}{2}\right]$  and u = u(x, t). Here the feedback integral is weighted by a constant which is the inverse domain length  $L_x = \|\Omega\|$ . Factually field u(x, t) is averaged and the feedback acts homogeneously on the systems dynamics.

In order to gain a feedback regarding field u at a specific position  $x = x_0$  more prominently than at the remaining points  $\chi \in \Omega \setminus x_0$  the weighting constant  $1/L_x$  is replaced by a weighting function  $G(x,\chi)$  in the kernel of the feedback integral. For this weighting function it is postulated that it decreases asymptotically with increasing distance  $|x_0 - \chi|$  to position  $x_0$ . Additionally the feedback integral is changed to a convolution integral by integrating over  $\chi \in \Omega$ :

$$\dot{u}(x,t) = D_u u''(x,t) + \lambda u(x,t) - u(x,t)^3 + \kappa_1 - \kappa_4 \int_{-L_x/2}^{L_x/2} G(x,\chi) u(\chi,t) \, d\chi.$$
 (3.32)

Note, that the parameters  $\kappa_1$  and  $\kappa_2$  have been formally substituted by  $\kappa_1$  and  $\kappa_4$ . For an infinite system the kernel

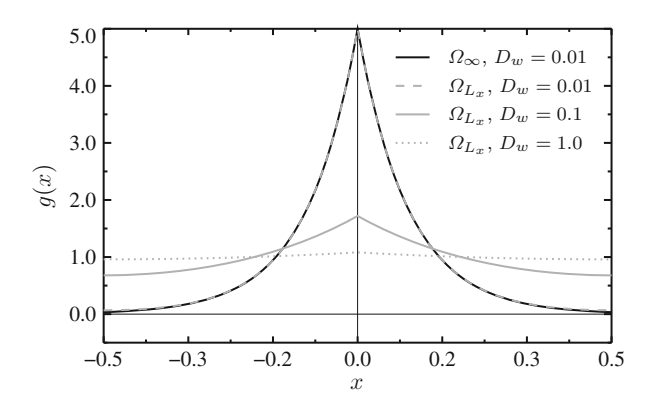


Fig. 3.10 Green's function as solution of (3.34) on an infinite domain  $\Omega_{\infty}$  (black curve) and for a finite domain  $\Omega_{L_x}$  of length  $L_x=1$  (gray curves). The figure illustrates that Green's function g(x) (3.33) evaluated on an infinite domain and the one computed for a finite domain (3.35) cannot be discriminated within plotting accuracy if the diffusion constant  $D_w \ll L_x$  is chosen significantly smaller than the size of the domain. With increasing constant  $D_w$  Green's function (3.35) for the finite domain converges to  $1/L_x$ , which corresponds to the normalization factor of the global feedback integral (3.28)

$$G(x,\chi) = g(|x-\chi|) = \frac{1}{2\sqrt{D_w}} \exp\left(-\frac{|x-\chi|}{\sqrt{D_w}}\right)$$
(3.33)

is an appropriate choice (Fig. 3.10).

The decay of the weighting function is determined by parameter  $D_w > D_u$ , which corresponds to a diffusion constants because the kernel  $g(|x - \chi|)$  (3.33) is Green's function which solves the differential equation

$$D_w g''(x) - g(x) = -\delta(x)$$
(3.34)

with  $x \in \mathbb{R}$  and source term  $\delta(x)$  being given by Dirac's function [3.42, p. 130]. From this equation the weighting function  $g(|x-\chi|)$  can be computed for a finite domain of length  $L_x$  with no-flux boundary conditions  $g'(x)|_{x=\pm\frac{L_x}{2}}=0$ :

$$g(x) = \frac{1}{2\sqrt{D_w}} \left[ \cosh\left(\frac{x}{\sqrt{D_w}}\right) \coth\left(\frac{L_x}{2\sqrt{D_w}}\right) + \sinh\left(\frac{x}{\sqrt{D_w}}\right) (1 - 2\theta_{\rm H}(x)) \right]$$
(3.35)

with  $\theta_{\rm H}(x)$  denoting Heaviside's function. From (3.35) follows that g(x) converges for  $D_w \to \infty$  against the limit  $1/L_x$ , which corresponds to the shadow system introduced by Nishiura [3.43]. Considering the re-substitution  $\kappa_1 = \kappa_1$  and  $\kappa_2 = \kappa_4$  it follows that field equation (3.29) exhibiting a global feedback is a limit of field equation

$$\dot{u}(x,t) = D_u u''(x,t) + \lambda u(x,t) - u(x,t)^3 + \kappa_1 - \kappa_4 \int_{-L_x/2}^{L_x/2} g(|x-\chi|) u(\chi,t) \, d\chi \quad (3.36)$$

featuring a local feedback. With respect to spatially extended systems of more than one spatial dimension (3.36) can be formulated as system of two coupled field equations:

$$\dot{u} = D_u \Delta u + \lambda u - u^3 - \kappa_4 w + \kappa_1, \tag{3.37a}$$

$$0 = D_w \Delta w + u - w \tag{3.37b}$$

with u = u(x,t), w = w(x,t) and  $x \in \Omega \subseteq \mathbb{R}^n$  for n = 1,2,3. Here, the local feedback integral has been replaced by a feedback field named w which reacts without time delay on changes of field u. Therefore (3.37) can be regarded as special case of a two-component reaction-diffusion system exhibiting a component w acting on a fast time scale  $T_F$  with  $\frac{\partial T_F}{\partial t} = \frac{1}{\theta}$  and  $|\theta| \ll 1$ :

$$\dot{u} = D_u \Delta u + \lambda u - u^3 - \kappa_4 w + \kappa_1, \tag{3.38a}$$

$$\theta \dot{w} = D_w \Delta w + u - w. \tag{3.38b}$$

This system of equations reduces to (3.37) for  $\theta \to 0$ . However, (3.38) is very instructive for understanding the reaction kinetics of the two components u and w. An local increase of component  $w(x_0)$  at point  $x_0 \in \Omega$  always decreases itself and field  $u(x_0)$  due to the negative sign of component w in (3.38a) and (3.38b). Therefore the component w is called inhibitor. On the other hand a local increase of  $u(x_0)$  increases field  $w(x_0)$  and triggers an autocatalytic process that increases  $u(x_0)$  if  $f'(u(x_0)) = \lambda - 3u(x_0)^2 > 0$  is fulfilled. Due to this property component u is called activator and system (3.38) is named activator-inhibitor-system. In the following section we investigate solutions of (3.38) in the limit of  $\theta \to 0$ , such that we are dealing with a reaction-diffusion system featuring a fast inhibitor (3.37).

# 3.3.2 The Turing-Instability

Homogeneous stationary solutions solutions  $u_0 = w_0$  of the two-component system (3.37) are given by the cubic equation

$$(\lambda - \kappa_4)u_0 - u_0^3 + \kappa_1 = 0. (3.39)$$

In contrast to the nullcline (3.13) of the local dynamics (3.12) of the one-component field equation (3.11) the cubic equation (3.39) exhibits an effective control parameter  $\lambda_{\rm eff} = \lambda - \kappa_4$ , such that a variation of parameter  $\kappa_4$  leads to an effective change of the cubic nonlinearity. Therefore the fixed points  $u_0 = w_0$  of (3.37) are computed via substituting  $\lambda = \lambda_{\rm eff}$  in (3.15). Given this substitution the bistability condition  $0 < |\kappa_1| \le |\kappa_{1,\rm c}|$  (3.14) holds, too. One can also apply the stability considerations on basis of the potential approach  $V_\ell''(u)|_{u=u_0} = -V_{\rm us}''(u)|_{u=u_0} > 0$  (3.17) as visualized in Fig. 3.1b.

The stability of the homogeneous solutions  $u_0(x) = w_0(x) = u_0 = w_0$  with  $x \in \mathbb{R}$  is analyzed by Turing's approach [3.44]. Here the dynamics of small fluctuations of wave number  $k \in \mathbb{R}$  perturbing the homogeneous solutions are considered:

$$\tilde{\boldsymbol{u}}_k(x,t) = \begin{pmatrix} A_k(t) \\ B_k(t) \end{pmatrix} e^{ikx}.$$
(3.40)

Substituting  $(u, w)^{T} = (u_0, u_0)^{T} + \tilde{u}_k(t)$  into (3.37) and linearizing the nonlinear characteristic  $f(u) = \lambda u - u^3$  around the homogeneous solution  $u_0$ 

$$f(u_0 + A_k e^{ikx}) \approx f(u_0) + f'(u_0) A_k e^{ikx}$$
 (3.41)

leads to the following dynamics of the perturbation amplitudes:

$$\begin{pmatrix} \dot{A}_k(t) \\ 0 \end{pmatrix} = \begin{pmatrix} -D_u k^2 + f'(u_0) & -\kappa_4 \\ 1 & -D_w k^2 - 1 \end{pmatrix} \begin{pmatrix} A_k(t) \\ B_k(t) \end{pmatrix}. \tag{3.42}$$

This system of equations can be simplified by solving the second equation with respect to amplitude  $B_k(t) = A_k(t)/(D_w k^2 + 1)$  and substituting the result into the first equation

$$\dot{A}_k(t) = \left(f'(u_0) - D_u k^2 - \frac{\kappa_4}{1 + D_w k^2}\right) A_k(t). \tag{3.43}$$

From this relation it becomes clear, that perturbations of wave number k are fading away if

$$f'(u_0) < D_u k^2 + \frac{\kappa_4}{1 + D_w k^2} =: f_T(k)$$
 (3.44)

is fulfilled. Violating this stability criterion by  $f'(u_0) = f_T(k)$  enables the destabilization of the homogeneous state by fluctuations of critical wave number

$$k_{\rm c} = \sqrt{\sqrt{\frac{\kappa_4}{D_u D_w}} - \frac{1}{D_w}} \tag{3.45}$$

(Fig. 3.11). Note, that on a finite domain  $\Omega$  the amplitude of a perturbation increases if at least one of the domain dimensions  $L_c \in \{L_x, L_y, L_z\}$  is a multiple of the half critical wavelength  $\lambda_c = 2\pi/k_c$  such that

$$L_{\rm c} = \eta \frac{\lambda_{\rm c}}{2} = \eta \frac{\pi}{k_{\rm c}} \tag{3.46}$$

if fulfilled for  $\eta \in \mathbb{N}$ . The same consideration holds for perturbations of the wave number interval becoming unstable for  $f'(u_0) > f_T(k)$ . Now consider a homogeneous system violating the stability criterion (3.44) where the perturbation

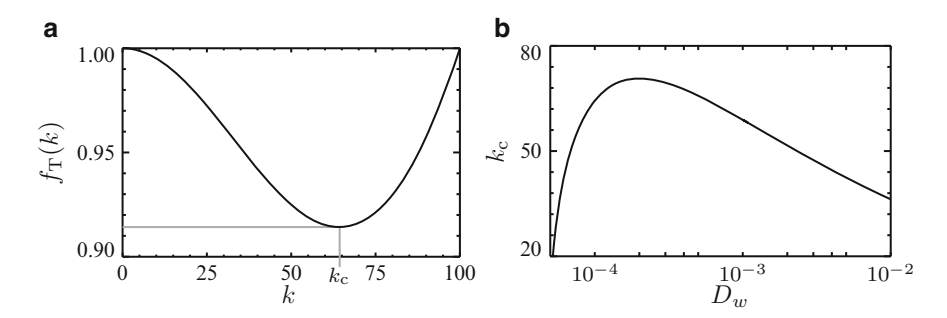


**Fig. 3.11** Neutral curve of Turing's instability. (a) Neutral curve  $f_{\rm T}(k) = f'(u_0)$  (3.44) determining the critical wave number  $k_{\rm c}$ . (b) Semilogarithmic plot of the critical wave number  $k_{\rm c}$  (3.45). In this scenario the largest critical wave number is destabilized for  $D_w = 4 \frac{D_u}{\kappa_4}$ . Parameters:  $D_u = 5 \cdot 10^{-5}$ ,  $\kappa_4 = 1.0$ 

cannot increase because all dimensions of the domain are smaller than  $L_c$  (3.46). In this scenario the homogeneous system will switch spontaneously to a periodically structured state if one of its dimensions is enlarged above the critical size (3.46).

This kind of spatial destabilization has been predicted by Turing [3.44] in his famous work on morphogenesis. Experimental verification of the Turing-instability has been found in electric networks [3.45, 3.46], gas discharge system [3.47–3.50] and chemical systems [3.51, 3.52] with the latter also showing three-dimensional Turing-structures [3.53]. Practical implications of the Turing instability exist for semiconductor systems, e.g. thyristors can be destroyed by the instability [3.54].

# 3.3.3 Stationary Solutions

In analogy to the strategy applied in Sects. 3.1.2 and 3.2.2 for identifying localized solutions this section starts with the investigation of stationary solutions of (3.37) on a one-dimensional domain  $\Omega \subset \mathbb{R}$ . For stationary solutions  $\bar{u}(x) = (\bar{u}(x), \bar{w}(x))^T = (\bar{u}, \bar{w})^T$  Eq. (3.37) transforms to

$$0 = D_u \bar{u}'' + \lambda \bar{u} - \bar{u}^3 - \kappa_4 \bar{w} + \kappa_1, \tag{3.47a}$$

$$0 = D_w \bar{w}'' + \bar{u} - \bar{w}. \tag{3.47b}$$

Concerning solutions of these equations a functional  $\mathfrak{F}(\bar{u}, \bar{w}, \bar{p}, \bar{q}) = \mathfrak{F}$  can be deduced by defining gradient dependent variables

$$\bar{p} := D_u \bar{u}', \tag{3.48a}$$

$$\bar{q} := -\kappa_4 D_w \bar{w}' \tag{3.48b}$$

[3.29, p. 100ff], which hold the following relations

$$\bar{u}' = \frac{\partial}{\partial \bar{p}} \mathfrak{F} = \frac{1}{D_u} \bar{p},$$

$$\bar{w}' = \frac{\partial}{\partial \bar{q}} \mathfrak{F} = -\frac{1}{\kappa_4 D_w} \bar{q},$$

$$\bar{p}' = -\frac{\partial}{\partial \bar{u}} \mathfrak{F} = \kappa_4 \bar{w} - \lambda \bar{u} + \bar{u}^3 - \kappa_1,$$

$$\bar{q}' = -\frac{\partial}{\partial \bar{w}} \mathfrak{F} = \kappa_4 \bar{w} - \kappa_4 \bar{u}$$
(3.49a)

for

$$\mathfrak{F} = \frac{1}{2D_{u}}\bar{p}^{2} - \frac{1}{2\kappa_{4}D_{w}}\bar{q}^{2} + \frac{\lambda}{2}\bar{u}^{2} + \frac{\kappa_{4}}{2}\bar{w}^{2} - \frac{1}{4}\bar{u}^{4} - \kappa_{4}\bar{u}\bar{w} + \kappa_{1}\bar{u}$$

$$= \frac{1}{2D_{u}}\bar{p}^{2} - \frac{1}{2\kappa_{4}D_{w}}\bar{q}^{2} + V_{r}(\bar{u},\bar{w}).$$
(3.49b)

By interpreting the dimensional coordinate x as time coordinate  $\mathfrak{F}$  becomes a Hamilton-functional describing the dynamics of a particle moving in potential  $V_r(\bar{u}, \bar{w})$ . Note, that in contrast to classical mechanics one summand of the *kinetic energy* is always negative due to the negative inertia defined in (3.48b). This variational approach for determining non-trivial stationary solutions of reaction-diffusion systems has been introduced by Bode in [3.29] and has been formalized on basis of skew-gradient systems [3.55, 3.56].

Homogeneous solutions of two-component system (3.47) are attractors of the four-dimensional phase space spawned by  $e_{\bar{u}}$ ,  $e_{\bar{w}}$ ,  $e_{\bar{p}}$ , and  $e_{\bar{q}}$ . In phase space these attractors are the points  $(u_0^{\pm}, u_0^{\pm}, 0, 0)^{\mathrm{T}}$  which are determined by the fixed points  $u_0^{\pm} = w_0^{\pm}$  of the local dynamics (3.39) and definition (3.48). For

$$f'(u_0^{\pm}) \le -\frac{D_u}{D_w} - 2\sqrt{\frac{D_u \kappa_4}{D_w}} \tag{3.50}$$

the attractors are asymptotically stable fixed points of the *spatial dynamics* (3.49) while they are asymptotically stable foci for

$$-\frac{D_u}{D_w} - 2\sqrt{\frac{D_u \kappa_3}{D_w}} < f'(u_0^{\pm}) < f_{\rm T}(k_{\rm c}), \tag{3.51}$$

which is visualized in Fig. 3.12. Here the upper limit  $f_T(k_c)$  of condition (3.51) depends on the critical wavelength  $k_c$  (3.45) of the Turing-nullcline  $f_T(k)$  (3.44). Concerning localized structures, condition (3.51) means that they exhibit characteristic oscillations while decaying to the homogeneous ground state. If (3.50) holds, they will decay monotonically against the homogeneous ground state. This behavior can also be shown for two- and three-dimensional structures if a corresponding perturbation approach is considered [3.27, 3.57].

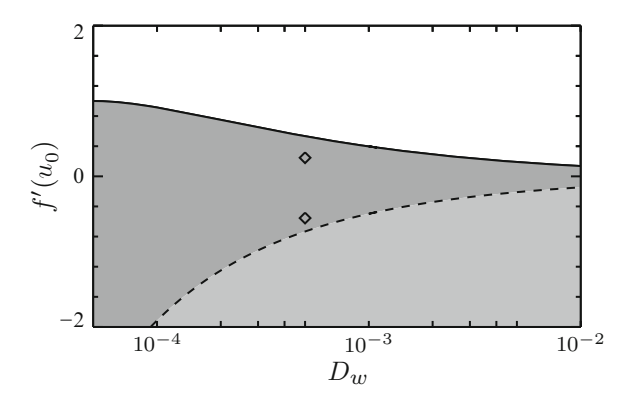


Fig. 3.12 Spatial decay characteristic of localized structures visualized as function of diffusion constant  $D_w$  and slope  $f'(u_0)$  of the nonlinearity evaluated at the homogeneous ground state [3.72]. The *dark shaded* area refers to solutions decaying oscillatory to the homogeneous ground state (3.51). The *light shaded* area corresponds to solutions decaying monotonously to the ground state. *Diamonds* mark parameters for the structures depicted in Fig. 3.13. Systems with parameters located above the *solid curve*  $f_T(k_c)$  violate condition (3.44) such that the respective homogeneous solutions  $u_0$  are unstable against periodic perturbations of wavelength  $k \approx k_c$ . Parameters:  $D_u = 5 \cdot 10^{-5}$ ,  $\kappa_4 = 1.0$ 

In case of bistability the two-component system (3.37) exhibits front solutions which correspond to heteroclinic orbits in four-dimensional phase space. For  $\kappa_1 = 0$  these fronts are stationary and undergo a non-equilibrium-Ising-Bloch-bifurcation [3.19, 3.58] to propagating fronts for  $\kappa_1 \neq 0$ . The direction of propagation is determined by the dominance rule. It states that the front propagation extends the homogeneous state which dominates the dynamics by inclosing the largest area between the respective branches of the nullclines (Fig. 3.13a, b).

From the dominance rule follows that two separated fronts will approach each other if they are enclosing the not dominating homogeneous ground state. In this context separation implies a distance being large with respect to the length scale of the fronts (Fig. 3.3b). The interaction of slowly propagating fronts is discriminated into two groups: For fronts declining monotonously against the enclosed homogeneous ground state the interaction is entirely repulsive. If the fronts decline in an oscillatory manner against the enclosed homogeneous ground state they will experience a repulsive or attractive interaction depending on the distance between them [3.59]. From this observation follows that fronts which approach each other slowly can form a front-front-pair (Fig. 3.13c, d). Note, that for purely repulsive interaction there is one distinct distance at which the *momentum* of propagation and the repulsive interaction vanishes. On the other hand front-pairs forming in the oscillatory parameter regime can lock in different positions due to the fact that there are several points at which the alternating interaction vanishes and the repulsive interaction increases with decreasing distance between them. However, in every case the local repulsion has to be large enough in order to compensate the intrinsic front propagation.

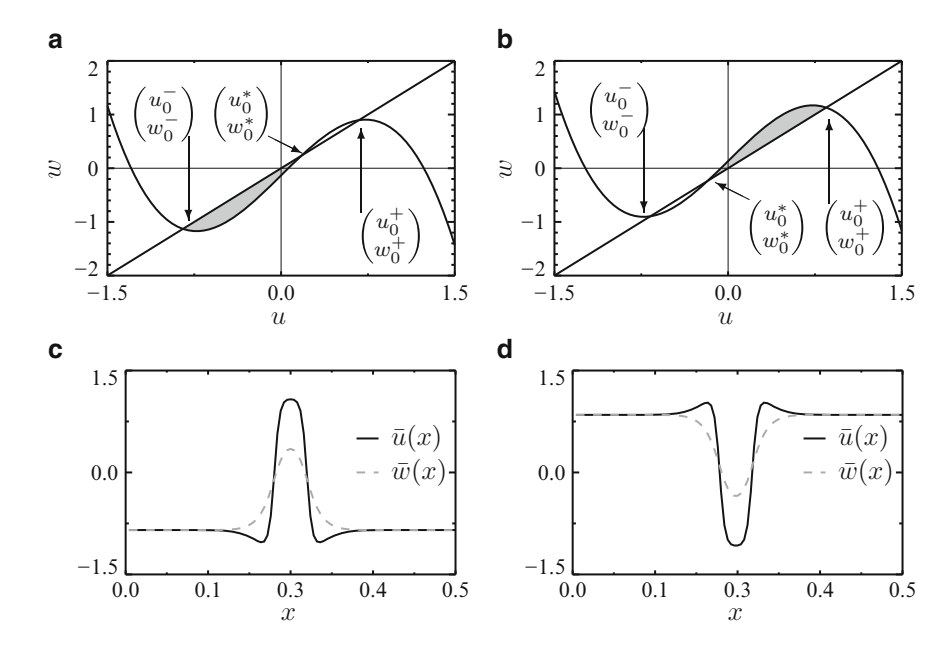


Fig. 3.13 Nullclines of the two-component system and localized solutions for  $\kappa_1 = \pm 0.1$ . (a) and (b) Nullclines of the local dynamics of the two-component system (3.37): Fronts propagate into the direction which extends the homogeneous ground state  $(u_0^{\pm}, w_0^{\pm})^{\mathrm{T}}$  claiming the largest area enclosed by the nullclines (shaded areas). (c) and (d) Stationary solutions corresponding to the nullclines depicted in (a) and (b). The oscillating tails of these solutions (cf. diamonds in Fig. 3.12) are just weakly pronounced and cannot be discriminated with respect to the plotting accuracy. Due to the symmetry of the cubic nonlinearity the localized structures of subfigures (c) and (d) are related by  $\bar{u}_{\kappa_1=0.1} = -\bar{u}_{\kappa_1=-0.1}$ . Parameters:  $D_u = 5 \cdot 10^{-5}$ ,  $D_w = 5 \cdot 10^{-4}$ ,  $\lambda = 1.6$ ,  $\kappa_1 = \pm 0.1$ ,  $\kappa_4 = 1.0$ ,  $\Omega = [0, 0.5]$ ,  $\Delta_x = 5 \cdot 10^{-3}$ 

Such front-front-pairs are localized solutions of (3.47) and are represented in phase space by a homoclinic orbit which starts from the dominant homogeneous ground state and approaches the same state asymptotically. Note, that in contrast to the heteroclinic orbit of trigger fronts a homoclinic orbit does not reach the state corresponding to the non-dominant homogeneous solution. We conclude, that in general bistability of the local dynamics is not needed in order to form localized stationary solutions. An example for this statement is given in Fig. 3.14 showing a two-dimensional localized structure  $\bar{u}(x) = (\bar{u}(x), \bar{w}(x))^T = (\bar{u}, \bar{w})^T$  of a monostable system (Fig. 3.14b). The solution has been computed from

$$0 = D_u \Delta \bar{u} + \lambda \bar{u} - \bar{u}^3 - \kappa_4 \bar{w} + \kappa_1, \tag{3.52a}$$

$$0 = D_w \Delta \bar{w} + \bar{u} - \bar{w},\tag{3.52b}$$

with parameters given in the caption of Fig. 3.14. Note, that in contrast to (3.47) the diffusion operator is represented by a Laplacian. The oscillating tails of the simulated structure are clearly visible in the surface plot (Fig. 3.14a) of the

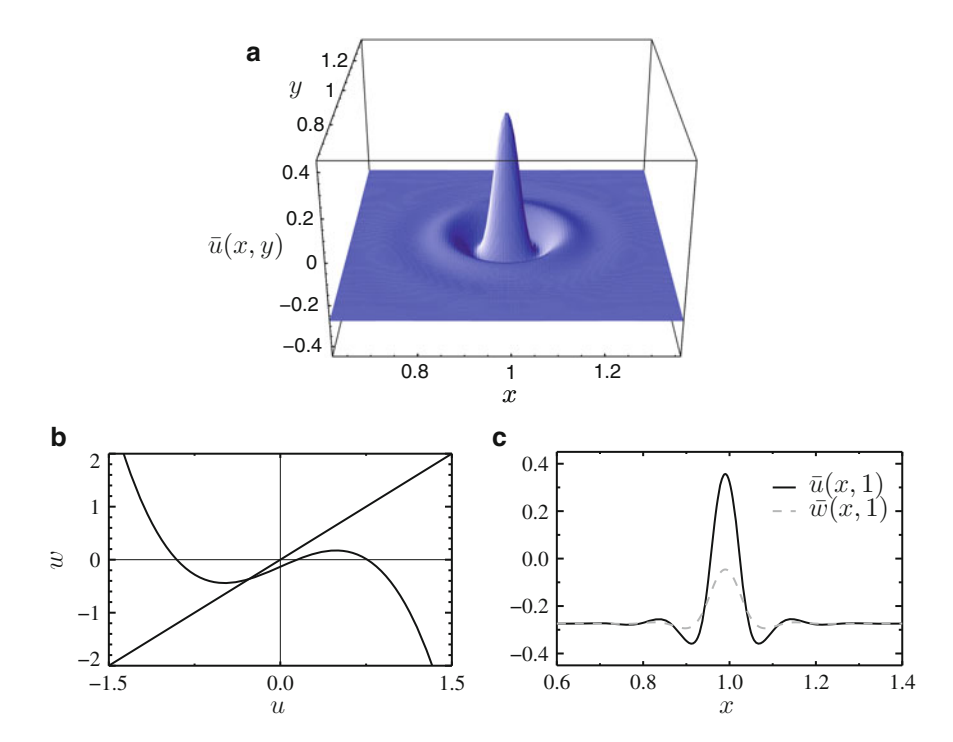


Fig. 3.14 Localized structure with prominent oscillating tails simulated on a two-dimensional domain. (a) Surface plot of distribution  $\bar{u}(x,y)$ . (b) Nullclines of the local dynamics showing a monostable system. (c) Intersection taken at the center of the localized structure. Parameters of (3.52):  $D_u = 1.1 \cdot 10^{-4}$ ,  $D_w = 9.64 \cdot 10^{-4}$ ,  $\lambda = 0.71$ ,  $\kappa_4 = 1.0$ ,  $\kappa_1 = -0.1$ ,  $\Delta_x = 2.5 \cdot 10^{-3}$ ,  $\Omega = [0, 2]^2$ , no-flux boundary condition

activator distribution  $\bar{u}(x, y)$  and its intersection (Fig. 3.14c) taken at the center of the structure. Note, the similarity of Fig. 3.14a with the experimental results of luminance distributions observed for current density filaments (Fig. 2.8).

The stationary solution introduced in this section can be regarded as dissipative soliton, because they are stable against small perturbations [3.60] and act as basic module for more complex structures [3.61].

### 3.3.4 Delayed Inhibition

A very import class of reaction-diffusion systems are of activator-inhibitor type with the latter acting on a time-scale  $T_S$  being slower than the time-scale of the activator. In order to discriminate temporally delayed inhibition from the fast inhibition discussed in Sect. 3.3.1 the relation between both time-scales is set to  $\frac{\partial T_S}{\partial t} = \frac{1}{\tau}$  with  $\tau > 1$  and a new field v = v(x, t) is introduced, such that the modified version of (3.38) reads

$$\dot{u} = D_u \Delta u + f(u) - \kappa_3 v + \kappa_1, \tag{3.53a}$$

$$\tau \dot{v} = D_v \Delta v + u - v \tag{3.53b}$$

with  $f(u) = \lambda u - u^3$ . In order to understand the effect of slow inhibition on the stability of one-dimensional homogeneous solutions  $u(x) = v(x) = u_0 = v_0$  the approach outlined in Sect. 3.3.2 is considered. Therefore the dynamics of small fluctuations  $u_k(x,t)$  (3.40) perturbing the homogeneous state of a one-dimensional system are considered. Denoting the amplitude of fluctuations perturbing the homogeneous activator field with  $A_k(t)$  and the amplitude of fluctuations perturbing the homogeneous inhibitor field with  $B_k(t)$  the following set of differential equations is derived:

$$\begin{pmatrix} \dot{A}_k(t) \\ \dot{B}_k(t) \end{pmatrix} = \begin{pmatrix} -D_u k^2 + f'(u_0) & -\kappa_3 \\ \frac{1}{\tau} & -\frac{D_v k^2 + 1}{\tau} \end{pmatrix} \begin{pmatrix} A_k(t) \\ B_k(t) \end{pmatrix} =: \underline{\boldsymbol{D}} \begin{pmatrix} A_k(t) \\ B_k(t) \end{pmatrix}. \quad (3.54)$$

Note, that in contrast to the dynamics of perturbations deduced from (3.38) the time derivative of the inhibitor perturbations does not vanish and the stability considerations have to apply the determinant criterion

$$\det \underline{\boldsymbol{D}} > 0 \tag{3.55a}$$

and the trace criterion

$$trace \mathbf{D} < 0 \tag{3.55b}$$

[3.13]. From the determinant criteria follows that the homogeneous state  $u_0$  is unstable against small perturbations of wave number k if the Turing-condition

$$f'(u_0) < D_u k^2 + \frac{\kappa_3}{1 + D_v k^2} =: f_{T'}(k)$$
 (3.56a)

is violated. Obviously this condition is the same as the one being found for the two-component system with fast inhibition (3.44). This is reasonable because the Turing-instability is a spatial phenomenon which is independent of the time-scale the feedback mechanism is acting on. On the other hand this time-scale is relevant for oscillatory instabilities induced by violating the trace criterion

$$f'(u_0) < \left(D_u + \frac{D_v}{\tau}\right)k^2 + \frac{1}{\tau} =: f_{\rm H}(k).$$
 (3.56b)

The corresponding Hopf-modes can be excited for  $\tau > 1/f'(u_0)$  leading to oscillations of the homogeneous ground state.

Time-delayed inhibition also influences the velocity of front propagation. It is observed, that an increase of time-scale parameter  $\tau$  increases the propagation

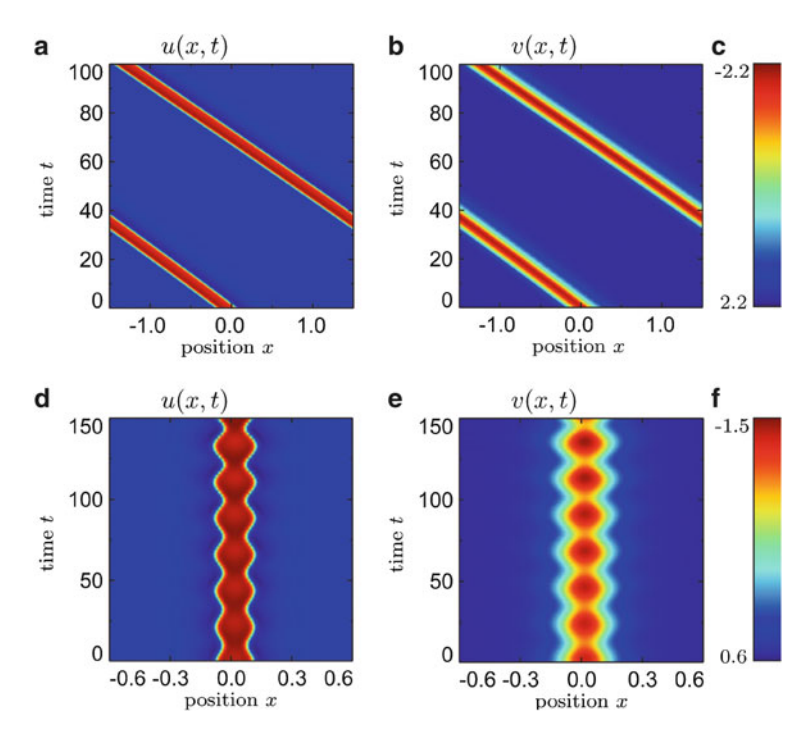


**Fig. 3.15** Propagating and breathing dissipative solitons in two-component reaction-diffusion systems [3.64, Fig. 2.9]. Parameters of (3.53):  $D_v = 0.01$ ,  $\lambda = 4.67$ ,  $\kappa_1 = -1.126$ ,  $\kappa_3 = 3.33$ ,  $\Omega = [-1.5, 1.5]$ , periodic boundary condition. (a)–(c)  $D_u = 1.5 \cdot 10^{-3}$ ,  $\tau = 4.0$ , (d)–(f)  $D_u = 4.67 \cdot 10^{-4}$ ,  $\tau = 5.0$ 

velocity of fronts. In addition, the direction of front propagation does not depend on the dominance rule anymore for sufficient large values of  $\tau$  [3.62].

In systems with more than one spatial dimension the propagation velocity depends on the local curvature of the front [3.63] just as in one-component systems (Sect. 3.2.3). Time-delayed inhibition also causes the destabilization of localized stationary structures. In one-dimensional systems this leads to so-called pulses (Fig. 3.15a–c) or breathing domains (Fig. 3.15d–f). Concerning experimental systems the most-prominent representatives are nerve pulses (Fig. 1.1c), or breathing spots in the FIZ reaction (Fig. 2.6). On domains with more than one spatial dimension the transition from stationary to moving structures is accompanied by an uncontrolled enlargement of the structure in the directions being perpendicular to the direction of motion. In two-dimensional systems such kind of destabilization leads to the formation of running planar fronts or spirals (Fig. 3.16). However, mechanisms stabilizing the shape of a structure while enabling directed propagation via time-delayed inhibition are discussed in detail in Sect. 3.4. Here, we continue with the application of front propagation for the self-organized formation of Voronoi diagrams.

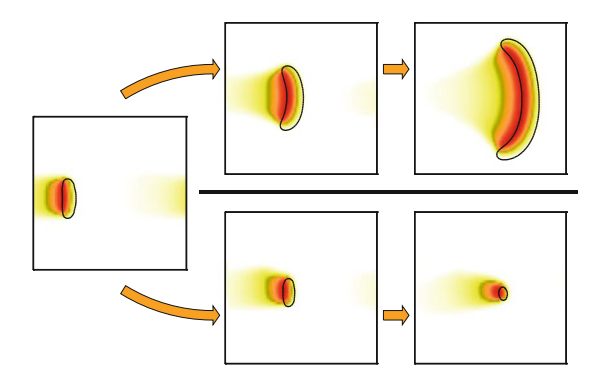


**Fig. 3.16** Typical destabilization of a propagating localized structure in a two-component reaction-diffusion system [3.42, p. 78]. Either the localized solution vanishes (*bottom*) or expands to a spiral (*top*). The images are false-color representations of the inhibitor superimposed by a contour plot of the activator for u(x, y) = 0. Parameters of (3.53):  $\tau = 25.0$ ,  $D_u = 10^{-3}$ ,  $D_v = 1.25 \cdot 10^{-3}$ ,  $\lambda = 2.0$ ,  $\kappa_1 = -0.775$ ,  $\kappa_3 = 1.0$ ,  $\Omega = [0, 2.3]^2$ ,  $\Delta x = 0.026$ ,  $\Delta t = 0.035$ , cyclic boundary conditions

#### 3.3.5 Voronoi-Diagrams

An applied example for the self-organization of localized structures is the solution of the nearest neighbor problem, which is visualized by so-called Voronoi-diagrams. These diagrams describe the spatial tessellation of a domain with respect to a given set of reference points, such that each part comprises one reference point and all other points of the domain which are closer to this certain reference point than to all other reference points [3.65, 3.66].

In two-component systems Voronoi-diagrams can be easily formed by applying the mechanisms of front-propagation and interaction discussed in the previous section. In order to illustrate the self-organized solution of the nearest neighbor problem we choose the two-component reaction-diffusion system (3.53) with time-delayed inhibition and a set of reference points (Fig. 3.17a) on a quadratic domain  $\Omega$  which is repeated cyclically.

The simulation depicted in Fig. 3.17 shows a bistable reaction-diffusion system being in the non-dominant ground state. By sufficiently large perturbations located at the reference points of the nearest neighbor problem the system can be switched into the dominant ground state (Fig. 3.17a). From these local excitations trigger fronts spread across the domain (Fig. 3.17b) approaching each other. Note, that due to the topology of the domain the fronts apparently propagate across the domain boundaries whereby leaving the domain on one side and entering it on the facing site. Due to their slow propagation velocity the colliding fronts do not merge but form front-front-pairs which follow the intersections of the domain defined by the nearest neighbor problem (Fig. 3.17c–e). Altogether the front-front-pairs reproduce the directly computed Voronoi-diagram very well (*gray* lines in Fig. 3.17), although

there are slight deviations due to the interaction of front-triples and the minimization of local front curvatures (Fig. 3.17f).

The five stationary structures forming in the course of the simulation can be regarded as localized structures, because their position is well defined with respect to the reference points of the nearest neighbor problem. Such structures and their process of formation are well known from chemical systems [3.67, 3.68]. It illustrates the fact, that within the same system localized stationary structures with very different shapes can coexist. In the present example the individual shape of a structure forms mainly due to the interaction with its neighbored structures building a super-structure with well-defined properties (Fig. 3.17f). However, this kind of structure formation is possible, because perturbations of a certain size switch the system locally into a different state. Concerning one-component systems these so-called critical nuclei have been discussed in view of initiating trigger fronts (Sect. 3.2.2–3.2.4). Concerning two-component systems we are continuing the discussion with respect to critical nuclei of dissipative soliton.

#### 3.3.6 Critical Nuclei of Dissipative Solitons

In one-component reaction-diffusion systems (3.11) critical nuclei are unstable stationary solutions (Fig. 3.8), which are embedded into the non-dominant ground state. For appropriate perturbations they either decay towards the non-dominant ground state or initiate trigger-fronts switching the system dynamically into the dominating ground state (Fig. 3.7). The same type of critical nuclei exists in bistable two-component reaction-diffusion systems as well as a different type, which is embedded into the dominant ground state and for appropriate perturbations decays to the surrounding ground state or relaxes to a stable localized solution. Because the latter type of critical nuclei plays a crucial role for the understanding of generation mechanisms of dissipative solitons with distinct oscillating tails, it is investigated on basis of the following system of equations

$$\dot{u} = D_u \Delta u + \lambda u - u^3 - \kappa_3 v + \kappa_1 - \frac{\kappa_2}{\|\Omega_{\square}\|} \int_{\Omega_{\square}} u d\Omega_{\square}, \tag{3.57a}$$

$$\tau \dot{v} = D_v \Delta v + u - v, \tag{3.57b}$$

with u = u(x,t), v = v(x,t) and  $x \in \Omega_{\square} = \left[-\frac{L_x}{2}, \frac{L_x}{2}\right] \times \left[-\frac{L_x}{2}, \frac{L_x}{2}\right]$ . Note, that this reaction-diffusion system is an extension of (3.53) derived by substituting parameter  $\kappa_1$  by an effective control parameter  $\kappa_{1,\text{eff}}$  (3.28) introducing a global feedback.

Due to the fact that critical nuclei are radial symmetric solutions of (3.57), the latter is transformed to polar coordinates

$$\frac{\partial}{\partial t}u = D_u \left[ \frac{1}{r} \frac{\partial}{\partial r} \left( r \frac{\partial}{\partial r} \right) + \frac{1}{r^2} \frac{\partial^2}{\partial \phi^2} \right] u + \lambda u - u^3 - \kappa_3 v + \kappa_1 
- \frac{\kappa_2}{\|\Omega_0\|} \int_{\Omega_0} u \, r d\Omega_0,$$
(3.58a)

$$\tau \frac{\partial}{\partial t} v = D_v \left[ \frac{1}{r} \frac{\partial}{\partial r} \left( r \frac{\partial}{\partial r} \right) + \frac{1}{r^2} \frac{\partial^2}{\partial \phi^2} \right] v + u - v, \tag{3.58b}$$

with  $u = u(r, \phi, t)$ ,  $v = v(r, \phi, t)$  and  $(r, \phi)^T \in \Omega_o = \left[0, \frac{L_x}{2}\right] \times \left[0, 2\pi\right]$ . For radial symmetric stationary solutions  $\bar{u} = \bar{u}(r)$  the equations simplify to

$$0 = D_u \left( \frac{\partial^2}{\partial r^2} + \frac{1}{r} \frac{\partial}{\partial r} \right) \bar{u} + \lambda \bar{u} - \bar{u}^3 - \kappa_3 \bar{v} + \kappa_1 - \frac{8\kappa_2}{L_v^2} \int_0^{\frac{L_x}{2}} \bar{u} \, r \, dr, \qquad (3.59a)$$

$$0 = D_v \left( \frac{\partial^2}{\partial r^2} + \frac{1}{r} \frac{\partial}{\partial r} \right) \bar{v} + \bar{u} - \bar{v}$$
 (3.59b)

with boundary condition  $\frac{\partial}{\partial r} \bar{u}\big|_{r=0} = 0$ . In order to discriminate critical nuclei from stable localized structures the numerical solutions  $\bar{u}(r)$  of (3.59) are tested on their sensibility to perturbations of type

$$\tilde{\boldsymbol{u}}(r,\phi,t) = \sum_{\mu=0}^{\infty} \tilde{\boldsymbol{u}}_{\mu}(r,t) \cos(\mu\phi). \tag{3.60a}$$

Because the perturbation  $\tilde{u}_{\mu}(r,t)$  is assumed to be continuous and differentiable, the additional boundary conditions

$$\frac{\partial}{\partial r} \tilde{\mathbf{u}}_0(r,t)|_{r=0} = 0 \text{ and} \tag{3.60b}$$

$$\tilde{\mathbf{u}}_{\mu}(r,t)\big|_{r=0} = 0 \text{ for } \mu = 1, 2, \dots$$
 (3.60c)

have to be fulfilled [3.42, p. 27]. The perturbation composes from a breathing mode ( $\mu = 0$ ), a Goldstone-mode ( $\mu = 1$ ) and higher deformation modes ( $\mu \ge 2$ ), which are exemplarily pictured in Fig. 3.18. Inserting

$$\mathbf{u}(r,\phi,t) = \bar{\mathbf{u}}(r) + \tilde{\mathbf{u}}(r,\phi,t) \tag{3.61}$$

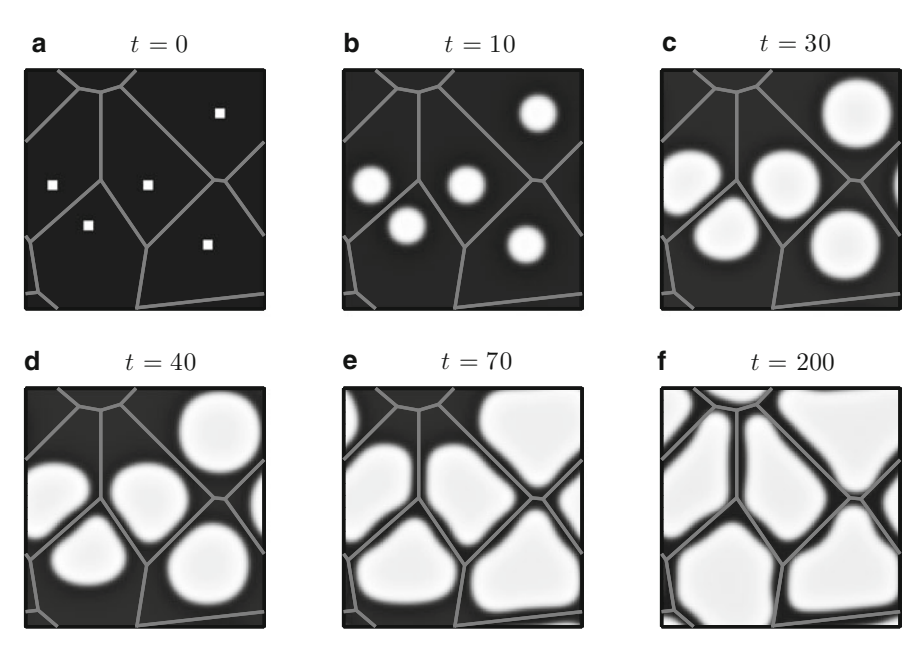


Fig. 3.17 Self-organization of a Voronoi-diagram on a two-dimensional domain with cyclical boundary condition [3.67]. Light areas correspond to high values of activator field u, dark areas to low values. Grey lines show the tessellation of the domain with respect to the reference points marked in (a) as perturbations of the homogeneous activator field. (b)–(e) These perturbations initiate trigger fronts propagating across the domain until their interacting with other trigger fronts forms the spatial tessellation of the domain. (f) Due to the interaction of closely neighbored front-front-pairs the stationary diverges slightly from the Voronoi-diagram computed via a conventional algorithm (grey lines). Parameters:  $D_u = 2 \cdot 10^{-4}$ ,  $D_v = 9.64 \cdot 10^{-4}$ ,  $\lambda = 2$ ,  $\kappa_1 = 0.1$ ,  $\kappa_3 = 1$ ,  $\tau = 1.1$ ,  $\Omega = [0, 1]^2$ , cyclic boundary condition,  $\Delta_x = 0.01$ ,  $\Delta_t = 0.01$ 

into (3.58) while linearizing the cubic term around  $\bar{u}$  leads to the following set of equations

$$\frac{\partial}{\partial t}\tilde{u}_{\mu} = D_{u} \left[ \frac{\partial^{2}}{\partial r^{2}} + \frac{1}{r} \frac{\partial}{\partial r} - \frac{n^{2}}{r^{2}} \right] \tilde{u}_{\mu} + (\lambda - 3\bar{u}^{2}) \tilde{u}_{\mu} - \kappa_{3}\tilde{v}_{\mu} + \kappa_{1}$$

$$- \frac{\kappa_{2}}{\|\Omega_{\circ}\|} \int_{\Omega_{\circ}} \tilde{u}_{\mu} r d\Omega_{\circ}, \qquad (3.62a)$$

$$\tau \frac{\partial}{\partial t} \tilde{v}_{\mu} = D_{v} \left[ \frac{\partial^{2}}{\partial r^{2}} + \frac{1}{r} \frac{\partial}{\partial r} - \frac{n^{2}}{r^{2}} \right] \tilde{v}_{\mu} + \tilde{u}_{\mu} - \tilde{v}_{\mu}. \tag{3.62b}$$

These equations are linearized to

$$\dot{\tilde{\boldsymbol{u}}}_{\mu} = \mathcal{D}\left(\bar{\boldsymbol{u}}\right)\tilde{\boldsymbol{u}}_{\mu} \tag{3.63}$$

introducing the linear operator  $\mathcal{D}(\bar{u})$ . Of course this linear equation can be formulated as eigenvalue equation

$$\nu_{\mu} \mathcal{F}_{\mu} = \mathcal{D}\left(\bar{\boldsymbol{u}}\right) \mathcal{F}_{\mu} \tag{3.64}$$

with eigenmode  $\mathcal{F}_{\mu} = \tilde{\boldsymbol{u}}_{\mu}$ . Therefore a stationary solution is stable against perturbations of eigenmode  $\mathcal{F}_{\mu}$  if the respective eigenvalue  $v_{\mu}$  holds  $\Re v_{\mu} < 0$ . The global stability of a stationary solution is determined by the first  $\mu = 1, \ldots, n$  eigenmodes [3.69, 3.70]. Examples for numerically computed eigenmodes  $\mathcal{F}_{\mu}$  are shown in Fig. 3.18.

This stability analysis is carried out with the following set of parameters

$$D_u = 6 \cdot 10^{-5}, \ D_v = 6 \cdot 10^{-4}, \ \lambda = 0.8, \ \kappa_1 = -1.58,$$
  
 $\kappa_2 = 5, \kappa_3 = 1, \ \tau = 1.0, \ \Omega = [0, 0.5], \ \Delta_x = 0.01$ 

$$(3.65)$$

whereby the existence and stability of localized solutions is investigated for varied parameter  $\kappa_1$ . The chosen parameters define a monostable reaction-diffusion system of which the homogeneous ground state  $u_0 = v_0$  is the real solution of  $(\lambda - \kappa_2 - \kappa_3)u - u^3 + \kappa_1 = 0$  solving for  $u_0 = -0.2978$ . At the Turing-bifurcation point  $\kappa_{1,c} = -1.58$  the homogeneous ground state can be destabilized by perturbations of wave number  $k_c = 60$  which follows from (3.45) by substituting parameter  $D_w$  with  $D_v$  and parameter  $\kappa_4$  with  $\kappa_3$ .

The existence and stability of localized stationary solutions for varied control parameter  $\varkappa_1$  is visualized in Fig. 3.19. The diagram shows the amplitude  $\hat{u}_{ls}(\varkappa_1) = (\max \bar{u} - \min \bar{u})$  of the activator distribution as function of the control parameter. Due to the subcriticality of the Turing-bifurcation the unstable localized solutions (*dotted* curve) branch backwards from the bifurcation point. The amplitude of these localized structures increases with decreasing control parameter  $\varkappa_1$  until the critical value  $\varkappa_1 = \varkappa_{1,DS} = -2.3$  is reached which is a saddle-node bifurcation point from which a branch of stable and unstable solutions emerge. For  $\varkappa_1 < \varkappa_{1,DS}$  localized solutions of (3.59) don't exist. The activator amplitude  $\hat{u}_{ls}$  of the stable stationary solutions (*solid* curve) increases with increasing control parameter  $\varkappa_1$  until the stability is lost at  $\varkappa_1 \approx -1.71$ . At  $\varkappa_1 \approx -1.64$  these unstable structures vanish for the benefit of periodic structures with large amplitudes. From the two localized solutions found in the parameter range  $-2.3 < \varkappa_1 \lesssim -1.64$  the smaller one can be identified as critical nucleus of the larger one by solving the time-dependent field equations (3.53) with the perturbed critical nucleus as initial condition.

Due to the fact that the amplitude of the critical nucleus becomes very small in the vicinity of the Turing-bifurcation point  $\varkappa_{1,c}$  a homogeneous system can be destabilized by small localized perturbations in favor of localized structures with large amplitudes for  $\varkappa_1 < \varkappa_{1,c}$ . In this scenario the perturbation has to be slightly larger and broader than the critical nucleus. However, these dissipative solitons featuring large amplitudes are also unstable due to the vicinity of the Turing-bifurcation point respectively  $\varkappa_1 \gtrsim -1.64$ . Their instability can be explained by the distinct oscillatory tails of the localized structures which compete with the critical nuclei, such that new dissipative solitons are likely to ignite from the oscillating tails of the first one. A quantitative validation of this explanation is discussed in

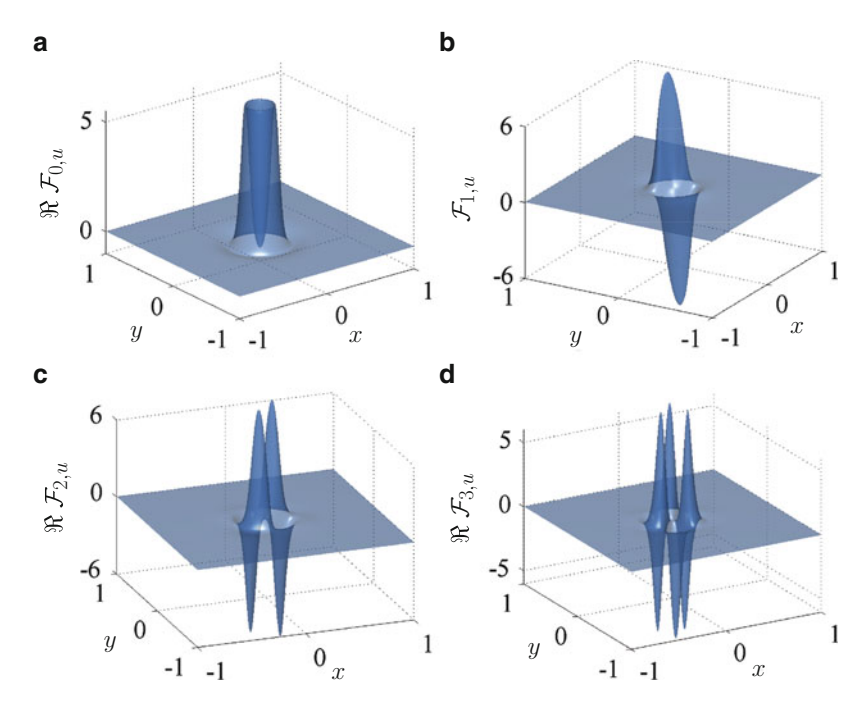


**Fig. 3.18** Eigenmodes  $\mathcal{F}_{\mu}$  of dissipative soliton with monotonic tails [3.71, Fig. 7.2]. Figures show the real part of the activator component. (a)  $\mu=0$  Breathing mode. (b)  $\mu=1$  Goldstone mode. (c)  $\mu=2$ . (d)  $\mu=3$ . Parameters of (3.57):  $D_u=4.7\cdot10^{-3}$ ,  $D_v=0.01$ ,  $\lambda=4.67$ ,  $\kappa_1=-1.04$ ,  $\kappa_2=0.0$ ,  $\kappa_3=3.33$ 

Sect. 7.4.2 where the generation mechanisms of dissipative solitons are regarded in greater detail.

From the two-component reaction-diffusion system with local feedback it is a small step to three-component reaction-diffusion systems if the transition from global to local feedback (Sect. 3.2.4) is carried out once more. These systems are interesting because they enable the investigation of the dynamics and interaction of several moving dissipative solitons.

# 3.4 Three-Component Reaction-Diffusion Systems

# 3.4.1 Propagating Dissipative Solitons

From experimental observations it is known (Chap. 2), that dissipative solitons do not only exist as stationary structures, but are found to be moving entities in the majority of observations. Concerning reaction-diffusion systems a mechanism for imposing dynamic instabilities is delayed inhibition. In case of homogeneous

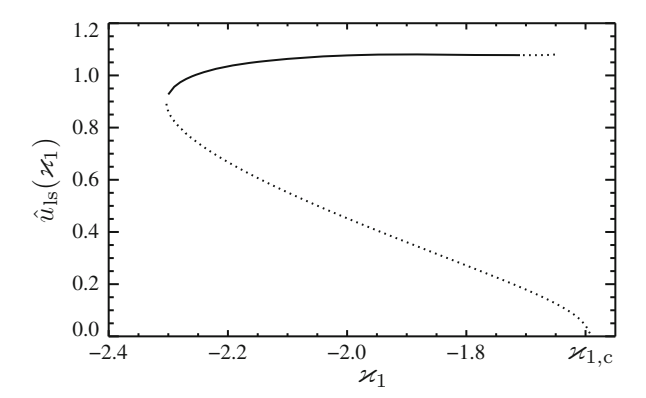


Fig. 3.19 Amplitude of activator peaks  $\hat{u}(x_1)_{ls} = (\max \bar{u} - \min \bar{u})$  computed in the vicinity of a subcritical Turing-bifurcation for a two-component reaction-diffusion system with global feedback (3.59) [3.72, p. 81]. The amplitude is plotted as function of control parameter  $x_1$ . Solid curves refer to stable solutions, dotted curves to unstable solutions. Parameters from (3.65)

solutions delayed inhibition triggers harmonic oscillations if the stability criterion  $f'(u_0) < f_H(k)$  (3.56b) is violated. But how does delayed inhibition act on localized structures? Consider a localized one-dimensional stationary solution  $\bar{u} = \bar{u}(x)$ of the two-component reaction-diffusion system (3.53) on a periodic domain and assume, that the time scale constant  $\tau$  is larger than one. In this case the inhibitor field reacts slowly on local perturbations of the activator field, such that its stabilizing effect is reduced. In this situation the localized structure is sensible to perturbations breaking the mirror symmetry of the structure. For example shifting the peaks of activator and inhibitor distribution slightly against each other induces a propagating dissipative soliton: Due to the slow response of the inhibitor the activator peak is able to expand to the side exhibiting a lower inhibitor concentration. Of course this effect might lead to the destruction of the localized structure, but if the inhibitor is only moderately slower than the activator the inhibitor peak will at least be able to follow the activator peak leading to a continuously propagating dissipative soliton. In this respect the inhibitor has a stabilizing effect on the propagating structure. In one-dimensional systems such propagating dissipative solitons are called pulses [3.73–3.77].

On two-dimensional domains  $\Omega \subseteq \mathbb{R}^2$  the transition from a localized stationary dissipative soliton to a propagating one cannot be realized on basis of (3.53), because the inhibitor stabilizes the dissipative soliton only in the direction of motion but not perpendicular to it. Therefore the activator either spreads or shrinks perpendicular to the direction of motion which typically leads to the formation of spirals or the vanishing of the structure (Fig. 3.16). In this scenario propagating dissipative solitons can only be stabilized by periodic inhomogeneities, e.g. in form of sparse spatial discretization [3.78], or in the limit of extreme time scale separation [3.79, 3.80], which renders the computation of numerical solutions difficult, or by including global feedback (3.57) [3.81], which in general is only suitable for finite

domains. However, in case of several possibly interacting dissipative solitons global feedback mechanisms are also problematic, because the feedback integral is not sensible to perturbations enlarging one dissipative soliton and shrinking another one by the same amount of activator. This leads to the successive vanishing of localized structures until only one large dissipative soliton remains [3.41, 3.82]. However, simulations show [3.83], that global feedback is able to stabilize several dissipative solitons at least temporarily, if the initial conditions are constructed from a single propagating dissipative solitons being properly relaxed.

Following the considerations of Sect. 3.3.1 the global feedback mechanism is replaced by a local feedback mechanism

$$\dot{u}(\mathbf{x},t) = D_u \Delta u(\mathbf{x},t) + \lambda u(\mathbf{x},t) - u(\mathbf{x},t)^3 - \kappa_3 v(\mathbf{x},t) + \kappa_1$$
$$-\kappa_4 \int_{\Omega} g(\mathbf{x} - \mathbf{\chi}) u(\mathbf{\chi},t) d\mathbf{\chi}, \tag{3.66a}$$

$$\tau \dot{v}(\mathbf{x},t) = D_v \Delta v(\mathbf{x},t) + u(\mathbf{x},t) - v(\mathbf{x},t), \tag{3.66b}$$

with  $g(x - \chi)$  denoting Green's function. Of course this two-component reaction-diffusion system with local feedback can be formulated as three-component reaction-diffusion system by introducing a feedback field w = w(x) with  $D_w > D_u$ :

$$\dot{u} = D_u \Delta u + \lambda u - u^3 - \kappa_3 v - \kappa_4 w + \kappa_1, \tag{3.67a}$$

$$\tau \dot{v} = D_v \Delta v + u - v, \tag{3.67b}$$

$$0 = D_w \Delta w + u - w. \tag{3.67c}$$

Its homogeneous solution  $\mathbf{u}_0 = (u_0, v_0, w_0)^T$  with  $u_0 = v_0 = w_0$  can be computed by substituting parameter  $\lambda$  in (3.15) with  $(\lambda - \kappa_3 - \kappa_4)$ . Considering the same substitution for  $\kappa_{1,c}$  (3.14) also the bistability criterion  $0 < |\kappa_1| \le |\kappa_{1,c}|$  holds. The homogeneous solution  $\mathbf{u}_0$  is stable against perturbations of wave number k (cf. Sect. 3.3.2), if in accordance to (3.44) and (3.56a) the determinant criterion

$$f'(u_0) < f_{\rm T}(k) + \frac{\kappa_3}{1 + D_v k^2} = f_{\rm T'}(k) + \frac{\kappa_4}{1 + D_w k^2}$$
 (3.68a)

and the trace criterion (3.56b)

$$f'(u_0) < f_{\rm H}(k) + \frac{\kappa_4}{1 + D_w k^2} \tag{3.68b}$$

hold. While the violation of the determinant criterion (3.68a) triggers a Turing-instability (cf. Sect. 3.3.4) violating the trace criterion (3.68b) enables a wave instability [3.42, p. 14ff] which e.g. is observed in chemical systems [3.84].

Increasing the time-scale parameter  $\tau$  of the inhibitor equation (3.67b) over a critical value  $\tau_c$  [3.85, 3.86] destabilizes stationary localized solutions of the

three-component reaction-diffusion systems dynamically such that the structures become unstable against perturbations breaking their mirror symmetry and start to propagate continuously with a well defined velocity. This so-called onset of propagation is discussed in the following chapter. However, for the stabilization of propagating structures it is generally not necessary that the feedback field w reacts instantaneously on perturbations of the activator field if its response is fast enough in order to prevent a breathing instability [3.42, p. 49]. Therefore system (3.67) can be expanded to the more general case of a second inhibitor acting on time scale  $1/\theta$ :

$$\dot{u} = D_u \Delta u + \lambda u - u^3 - \kappa_3 v - \kappa_4 w + \kappa_1, \tag{3.69a}$$

$$\tau \dot{v} = D_v \Delta v + u - v,\tag{3.69b}$$

$$\theta \dot{w} = D_w \Delta w + u - w \tag{3.69c}$$

with u = u(x, t), v = v(x, t), w = w(x, t) and  $x \in \Omega \subseteq \mathbb{R}^n$  for n = 1, 2, 3. Note, that the time scale of the activator u is set to 1 and acts as reference time scale for the inhibitors. Choosing the relation between the time-scales to  $0 \le \theta < 1 \le \tau$  renders the inhibiting field v being slower than the inhibiting field v such that v is called *slow inhibitor* while v is called *fast inhibitor* [3.82, 3.86]. However, due to the their role in forming dissipative solitons the notion *driving inhibitor* v and *stabilizing inhibitor* v is also appropriate.

In order to explain the difference between the inhibiting components of (3.69) a uniformly propagating dissipative soliton is presented in Fig. 3.20. It shows combined surface plots of fields u, v, and w as solution of

$$\dot{u} = D_u \left(\frac{1}{r} \frac{\partial}{\partial r} + \frac{\partial^2}{\partial r^2} + \frac{\partial^2}{\partial h^2}\right) u + \lambda u - u^3 - \kappa_3 v - \kappa_4 w + \kappa_1, \tag{3.70a}$$

$$\tau \dot{v} = D_v \left(\frac{1}{r} \frac{\partial}{\partial r} + \frac{\partial^2}{\partial r^2} + \frac{\partial^2}{\partial h^2}\right) v + u - v, \tag{3.70b}$$

$$\theta \dot{w} = D_w \left( \frac{1}{r} \frac{\partial}{\partial r} + \frac{\partial^2}{\partial r^2} + \frac{\partial^2}{\partial h^2} \right) w + u - w, \tag{3.70c}$$

which is derived by transforming (3.69) into a cylindrical coordinate system and taking into account that a propagating dissipative soliton has a rotational symmetry with respect to its direction of motion. Therefore the angular dependency of fields u, v and w vanishes if the h-coordinate is chosen as symmetry axes. Figure 3.20 illustrates that the activator distribution u(r,h) (red) of the propagating dissipative soliton is distorted with respect to its direction of motion which is in contrast to the radial symmetry of a stationary structure (Fig. 3.14a). In the current example the significant distortion results from the large offset between the excitation of the activator field u (red) and the driving inhibitor field v (green). Due to its large time scale constant ( $\tau = 48$ ) the driving inhibitor reacts with a significant delay to changes of the activator field. It also degrades much more slowly than the activator and therefore has an extended tail. In contrast to this observation is the excitation of the stabilizing inhibitor field w (blue surface in Fig. 3.20) which surrounds the entire activator excitation completely whereby providing an accompanying stabilization

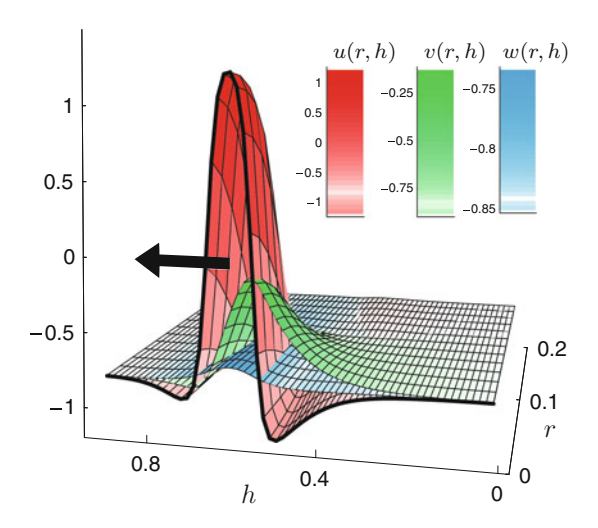


Fig. 3.20 Three-dimensional propagating dissipative soliton simulated in a cylindrical coordinate system [3.87]. Due to the rotational symmetry of the structure with respect to its direction of motion the angular component  $\phi$  vanishes (3.70). The components u, v, and w are shown as red, green and blue surfaces. The figure suggests, that the localized excitation of the activator field u is pushed by the following excitation of the slow inhibitor field v while being stabilized by the surrounding excitation of the fast inhibitor w. Therefore the inhibiting fields v and w might be attributed driving and stabilizing inhibitors, respectively. Parameters: v = 48.0, v = 0.5,  $v = 1.5 \cdot 10^{-4}$ ,  $v = 1.86 \cdot 10^{-4}$ , v = 1.00,  $v = 1.86 \cdot 10^{-4}$ , v = 1.00, v = 1.80, v =

feedback. This of course is only possible because the stabilizing inhibitor is able to react with negligible delay on changes of the activator field due to its small time scale constant ( $\theta = 0.5$ ).

The difference between a propagating dissipative soliton being simulated with parameters far from the onset of propagation and a propagating dissipative soliton close to the onset of propagation becomes clear by comparing the figure discussed before with Fig. 3.21. Here the time scale parameter  $\tau$  is chosen to be slightly supercritical with respect to the onset of propagation. Additionally the slow inhibitor field does not diffuse  $(D_v=0)$  such that the excitations of activator and slow inhibitor fields are identical but slightly shifted with respect to the direction of motion. Due to its large diffusion constant and its small time scale constant the stabilizing inhibitor surrounds the peaks of the activator and the driving inhibitor. Note, that the fast inhibitor only degrades the activator field but interacts with the slow inhibitor field indirectly via the activator.

Due to vicinity of the onset of propagation and the resulting weak symmetry breaking the dissipative soliton depicted in Fig. 3.21 propagates slowly. The dynamics and interaction of this kind of dissipative solitons and their transition from stationary to propagating structures are thoroughly discussed in the following two chapters. This ultimately leads to a stochastic time series analysis technique enabling the identification of the onset of propagation and the interaction law of

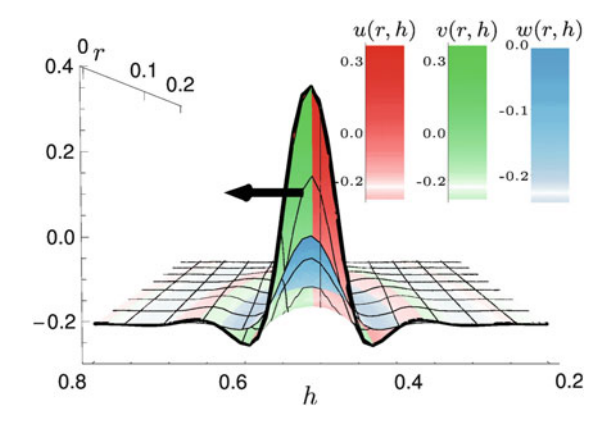


Fig. 3.21 Slowly propagating dissipative soliton visualized as surface plots of its components. Due to the fact that the time scale parameter  $\tau$  is just slightly super critical with respect to the onset of propagation of the dissipative soliton its radial symmetry is barely broken. The only visible hint is the intersection of the surfaces of activator and slow inhibitor fields close to the center of the dissipative soliton. The components u, v, and w are shown as red, green and blue surfaces, respectively. Note, that the dissipative soliton is seen from the inside, such that the excitation of the driving inhibitor field seems to be head on concerning the direction of motion. Instead, it just shields the leading excitation of the activator field. Parameters:  $D_u = 1.3 \cdot 10^{-4}, D_v = 0, D_w = 9.64 \cdot 10^{-4}, \lambda = 0.95, \kappa_3 = 0.25, \kappa_4 = 1.0, \tau = 4.01, \theta = 0.1, \kappa_1 = -0.08, \Omega = [0, 0.44] \times [0, 0.88], \frac{\partial}{\partial r} u(r, h)|_{r=0,L_r} = 0, u(r, h)|_{h=0} = u(r, h)|_{h=L_h}, \Delta_x = 0.0147, \Delta_t = 0.01$ 

dissipative solitons experimentally. Dissipative solitons far away from the onset of propagation which are known to undergo generation and annihilation processes via interaction processes are topic of the seventh chapter closing the overview on dissipative solitons in reaction-diffusion systems.

# 3.4.2 Complex Dissipative Solitons

From previous sections it is know that, in the vicinity of the Turing-bifurcation dissipative solitons exhibit oscillatory tails (Fig. 3.14). In certain parameters regions the amplitude of these tails increases, such that a ring is formed which surrounds the central filament (Fig. 3.22a). Notably, these systems also exhibit the standard type of dissipative solitons, such that the interaction between both types can be examined numerically [3.42]. The investigations show, that the target-like dissipative solitons propagate more slowly than the standard type and that the central filament of the target structure is likely to become unstable for slightly increased velocities.

For a different parameter set another class of solitary structures can be observed, which can be described as ring-like dissipative solitons (Fig. 3.22b). These structures are constructed from the intersection of a single dissipative soliton which is projected onto a circle of a certain diameter. Due to its curvature the ring

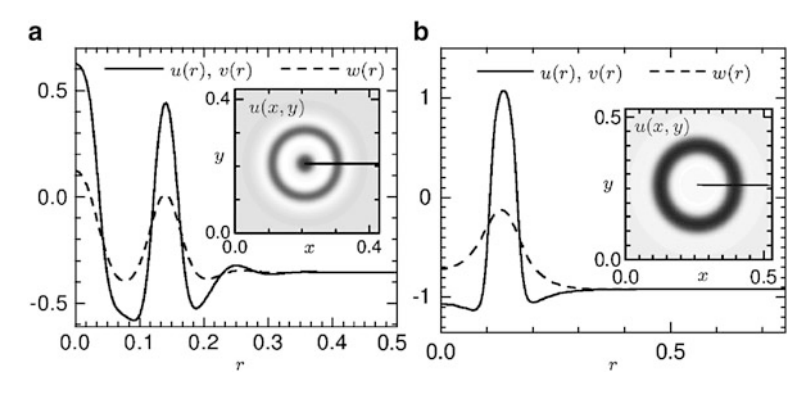


**Fig. 3.22** Dissipative solitons with complex internal structure [3.42]. The subfigures show intersections of the complex dissipative solitons which are accompanied by inlays visualizing the spatial activator distribution of the structures. Parameters: (a)  $D_u = 6.46 \cdot 10^{-5}$ ,  $D_v = 0$ ,  $D_w = 5.66 \cdot 10^{-4}$ ,  $\lambda = 1.84$ ,  $\kappa_3 = 1.0$ ,  $\kappa_4 = 1.0$ ,  $\tau = 0$ ,  $\theta = 0$ ,  $\kappa_1 = -0.102$ , (b)  $D_u = 1.37 \cdot 10^{-4}$ ,  $D_v = 0$ ,  $D_w = 2.73 \cdot 10^{-3}$ ,  $\lambda = 2.5$ ,  $\kappa_3 = 1.0$ ,  $\kappa_4 = 1.0$ ,  $\tau = 0$ ,  $\theta = 0$ ,  $\kappa_1 = -0.32$ 

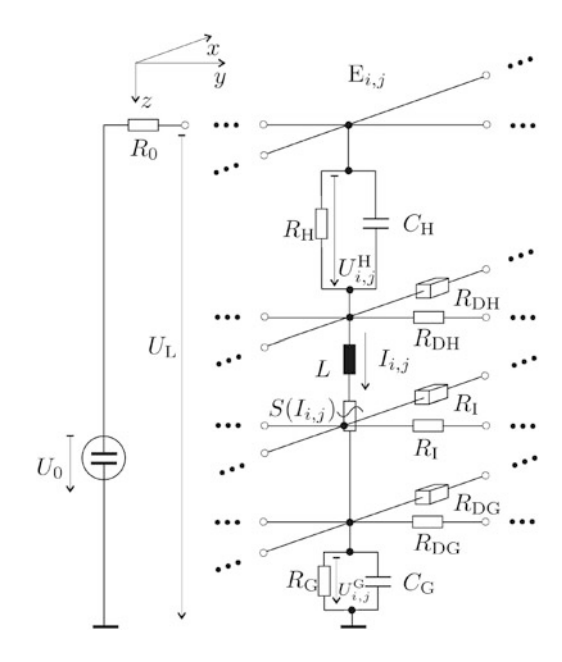
either extends or shrinks. In the latter case the shrinking can be stopped by the repulsion of approaching ring fronts, such that a stationary structure forms. Like the target-like dissipative soliton the ring-like structure can propagate and interact with co-existing ordinary dissipative solitons. In this context simulations show, that the ring-like dissipative soliton pertains its stability within a larger parameter region at least compared to the target-like dissipative soliton. It also is much more robust in interaction processes with simple dissipative solitons, in which most likely a vibrational mode is excited [3.42].

The existence of these ring-like dissipative solitons is also interesting from the experimental point of view, because similar structures are e.g. observed in the BZ-AOT system [3.88].

# 3.4.3 Phenomenological Context

Due to its very general ansatz the three-component reaction-diffusion system (3.69) is considered as phenomenological model for three very different experimental systems: the BZ-AOT reaction (Sect. 2.1.4), the semiconductor-gas discharge system (Sect. 2.2), and an electrical network of nonlinear oscillators. In case of the BZ-AOT reaction [3.89, 3.90] the activator is associated with the radical  $BrO_2^{\bullet}$ , while the stabilizing and driving inhibitors can be identified as  $Br_2$  (oil soluble) and  $Br^-$  (water soluble), respectively. In this context three-component reaction-diffusion system is applied for simulating the interaction of continuously propagating and jumping dissipative solitons on one-dimensional domains [3.91] as well as jumping waves in spatially extended systems [3.90].

Fig. 3.23 Nonlinear oscillator realizing one element of an analog three-component reaction-diffusion processor. At the heard of the oscillator is a nonlinear resistor with characteristic  $S(I_{i,j})$  which is connected in series with inductance L. Both are sandwiched between RC elements  $R_{\rm H}C_{\rm H}$  and  $R_{\rm G}C_{\rm G}$ . The nonlinear resistor and the RC-elements are coupled via resistors  $R_{\rm DH}$ ,  $R_{\rm DG}$ , and  $R_{\rm I}$  to their neighbored elements  $E_{i-1,j}, E_{i+1,j}, E_{i,j-1},$  $E_{i,j+1}$ . Boundary elements are connected cyclically to elements of the opposite boundary (Circuit diagram adapted from [3.57, p. 10])



In case of the semiconductor-gas discharge system the three-component reaction diffusion system has been applied for investigating the dynamics and interaction of current density filaments [3.92–3.94]. In this system the self-activation is caused by avalanche multiplication of charged carriers in the gas, while the voltage drop at the high-ohmic electrode plays the role of the (driving) inhibitor [3.92, 3.95]. Surface charges on the electrodes have an inhibitory role, too, as it diminishes the electric field in the gas [3.96]. Due to the low mobility of the surface charges, their distribution can be nonuniform giving rise to the observable filamentary structure of the discharge.

There also is a hypothetical setup founding on the self-organization phenomena observed for electrical networks of nonlinear oscillators [3.97, 3.98]. The elements of these circuits basically consist of an RC-element and a nonlinear resistor connected in series with an inductance. The elements of each layer are coupled laterally to the neighbored elements via resistors, such that spatiotemporal structure formation phenomena in one-dimensional systems [3.46, 3.62, 3.99, 3.100] and two-dimensional systems [3.101] can be observed. An extension of this setup has been originally discussed by Or-Guil, who proposed an additional layer of RC-elements realizing a second inhibitory component [3.102, p. 135]. One element  $E_{i,j}$  of the two-dimensional network is shown in Fig. 3.23. A detailed description of the nonlinear resistor and its spatial coupling is given by Schmeling [3.103].

The state of each element  $E_{i,j}$  is defined by current  $I_{i,j}$  and the voltage dropping at the RC-elements:

$$L\dot{I}_{i,j} = \frac{\gamma}{R_{\rm I}} (I_{i-1,j} + I_{i+1,j} + I_{i,j-1} + I_{i,j+1} - 4I_{i,j}) - S(I_{i,j})$$

$$- U_{i,j}^{\rm G} - U_{i,j}^{\rm H} + U_0 - R_0 \sum_{i,j}^{N_i, N_j} I_{i,j},$$

$$C_{\rm G}\dot{U}_{i,j}^{\rm G} = \frac{1}{R_{\rm DG}} (U_{i-1,j}^{\rm G} + U_{i+1,j}^{\rm G} + U_{i,j-1}^{\rm G} + U_{i,j+1}^{\rm G} - 4U_{i,j}^{\rm G}) + I_{i,j} - \frac{U_{i,j}^{\rm G}}{R_{\rm G}},$$

$$(3.71a)$$

$$C_{\rm H}\dot{U}_{i,j}^{\rm H} = \frac{1}{R_{\rm DH}} (U_{i-1,j}^{\rm H} + U_{i+1,j}^{\rm H} + U_{i,j-1}^{\rm H} + U_{i,j+1}^{\rm H} - 4U_{i,j}^{\rm H}) + I_{i,j} - \frac{U_{i,j}^{\rm H}}{R_{\rm H}}$$

with 
$$i = 1, \dots N_i$$
 and  $j = 1 \dots N_j$ .

In these equations the local coupling of neighboured network elements is reflected by the difference terms, while the global coupling of all oscillators is reflected by sum  $\sum_{i,j}^{N_i,N_j} I_{i,j}$  in (3.71a). In order to investigate these  $3N_iN_j$  differential equations the following normalization in introduced:

$$u_{i,j} = u_{i,j}(t) = \frac{I_{i,j}(t_{e}) - \bar{I}}{\hat{I}}, \qquad v_{i,j} = v_{i,j}(t) = \frac{U_{i,j}^{G}(t_{e}) - \bar{U}^{G}}{\hat{U}^{G}},$$

$$w_{i,j} = w_{i,j}(t) = \frac{U_{i,j}^{H}(t_{e}) - \bar{U}^{H}}{\hat{U}^{H}}, \qquad t = \frac{R_{I}}{L}t_{e}.$$
(3.72)

Here currents  $\bar{I}$  and  $\hat{I}$  are chosen with respect to the nonlinear resistor S(I) [3.103, p. 17ff], while the remaining quantities are coupled by

$$\hat{U}^{G} = R_{G}\hat{I}, \quad \bar{U}^{G} = R_{G}\bar{I},$$

$$\hat{U}^{H} = R_{H}\hat{I}, \quad \bar{U}^{H} = R_{H}\bar{I}.$$
(3.73)

Substituting (3.72) in (3.71) while accounting for (3.73), and introducing normalization constants

$$D_{u} = \frac{\gamma \Delta_{x}^{2}}{R_{I}^{2}}, \qquad f(u_{i,j}) = -\frac{S(\hat{I}u_{i,j}(t) + \bar{I})}{\hat{I}R_{I}},$$

$$D_{v} = \frac{R_{G}\Delta_{x}^{2}}{R_{DG}}, \qquad \tau = \frac{R_{G}R_{I}C_{G}}{L},$$

References 85

$$D_{w} = \frac{R_{H} \Delta_{x}^{2}}{R_{DH}}, \qquad \theta = \frac{R_{H} R_{I} C_{H}}{L},$$

$$\kappa_{1} = \frac{U_{0}}{\hat{I}} - \frac{\bar{I}}{\hat{I} R_{I}} (R_{G} + R_{H} + N_{i} N_{j} R_{0}), \quad \kappa_{2} = \frac{N_{i} N_{j} R_{0}}{R_{I}},$$

$$\kappa_{3} = \frac{R_{G}}{R_{I}}, \qquad \kappa_{4} = \frac{R_{H}}{R_{I}}$$
(3.74)

leads to the following system of differential equations:

$$\dot{u}_{i,j} = D_u \frac{u_{i-1,j} + u_{i+1,j} + u_{i,j-1} + u_{i,j+1} - 4u_{i,j}}{\Delta_x^2} + f(u_{i,j})$$

$$-\kappa_3 v_{i,j} - \kappa_4 w_{i,j} + \kappa_1 - \frac{\kappa_2}{N_i N_j} \sum_{i,j}^{N_i, N_j} u_{i,j},$$
(3.75a)

$$\tau \dot{v}_{i,j} = D_v \frac{v_{i-1,j} + v_{i+1,j} + v_{i,j-1} + v_{i,j+1} - 4v_{i,j}}{\Delta_x^2} + u_{i,j} - v_{i,j}, \quad (3.75b)$$

$$\theta \dot{w}_{i,j} = D_w \frac{w_{i-1,j} + w_{i+1,j} + w_{i,j-1} + w_{i,j+1} - 4w_{i,j}}{\Delta_x^2} + u_{i,j} - w_{i,j}$$
(3.75c)

with 
$$i = 1, \ldots N_i$$
 and  $j = 1, \ldots N_j$ .

Note, that the normalization (3.74) introduces a length interval  $\Delta_x$  such that the difference terms in (3.75) can be interpreted as approximation of the two-dimensional Laplace-Operator [3.104, p. 15ff]. Furthermore the global feedback approximates the integral of u on domain  $\Omega$  with  $\|\Omega\| = N_i N_j$ . Therefore (3.75) becomes a three-component reaction-diffusion term with global feedback

$$\dot{u} = D_u \Delta u + f(u) - \kappa_3 v - \kappa_4 w + \kappa_1 - \frac{\kappa_2}{\|\Omega\|} \int_{\Omega} u \, d\Omega, \tag{3.76a}$$

$$\tau \dot{v} = D_v \Delta v + u - v,\tag{3.76b}$$

$$\theta \dot{w} = D_w \Delta w + u - w. \tag{3.76c}$$

Consequently, for f'(u) > 0 and  $\kappa_3, \kappa_4 > 0$  the considered setup can be regarded as analog processor for three-component reaction-diffusion systems.

#### References

- 3.1. E. Schrödinger, Was Ist Materie? (Supposé, Köln, 2002)
- 3.2. T. Kapitaniak, S.R. Bishop, *The Illustrated Dictionary of Nonlinear Dynamics and Chaos* (Wiley, Chichester, 1999)
- 3.3. H.-G. Purwins, G. Klempt, J. Berkemeier, Festkörperprobleme 27, 27 (1987)

- 3.4. P. Heyward, M. Ennis, A. Keller, M.T. Shipley, J. Neurosci. 21(14), 5311 (2001)
- 3.5. R. Luther, Z. Elektrochem. 12, 596 (1906)
- 3.6. P. Blanchedeau, J. Boissonade, P.D. Kepper, Phys. D **147**(3–4), 283 (2000)
- 3.7. H.M. Gibbs, Optical Bistability: Controlling Light with Light (Academic, Orlando, 1985)
- 3.8. D. Becker, Frontausbreitung und Filamentstrukturen in einem zweidimensionalen gleichspannungsbetriebenen Gasentladungssystem. Master's thesis, Institut für Angewandte Physik, Westfälische Wilhelms-Universität Münster, 1994
- C. Goßen, F.-J. Niedernostheide, H.-G. Purwins, in *Nonlinear Dynamics and Pattern Formation in Semiconductors and Devices*, ed. by F.-J. Niedernostheide. Springer Proceedings in Physics, vol. 79 (Springer, Berlin, 1995), pp. 112–132
- 3.10. S. Bose, P. Rodin, E. Schöll, Phys. Rev. E 62(2), 1778 (2000)
- 3.11. C. Cheianov, P. Rodin, E. Schöll, Phys. Rev. B **62**(15), 9966 (2000)
- 3.12. O. Freyd, Parallele Hardware-Realisation eines Neuronalen Netzes mit Hilfe einer analogen Halbleiterkopplungsstruktur. Dissertation, Institut für Angewandte Physik, Westfälische Wilhelms-Universität Münster, 2001
- 3.13. S.H. Strogatz, Nonlinear Dynamics and Chaos. With Applications to Physics, Biology, Chemistry and Engineering, 5th edn. (Addison-Wesley, Reading, 1996)
- 3.14. H. Brezis, F. Browder, Adv. Math. 135, 76 (1998)
- 3.15. B. Denardo, B. Galvin, A. Greenfield, A. Larraza, S. Putterman, W. Wright, Phys. Rev. Lett. 68(11), 1730 (1992)
- 3.16. P.C. Fife, *Mathematical Aspects of Reacting and Diffusing Systems*. Lecture Notes in Biomathematics, vol. 28 (Springer, Berlin, 1979)
- 3.17. G. Baumann, Mathematica in Theoretical Physics. Selected Examples from Classical Mechanics to Fractals (Springer, New York, 1996)
- 3.18. E.D. Solmentsev, in *Encyclopaedia of Mathematics*, vol. 2, ed. by M. Hazewinkel (Kluwer, Dordrecht, 1995), pp. 450–451
- 3.19. A. Hagberg, E. Meron, Nonlinearity 7, 805 (1994). doi:10.1088/0951-7715/7/3/006
- 3.20. R. Rajaraman, Solitons and Instantons. An Introduction to Solitons and Instantons in Quantum Field Theory (Elsevier, Amsterdam, 2003)
- G.L. Alfimov, V.M. Eleonsky, N.E. Kulagin, L.M. Lerman, V.P. Silin, Phys. D 44, 168 (1990)
- 3.22. S. Wolfram, *Das Mathematica Buch: Mathematica Version 3*, 3rd edn. (Addison-Wesley-Longman, Bonn, 1997)
- 3.23. F. Schlögl, Z. Phys. **253**, 147 (1972)
- 3.24. E.C. Zeeman, in *Structural Stability in Physics*, ed. by W. Güttlinger, H. Eikemeier. Proceedings of Two International Symposia on Application of Catastrophe Theory and Topological Concepts in Physics. Tübingen. Federal Republic of Germany, 2–6 May and 11–14 December 1978. Springer Series in Synergetics, vol. 4 (Springer, Berlin, 1980), pp. 12–22
- 3.25. D. Aubin, Growing Explanations: Historical Perspective on the Sciences of Complexity (Duke University Press, Durham, 2004), chap. Forms of Explanations in the Catastrophe Theory of Rene Thom: Topology, Morphogenesis, and Structuralism, pp. 95–130
- 3.26. H.P. McKean Jr., Adv. Math. 4, 209 (1970)
- 3.27. P. Schütz, Strukturen mit großen Amplituden in Reaktions–Diffusions–Systemen vom Aktivator–Inhibitor–Typ. Dissertation, Institut für Angewandte Physik, Westfälische Wilhelms–Universität Münster, 1995
- 3.28. G. Flores, J. Differ. Equ. 80(2), 306 (1989)
- 3.29. M. Bode, Beschreibung strukturbildender Prozesse in eindimensionalen Reaktions-Diffusions-Systemen durch Reduktion auf Amplitudengleichungen und Elementarstrukturen. Dissertation, Institut für Angewandte Physik, Westfälische Wilhelms-Universität Münster, 1993
- 3.30. T. Kawahara, M. Tanaka, Phys. Lett. A **97**(8), 311 (1983). doi:10.1016/0375-9601(83) 90648-5
- 3.31. H. Yagisita, Publ. Res. Inst. Math. Sci. 39(1), 117 (2003). doi:10.2977/prims/1145476150
- 3.32. Y. Fukao, Y. Morita, H. Ninomiya, Taiwan. J. Math. 8, 15 (2004)

References 87

3.33. Y. Morita, H. Ninomiya, J. Dyn. Differ. Equ. 18, 537 (2006). doi:10.1007/s10884-006-9046-x

- 3.34. Y. Morita, H. Ninomiya, Sugaku Expo. **23**, 213 (2010)
- 3.35. R.G. Casten, C.J. Holland, J. Differ. Equ. 27(2), 266 (1978)
- 3.36. S.A. Hassan, D.H. Zanette, Phys. A 214, 435 (1995)
- 3.37. T. Bountis, C.F. Starmer, A. Bezerianos, Prog. Theor. Phys. Suppl. 139, 12 (2000)
- 3.38. A.S. Mikhailov, Foundations of Synergetics I. Distributed Active Systems. Springer Series in Synergetics, vol. 51 (Springer, Berlin, 1990)
- 3.39. G.H. Markstein, J. Aeronaut. Sci. 18(3), S. 199 (1951)
- 3.40. Y.P. Raizer, Gas Discharge Physics, 2nd edn. (Springer, Berlin, 1997)
- 3.41. L. Schimansky-Geier, C. Zülicke, E. Schöll, Z. Phys. B 84, 433 (1991)
- 3.42. C.P. Schenk, Numerische und analytische Untersuchung solitärer Strukturen in zwei- und dreikomponentigen Reaktions-Diffusions-Systemen. Dissertation, Institut für Angewandte Physik, Westfälische Wilhelms-Universität Münster, 1999. Figures published with kind permission of the author.
- 3.43. Y. Nishiura, SIAM J. Math. Anal. 13(4), 555 (1982)
- 3.44. A.M. Turing, Philos. Trans. R. Soc. B 237, 37 (1952)
- 3.45. J. Berkemeier, T. Dirksmeyer, G. Klempt, H.-G. Purwins, Z. Phys. B 65, 255 (1986)
- 3.46. T. Dirksmeyer, R. Schmeling, J. Berkemeier, H.-G. Purwins, in *Proceedings of the NATO Advanced Study Institute on Patterns, Defects and Materials Instabilities* Cargése, 4–15 September 1989, ed. by D. Walgraef, N.M. Ghoniem. NATO ASI Series E, Applied Sciences, vol. 183 NATO (Kluwer, Dordrecht, 1990), pp. 91–107
- 3.47. H. Willebrand, C. Radehaus, F.-J. Niedernostheide, R. Dohmen, H.-G. Purwins, Phys. Lett. A 149(2–3), 131 (1990)
- 3.48. Yu.A. Astrov, E. Ammelt, S. Teperick, H.-G. Purwins, Phys. Lett. A 211(3), 184 (1996)
- 3.49. E. Ammelt, Yu.A. Astrov, H.-G. Purwins, Phys. Rev. E **55**(6), 6731 (1997)
- 3.50. E. Ammelt, Yu.A. Astrov, H.-G. Purwins, Phys. Rev. E 58(6), 7109 (1998)
- 3.51. Q. Ouyang, H.L. Swinney, Nature 352, 610 (1991). doi:10.1038/352610a0
- 3.52. A. de Wit, Adv. Chem. Phys. **109**, 435 (1999)
- 3.53. P. de Kepper, J.J. Perraud, E. Dulos, Int. J. Bifurc. Chaos 4(5), 1215 (1994)
- 3.54. A.V. Gorbatyuk, R.B. Rodin, Sov. Tech. Phys. Lett. **17**(7), 519 (1990)
- 3.55. C.N. Chen, X.J. Hu, Commun. Partial Differ. Equ. **33**(2), 189 (2008). doi:10.1080/03605300601188755
- 3.56. Y.P. Lin, S. yaur Tzeng, Taiwan J. Math. **14**(5), 1849 (2010)
- 3.57. A. Moskalenko, Dynamische gebundene Zustände und Drift-Rotations-Dynamik von dissipativen Solitonen. Master's thesis, Institut für Angewandte Physik, Westfälische Wilhelms-Universität Münster, 2002
- 3.58. P. Coullet, J. Lega, B. Houchmanzadeh, J. Lajzerowicz, Phys. Rev. Lett. **65**(11), 1352 (1990)
- 3.59. M. Bode, H.-G. Purwins, Phys. D 86, 53 (1995)
- 3.60. T. Ohta, M. Mimura, R. Kobayashi, Phys. D **34**, 115 (1989)
- 3.61. C.P. Schenk, P. Schütz, M. Bode, H.-G. Purwins, Phys. Rev. E 57(6), 6480 (1998)
- 3.62. M. Bode, A. Reuter, R. Schmehling, H.-G. Purwins, Phys. Lett. A 185, 70 (1994)
- 3.63. A. Hagberg, E. Meron, Phys. Rev. Lett. **78**(6), 1166 (1997)
- 3.64. H.U. Bödeker, Universal properties of self-organized localized structures. Dissertation, Institut für Angewandte Physik, Westfälische Wilhelms–Universität Münster, 2007. http://nbn-resolving.de/urn/resolver.pl?urn=urn:nbn:de:hbz:6-68579565596. Figures published with kind permission of the author
- 3.65. G.F. Voronoi, J, Reine Angew. Math. 134, 198 (1908)
- 3.66. A. Okabe, B. Boots, K. Sugihara, S.N. Chiu, Spatial Tessellations: Concepts and Applications of Voronoi Diagrams, 2nd edn. (Wiley, Chichester, 2000)
- 3.67. B. de Lacy Costello, A. Adamatzky, N. Ratcliffe, A.L. Zanin, A.W. Liehr, H.-G. Purwins, Int. J. Bifurc. Chaos 14(7), 2187 (2004). doi:10.1142/S021812740401059X. Copyright 2004 World Scientific Publishing
- 3.68. D. Tolmachiev, A. Adamatzky, Adv. Mater. Opt. Electron. 6, 191 (1996)

- 3.69. Y. Nishiura, Dyn. Rep. 3, 25 (1994)
- 3.70. Y. Nishiura, Far-From-Equilibrium Dynamics. Translations of Mathematical Monographs, vol. 209 (American Mathematical Society, Providence, 2002)
- 3.71. S.V. Gurevich, Lateral self-organization in nonlinear transport systems described by reaction-diffusion equations. Dissertation, Institut für Angewandte Physik, Westfälische Wilhelms-Universität Münster, 2007. http://nbn-resolving.de/urn/resolver.pl?urn=urn:nbn: de:hbz:6-09569604103. Figures published with kind permission of the author
- 3.72. A.W. Liehr, Dissipative Solitonen in Reaktions-Diffusions-Systemen. Dissertation, Institut für Angewandte Physik, Westfälische Wilhelms-Universität Münster, 2003
- 3.73. R. FitzHugh, Biophys. J. 1, 445 (1962)
- 3.74. J. Nagumo, S. Arimoto, S. Yoshizawa, Proc. IRE **50**, 2061 (1962)
- 3.75. M.D. Graham, S.L. Lane, D. Luss, J. Phys. Chem. 97, 7564 (1993)
- 3.76. C. Elphick, A. Hagberg, B.A. Malomed, E. Meron, Phys. Lett. A 230(1-2), 33 (1997)
- 3.77. H. Hempel, I. Schebesch, L. Schimansky-Geier, Eur. Phys. J. B 2, 399 (1998)
- 3.78. V. Nekorkin, A. Dmitrichev, J. Bilbault, S. Binczak, Phys. D 239, 972 (2010). doi:10.1016/j.physd.2010.02.004
- 3.79. C. Muratov, V. Osipov, Phys. Rev. E **53**(4), 3101 (1996)
- 3.80. L.M. Pismen, Phys. Rev. Lett. **86**(15), 548 (2001)
- 3.81. I. Schebesch, Numerische und analytische Untersuchungen an einem Reaktions-Diffusions-System in der Nähe eines singulären Grenzfalls. Master's thesis, Institut für Angewandte Physik, Westfälische Wilhelms-Universität Münster, 1994
- 3.82. C.P. Schenk, M. Or-Guil, M. Bode, H.-G. Purwins, Phys. Rev. Lett. 78, 3781 (1997)
- 3.83. K. Krischer, A. Mikhailov, Phys. Rev. Lett. **73**(23), 3165 (1994)
- 3.84. A.M. Zhabotinsky, M. Dolnik, I.R. Epstein, J. Chem. Phys. 103(23), 10306 (1995)
- 3.85. M. Or-Guil, M. Bode, C.P. Schenk, H.-G. Purwins, Phys. Rev. E 57(6), 6432 (1998)
- 3.86. M. Bode, A.W. Liehr, C.P. Schenk, H.-G. Purwins, Phys. D **161**(1–2), 45 (2002)
- 3.87. A.W. Liehr, A.S. Moskalenko, M.C. Röttger, J. Berkemeier, H.-G. Purwins, in *High Performance Computing in Science and Engineering '02. Transactions of the High Performance Computing Center Stuttgart (HLRS) 2002*, ed. by E. Krause, W. Jäger (Springer, Berlin, 2003), pp. 48–61
- 3.88. V.K. Vanag, I.R. Epstein, Phys. Rev. Lett. **92**(12), 128301 (2004). doi:10.1103/PhysRevLett. 92.128301
- 3.89. V.K. Vanag, I.R. Epstein, Chaos 18(2), 026107 (2008). doi:10.1063/1.2900555
- A.A. Cherkashin, V.K. Vanag, I.R. Epstein, J. Chem. Phys. 128(20) (2008). doi:10.1063/1. 2924119
- L. Yang, A.M. Zhabotinsky, I.R. Epstein, Phys. Chem. Chem. Phys. 8, 4647 (2006). doi: 10.1039/b609214d
- 3.92. H. Bödeker, M.C. Röttger, A.W. Liehr, T. Frank, R. Friedrich, H.-G. Purwins, Phys. Rev. E 67(056220), 1 (2003). doi:10.1103/PhysRevE.67.056220
- 3.93. H. Bödeker, A.W. Liehr, T.D. Frank, R. Friedrich, H.-G. Purwins, New J. Phys. 6(62), 1 (2004)
- 3.94. S.V. Gurevich, H.U. Bödeker, A.S. Moskalenko, A.W. Liehr, H.-G. Purwins, Phys. D 199(1–2), 115 (2004). doi:10.1016/j.physd.2004.08.020
- 3.95. A.W. Liehr, H.U. Bödeker, M.C. Röttger, T.D. Frank, R. Friedrich, H.-G. Purwins, New J. Phys. 5(89), 1 (2003). http://stacks.iop.org/1367-2630/5/89
- 3.96. E.L. Gurevich, A.W. Liehr, S. Amiranashvili, H.-G. Purwins, Phys. Rev. E **69**(036211), 1 (2004)
- 3.97. H.-G. Purwins, C. Radehaus, J. Berkemeier, Z. Naturforschung 43a(1), 17 (1988)
- 3.98. H.-G. Purwins, H.U. Bödeker, A.W. Liehr, in *Dissipative Solitons*, ed. by N. Akhmediev, A. Ankiewicz (Springer, Berlin, 2005), pp. 267–308
- 3.99. A. Kulka, M. Bode, H.-G. Purwins, Phys. Lett. A 233, 33 (1995)
- 3.100. G. Heidemann, M. Bode, H.-G. Purwins, Phys. Lett. A **177**, 225 (1993)

References 89

3.101. J. Berkemeier, Ein elektronisches Modell zur Beschreibung der Selbststrukturierung in homogenen Systemen. Dissertation, Institut für Angewandte Physik, Westfälische Wilhelms-Universität Münster, 1987

- 3.102. M. Or-Guil, Elementare Anregungen und ihre Wechselwirkung. Untersuchungen von Reaktions-Diffusions-Modellen im Vergleich mit elektrischen Durchbruchsexperimenten. Dissertation, Institut für Angewandte Physik, Westfälische Wilhelms-Universität Münster, 1997
- 3.103. R. Schmeling, Experimentelle und numerische Untersuchungen von Strukturen in einem Reaktions-Diffusions-System anhand eines elektrischen Netzwerks. Dissertation, Institut für Angewandte Physik, Westfälische Wilhelms-Universität Münster, 1994
- 3.104. D. Marsal, Finite Differenzen und Elemente. Numerische Lösung von Variationsproblemen und partiellen Differentialgleichungen (Springer, Berlin, 1989)

# Chapter 4 **Dynamics**

It is interesting that bifurcation introduces in a sense "history" into physics.

Ilya Prigogine, Nobel lecture 1977 [4.1].

**Abstract** The dynamics of dissipative solitons are introduced by discussing the destabilization of localized structures breaking their mirror symmetry. In this context the central concept of critical modes is introduced and discussed on basis of single dissipative solitons and their basic bound states. These considerations lead to analytic expression for the drift- and rotational velocities of the structures in the vicinity of the bifurcation point. In particular we will discuss the fact, that under certain circumstances bound states of dissipative solitons propagate uniformly while unbound dissipative solitons are stationary. Finally, the dynamics of dissipative solitons in the vicinity of the drift-bifurcation are deduced.

#### 4.1 Bifurcations

It is a well known phenomena that stationary dissipative solitons in reaction diffusion systems can undergo a transition to different kinds of dynamic states [4.2–4.7]. Namely, they are able to change their shape periodically, which is called breathing, or they start to move with well defined velocity, which is called propagation. An extension of the latter is the rotation of bound states of dissipative solitons. However, all cases have in common, that close to the bifurcation point the shape of the dissipative solitons only slightly deviates from the stationary state. With increasing excitation of the relevant modes the shape transforms more and more until the structure as a whole either collapses (Fig. 3.16) or develops to a regular structure (Fig. 7.5).

In order to characterize these bifurcations in parameter space we are starting with a two-dimensional stationary dissipative soliton solving (3.69) for

$$D_u = 0.08, \ D_v = D_w = 1, \ \lambda = 2, \ \kappa_1 = -0.33,$$
  
 $\kappa_3 = \kappa_4 = 0.5, \tau = \theta = 0.$  (4.1)

The stability of this localized solution with respect to angular perturbation modes (3.60a) is analyzed for  $(\tau,\theta) \in [0,30] \times [0,30]$  (Fig. 4.1a). Note, that parameter set (4.1) effectively reduces the three-component reaction-diffusion system (3.69) to a two-component system (3.38) because the identity of diffusion constants  $D_v$ ,  $D_w$ , and coupling constants  $\kappa_3$ ,  $\kappa_4$  leads to identical distributions of inhibiting components v and w. The result of this analysis is depicted in Fig. 4.1a which shows the 0-isoclines of eigenvalues related to destabilization modes  $\mu=0$  and  $\mu=1$  in  $\tau-\theta$ -parameter-space. First of all it is evident that the isoclines are symmetric to the angle bisector, which is caused by the indifference of the inhibiting components.

The diagram also shows a clear order of bifurcations: Starting with small time constants  $\tau, \theta \ll 1$  and increasing one of them first of all destabilizes the  $\mu = 0$  modes causing a breathing of the dissipative soliton if the structure is subject to noise, while the  $\mu = 1$  mode is destabilized for larger values of the time scale constants [4.8–4.10].

In a second scenario we are qualifying for a full three-component system by switching the inhibitor distribution v to a copy of the activator distribution ( $D_v = 0$ ) and adapting the reaction terms:

$$D_u = 0.08, D_v = 0, D_w = 1, \lambda = 3, \kappa_1 = -0.33,$$
  
 $\kappa_3 = \kappa_4 = 1, \tau = \theta = 0.$  (4.2)

By increasing the time constant  $\tau$  of inhibitor v the latter becomes a time-delayed copy of the activator distribution. In this scenario the order of bifurcations is identical to the previous one, if the time scale constants of both inhibitors are small and the time scale constant  $\theta$  of the diffusing inhibitor w is increased (Fig. 4.1b). This is reasonable, because this scenario resembles the situation discussed in Fig. 4.1a. However, if the time-scale constant  $\theta$  of the diffusing inhibitor w is small and the time-scale constant  $\tau$  of the non-diffusing inhibitor is increased the order of bifurcations change. As a consequence the stationary dissipative soliton first of all becomes unstable with respect to the propagation mode (*dashed* line, inlay of Fig. 4.1b) and only for larger values of  $\tau$  becomes additionally unstable for the breathing mode (*solid* line, inlay of Fig. 4.1b). This is exactly the case discussed in the following sections in order to understand the so-called drift-bifurcation from a theoretical point of view and derive the dynamics of propagating dissipative solitons in the vicinity of the drift-bifurcation point.

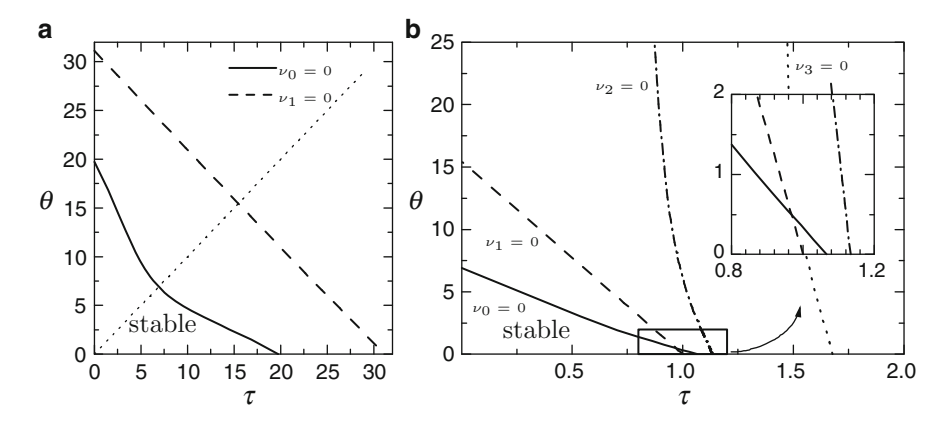


Fig. 4.1 Nullclines of eigenvalues  $\nu_{\mu}$  for  $\mu=0,1,2,3$ . Examples of the respective eigenmodes are depicted in Fig. 3.18. Stable dissipative solitons exist in the *lower left corner* of the diagrams. Figures annotated from [4.11, p. 49]. Parameters: (a) from (4.1), (b) from (4.2)

## 4.2 Shape-Preserving Destabilizations

It is a well known phenomenon, that, under certain circumstances, stationary structures of dissipative systems undergo a transition to propagating structures due to a change of system parameters. Concerning spatially periodic patterns this bifurcation is reported for periodically destabilized flame fronts [4.12], two-dimensional flame patterns [4.13], parametrically driven surfaces of liquids [4.14], Rayleigh-Bénard convection in cylinders [4.15,4.16], the printer's instability [4.17–4.19], and hexagonal patterns of current density filaments in ac-driven gas-discharge systems [4.20].

For a large variety of systems a general understanding of this dynamic destabilization can be established by means of symmetry considerations [4.21–4.23], which in most cases enable an abstract classification of the occurring bifurcations. In contrast to this more general approach the following sections address the problem of quantifying the instability by directly examining the unstable modes of the structures. This ansatz enables not only the identification of bifurcation points but also the computation of propagation velocities close to the bifurcation point. While the dynamics of propagating patterns are highly influenced by the geometry of the considered domain the following considerations focus on localized structures which are separated from the domain boundaries such that the deduced dynamics is independent of the domain geometry.

#### 4.2.1 Goldstone-Mode

For localized solutions of one-component reaction-diffusion systems (3.3) with symmetric potential it has been pointed out in Sect. 3.1.2, that all fronts  $u_F^+(x)$  (3.8)

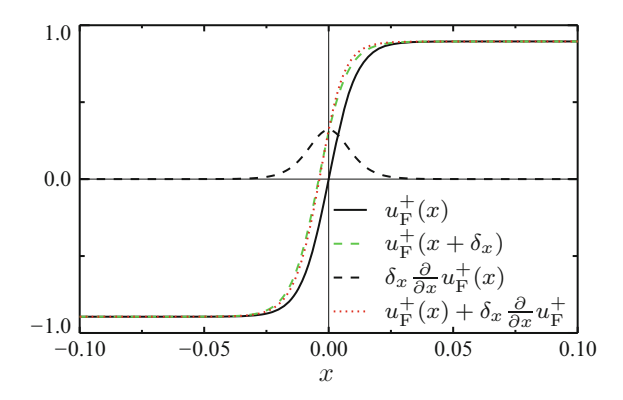


**Fig. 4.2** Displacement of front  $u_F^+(x)$  by  $\delta_x$ . The displaced front  $u_F^+(x+\delta_x)$  (dashed green curve) can be constructed from front  $u_F^+(x)$  (solid black curve) by adding a Goldstone-mode  $\frac{\partial}{\partial x}u_F^+(x)$  (black dashed curve), which is weighted by the displacement  $\delta_x$ . The resulting front (red dotted curve) agrees in the scope of the approximation  $\delta_x \ll 1$  very well with the directly shifted front (green dotted curve). Parameters:  $\lambda = 0.8$ ,  $D_u = 5 \cdot 10^{-5}$ ,  $\delta_x = 5 \cdot 10^{-3}$ 

shifted by  $\pm \delta_x \in \mathbb{R}$  are stationary solutions of the system (3.3). This is due to the translational invariance of the system. In a more general notation this relation can be written as

$$\frac{\partial}{\partial t}u_{\rm F}^{+}(x+\delta_{x}) = F\left(u_{\rm F}^{+}(x+\delta_{x})\right) = 0,\tag{4.3}$$

if the right hand side of (3.3) is substituted by the nonlinear operator F(u). In order to check the validity of this mathematical statement the first order series expansion of the displaced front  $u_F^+(x + \delta_x)$  around the original front  $u_F^+(x)$  is computed for  $\delta_x \ll 1$ :

$$u_{\rm F}^+(x+\delta_x) \approx u_{\rm F}^+(x) + \delta_x \frac{\partial}{\partial x} u_{\rm F}^+(x). \tag{4.4}$$

Note, that the term

$$\delta_x \frac{\partial}{\partial x} u_{\rm F}^+(x) = \delta_x \frac{\lambda}{\sqrt{2D_u}} \operatorname{sech}^2\left(x\sqrt{\frac{\lambda}{2D_u}}\right) \tag{4.5}$$

is composed from the so-called Goldstone-mode  $\frac{\partial}{\partial x}u_F^+(x)$  and the displacement  $\delta_x$ . Literally speaking, (4.4) means that a front  $u_F^+(x)$  can be displaced by a small distance  $\delta_x$  by adding a respective perturbation in form of the Goldstone-mode  $\frac{\partial}{\partial x}u_F^+(x)$  (Fig. 4.2).

In order to understand the influence of the Goldstone-mode on the stability of the stationary solution, approximation (4.4) is inserted into (4.3) and the first order series expansion is computed:

$$0 = F\left(u_{\mathrm{F}}^{+}(x+\delta_{x})\right)$$

$$\approx F\left(u_{\mathrm{F}}^{+}(x) + \delta_{x}\frac{\partial}{\partial x}u_{\mathrm{F}}^{+}(x)\right)$$

$$\approx F\left(u_{\mathrm{F}}^{+}(x)\right) + \delta_{x}\mathcal{D}\left(u_{\mathrm{F}}^{+}(x)\right)\frac{\partial}{\partial x}u_{\mathrm{F}}^{+}(x),$$
(4.6)

here operator  $\mathcal{D}\left(u_{\mathrm{F}}^{+}(x)\right)$  denotes the Fréchet-derivative of operator F(u) evaluated at  $u_{\mathrm{F}}^{+}(x)$ . Because  $F\left(u_{\mathrm{F}}^{+}(x)\right)$  is zero, just as well as  $F\left(u_{\mathrm{F}}^{+}(x+\delta_{x})\right)$ , (4.6) can only be fulfilled if

$$\mathcal{D}\left(u_{F}^{+}(x)\right) \frac{\partial}{\partial x} u_{F}^{+}(x) \stackrel{(3.3)}{=} D_{u} \frac{\partial^{3}}{\partial x^{3}} u_{F}^{+}(x) + \lambda \frac{\partial}{\partial x} u_{F}^{+}(x) - 3 \left(u_{F}^{+}(x)\right)^{2} \frac{\partial}{\partial x} u_{F}^{+}(x) = 0 \quad (4.7)$$

holds, which can be checked by inserting  $u_F^+(x)$  (3.8) in (4.7). From a more abstract point of view this means, that the Goldstone-mode  $\frac{\partial}{\partial x}u_F^+(x)$  is an eigenmode of the linear operator  $\mathcal{D}\left(u_F^+(x)\right)$  with zero eigenvalue and therefore does not influence the stability of the front.

These stability considerations also apply for partial differential equations

$$\frac{\partial}{\partial t} \mathbf{u} = \mathbf{F} \left( \nabla, \mathbf{u}, \kappa \right) \tag{4.8}$$

with  $F(\nabla, u, \kappa)$  being a nonlinear operator acting on the m components of field  $u = u(x) = (u_1(x), \dots, u_m(x))^T$  defined for  $x \in \mathbb{R}^n$ . Furthermore, it is assumed that the solutions of (4.8) depend on parameter vector  $\kappa$  and at least one stationary solution  $\bar{u}(x;\kappa) = \bar{u}$  exists. In this case the dynamics of slightly perturbed stationary solutions  $u = \bar{u} + \tilde{u}$  is determined by the dynamics of the eigenmodes of the linear operator  $\mathcal{D}(\bar{u};\kappa)$ , that is

$$\frac{\partial}{\partial t}\tilde{\boldsymbol{u}} = \mathcal{D}(\bar{\boldsymbol{u}}; \boldsymbol{\kappa})\tilde{\boldsymbol{u}}. \tag{4.9}$$

If the considered system (4.8) furthermore exhibits continuous symmetries with respect to a coordinate transformation  $x_i \to x_i + \delta_{x_i}$  with  $\delta_{x_i} \in \mathbb{R}$  and the stationary solution additionally depends in a non-trivial way on the coordinate  $x_i$ , then

$$\mathcal{G}_{x_i} = \frac{\partial}{\partial x_i} \bar{\boldsymbol{u}} \tag{4.10}$$

is a Goldstone-mode of  $\bar{u}$  and therefore an eigenmode of the linear operator  $\mathcal{D}(\bar{u}; \kappa)$  with eigenvalue 0:

$$\mathcal{D}(\bar{\boldsymbol{u}}, \boldsymbol{\kappa})\mathcal{G}_{x_i} = 0. \tag{4.11}$$

Because the Goldstone-modes are characterized by a discrete eigenvalue, they are different from Goldstone-bosons which have a continuous spectrum of eigenvalues

whose smallest eigenvalue is equal to zero [4.24, p. 151]. Note, that (4.11) is a special case of eigenvalue equation (3.64) with  $\mathcal{F}_1 = \mathcal{G}_x$ . In general, the complex eigenfunctions  $\mathcal{F}_{\mu}$  of (3.64) can be computed numerically for  $\mu = 0, 2, 3, \ldots$  (Fig. 3.18) and e.g. for  $\nu_0 = \pm i\omega$  describe the bifurcation point of the breathing instability [4.5].

## 4.2.2 Propagator-Mode

The Goldstone-modes discussed in the foregoing section do not cause a destabilization of stationary solutions  $\bar{u}$  due to their neutrality concerning the dynamics of small perturbations. On the other hand such a destabilization can occur if an additional mode exactly matches the Goldstone-mode  $\mathcal{G}_{x_i}$  at a certain critical representative  $\kappa_c$  of control parameter vector  $\kappa$ . In this scenario we are dealing with a degenerated eigenvalue problem, such that the eigenbasis has to be expanded by a generalized eigenmode  $\mathcal{P}_{x_i}$  in order to describe the eigenvalue problem completely.

For this purpose the generalized eigenmode  $\mathcal{P}_{x_i}$  of linear operator  $\mathcal{D}(\bar{u}, \kappa_c)$  with eigenvalue  $v_i$  is computed with the ansatz

$$(\mathcal{D}(\bar{\boldsymbol{u}}, \kappa_{c}) - \nu_{i} \,\hat{\boldsymbol{1}})^{2} \mathcal{P}_{x_{i}} = 0, \tag{4.12}$$

whereby  $\hat{1}$  denotes the unity operator. By inserting the degenerated eigenvalue  $v_i = 0$  of the Goldstone-mode  $\mathcal{G}_{x_i}$  the following relation is deduced

$$\mathcal{D}(\bar{\boldsymbol{u}}, \kappa_{c})^{2} \mathcal{P}_{x_{i}} = \mathcal{D}(\bar{\boldsymbol{u}}, \kappa_{c}) \mathcal{D}(\bar{\boldsymbol{u}}, \kappa_{c}) \mathcal{P}_{x_{i}} = 0. \tag{4.13}$$

Because of (4.11) this equation is only fulfilled if the linear operator  $\mathcal{D}(\bar{u}, \kappa_c)$  applied to the generalized eigenmode  $\mathcal{P}_{x_i}$  exactly returns the Goldstone-mode  $\mathcal{G}_{x_i}$ :

$$\mathcal{D}(\bar{\boldsymbol{u}}, \boldsymbol{\kappa}_{c}) \mathcal{P}_{x_{i}} = \mathcal{G}_{x_{i}}. \tag{4.14}$$

Therefore, exciting the generalized eigenmode  $\mathcal{P}_{x_i}$  of a localized structure  $\bar{\boldsymbol{u}}$  permanently generates the corresponding Goldstone-mode  $\mathcal{G}_{x_i}$  and results into a continuous shifting of stationary solution  $\bar{\boldsymbol{u}}$  in direction  $\boldsymbol{e}_{x_i}$ . This scenario describes a drift-bifurcation occurring at  $\boldsymbol{\kappa} = \boldsymbol{\kappa}_c$  [4.3]. Note, that these considerations even hold for arbitrary directions  $\boldsymbol{e}_{x_i} = \boldsymbol{r} \in \mathbb{R}^n$  as long as  $\mathcal{G}_r = \frac{\partial}{\partial r} \boldsymbol{u} \neq \boldsymbol{0}$ , which is discussed in Sect. 4.2.4.

Because the presented formalism has been basically developed in the context of front propagation (cf. [4.25]) the name *propagator-mode* for the generalized eigenmode  $\mathcal{P}_{x_i}$  is well established. However, in the present context it is used for arbitrary excitable modes of localized structures leading to a translational or rotational motion.

While the analytical representation of the propagator mode has not to be known in order to discuss drift- and rotational-bifurcations, it is essentially needed for investigating the dynamics of dissipative solitons close to the onset of propagation. Note, that (4.14) does not define the propagator mode uniquely (cf. [4.25, S. 275]). Because of the neutrality of the Goldstone-mode all elements of  $\{\mathcal{P}_{x_i} + a\mathcal{G}_{x_i} | a \in \mathbb{R}\}$  act as propagator mode. Therefore we have a certain degree of freedom to choose an appropriate analytical representation of the propagator mode (cf. Sect. 4.3.3).

## 4.2.3 Complementary Modes

In order to understand the prerequisites ensuring the solvability of (4.14) a complementary Goldstone-mode is introduced [4.26, S. 42]. It is defined as eigenmode  $\mathcal{G}_{x_i}^{\dagger}$  of operator  $\mathcal{D}^{\dagger}(\bar{u}, \kappa_c)$  with eigenvalue zero:

$$\mathcal{D}^{\dagger}(\bar{\boldsymbol{u}}, \boldsymbol{\kappa}_{\mathrm{c}})\mathcal{G}_{x_{i}}^{\dagger} = 0. \tag{4.15}$$

Note, that operator  $\mathcal{D}^{\dagger}(\bar{u}, \kappa_c)$  is adjoined to linear operator  $\mathcal{D}(\bar{u}, \kappa_c)$ . By introducing a scalar product  $\langle \cdot | \cdot \rangle$  as integration over domain  $\Omega$  and projecting (4.14) onto the complementary Goldstone-mode  $\mathcal{G}_{x_i}^{\dagger}$  leads to the following calculation:

$$\langle \mathcal{G}_{x_{i}}^{\dagger} | \mathcal{G}_{x_{i}} \rangle = \langle \mathcal{G}_{x_{i}}^{\dagger} | \mathcal{D}(\bar{\boldsymbol{u}}, \boldsymbol{\kappa}_{c}) \mathcal{P}_{x_{i}} \rangle$$

$$\Rightarrow \langle \mathcal{G}_{x_{i}}^{\dagger} | \mathcal{G}_{x_{i}} \rangle = \langle \mathcal{D}^{\dagger}(\bar{\boldsymbol{u}}, \boldsymbol{\kappa}_{c}) \mathcal{G}_{x_{i}}^{\dagger} | \mathcal{P}_{x_{i}} \rangle$$

$$\Rightarrow \langle \mathcal{G}_{x_{i}}^{\dagger} | \mathcal{G}_{x_{i}} \rangle = 0. \tag{4.16}$$

Therefore the bifurcation point  $\kappa_c$  at which the propagator-mode  $\mathcal{P}_{x_i}$  matches the Goldstone-mode  $\mathcal{G}_{x_i}$  can be computed analytically by solving (4.14) if the Goldstone-mode  $\mathcal{G}_{x_i}$  is orthogonal to the complementary Goldstone-mode  $\mathcal{G}_{x_i}^{\dagger}$ .

In order to evaluate the solvability condition (4.16) the complementary Goldstone-mode  $\mathcal{G}_{x_i}^{\dagger}$  has to be known. In case of the three-component reaction-diffusion system (3.69) it derives from the fact that the linear operator  $\mathcal{D}(\bar{u}, \kappa_c)$  can be decomposed into a diagonal invertible parameter matrix  $\mathcal{M}(\kappa_c)$  and a self-adjoined operator  $\mathcal{L}(\bar{u}, \kappa_c)$  [4.27]:

$$\mathcal{D}(\bar{\boldsymbol{u}}, \kappa_c) = \mathcal{M}(\kappa_c) \mathcal{L}(\bar{\boldsymbol{u}}, \kappa_t). \tag{4.17}$$

The parameter matrix  $\mathcal{M}(\kappa_c)$  depends on the critical parameter  $\kappa_c$  but not on the stationary solution  $\bar{u}$ , while the linear operator  $\mathcal{L}(\bar{u}, \kappa_c)$  depends on the stationary solution and on all non-critical parameters  $\kappa_c$ . Note, that the Goldstone-mode  $\mathcal{G}_{x_i}$  (4.11) is an eigenvector of  $\mathcal{L}(\bar{u}, \kappa_c)$  with eigenvalue zero.

By substituting definition (4.17) into the eigenvalue equation of the complementary Goldstone-mode (4.15)

$$0 = \mathcal{D}^{\dagger}(\bar{\boldsymbol{u}}, \kappa_{c})\mathcal{G}_{x_{i}}^{\dagger} = (\mathcal{M}(\kappa_{c})\mathcal{L}(\bar{\boldsymbol{u}}, \kappa_{c}))^{\dagger}\mathcal{G}_{x_{i}}^{\dagger} = \mathcal{L}(\bar{\boldsymbol{u}}, \kappa_{c})\mathcal{M}(\kappa_{c})\mathcal{G}_{x_{i}}^{\dagger}, \tag{4.18}$$

we find, that the eigenvalue equation of the complementary Goldstone-mode (4.15) is solvable within the scope of the discussed scenario (4.17) if the product of parameter matrix  $\mathcal{M}(\kappa_c)$  and complementary Goldstone-mode  $\mathcal{G}_{x_i}^{\dagger}$  results in the Goldstone-mode:

$$\mathcal{M}(\kappa_{c})\mathcal{G}_{x_{i}}^{\dagger} = \mathcal{G}_{x_{i}}. \tag{4.19}$$

Therefore the complementary Goldstone-mode  $\mathcal{G}_{x_i}^{\dagger}$  can be analytically expressed in terms of  $\mathcal{G}_{x_i}$ 

$$\mathcal{G}_{x_i}^{\dagger} = \mathcal{M}(\kappa_c)^{-1} \mathcal{G}_{x_i}. \tag{4.20}$$

Because the Goldstone-mode  $\mathcal{G}_{x_i}$  of a known stationary solution  $\bar{\boldsymbol{u}}$  can be computed by differentiation of the solution with respect to coordinate  $x_i$ , the complementary Goldstone-mode has not to be computed numerically which is the case for more arbitrary cases of the linear operator  $\mathcal{D}(\bar{\boldsymbol{u}}, \kappa)$  (e.g. [4.28, 4.29]).

Furthermore the critical point  $\kappa_c$  in parameter space, at which the propagatormode  $\mathcal{P}_{x_i}$  (4.14) destabilizes the stationary structure  $\bar{u}$  to a propagating one, is determined by the solvability condition (4.16), because  $\kappa_c$  contributes via the parameter matrix  $\mathcal{M}(\kappa_c)$  to the computation of the complementary Goldstone-mode  $\mathcal{G}_{x_i}^{\dagger}$  (4.20).

For the deduction of dynamic equations another complementary mode, the complementary propagator mode  $\mathcal{P}_{x_i}^{\dagger}$  is needed. It is defined correspondingly to the definition of the complementary Goldstone-mode (4.15) by

$$\mathcal{D}^{\dagger}(\bar{\boldsymbol{u}}, \boldsymbol{\kappa}_{c}) \mathcal{P}_{x_{i}}^{\dagger} = \mathcal{G}_{x_{i}}^{\dagger}. \tag{4.21}$$

In Sect. 4.2.2 it has been mentioned, that the propagator mode is not defined uniquely. The same holds for the complementary propagator mode, because all elements of  $\{\mathcal{P}_{x_i}^{\dagger} + a\mathcal{G}_{x_i}^{\dagger} | a \in \mathbb{R}\}$  act as complementary propagator mode.

# 4.2.4 Drift- and Rotational-Bifurcation

Already in the foregoing chapter the existence of localized stationary solutions of three-component reaction-diffusion system (3.69) have been discussed. These dissipative solitons exhibit rotational symmetry and pronounced oscillatory tails in the vicinity of the Turing-bifurcation. It has been shown by Schenk et al. [4.30], that the oscillating tails mediate attractive or repulsive interaction between neighbored dissipative solitons, such that they can arrange in several well defined distances. Two examples of dissipative solitons being bound in different binding

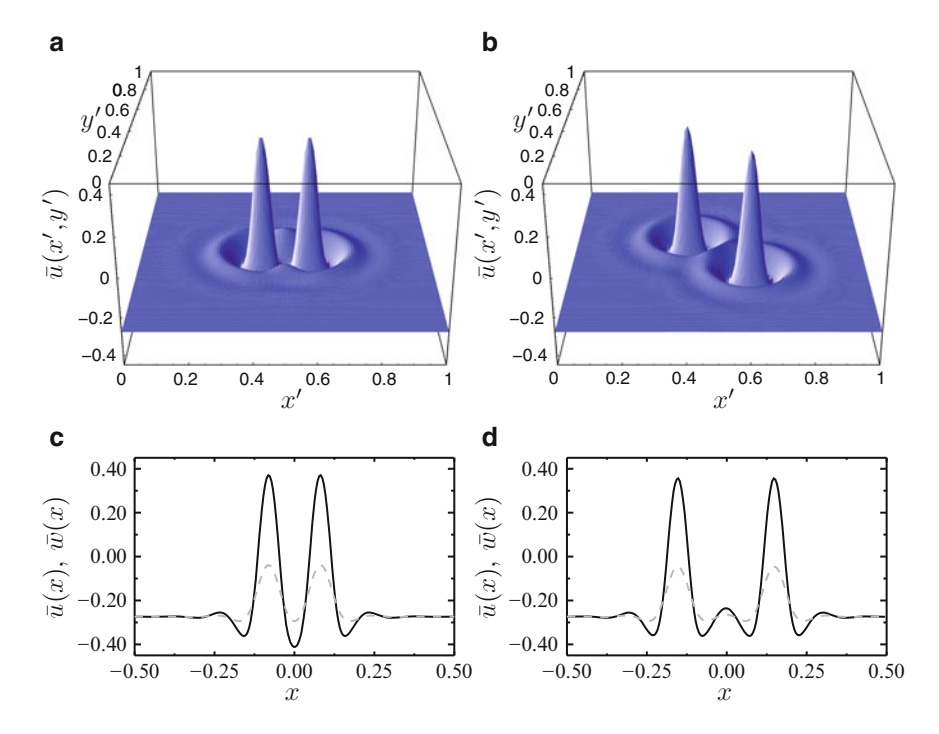


Fig. 4.3 Typical stationary bound states in a two-dimensional reaction-diffusion system. The plots show the configurations with the first (subfigures (a) and (c)) and second (subfigures (b) and (d)) smallest binding distances. Each configuration is shown as surface plot of activator  $\bar{u}(x,y)$  respectively  $\bar{u}(x',y')$  (upper row) and as intersection of the activator distribution  $\bar{u}(x)$  (black curve) and stabilizing inhibitor distribution  $\bar{w}(x)$  (dashed curve) along the longitudinal axis of the bound state (lower row). For the intersections the coordinate system is transformed, such that the center of the structure is located at the origin of the coordinate system and the longitudinal axis of the stationary bound state is parallel to the x-axis of the coordinate system. The intersection of the driving inhibitor  $\bar{v}$  is not shown because it is identical to the activator distribution for parameter set (4.22) and  $\tau = 3.04$ . Solutions computed on domain  $\Omega = [0, 1]^2$  with no-flux boundary condition,  $\Delta_x = 5 \cdot 10^{-3}$ , and  $\Delta_t = 0.1$ 

distances are shown in Fig. 4.3 as solutions of the three-component reaction-diffusion system (3.69) with parameters

$$D_u = 1.1 \cdot 10^{-4}, \ D_v = 0, \ D_w = 9.64 \cdot 10^{-4}, \ \lambda = 1.01,$$
  
 $\kappa_1 = -0.1, \ \kappa_3 = 0.3, \ \kappa_4 = 1, \ \tau = 3.32, \theta = 0.$  (4.22)

Note, that this parameter set represents the limit of a two-component reaction-diffusion system with local feedback (3.66) which prevents us from dealing with the breathing instability of the single dissipative soliton [4.3] and later on will enable the deduction of *reduced dynamics* (Sect. 5.2.1). However, numerical stability analysis shows (Fig. 4.1), that for  $D_w > D_v$  and  $\tau \gg \theta > 0$  the drift destabilization occurs

before the breathing instability if  $\tau$  or  $\theta$  are chosen as control parameter. Therefore, we will consider the more general case  $\theta \neq 0$  for the following analysis and discuss the limit  $\theta \to 0$  wherever appropriate.

The exclusion of internal degrees of freedom is also applied to the considered bound states, which are regarded as rigid structures. This assumption definitely holds for the undisturbed stationary structure and uniformly propagating structures in the direct vicinity of the drift-bifurcation point. While the assumption of rigid bound states is dropped later on (Chap. 5), it is consequently used for the following considerations and leads to the interpretation of a bound state as singular structure breaking the translational and rotational symmetry of the investigated system (3.69). Therefore the bound states do not only have Goldstone-modes of translation but also Goldstone-modes of rotation, such that a stationary bound state can be destabilized to an uniformly moving or a uniformly rotating structure. In the following sections these drift-, respectively rotational bifurcation is investigated by means of bound states of dissipative solitons (Fig. 4.3) observed as solutions of the two-dimensional three-component reaction-diffusion system (3.69). Of course the presented formalism can easily be generalized to structures of higher dimensional systems.

Having a stationary localized structure  $\bar{u}$  at hand (Fig. 4.3) we start by linearizing the underlying reaction-diffusion system (3.67) according to ansatz (4.9). The next step is to choose a suitable control parameter which destabilizes the stationary solution at a certain critical value  $\kappa_c$  to a propagating one and perform the decomposition of the linear operator (4.17). For this purpose the time scale parameters  $\tau$  or  $\theta$  are suitable candidates, since stationary structures  $\bar{u}$  do not depend on them for  $\tau < \tau_c$  and  $\theta < \theta_c$ . Therefore the linear operator  $\mathcal{D}(\bar{u}, \kappa)$  is decomposed into a parameter matrix

$$\mathcal{M}(\tau,\theta) = \begin{pmatrix} 1 & 0 & 0 \\ 0 - \frac{1}{\kappa_3 \tau} & 0 \\ 0 & 0 & -\frac{1}{\kappa_4 \theta} \end{pmatrix}$$
(4.23)

which depends on the time scale parameters but not on the stationary solution  $\bar{u}$ , and a solution-dependent operator

$$\mathcal{L}(\bar{\boldsymbol{u}}, \kappa_{\chi}) = \begin{pmatrix} D_{\boldsymbol{u}}\Delta + \lambda - 3\bar{\boldsymbol{u}}^2 & -\kappa_3 & -\kappa_4 \\ -\kappa_3 & -\kappa_3 D_{\boldsymbol{v}}\Delta + \kappa_3 & 0 \\ -\kappa_4 & 0 & -\kappa_4 D_{\boldsymbol{w}}\Delta + \kappa_4, \end{pmatrix}$$
(4.24)

which does not depend on the time-scale parameters. Now, we are free to choose one of the time-scale parameters as control parameter and for historical reasons decide in favor of  $\tau$  [4.3].

By substituting parameter matrix  $\mathcal{M}(\tau, \theta)$  (4.23) in (4.20) and evaluating the solvability condition (4.16) with respect to (4.10) the bifurcation point  $\tau_{c_{x_i}}$  at which

the Goldstone-Mode  $\mathcal{G}_{x_i}$  is generated by the respective propagator-mode  $\mathcal{P}_{x_i}$  (4.14) is computed to

$$\tau_{c_{xi}} = \frac{\left\langle \left(\frac{\partial}{\partial x_i} \bar{u}\right)^2 \right\rangle - \kappa_4 \theta \left\langle \left(\frac{\partial}{\partial x_i} \bar{w}\right)^2 \right\rangle}{\kappa_3 \left\langle \left(\frac{\partial}{\partial x_i} \bar{v}\right)^2 \right\rangle}.$$
(4.25)

Here  $\langle \cdot \rangle$  comprises integration over the domain. The variable  $x_i$  determines the type of the considered bifurcation. Choosing  $x_i$  from the Cartesian coordinates x or y results in bifurcation points of drift-bifurcations destabilizing the structure with respect to an uniform motion in direction of  $e_x$  or  $e_y$ , respectively. Choosing  $x_i$  to the angle  $\phi$  of a polar coordinate system whose origin is located at the center of the structure results in the bifurcation point of a rotational-bifurcation. In this scenario the structure is destabilized to uniform rotation. Note, that the radial coordinate  $\varrho$  of the polar coordinate system is not considered, because the related Goldstone-mode  $\mathcal{G}_{\varrho}$  refers to internal degrees of freedom [4.31], which are neglected in the following considerations in order to simplify matters. Furthermore, it is most convenient to shift the Cartesian reference frame, such that the longitudinal axis of the structure is parallel to the x-axis (Fig. 4.3c, d).

How does this bifurcation scenario apply to a single stationary soliton  $\bar{u}$  as discussed by Or-Guil et al. [4.3]? Again, we consider a polar coordinate system whose origin is located at the center of the structure and compute the angular derivative  $\frac{\partial}{\partial \phi} \bar{u}$  of the dissipative soliton. Due to its rotational symmetry (Fig. 3.14) the angular derivative vanishes and therefore the Goldstone-mode  $\mathcal{G}_{\phi}$  of rotation does not exist and a rotational bifurcation cannot happen. The rotational symmetry also induces, that all translational propagator-modes  $\{\mathcal{P}_x \cos \phi_0 + \mathcal{P}_y \sin \phi_0 | \phi_0 \in [0, 2\pi]\}$  become unstable at  $\tau = \tau_{c_x} = \tau_{c_y}$  and an arbitrary one can be exited which initiates uniform propagation along  $(e_x \cos \phi_0 + e_y \sin \phi_0)$  for  $\tau > \tau_{c_x}$ .

The situation is completely different, if the stationary structure  $\bar{u}$  is not radially symmetric (Fig. 4.3). These kind of structures exhibit a Goldstone-mode  $\mathcal{G}_{\phi}$  corresponding to the rotational degree of freedom and additional Goldstone-modes referring to propagation along the longitudinal axis  $\mathcal{G}_x$  and the lateral axis  $\mathcal{G}_y$  of the stationary structure (Fig. 4.4). In order to compare the values of these bifurcation points defined by (4.25) the case of a bound state propagating into an arbitrary direction ( $e_x \cos \phi_0 + e_y \sin \phi_0$ ) with  $\phi_0 \in [0, 2\pi]$  should also be considered. The latter scenario implies the excitation of a propagator-mode  $\mathcal{P}_e$  which generates a Goldstone-mode being a linear combination of Goldstone-modes  $\mathcal{G}_x$  and  $\mathcal{G}_y$ . Defining this Goldstone-mode as

$$\mathcal{G}_e = a\mathcal{G}_x + b\mathcal{G}_y \tag{4.26}$$

with  $a, b \in \mathbb{R}$  and inserting this ansatz into solvability condition (4.16) while taking into account that the unsymmetric terms vanish

$$\left\langle \frac{\partial}{\partial x}\bar{u} \middle| \frac{\partial}{\partial y}\bar{u} \right\rangle = \left\langle \frac{\partial}{\partial x}\bar{v} \middle| \frac{\partial}{\partial y}\bar{v} \right\rangle = \left\langle \frac{\partial}{\partial x}\bar{w} \middle| \frac{\partial}{\partial y}\bar{w} \right\rangle = 0, \tag{4.27}$$

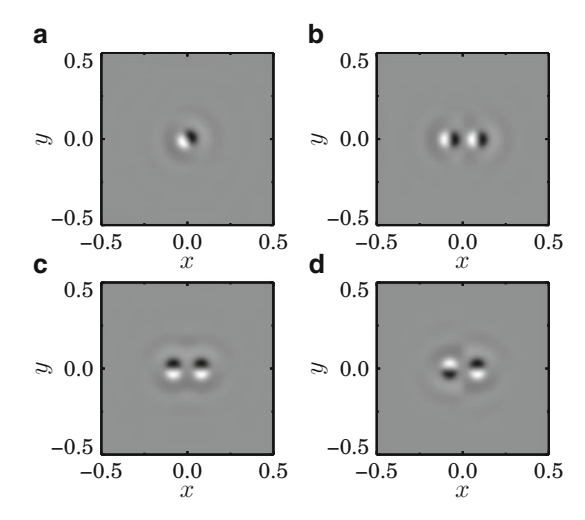


Fig. 4.4 Goldstone-modes (4.10) of a single dissipative soliton and a pair of dissipative solitons being bound in the smallest possible binding distance. The subfigures show gray-scale images of the respective activator distributions  $\frac{\partial}{\partial x_i}\bar{u}$  (4.10). (a) Activator distribution of Goldstone-mode  $(\mathcal{G}_x\cos\phi_0+\mathcal{G}_y\sin\phi_0)$  with  $\phi_0=\frac{\pi}{6}$  computed for a single dissipative soliton. This mode corresponds to a translation into direction  $e=(\frac{\sqrt{3}}{2},\frac{1}{2})$ . Note, that due to the rotational symmetry of the single dissipative soliton additional translational Goldstone-modes exist for  $\phi_0\in[0,2\pi]$ . (b) Activator component  $\frac{\partial}{\partial x}\bar{u}$  of the translational Goldstone-mode  $\mathcal{G}_x$  referring to a translation along the longitudinal axis of the bound state. (c) Activator component  $\frac{\partial}{\partial y}\bar{u}$  of translational Goldstone-mode  $\mathcal{G}_y$  corresponding to a translation along the lateral axis of the bound state and (d) activator distribution  $\frac{\partial}{\partial \phi}\bar{u}$  of the rotational Goldstone-mode  $\mathcal{G}_{\phi}$ . Parameters from (4.22)

the bifurcation point  $\tau_{c_e}$  can be expressed by means of the bifurcation points  $\tau_{c_x}$  and  $\tau_{c_y}$ :

$$\tau_{c_e} = \frac{a^2 \left\langle \left(\frac{\partial}{\partial x} \bar{v}\right)^2 \right\rangle}{a^2 \left\langle \left(\frac{\partial}{\partial x} \bar{v}\right)^2 \right\rangle + b^2 \left\langle \left(\frac{\partial}{\partial y} \bar{v}\right)^2 \right\rangle} \tau_{c_x} + \frac{b^2 \left\langle \left(\frac{\partial}{\partial x} \bar{v}\right)^2 \right\rangle}{a^2 \left\langle \left(\frac{\partial}{\partial x} \bar{v}\right)^2 \right\rangle + b^2 \left\langle \left(\frac{\partial}{\partial y} \bar{v}\right)^2 \right\rangle} \tau_{c_y}. \tag{4.28}$$

If the stationary structure does not exhibit radial symmetry but mirror symmetry, the bifurcation point  $\tau_{c_e}$  is always located in between the bifurcation points  $\tau_{c_x}$  and  $\tau_{c_y}$ . It follows that for  $\tau > \tau_{c_x}$  not only the longitudinal propagator-mode  $\mathcal{P}_x$  but also a continuous band of linear combinations (4.26) of lateral and longitudinal propagator-modes can be excited.

In order to discuss the order of the drift- and rotational-bifurcations on basis of a concrete example, we choose  $D_v = 0$  resulting in  $\bar{u} = \bar{v}$  for a stationary solution u. Furthermore the time-scale parameter  $\theta$  is chosen to  $\theta = 0.8$ , such that

**Table 4.1** Bifurcation points  $\tau_{c_{xi}}$  (4.29) and form factors  $Q_{x_i}$  (4.44) for different configurations of mirror-symmetric bound states of two dissipative solitons. The values of the first two rows refer to the images presented in Fig. 4.3a, b, respectively

	$ au_{\mathrm{c}_x}$	$ au_{\mathrm{c}_y}$	$ au_{\mathrm{c}_\phi}$	$Q_x$	$Q_y$	$Q_{\phi}$
First bound state	3.0359	3.0364	3.0314	1934.7	1942.5	13.88
Second bound state	3.0397	3.0398	3.0393	1988.6	1996.7	47.34
Third bound state	3.0408	3.0409	3.0409	2002.6	2004.2	104.2

Note, that the bifurcation point  $\tau_c$  of a single dissipative soliton is located at  $\tau_c = 3.0399$  for the chosen parameters, which are taken from (4.22) with  $\theta = 0.8$ 

neutral modes are destabilized before non-neutral modes become unstable. Now the bifurcation points  $\tau_{c_{x_i}}$  (4.25) with  $x_i = x, y, \phi$  can be computed by

$$\tau_{c_{xi}} = \frac{1}{\kappa_3} - \theta \frac{\kappa_4}{\kappa_3} \frac{\left\langle (\frac{\partial}{\partial x_i} \bar{w})^2 \right\rangle}{\left\langle (\frac{\partial}{\partial x_i} \bar{u})^2 \right\rangle}.$$
 (4.29)

For two dissipative solitons in the closest possible bound state (Fig. 4.3a) one finds the bifurcation points  $\tau_{c_x} = 3.0359$ ,  $\tau_{c_y} = 3.0364$ , and  $\tau_{c_\phi} = 3.0314$  (Table 4.1). Therefore, by increasing the control parameter  $\tau$  the first propagator-mode becoming unstable is the rotational propagator-mode  $\mathcal{G}_{\phi}$  followed by the longitudinal propagator mode  $\mathcal{G}_x$  and the continuous family of propagator-modes  $\mathcal{G}_e$  (4.28). The hierarchy of bifurcation points is visualized in Fig. 4.5. Here, the value of  $\tau_{c_e}$  is plotted as function of arctan  $\frac{b}{a}$  for the structure presented in Fig. 4.3a. Also shown are the bifurcation points  $\tau_{c_\phi} < \tau_{c_x} < \tau_{c_y}$ , which are represented by horizontal lines, because they do not depend on parameters a and b (4.25). Having in mind, that the propagator-mode with the smallest bifurcation point can most easily be excited, the bound states will most likely start to rotate.

Of course, this also holds for bound states with the second smallest binding distance (Table 4.1). Admittedly for increasing binding distances the values of the bifurcation points  $\tau_{c_x}$ ,  $\tau_{c_y}$ , and  $\tau_{c_{\phi}}$  move closer, until their interaction is negligible and the respective bifurcation points cannot be discriminated from the bifurcation point of a single dissipative soliton at  $\tau_c = 3.0399$ .

From (4.29) it becomes clear, that the bifurcation points of drift- and rotational-bifurcation are identical for  $\theta \to 0$ :

$$\tau_{\rm c} = \tau_{\rm c_x} = \tau_{\rm c_y} = \tau_{\rm c_\phi} = \frac{1}{\kappa_3}.$$
(4.30)

Therefore the bifurcation points discussed by OrGuil et al. [4.3] cannot be discriminated and the dynamics of a bound state at  $\tau > \tau_c$  depends at the same time on the longitudinal-, lateral-, and rotational-propagator-mode as well as on their coupling among each other [4.26, 4.32–4.34]. In case of mirror symmetric bound states this coupling results into an instability of the propagation into the lateral direction.

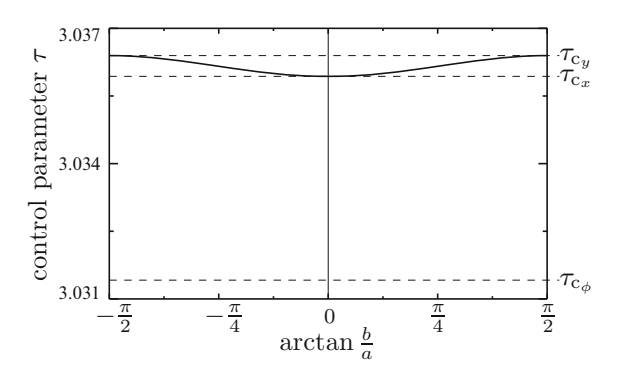


Fig. 4.5 Relation between the bifurcation points of propagation for a bound state of two dissipative solitons. The *solid curve* shows the continuous family of drift-bifurcation points  $\tau_{c_e}$  (4.28) as function of arctan  $\frac{b}{a}$ . The *dashed lines* indicate the bifurcation points  $\tau_{c_{\phi}} < \tau_{c_x} < \tau_{c_y}$ . Parameters from (4.22) with  $\Delta_x = 1.25 \cdot 10^{-3}$ ,  $\left\{ (\frac{\partial}{\partial x} \bar{v})^2 \right\} = 2.236$ ,  $\left\{ (\frac{\partial}{\partial y} \bar{v})^2 \right\} = 2.062$ , and  $\tau_{c_{xi}}$  from Table 4.1

Consequently a bound state moving along its lateral axis will always change to a longitudinal translation or rotation if it is subject to fluctuations.

#### 4.2.5 Translational and Rotational Velocities

In this section we are deriving the translational and rotational velocities  $\bar{c}_{x_i}$  of a self-organized structure (e.g. Fig. 4.3) which propagates uniformly for  $\tau > \tau_{c_{x_i}}$  into direction of  $e_{x_i}$  [4.27]. Therefore, the corresponding vector field u(x,t) is transformed in a coordinate system moving parallel to the  $x_i$ -axis with velocity  $c_{x_i}$ :

$$\mathbf{u}(\mathbf{x},t) = \mathbf{u}(x_i - c_{x_i}t, \mathbf{x}_{\lambda}, t) = \mathbf{u}. \tag{4.31}$$

Here vector  $x_{\lambda}$  comprises all spatial variables exclusive  $x_i$ . Transforming (4.8) to the co-moving frame

$$\frac{\partial}{\partial t} \widetilde{\boldsymbol{u}} = c_{x_i} \frac{\partial}{\partial x_i} \widetilde{\boldsymbol{u}} + \boldsymbol{F}(\widetilde{\boldsymbol{u}}; \boldsymbol{\kappa})$$
(4.32)

and considering stationary solutions  $\hat{\vec{u}}$  of this equation leads to

$$\bar{c}_{x_i} \frac{\partial}{\partial x_i} \hat{\vec{u}} + F(\hat{\vec{u}}; \kappa) = 0. \tag{4.33}$$

Its solutions are structures which propagate uniformly with velocity  $\bar{c}_{x_i}$  into direction  $e_{x_i}$ . Starting from this ansatz the uniform propagation velocity  $\bar{c}_{x_i}$  can

be computed in the vicinity of the bifurcation point  $\kappa_c$  by projecting (4.33) onto the complementary Goldstone-mode (4.20)

$$\hat{\vec{\mathcal{G}}}_{x_i}^{\dagger} = \mathcal{M}^{-1}(\kappa_c) \frac{\partial}{\partial x_i} \hat{\vec{\boldsymbol{u}}}.$$
 (4.34)

Having this very general approach in mind we compute the angular velocity  $\bar{c}_{\phi}$  of a bound state of two dissipative solitons (Fig. 4.3) which rotates uniformly for  $\tau > \tau_{c_{\phi}}$ . For this purpose the respective vector field  $\boldsymbol{u}$  is transformed to a co-rotating polar coordinate system

$$\boldsymbol{u}(\boldsymbol{x},t) = \stackrel{\curvearrowright}{\boldsymbol{u}}(\phi - \bar{c}_{\phi}t, r, t) = \stackrel{\curvearrowright}{\boldsymbol{u}}. \tag{4.35}$$

This ansatz is inserted into the three-component reaction-diffusion system (3.69) and evaluated for the stationary solution  $\vec{u} = (\vec{u}, \vec{v}, \vec{w})^T$ :

$$0 = \bar{c}_{\phi} \frac{\partial}{\partial \phi} \stackrel{\curvearrowright}{u} + D_{u} \Delta \stackrel{\curvearrowright}{u} + \lambda \stackrel{\curvearrowright}{u} - \stackrel{\curvearrowright}{u}^{3} - \kappa_{3} \stackrel{\curvearrowright}{v} - \kappa_{4} \stackrel{\curvearrowright}{w} + \kappa_{1}, \tag{4.36a}$$

$$0 = \bar{c}_{\phi} \frac{\partial}{\partial \phi} \stackrel{\curvearrowright}{\vec{v}} + (D_{v} \Delta \stackrel{\curvearrowright}{\vec{v}} + \stackrel{\curvearrowright}{\vec{u}} - \stackrel{\curvearrowright}{\vec{v}}) / \tau, \tag{4.36b}$$

$$0 = \bar{c}_{\phi} \frac{\partial}{\partial \phi} \stackrel{\curvearrowright}{\vec{w}} + (D_w \Delta \stackrel{\curvearrowright}{\vec{w}} + \stackrel{\curvearrowright}{\vec{u}} - \stackrel{\curvearrowright}{\vec{w}})/\theta.$$
 (4.36c)

Following the described approach, (4.36) is projected onto the respective complementary Goldstone-mode (4.34). By integration of parts all unsymmetric terms vanish such that the angular velocity  $\bar{c}_{\phi}$  is determined by

$$\bar{c}_{\phi}\left(\left\langle \left(\frac{\partial}{\partial \phi} \stackrel{\curvearrowright}{u}\right)^{2}\right\rangle - \tau \kappa_{3} \left\langle \left(\frac{\partial}{\partial \phi} \stackrel{\curvearrowright}{v}\right)^{2}\right\rangle - \theta \kappa_{4} \left(\left(\frac{\partial}{\partial \phi} \stackrel{\curvearrowright}{w}\right)^{2}\right\rangle\right) = 0. \tag{4.37}$$

This equation always has a trivial solution  $\bar{c}_{\phi} = 0$ , which corresponds to the stationary solution  $\bar{u} = \stackrel{\frown}{u}|_{\bar{c}_{\phi}=0}$  of the resting coordinate system. Additionally, it has solutions depending on the time-scale parameters  $\tau$  and  $\theta$ . In order to understand these solutions, we are investigating the case of an inhibitor, which does not diffuse, because in this case the activating component can be expressed in terms of the not diffusing inhibitor. Without loss of generality and in accordance with the foregoing examples (cf. Fig. 4.3) we choose  $D_v = 0$  and derive the following expression for the stationary activator component in the co-rotating frame from (4.36b):

$$\hat{\bar{u}} = \hat{\bar{v}} - \bar{c}_{\phi} \tau \frac{\partial}{\partial \phi} \hat{\bar{v}}. \tag{4.38}$$

Inserting this term into (4.37) and performing some elementary transformations one finds

$$0 = \bar{c}_{\phi} \tau^{2} \left\langle \left( \frac{\partial^{2}}{\partial \phi^{2}} \stackrel{\curvearrowright}{\bar{v}} \right)^{2} \right\rangle \left[ \bar{c}_{\phi}^{2} - \frac{\kappa_{3}}{\tau^{2}} \frac{\left\langle \left( \frac{\partial}{\partial \phi} \stackrel{\curvearrowright}{\bar{v}} \right)^{2} \right\rangle}{\left\langle \left( \frac{\partial^{2}}{\partial \phi^{2}} \stackrel{\curvearrowright}{\bar{v}} \right)^{2} \right\rangle} \left( \tau - \frac{1}{\kappa_{3}} - \theta \frac{\kappa_{4}}{\kappa_{3}} \frac{\left\langle \left( \frac{\partial}{\partial \phi} \stackrel{\curvearrowright}{\bar{w}} \right)^{2} \right\rangle}{\left\langle \left( \frac{\partial}{\partial \phi} \stackrel{\curvearrowright}{\bar{v}} \right)^{2} \right\rangle} \right) \right], (4.39)$$

which obviously has a quadratic term giving two non-trivial solutions of  $\bar{c}_{\phi}$ . These are the angular velocities of clockwise and counterclockwise rotation. Because the stationary solution  $\vec{u}$  of the co-rotating frame are generally not known, we evaluate (4.39) in the vicinity of the rotational bifurcation  $\tau \approx \tau_{c_{\phi}}$  (4.25) for which only stationary structures with  $c_{\phi} = 0$  or slowly rotating structures with  $|\bar{c}_{\phi}| \ll 1$  exist. Therefore, we assume  $\vec{u} \approx \vec{v}$  from (4.38) and estimate the stationary solution  $\vec{u}$  of the slowly co-rotating frame by the stationary solutions  $\vec{u}$  of the resting coordinate system:  $\vec{u} \approx \vec{v}$ . Consequently (4.39) simplifies to

$$0 = \bar{c}_{\phi} \tau_{c_{\phi}}^{2} \left( \left( \frac{\partial^{2}}{\partial \phi^{2}} \bar{u} \right)^{2} \right) \left[ \bar{c}_{\phi}^{2} - \frac{\kappa_{3}}{\tau_{c_{\phi}}^{2} Q_{\phi}} (\tau - \tau_{c_{\phi}}) \right]. \tag{4.40}$$

Here variable  $Q_{\phi}$  denotes a so-called form factor

$$Q_{\phi} = \frac{\left\langle \left(\frac{\partial^2}{\partial \phi^2} \bar{u}\right)^2 \right\rangle}{\left\langle \left(\frac{\partial}{\partial \phi} \bar{u}\right)^2 \right\rangle},\tag{4.41}$$

which is computed from the stationary activator distribution  $\bar{u}$ . Example form factors for the bound states shown in Fig. 4.3 are listed in Table 4.1. According to (4.40) two new real solutions bifurcate at  $\tau = \tau_{c_{\phi}}$  from the trivial solution branch  $\bar{c}_{\phi} = 0$ , such that the considered bound state is either stationary or rotates for  $\tau > \tau_{c_{\phi}}$  clockwise or counterclockwise with angular velocity

$$\bar{c}_{\phi}(\tau) = \pm \sqrt{\frac{\kappa_3}{\tau_{c_{\phi}}^2 Q_{\phi}} (\tau - \tau_{c_{\phi}})}.$$
(4.42)

Having the stability considerations of Sect. 3.1.1 in mind we conclude, that the stationary state  $c_{\phi} = 0$  is stable for  $\tau < \tau_{c_{\phi}}$  and becomes unstable at the bifurcation point  $\tau = \tau_{c_{\phi}}$  at which the stable solutions (4.42) branch off.

According to the described ansatz the translational velocities are computed to

$$\bar{c}_{x_i}(\tau) = \pm \sqrt{\frac{\kappa_3}{\tau_{c_{x_i}}^2 Q_{x_i}} (\tau - \tau_{c_{x_i}})}$$
(4.43)

where  $x_i = x$  denotes longitudinal propagation of the bound state and  $x_i = y$  lateral propagation. Corresponding to (4.41) the respective form factor  $Q_{x_i}$  is given as

$$Q_{x_i} = \frac{\left\langle \left(\frac{\partial^2}{\partial x_i^2} \bar{u}\right)^2 \right\rangle}{\left\langle \left(\frac{\partial}{\partial x_i} \bar{u}\right)^2 \right\rangle}.$$
 (4.44)

The qualitative change of the discussed system is characterized by the fact that the stationary solution is rendered unstable while additional dynamic solutions become relevant. This qualitative change of topology is classified as drift-pitchfork-bifurcation [4.35]. However, in the following section this bifurcation is abbreviated as drift- or rotational-bifurcation (cf. [4.27,4.36]).

Of course (4.43) is also valid for a single dissipative soliton. In this case the form factor  $Q = Q_x = Q_y$  (4.44) can either be evaluated with respect to an arbitrary Cartesian coordinate or the radial coordinate of a polar coordinate system

$$Q = \frac{3}{4} \frac{\int_0^\infty \left( r(\frac{\partial^2}{\partial r^2} \bar{u})^2 + \frac{1}{r} (\frac{\partial}{\partial r} \bar{u})^2 \right) dr}{\int_0^\infty r(\frac{\partial}{\partial r} \bar{u})^2 dr} , \qquad (4.45)$$

which takes the radial symmetry into account.

Simulations of the three-component reaction-diffusion system (3.69) verify the theoretical prediction, that a stationary bound state will be destabilized by noise to a uniformly rotating one, if time scale parameter  $\tau$  is chosen larger than  $\tau_{c_{\phi}}$ . Furthermore the simulations of a bound state consisting of two dissipative solitons confirm, that the angular velocity  $\bar{c}_{\phi}$  in the vicinity of the bifurcation point  $\tau_{c_{\phi}}$  increases with the square root of the distance  $(\tau - \tau_{c_{\phi}})$  of control parameter  $\tau$  from the bifurcation point (Fig. 4.6). The same holds for the longitudinal velocity  $\tau_{c_x}$  of the bound state. In accordance with the foregoing considerations (Fig. 4.5) the translation becomes possible for significantly larger values of the control parameter  $\tau > \tau_{c_x} > \tau_{c_{\phi}}$ . Although the translation into the lateral direction of the bound state is also possible for  $\tau > \tau_{c_y}$  (cf. Table 4.1) the related velocities are not shown in Fig. 4.6 due to the inherent instability of this propagation mode [4.26, 4.32, 4.33], such that the equilibrium velocity of the lateral motion cannot be determined from simulations with adequate accuracy.

Note, that in addition to the discussed destabilization scenario which is characterized by an unchanged shape of the considered structure also a bifurcation due to a change of shape can occur. Concerning one-dimensional systems this kind of bifurcation has been shown e.g. by Osipov [4.37] on basis of the FitzHugh-Nagumo-model [4.38,4.39], and by Hempel et al. [4.40] on basis of the Rinzel-Keller-model. For the three-component reaction-diffusion system this kind of drift-bifurcation will occur, if the change of a control parameter leads to change of shape of the considered structure and therefore by means of the respective form factor to a change of the bifurcation point (4.29) [4.41, 4.42]. For three-component reaction-diffusion systems with modified coupling terms a change of chape can induce a rotational motion even for a single dissipative soliton, if a  $\mu = 2$  mode (Fig. 3.18c) is destabilized [4.34].

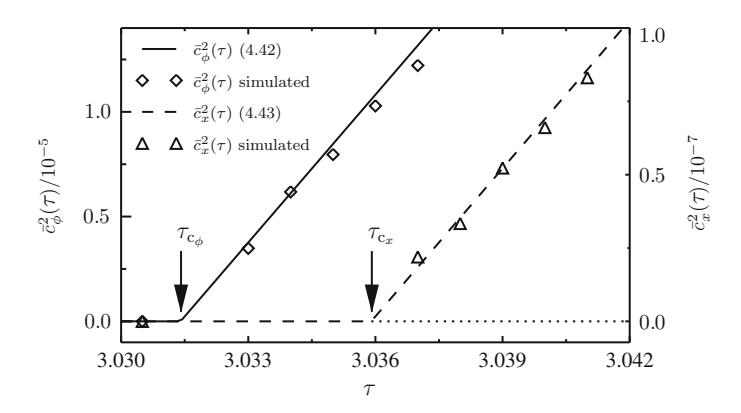


Fig. 4.6 Rotational- and drift-bifurcation of a dissipative soliton molecule in first bound state (Fig. 4.3a). Both the theoretically deduced velocities (*lines*) and the velocities obtained from simulations of the field equations (*symbols*) are squared and plotted as function of the control parameter  $\tau$ . The bound state is stationary for  $\tau \leq \tau_{c_{\phi}}$  and is able to rotate for  $\tau > \tau_{c_{\phi}}$ , while the stationary state is unstable. For  $\tau > \tau_{c_x}$  also longitudinal translation is possible. The propagation velocities increase with the square of the distance between control parameter  $\tau$  and the respective bifurcation point. Parameters from (4.22) with  $\theta = 0.8$  (Figure reproduced from [4.27])

Despite of the prediction of the drift- and rotational-velocities of dissipative solitons' bound states the presented investigations clarify, that individual dissipative solitons can have quite different properties than their bound states. For example for  $\theta=0.8$  and  $\tau_{c_x}<\tau<\tau_c$  a bound state of dissipative solitons can exhibit uniform rotation or translation (Table 4.1) while separated dissipative solitons are stationary. This effect resembles a kind of synergetic dynamics which e.g. have been observed in a.c.-driven gas-discharge systems with high ohmic barrier [4.43]. Bode interpreted this phenomenon as pair effect [4.44, S. 46ff].

# **4.3** Equations of Motion

In order to describe the dynamics of dissipative solitons by equations of motions we are considering a three-component reaction-diffusion system in the limit  $\theta \to 0$  (3.66) on a one-dimensional domain:

$$\frac{\partial}{\partial t}u(x,t) = D_u \frac{\partial^2}{\partial x^2}u(x,t) + f(u(x,t)) - \kappa_3 v(x,t) + \kappa_1 
- \kappa_4 \int_{\Omega} g(x-\chi)u(\chi,t) d\chi,$$
(4.46a)

$$\tau_{\frac{\partial}{\partial t}}v(x,t) = D_v \frac{\partial^2}{\partial x^2}v(x,t) + u(x,t) - v(x,t), \tag{4.46b}$$

$$f(u(x,t)) = \lambda u(x,t) - u(x,t)^{3}$$
(4.46c)

with  $g(x - \chi)$  denoting Green's function. Assuming, that for a certain set of parameters a stationary solution  $\bar{u}$  exists, its equations of motion are derived in four steps:

- 1. Transformation to homogeneous state  $u_0 = 0$ ,
- 2. Specify complementary modes,
- 3. Perturbation ansatz,
- 4. Projection onto complementary modes,
- 5. Reduced dynamics.

## 4.3.1 Transformation to Homogeneous State $u_0 = 0$

In order to account for infinite domains the considered reaction-diffusion system is transformed to a system with homogeneous state  $u_0 = 0$  by introducing

$$\mathbf{u}_{n}(x,t) = \mathbf{u}(x,t) - \mathbf{u}_{0} \text{ with } \mathbf{u}_{n}(x,t) = (u_{n}(x,t), v_{n}(x,t))^{T}.$$
 (4.47)

Inserting  $u(x) = u_n(x) + u_0$  into the cubic nonlinearity f(u) (4.46c) leads to the following expression:

$$f(u_n(x) + u_0) = f(u_0) + f'(u_0)u_n(x) - 3u_0u_n(x)^2 - u_n(x)^3.$$
(4.48)

Therefore (4.46) can be rewritten to

$$\frac{\partial}{\partial t}u_{\rm n}(x,t) = D_u \frac{\partial^2}{\partial x^2}u_{\rm n}(x,t) + f'(u_0)u_{\rm n}(x,t) + N\left(u_{\rm n}(x,t)\right) - \kappa_3 v_{\rm n}(x,t) 
- \kappa_4 \int_{\Omega} g(x-\chi)u_{\rm n}(\chi,t)\mathrm{d}\chi,$$
(4.49a)

$$\tau \frac{\partial}{\partial t} v_{\mathbf{n}}(x,t) = D_{v} \frac{\partial^{2}}{\partial x^{2}} v_{\mathbf{n}}(x,t) + u_{\mathbf{n}}(x,t) - v_{\mathbf{n}}(x,t), \tag{4.49b}$$

$$N(u_{n}(x,t)) = -3u_{0}u_{n}(x,t)^{2} - u_{n}(x,t)^{3}.$$
(4.49c)

Note, that the offset parameter  $\kappa_1$  has not been diminished, but still influences the system via the homogeneous state  $u_0 = u_0(\kappa_1)$  (3.15).

Introducing the linear operator  $\mathcal{L}$  with

$$\mathcal{L}u(x,t) = D_u \frac{\partial^2}{\partial x^2} u(x,t) + f'(u_0(\kappa_1))u(x,t) - \kappa_4 \int_{\Omega} g(x-\chi)u(\chi,t) d\chi \quad (4.50)$$

where  $g(\cdot)$  denotes Green's function (3.33). Renaming  $u_n(x,t)$  to u = u(x,t) leads to the following one-dimensional reaction-diffusion system

$$\frac{\partial}{\partial t}u = \mathcal{L}u - \kappa_3 v + N(u),\tag{4.51}$$

$$\tau \frac{\partial}{\partial t} v = u - v. \tag{4.52}$$

with homogeneous ground state  $u_0 = 0$ .

## 4.3.2 Specify Complementary Modes

Concerning a stationary state  $\bar{u} = (\bar{u}, \bar{v})$  the system can be linearized to

$$\frac{\partial}{\partial t}\bar{u} = \mathcal{D}(\bar{u};\tau)\bar{u} = 0 \tag{4.53}$$

with linear operator

$$\mathcal{D}(\bar{\boldsymbol{u}};\tau) = \mathcal{M}(\tau) \begin{pmatrix} \mathcal{L} + N'(\bar{\boldsymbol{u}}) & -\kappa_3 \\ -\kappa_3 & +\kappa_3 \end{pmatrix}$$
(4.54)

and parameter matrix

$$\mathcal{M}(\tau) = \begin{pmatrix} 1 & 0 \\ 0 & -\frac{1}{\tau \kappa_3} \end{pmatrix}. \tag{4.55}$$

At the drift-bifurcation point  $\tau_c$  (4.25) the Goldstone-mode

$$\mathcal{G}_{x}(x) = \begin{pmatrix} \frac{\partial}{\partial x} \bar{u}(x) \\ \frac{\partial}{\partial x} \bar{u}(x) \end{pmatrix} \tag{4.56}$$

of  $\mathcal{D}(\bar{\pmb{u}};\tau)$  is accomplished by propagator-mode

$$\mathcal{P}_{x}(x) = \begin{pmatrix} 0\\ -\frac{1}{\kappa_{3}} \frac{\partial}{\partial x} \bar{u}(x) \end{pmatrix} \tag{4.57}$$

[4.10,4.45]. From this equation follows that the propagator mode  $\mathcal{P}_x(x)$  can be interpreted as displacement of the inhibitor distribution against the localized activator distribution. This displacement is negative, such that an excitation of propagator-mode  $\mathcal{P}_x(x)$  with positive amplitude leads to a structure propagating with positive velocity. Therefore the activator distribution of a propagating dissipative soliton is always located ahead of the inhibitor distribution.

Concerning the adjoined operator  $\mathcal{D}^{\dagger}(\bar{u};\tau)$  the complementary Goldstone-mode deduces from solvability condition (4.16) respectively (4.20) to

$$\mathcal{G}_{x}^{\dagger}(x) = \begin{pmatrix} \frac{\partial}{\partial x}\bar{u}(x) \\ -\frac{\partial}{\partial x}\bar{u}(x) \end{pmatrix} \tag{4.58}$$

and the complementary propagator mode is chosen to

$$\mathcal{P}_{x}^{\dagger}(x) = \begin{pmatrix} \frac{1}{\kappa_{3}} \frac{\partial}{\partial x} \bar{u}(x) \\ 0 \end{pmatrix}. \tag{4.59}$$

With these critical modes at hand we can start to deduce the dynamics of dissipative solitons.

#### 4.3.3 Perturbation Ansatz.

Recalling the ansatz of Sect. 4.2.5 concerning the computation of equilibrium velocities close to the vicinity of the drift-bifurcation, we are starting with a stationary dissipative soliton  $\bar{u}$  in a co-moving frame. Additionally, we account for perturbations on three different time scales  $T_1$ ,  $T_2$  and  $T_3$ :

$$u(x,t) = \bar{u}(x - p(T_1, T_2, T_3)) - \epsilon \kappa_3 \alpha(T_1, T_2) \mathcal{P}_x (x - p(T_1, T_2, T_3)) + \epsilon^2 r(x, T_1) + \epsilon^3 R(x)$$
(4.60)

with time scales

$$T_i = \epsilon^i t, \tag{4.61}$$

propagator mode  $\mathcal{P}_x(x)$  (4.57) and propagator mode amplitude  $\alpha(T_1, T_2)$ . Note, that the factor  $\kappa_3$  has been introduced for historical reasons in order to match the perturbation ansatz presented in [4.45]. In (4.60) corrections of order  $\mathcal{O}^2$  are denoted  $r(x, T_1)$  and R(x).

Inserting the definition of propagator mode  $\mathcal{P}_x(x)$  (4.57) leads to the following ansatz

$$u(x,t) = \bar{u}(x - p(T_1, T_2, T_3)) + \epsilon^2 r_u(x, T_1) + \epsilon^3 R_u(x), \tag{4.62}$$

$$v(x,t) = \bar{u}(x - p(T_1, T_2, T_3)) + \epsilon \alpha(T_1, T_2) \frac{\partial}{\partial x} \bar{u}(x - p(T_1, T_2, T_3)) + \epsilon^2 r_v(x, T_1) + \epsilon^3 R_v(x).$$
(4.63)

Introducing a critical parameter  $\hat{\tau}$  by

$$\epsilon^2 \hat{\tau} = \tau - \tau_c \tag{4.64}$$

and inserting (4.62) and (4.64) into (4.50) while expanding the nonlinearity N(u) (4.49c) up to  $O(\epsilon^3)$  leads to the following equations

$$-\frac{\partial}{\partial x}\bar{u}\left\{\epsilon\frac{\partial}{\partial T_{1}}p + \epsilon^{2}\frac{\partial}{\partial T_{2}}p + \epsilon^{3}\frac{\partial}{\partial T_{3}}p\right\} + \epsilon^{3}\frac{\partial}{\partial T_{1}}r_{u}$$

$$= \mathcal{L}\bar{u} + N(\bar{u}) - \kappa_{3}\bar{u} - \epsilon\kappa_{3}\alpha\frac{\partial}{\partial x}\bar{u}$$

$$+ \epsilon^{2}\mathcal{L}r_{u} + \epsilon^{2}N'(\bar{u})r_{u} - \epsilon^{2}\kappa_{3}r_{v}$$

$$+ \epsilon^{3}\mathcal{L}R_{u} + \epsilon^{3}N'(\bar{u})R_{u} - \epsilon^{3}\kappa_{3}R_{v}, \qquad (4.65)$$

$$(\epsilon^{2}\hat{\tau} + \tau_{c}) \left[ -\frac{\partial}{\partial x} \bar{u} \left\{ \epsilon \frac{\partial}{\partial T_{1}} p + \epsilon^{2} \frac{\partial}{\partial T_{2}} p + \epsilon^{3} \frac{\partial}{\partial T_{3}} p - \epsilon^{2} \frac{\partial}{\partial T_{1}} \alpha - \epsilon^{3} \frac{\partial}{\partial T_{2}} \alpha \right\} \right.$$

$$\left. - \frac{\partial^{2}}{\partial x^{2}} \bar{u} \left\{ \epsilon^{2} \alpha \frac{\partial}{\partial T_{1}} p + \epsilon^{3} \alpha \frac{\partial}{\partial T_{2}} p + \epsilon^{4} \alpha \frac{\partial}{\partial T_{3}} p \right\} + \epsilon^{3} \frac{\partial}{\partial T_{1}} r_{v} \right]$$

$$= \bar{u} + \epsilon^{2} r_{u} + \epsilon^{3} R_{u} - \bar{u} - \epsilon \alpha \frac{\partial}{\partial x} \bar{u} - \epsilon^{2} r_{v} - \epsilon^{3} R_{v}. \tag{4.66}$$

For reasons of simplicity the arguments of  $\bar{u}$ , p,  $\alpha$ ,  $r_u$ ,  $r_v$ ,  $R_u$ , and  $R_v$  have been omitted. Because these equations have to be fulfilled for all time-scales simultaneously, we are sorting them by orders of  $\epsilon$ :

O(1):

$$\mathbf{0} = \begin{pmatrix} \mathcal{L}\bar{u} + N(\bar{u}) - \kappa_3 \bar{u} \\ 0 \end{pmatrix},\tag{4.67a}$$

 $O(\epsilon)$ :

$$\begin{pmatrix} \frac{\partial}{\partial T_1} p \\ -\tau_c \frac{\partial}{\partial T_1} p \end{pmatrix} \frac{\partial}{\partial x} \bar{u} = \begin{pmatrix} \kappa_3 \alpha \\ -\alpha \end{pmatrix} \frac{\partial}{\partial x} \bar{u}, \tag{4.67b}$$

 $O(\epsilon^2)$ :

$$-\left(\frac{\frac{\partial}{\partial T_2}p}{\frac{\partial}{\partial T_2}p} + \frac{\partial}{\partial T_1}\alpha\right) \frac{\partial}{\partial x}\bar{u} - \left(\frac{0}{\alpha\frac{\partial}{\partial T_1}p}\right) \frac{\partial^2}{\partial x^2}\bar{u}$$

$$= \begin{pmatrix} \mathcal{L} + N'(\bar{u}) & -\kappa_3 \\ \frac{1}{\tau_c} & -\frac{1}{\tau_c} \end{pmatrix} \begin{pmatrix} r_u \\ r_v \end{pmatrix} = \mathcal{D}\begin{pmatrix} r_u \\ r_v \end{pmatrix}, \tag{4.67c}$$

 $O(\epsilon^3)$ :

$$\begin{pmatrix}
-\frac{\partial}{\partial T_{3}}p \\
-\frac{\hat{\tau}}{\tau_{c}}\frac{\partial}{\partial T_{1}}p - \frac{\partial}{\partial T_{3}}p + \frac{\partial}{\partial T_{2}}\alpha
\end{pmatrix} \frac{\partial}{\partial x}\bar{u} - \begin{pmatrix} 0 \\ \alpha \frac{\partial}{\partial T_{2}}p \end{pmatrix} \frac{\partial^{2}}{\partial x^{2}}\bar{u} + \begin{pmatrix} \frac{\partial}{\partial T_{1}}r_{u} \\ \frac{\partial}{\partial T_{1}}r_{v} \end{pmatrix}$$

$$= \begin{pmatrix} \mathcal{L} + N'(\bar{u}) & -\kappa_{3} \\ \frac{1}{\tau_{c}} & -\frac{1}{\tau_{c}} \end{pmatrix} \begin{pmatrix} R_{u} \\ R_{v} \end{pmatrix} = \mathcal{D} \begin{pmatrix} R_{u} \\ R_{v} \end{pmatrix} \tag{4.67d}$$

with  $\mathcal{D}$  denoting the linear operator (4.54) at the bifurcation point.

# 4.3.4 Projection onto Complementary Modes

While O(1) (4.67a) represents the stationary system and is obviously fulfilled, Eqs. (4.67b)–(4.67d) are evaluated by projecting them onto the complementary Goldstone-mode  $\mathcal{G}_x^{\dagger}$  (4.58) and complementary propagator mode  $\mathcal{P}_x^{\dagger}$  (4.59).

Projection of  $O(\epsilon)$  (4.67b) onto  $\mathcal{P}_x^{\dagger}$ :

$$\left\langle \mathcal{P}_{x}^{\dagger} \left| \begin{pmatrix} \frac{\partial}{\partial T_{1}} p & \frac{\partial}{\partial x} \bar{u} \\ -\tau_{c} \frac{\partial}{\partial T_{1}} p & \frac{\partial}{\partial x} \bar{u} \end{pmatrix} \right\rangle - \left\langle \mathcal{P}_{x}^{\dagger} \left| \begin{pmatrix} \kappa_{3} \alpha & \frac{\partial}{\partial x} \bar{u} \\ -\alpha & \frac{\partial}{\partial x} \bar{u} \end{pmatrix} \right\rangle \right\rangle = 0$$

$$\Rightarrow \left\langle \left( \frac{\partial}{\partial x} \bar{u} \right)^{2} \right\rangle \left( \frac{\partial}{\partial T_{1}} p - \kappa_{3} \alpha \right) = 0$$

$$\Rightarrow \frac{\partial}{\partial T_{1}} p = \kappa_{3} \alpha. \tag{4.68}$$

Projection of  $O(\epsilon)$  (4.67b) onto  $\mathcal{G}_x^{\dagger}$  (4.58):

$$\left\langle \mathcal{G}_{x}^{\dagger} \middle| \left( -\frac{\partial}{\partial T_{1}} p \frac{\partial}{\partial x} \bar{u} \right) \right\rangle - \left\langle \mathcal{G}_{x}^{\dagger} \middle| \left( \kappa_{3} \alpha \frac{\partial}{\partial x} \bar{u} \right) \right\rangle = 0$$

$$\Rightarrow \left\langle \left( \frac{\partial}{\partial x} \bar{u} \right)^{2} \right\rangle \left( \frac{\partial}{\partial T_{1}} p + \tau_{c} \frac{\partial}{\partial T_{1}} p \right) - \left\langle \left( \frac{\partial}{\partial x} \bar{u} \right)^{2} \right\rangle (\kappa_{3} \alpha + \alpha) = 0$$

$$\Rightarrow \frac{\partial}{\partial T_{1}} p = \frac{1 + \kappa_{3}}{1 + \tau_{c}} \alpha \tag{4.69}$$

Comparing this equation with (4.68) determines the bifurcation point

$$\tau_{\rm c} = \frac{1}{\kappa_3},\tag{4.70}$$

because (4.69) basically evaluates the solvability condition (4.16). Projection of  $O(\epsilon^2)$  (4.67c) onto  $\mathcal{P}_x^{\dagger}$  (4.59):

$$\left\langle \mathcal{P}_{x}^{\dagger} \middle| \left( -\frac{\partial}{\partial T_{2}} p \frac{\partial}{\partial x} \bar{u} \right) - \frac{\partial}{\partial T_{2}} p \frac{\partial}{\partial x} \bar{u} - \frac{\partial}{\partial T_{1}} \alpha \frac{\partial}{\partial x} \bar{u} - \alpha \frac{\partial}{\partial T_{1}} p \frac{\partial^{2}}{\partial x^{2}} \bar{u} \right) \right\rangle = \left\langle \mathcal{P}_{x}^{\dagger} \middle| \mathcal{D} \begin{pmatrix} r_{u} \\ r_{v} \end{pmatrix} \right\rangle$$

$$\Rightarrow -\frac{1}{\kappa_{3}} \left\langle \left( \frac{\partial}{\partial x} \bar{u} \right)^{2} \right\rangle \frac{\partial}{\partial T_{2}} p = \left\langle \mathcal{D}^{\dagger} \mathcal{P}_{x}^{\dagger} \middle| \begin{pmatrix} r_{u} \\ r_{v} \end{pmatrix} \right\rangle$$

$$\stackrel{(4.21)}{\Rightarrow} -\frac{1}{\kappa_{3}} \left\langle \left( \frac{\partial}{\partial x} \bar{u} \right)^{2} \right\rangle \frac{\partial}{\partial T_{2}} p = \left\langle \mathcal{G}_{x}^{\dagger} \middle| \begin{pmatrix} r_{u} \\ r_{v} \end{pmatrix} \right\rangle. \tag{4.71}$$

The right hand side equals to zero because of Fredholm's alternative such that

$$\frac{\partial}{\partial T_2} p = 0. (4.72)$$

Projection of  $O(\epsilon^2)$  (4.67c) onto  $\mathcal{G}_x^{\dagger}$  (4.58):

$$\left\langle \mathcal{G}_{x}^{\dagger} \left| \begin{pmatrix} -\frac{\partial}{\partial T_{2}} p & \frac{\partial}{\partial x} \bar{u} \\ -\frac{\partial}{\partial T_{2}} p & \frac{\partial}{\partial x} \bar{u} - \frac{\partial}{\partial T_{1}} \alpha & \frac{\partial}{\partial x} \bar{u} - \alpha \frac{\partial}{\partial T_{1}} p & \frac{\partial^{2}}{\partial x^{2}} \bar{u} \end{pmatrix} \right\rangle = \left\langle \mathcal{G}_{x}^{\dagger} \left| \mathcal{D} \begin{pmatrix} r_{u} \\ r_{v} \end{pmatrix} \right\rangle \right.$$

$$\stackrel{(4.68)}{\Rightarrow} \left\langle \left( \frac{\partial}{\partial x} \bar{u} \right)^{2} \right\rangle \frac{\partial}{\partial T_{1}} \alpha + \kappa_{3} \alpha^{2} \left\langle \frac{\partial}{\partial x} \bar{u} \frac{\partial^{2}}{\partial x^{2}} \bar{u} \right\rangle = -\left\langle \mathcal{D}^{\dagger} \mathcal{G}_{x}^{\dagger} \left| \begin{pmatrix} r_{u} \\ r_{v} \end{pmatrix} \right\rangle \right.$$

$$\stackrel{(4.15)}{\Rightarrow} \left\langle \left( \frac{\partial}{\partial x} \bar{u} \right)^{2} \right\rangle \frac{\partial}{\partial T_{1}} \alpha + \kappa_{3} \alpha^{2} \left\langle \frac{\partial}{\partial x} \bar{u} \frac{\partial^{2}}{\partial x^{2}} \bar{u} \right\rangle = 0. \tag{4.73}$$

Because the term  $\left(\frac{\partial}{\partial x}\bar{u}\frac{\partial^2}{\partial x^2}\bar{u}\right)$  equals to zero, Eq. (4.73) results into

$$\frac{\partial}{\partial T_1}\alpha = 0. \tag{4.74}$$

The equations of third order (4.67d) do no need to be projected onto  $\mathcal{P}_x^{\dagger}$  (4.59) in order to calculate  $\frac{\partial}{\partial T_3} p$ , because the resulting term can be neglected as highest order, when all terms are consolidated up to  $O(\epsilon^2)$ .

Projection of  $O(\epsilon^3)$  (4.67d) onto  $\mathcal{G}_x^{\dagger}$  (4.58) while taking (4.68), (4.70), and (4.72) into account:

$$\left\langle \mathcal{G}_{x}^{\dagger} \middle| \left( -\frac{\partial}{\partial T_{3}} p \frac{\partial}{\partial x} \bar{u} - \frac{\partial}{\partial T_{2}} p \frac{\partial}{\partial x} \bar{u} - \frac{\partial}{\partial T_{3}} p \frac{\partial}{\partial x} \bar{u} - \frac{\partial}{\partial T_{3}} p \frac{\partial}{\partial x} \bar{u} - \frac{\partial}{\partial T_{2}} \alpha \frac{\partial}{\partial x} \bar{u} - \alpha \frac{\partial}{\partial T_{2}} p \frac{\partial^{2}}{\partial x^{2}} \bar{u} \right) \right\rangle \\
+ \left\langle \mathcal{G}_{x}^{\dagger} \middle| \left( \frac{\partial}{\partial T_{1}} r_{u} \right) \right\rangle = \left\langle \mathcal{G}_{x}^{\dagger} \middle| \mathcal{D} \left( \frac{R_{u}}{R_{v}} \right) \right\rangle = \left\langle \mathcal{D}^{\dagger} \mathcal{G}_{x}^{\dagger} \middle| \left( \frac{R_{u}}{R_{v}} \right) \right\rangle \stackrel{(4.15)}{=} 0 \\
\Rightarrow \left\langle \left( \frac{\partial}{\partial x} \bar{u} \right)^{2} \right\rangle \left( \hat{\tau} \kappa_{3}^{2} \alpha - \frac{\partial}{\partial T_{2}} \alpha \right) + \left\langle \frac{\partial}{\partial x} \bar{u} \left( \frac{\partial}{\partial T_{1}} r_{u} - \frac{\partial}{\partial T_{1}} r_{v} \right) \right\rangle = 0 \tag{4.75}$$

From (4.67c) it is known that

$$-\frac{\partial}{\partial T_2} p \frac{\partial}{\partial x} \bar{u} - \frac{\partial}{\partial T_1} \alpha \frac{\partial}{\partial x} \bar{u} - \alpha \frac{\partial}{\partial T_1} p \frac{\partial^2}{\partial x^2} \bar{u} = \frac{r_u}{\tau_c} - \frac{r_v}{\tau_c}.$$
 (4.76)

Taking the results from the previous calculations (4.68), (4.70), (4.72), and (4.74) into account and solving for  $r_v$  leads to

$$r_v = r_u - \alpha^2 \frac{\partial^2}{\partial x^2} \bar{u},\tag{4.77}$$

from which the  $T_1$ -derivative is calculated:

$$\frac{\partial}{\partial T_1} r_v = \frac{\partial}{\partial T_1} r_u - \kappa_3 \alpha^3 \frac{\partial^3}{\partial x^3} \bar{u}. \tag{4.78}$$

By substituting this equation into (4.75) and carrying out the partial integration the dynamics of  $\alpha$  on time scale  $T_2$  are derived:

$$\frac{\partial}{\partial T_2} \alpha = \hat{\tau} \kappa_3^2 \alpha - \kappa_3 \alpha^3 \frac{\left( (\frac{\partial^2}{\partial x^2} \bar{u})^2 \right)}{\left( (\frac{\partial}{\partial x} \bar{u})^2 \right)} = \hat{\tau} \kappa_3^2 \alpha - \kappa_3 Q_x \alpha^3 \tag{4.79}$$

with  $Q_x$  being the form factor defined in (4.44).

## 4.3.5 Reduced Dynamics

After evaluating (4.67) by the projection technique the relevant terms from first (4.68) and third order (4.79) are collected:

$$\epsilon \frac{\partial}{\partial T_1} p = \epsilon \kappa_3 \alpha, \tag{4.80a}$$

$$\epsilon^3 \frac{\partial}{\partial T_2} \alpha = \epsilon^3 \hat{\tau} \kappa_3^2 \alpha - \epsilon^3 \kappa_3 Q_x \alpha^3. \tag{4.80b}$$

Returning to the original time scale and substituting the definition of the critical parameter  $\hat{\tau}$  (4.64), while taking the bifurcation point  $\tau_c$  (4.70) into account leads to the following dynamics:

$$\dot{p} = \epsilon \kappa_3 \alpha, \tag{4.81a}$$

$$\epsilon \dot{\alpha} = \epsilon \kappa_3^2 \left( \tau - \frac{1}{\kappa_3} \right) \alpha - \epsilon^3 \kappa_3 Q_x \alpha^3. \tag{4.81b}$$

The final step consists of substituting  $\epsilon \alpha$  by  $\alpha$  in order to derive the reduced dynamics of a one-dimensional dissipative soliton, which is

$$\dot{p} = \kappa_3 \alpha, \tag{4.82a}$$

$$\dot{\alpha} = \kappa_3^2 \left( \tau - \frac{1}{\kappa_3} \right) \alpha - \kappa_3 Q_x \alpha^3. \tag{4.82b}$$

Of course this calculation can be carried out for dissipative solitons on *n*-dimensional domains by which the general form of the reduced dynamics is derived

$$\ddot{\boldsymbol{p}} = \kappa_3^2 \left( \tau - \frac{1}{\kappa_3} \right) \dot{\boldsymbol{p}} - \frac{Q}{\kappa_3} \dot{\boldsymbol{p}}^2 \dot{\boldsymbol{p}}. \tag{4.83}$$

These ordinary differential equation describes the dynamics of a particle with unity mass and velocity dependent friction. The equation also reflects the drift-bifurcation scenario for the limit  $\theta \to 0$  (Sect. 4.2), which describes the qualitative change of dynamics from damped to uniform motion due to a change of sign in term  $(\tau - \frac{1}{\kappa_3})$ . Therefore the stationary state  $\dot{p} = 0$  is unstable for  $\tau > 1/\kappa_3$  and the uniform motion with intrinsic velocity  $\dot{p} = \bar{c}_x$  (4.43) is the preferred state. Therefore, an arbitrary excitation  $\alpha_0 = \frac{1}{\kappa_3} \dot{p}(0)$  of the propagator mode will decay to the respective equilibrium value

$$\bar{\alpha} = \frac{1}{\kappa_3} \bar{c}_x \tag{4.84}$$

as

$$\dot{\alpha}(t) = \frac{\alpha_0 \sqrt{\kappa_3 \tau - 1} e^{\kappa_3^2 \tau t}}{\sqrt{e^{2\kappa_3^2 \tau t} Q \alpha_0^2 + e^{2\kappa_3 t} (\kappa_3 \tau - 1 - Q \alpha_0^2)}}.$$
(4.85)

This analytical solution of (4.83) can be regarded as test scenario for checking the implementation and validity of numerical solutions obtained from (4.83) or the corresponding field equations.

#### References

- I. Prigogine, in *Nobel Lectures*, ed. by T. Frängsmyr, S. Forsén (World Scientific, Singapore, 1993), pp. 263–285. Chapter Chemistry 1977
- 4.2. M. Suzuki, T. Ohta, M. Mimura, H. Sakaguchi, Phys. Rev. E 52(4), 3645 (1995)
- 4.3. M. Or-Guil, M. Bode, C.P. Schenk, H.-G. Purwins, Phys. Rev. E 57(6), 6432 (1998)
- 4.4. L.M. Pismen, Phys. Rev. Lett. 86(15), 548 (2001)
- 4.5. S.V. Gurevich, S. Amiranashvili, H.-G. Purwins, Phys. Rev. E 74, 066201 (2006). doi:10. 1103/PhysRevE.74.066201
- 4.6. A. Doelman, P. van Heijster, T. Kaper, J. Dyn. Differ. Equ. 21(1), 73 (2009). doi:10.1007/s10884-008-9125-2
- 4.7. M. Tarama, T. Ohta, L.M. Pismen, Phys. Rev. E 83(017201), 1 (2011)
- 4.8. S. Koga, Y. Kuramoto, Prog. Theor. Phys. **63**(1), 106 (1980)
- 4.9. Y. Nishiura, M. Mimura, SIAM J. Appl. Math. 49(2), 481 (1989)
- 4.10. A. Hagberg, E. Meron, Nonlinearity 7, 805 (1994), doi:10.1088/0951-7715/7/3/006
- 4.11. C.P. Schenk, Numerische und analytische Untersuchung solitärer Strukturen in zwei- und dreikomponentigen Reaktions-Diffusions-Systemen. Dissertation, Institut für Angewandte Physik, Westfälische Wilhelms-Universität Münster (1999). Figures published with kind permission of the author.
- 4.12. B.A. Malomed, M.I. Tribelsky, Phys. D 14, 67 (1984)
- 4.13. G.H. Gunaratne, M. El-Hamdi, M. Gorman, Mod. Phys. Lett. B 10(28), 1379 (1996)
- 4.14. J.P. Gollub, C.W. Meyer, Phys. D 6, 337 (1983)
- 4.15. V. Steinberg, G. Ahlers, D.S. Cannell, Phys. Scr. 32, 534 (1985)
- 4.16. C.A. Jones, M.R.E. Proctor, Phys. Lett. A 121(5), 224 (1987)
- 4.17. M. Rabaud, Y. Couder, S. Michalland, Eur. J. Mech. B/Fluid. 10(2), 253 (1991)
- 4.18. L.H. Pan, J.R. de Bruyn, Phys. Rev. Lett. **70**(12), 1791 (1993)

References 117

- 4.19. L. Pan, J.R. de Bruyn, Phys. Rev. E **49**(1), 483 (1994)
- 4.20. A.L. Zanin, E.L. Gurevich, A.S. Moskalenko, H.U. Bödeker, H.-G. Purwins, Phys. Rev. E **70**(3), 036202 (2004). doi:10.1103/PhysRevE.70.036202
- 4.21. J.D. Crawford, E. Knobloch, Phys. Lett. A 128(6-7), 327 (1988)
- 4.22. P. Coullet, G. Iooss, Phys. Rev. Lett. 64(8), 866 (1990)
- 4.23. R. Friedrich, Z. Phys. B **90**(3), 373 (1993)
- 4.24. R. Rajaraman, Solitons and Instantons. An Introduction to Solitons and Instantons in Quantum Field Theory (Elsevier, Amsterdam, 2003)
- 4.25. M. Bode, Phys. D **106**(3–4), 270 (1997)
- 4.26. A. Moskalenko, Dynamische gebundene Zustände und Drift-Rotations-Dynamik von dissipativen Solitonen. Master's thesis, Institut für Angewandte Physik, Westfälische Wilhelms-Universität Münster (2002)
- 4.27. A.S. Moskalenko, A.W. Liehr, H.-G. Purwins, Europhys. Lett. 63(3), 361 (2003)
- 4.28. D. Michaelis, U. Peschel, F. Lederer, D.V. Skryabin, W.J. Firth, Phys. Rev. E **63**(6), 066602 (2001)
- 4.29. D.V. Skryabin, A.G. Vladimirov, Phys. Rev. Lett. **89**(4), 044101 (2002)
- 4.30. C.P. Schenk, P. Schütz, M. Bode, H.-G. Purwins, Phys. Rev. E 57(6), 6480 (1998)
- 4.31. A.G. Vladimirov, J.M. McSloy, D.V. Skryabin, W.J. Firth, Phys. Rev. E 65(046606), 1 (2002)
- 4.32. A. Moskalenko, A.W. Liehr, M. Bode, H.-G. Purwins, in *International Conference on Theoretical Physics*, Paris, France, 22–27 July 2002, p. 321
- 4.33. A. Moskalenko, A.W. Liehr, M.C. Röttger, M. Bode, H.-G. Purwins, in *Verhandl. DPG (VI)*, vol. 37 (Deutsche Physikalische Gesellschaft e. V., 2002), vol. 37, p. 125. Frühjahrstagung des Arbeitskreises Festkörperphysik bei der DPG, Regensburg vom 11. bis 15.03.2002
- 4.34. T. Teramoto, K. Suzuki, Y. Nishiura, Phys. Rev. E 80(046208), 1 (2009). doi:10.1103/ PhysRevE.80.046208
- 4.35. M. Kness, L.S. Tuckermann, D. Barkley, Phys. Rev. A 46(8), 5054 (1992)
- 4.36. A.W. Liehr, H.U. Bödeker, M.C. Röttger, T.D. Frank, R. Friedrich, H.-G. Purwins, New J. Phys. **5**(89), 1 (2003). http://stacks.iop.org/1367-2630/5/89
- 4.37. V.V. Osipov, Phys. D 93, 143 (1996)
- 4.38. R. FitzHugh, Biophys. J. 1, 445 (1962)
- 4.39. J. Nagumo, S. Arimoto, S. Yoshizawa, Proc. IRE 50, 2061 (1962)
- 4.40. H. Hempel, I. Schebesch, L. Schimansky-Geier, Eur. Phys. J. B 2, 399 (1998)
- 4.41. S.V. Gurevich, H.U. Bödeker, A.S. Moskalenko, A.W. Liehr, H.-G. Purwins, in *Physics and Control (PhysCon). International Conference, August 20–22, 2003, Saint Petersburg*, ed. by A.L. Fradkov, A.N. Churilov (IEEE, Piscataway, 2003), pp. 601–606
- 4.42. S.V. Gurevich, H.U. Bödeker, A.S. Moskalenko, A.W. Liehr, H.-G. Purwins, Phys. D **199**(1–2), 115 (2004). doi:10.1016/j.physd.2004.08.020
- 4.43. I. Brauer, M. Bode, E. Ammelt, H.-G. Purwins, Phys. Rev. Lett. 84(18), 4104 (2000)
- 4.44. M. Bode, Pattern formation in complex dissipative systems: a particle approach. Habilitationsschrift, Institut für Angewandte Physik, Westfälische Wilhelms-Universität Münster, 1998
- 4.45. M. Bode, A.W. Liehr, C.P. Schenk, H.-G. Purwins, Phys. D 161(1-2), 45 (2002)

# **Chapter 5 Interaction of Slow Dissipative Solitudes**

Now the law of forces is of this kind; the forces are repulsive at very small distances, & become indefinitely greater & greater, as the distances are diminished indefinitely, in such a manner that they are capable of destroying any velocity, no matter how large it may be, with which one point may approach another, before ever the distance between them vanishes. When the distance between them is increased, they are diminished in such a way that at a certain distance, which is extremely small, the force becomes nothing. Then as the distance is still further increased, the forces are changed to attractive forces; these at first increase, then diminish, vanish, & become repulsive forces, which in the same way first increase, then diminish, vanish & become once more attractive; & so on, in turn, for a very great number of distances, which are all still very minute; [...]

P. Rogerio Josepho Boscovich, 1763 [5.1], cited from [5.2].

Abstract The following section accounts the interaction of slowly propagating dissipative solitons by means of a particle ansatz and a nonlinear perturbation analysis. This approach results into a reduction of the field dynamics to the position and excitation of the respective propagator mode where the interaction between dissipative solitons can be regarded approximately as classical central force. Starting from the reduced dynamics, scattering and the formation of bound states are investigated and compared to solutions of the underlying reaction-diffusion system, which shows good agreement between field and particle model. Also on basis of the reduced dynamics and under consideration of internal degrees of freedom the dynamics of rotating bound states are investigated which leads to the description of centrifugal forces and related distance dependent angular velocities. The chapter finishes with some general considerations on many-particle systems of dissipative solitons.

#### 5.1 Formation of Bound States

Systematic investigations on the formation of bound states of dissipative solitons started in the late eighties of the last century [5.3, S. 919f], when Elphick et al. investigated the formation of so-called *wave-trains* [5.4–5.6]. In this context OrGuil et al. were able to show on basis of a modified Barkley-model [5.7], that bound states of one or more propagating dissipative solitons can form, if the interaction is not monotonous and exhibits at least one relative maximum [5.8]. In contrast to these investigations are dissipative solitons with purely repulsive interaction which have been investigated by Ohta [5.9, 5.10] and Ei et al. [5.11]. While the phase dependency of interacting breathing dissipative solitons is reported by the working group of Nishiura [5.12], the following considerations concentrate on the interaction of propagating dissipative solitons without breathing mode destabilization.

While experimental evidence for the formation of bound states has been given in Sect. 2.2.5, we are starting to investigate the phenomenon on basis of the threecomponent reaction-diffusion system and continue by deducing the equations of motion for interacting dissipative solitons in the vicinity of the drift-bifurcation (Sect. 5.2). The presented approach builds upon a projection technique which had been introduced by Bode in order to describe the influence of inhomogeneities on the dynamics of trigger fronts [5.13]. It extends the ansatz of Sect. 4.3 by considering two dissipative solitons interacting on an n-dimensional domain, which is subject to spatial inhomogeneities [5.14]. The resulting order parameter equations constitute a so-called reduced dynamics (Sect. 5.2.1). Like in classical mechanics, a dissipative soliton would only change its direction of motion if a certain force is applied. Due to the dissipative nature of the investigated system we are dealing with a generalized type of interaction force which mediates the influence of parameter inhomogeneities (Sect. 5.2.2) and inherently the interaction between dissipative solitons (Sect. 5.2.3). The following sections address the elementary bound states of dissipative solitons (Sect. 5.2.4), and the validity of the reduced dynamics (Sect. 5.2.5), as well as scattering (Sect. 5.3), rotating bound states (Sect. 5.4) and the dynamics of complex bound states (Sect. 5.5). Finally, a small essay on many particle properties of dissipative solitons is given (Sect. 5.6).

The first example for the formation of bound states on basis of the three-component reaction-diffusion system shows a head-on collision on a three-dimensional domain. The initial condition is composed from two dissipative solitons, which are located at positions  $p_1$  and  $p_2$ :

$$p_2 = p_1 + d \parallel e_{\nu}. \tag{5.1a}$$

The particles are separated by distance d=0.8 and move towards each other, which implies anti-parallel propagator mode amplitudes

$$\alpha_1 = -\alpha_2 \parallel e_{\nu}. \tag{5.1b}$$

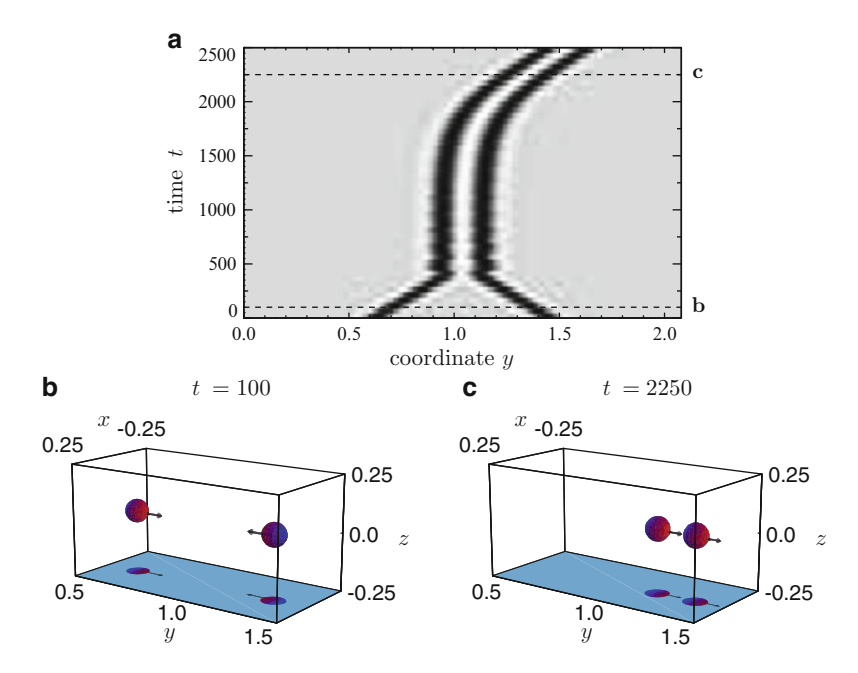


Fig. 5.1 Formation of a propagating bound state in a three-dimensional reaction-diffusion system. (a) Space-time-diagram of the evolving activator intersection u(x(y), t) with  $x(y) = (0, y, 0)^T$  taken along the symmetry axis of the system. (b) and (c) Snapshots of the three-dimensional activator-distribution plotted as isosurfaces of u(x) = -0.1. The colouring of the surfaces has been chosen with respect to the local concentrations of the slow inhibitor. *Red* and *blue* indicate low and high inhibitor concentrations, respectively. The direction of motion of the dissipative solitons is indicated by *arrows*. In order to enhance the spatial perception, shadows of all objects are projected onto the base of the domain. Parameters from (5.2)

Taken the cylindrical configuration of the initial condition into account the three-component reaction-diffusion system (3.70) is solved with the following parameters:

$$D_u = 1.3 \cdot 10^{-4}, \ D_v = 0, \ D_w = 9.64 \cdot 10^{-4}, \ \lambda = 0.95, \ \kappa_1 = -0.08,$$
  
 $\kappa_3 = 0.25, \ \kappa_4 = 1, \ \tau = 4.01, \ \theta = 0.01, \ \Delta_x = 0.0148, \ \Delta t = 0.01,$   
 $\Omega = ]0, 0.52] \times [0, 2.08]$  (5.2)

which provide stable propagating dissipative solitons with oscillating tails (cf. Fig. 3.21).

The result of the simulation is visualized in Fig. 5.1a as space-time diagram, which shows the formation processes as gray-scale image. The spatial coordinate of the image is the symmetry axis  $e_y \parallel d$  of the initial condition (5.1), such that the evolution of activator distribution u(x,t) with  $x = (0, y, 0)^T$  results into the depicted space-time diagram with *light* and *dark gray* shading referring to low and high activator concentrations, respectively. Therefore, the homogeneous ground

state can be identified as smooth *gray* area, whereas the centers of the dissipative solitons are visible as black regions, which are surrounded by the characteristic undershooting (*white*) of the localized activator distributions. At the beginning of the simulation the dissipative solitons move with their intrinsic velocity  $\bar{c}_x$  (4.43) towards each other (Fig. 5.1a). Note, that the reciprocal slope of these curves reflects the velocity of the dissipative solitons.

A snapshot of the approaching dissipative solitons is shown in Fig. 5.1b as isosurface of the activator distribution u(x) = -0.1 at t = 100. The shading of the isosurfaces indicates the concentration of the slow inhibitor with *red* and *blue* corresponding to low and high inhibitor concentrations, respectively. It can be clearly seen, that the dissipative solitons exhibit a low v-concentration at their front. As has been discussed in Sect. 3.4 the shift between activator peak and slow inhibitor peak is the cause of the ongoing propagation. The direction of motion is indicated by *arrows*.

The space-time diagram (Fig. 5.1a) shows, that the dissipative solitons approach each other up to a distance of  $d \approx 0.16$  (t = 400), whereupon they are repelled due to their repulsive interaction and their distance increases. However, their mutual attraction prevents the break off, such that a bound state of two dissipative solitons has formed. The space-time diagram also shows, that the distance oscillation decays, which is caused by the fact, that the corresponding eigenmode of the bound state is subcritical [5.15, S. 88ff]. Instead the applied noise of amplitude  $R = 10^{-5}$  leads to an excitation of the propagator mode, which has to be a longitudinal translation mode due to the cylindrical symmetry of the scattering problem (5.1), which has been explicitly factored into the simulated field Eq. (3.70). In this simulation the bound state starts to propagate uniformly into the direction of the y-axis (Fig. 5.1a,  $t \in [2,300;2,500]$ ). The travelling bound state is exemplary visualized at t = 2,250in Fig. 5.1c as isosurface of the activator distribution. Its shading shows that the slow inhibitor distribution is shifted with respect to the activator distribution against the direction of motion. Such kind of propagating dissipative solitons can be regarded as three-dimensional analogon to wave-train solutions known from one-dimensional reaction-diffusion systems [5.8].

# 5.2 Equations of Motion

## 5.2.1 Reduced Dynamics

Having in mind, that a reaction-diffusion system with two well separated dissipative solitons can be constructed by superposition of two stationary dissipative solitons, we are going to describe their dynamics by means of a particle approach representing each dissipative soliton by its position  $p_i$  and the amplitude  $\alpha_i$  of

appropriate propagator modes (Sect. 4.3.3). Additionally, spatial inhomogeneities  $\kappa_1(x)$  are introduced by means of a spatial mean  $\bar{\kappa}_1$ :

$$\kappa_1 = \kappa_1(\mathbf{x}) = \bar{\kappa}_1 + \underbrace{(\kappa_1(\mathbf{x}) - \bar{\kappa}_1)}_{=:\hat{\kappa}_1(\mathbf{x}) = \hat{\kappa}_1} = \bar{\kappa}_1 + \hat{\kappa}_1(\mathbf{x}) = \bar{\kappa}_1 + \hat{\kappa}_1$$
(5.3)

with  $\hat{\kappa}_1$  denoting the deviation from the spatial mean  $\bar{\kappa}_1$ . Substituting this definition into the three-component reaction-diffusion system (3.69) for the limit  $D_v \to 0$  and  $\theta \to 0$  (3.66) leads to

$$\dot{u}(\mathbf{x},t) = D_u \Delta u(\mathbf{x},t) + \lambda u(\mathbf{x},t) - u(\mathbf{x},t)^3 - \kappa_3 v(\mathbf{x},t) + \bar{\kappa}_1 + \hat{\kappa}_1(\mathbf{x})$$
$$-\kappa_4 \int_{\Omega} g(\mathbf{\chi} - \mathbf{x}) u(\mathbf{\chi},t) d\mathbf{\chi}, \tag{5.4a}$$

$$\tau \dot{v}(\mathbf{x},t) = D_v \Delta v(\mathbf{x},t) + u(\mathbf{x},t) - v(\mathbf{x},t). \tag{5.4b}$$

By substituting  $\kappa_1$  with  $\bar{\kappa}_1$  and  $\lambda$  with  $(\lambda - \kappa_3 - \kappa_4)$  in (3.15) the inhomogeneous reaction-diffusion system (5.4) is transformed, such that its homogeneous ground state  $u_0$  equals to zero (Sect. 4.3.1). Omitting the arguments of u, v and  $\hat{\kappa}_1$  for reasons of simplicity leads to

$$\frac{\partial}{\partial t}u = \mathcal{L}u - \kappa_3 v + N(u) + \hat{\kappa}_1, \tag{5.5a}$$

$$\tau \frac{\partial}{\partial t} v = u - v \tag{5.5b}$$

with nonlinear operator N(u) given by (4.49c). Equation (5.5a) also introduces the linear operator  $\mathcal{L}$ 

$$\mathcal{L}u = D_u \Delta u + f'(u_0(\hat{\kappa}_1)) u - \kappa_4 \int_{\Omega} g(\chi - x) u(\chi) d\chi$$
 (5.5c)

as generalization of (4.50) with  $g(\cdot)$  denoting Green's function (Sect. 3.3.1).

This reaction-diffusion system is well formulated for the following analysis because the activator (5.5a) mainly describes the stationary structures  $\bar{u} = (\bar{u}, \bar{v})^{\mathrm{T}} = (\bar{u}, \bar{u})^{\mathrm{T}}$ , while the inhibitor (5.5b) covers their propagation. In this context only radially symmetric stationary structures are considered, whose existence and stability is a prerequisite for the following analysis.

Linearizing the two-component reaction-diffusion system (5.5) around a stationary solution  $\bar{u} = (\bar{u}, \bar{u})$  leads to the operator  $\mathcal{D}(\bar{u}; \tau)$  (4.54). The respective Goldstone-modes

$$\mathcal{G}_{x_i}(x) = \begin{pmatrix} \frac{\partial}{\partial x_i} \bar{u}(x) \\ -\frac{\partial}{\partial x_i} \bar{u}(x) \end{pmatrix}$$
 (5.6)

have been discussed in Sect. 4.3. Additionally, at the drift-bifurcation point  $\tau_c = \frac{1}{\kappa_3}$  the propagator-modes

$$\mathcal{P}_{x_i}(\mathbf{x}) = \begin{pmatrix} 0 \\ -\frac{1}{\kappa_3} \frac{\partial}{\partial x_i} \bar{u}(\mathbf{x}) \end{pmatrix}$$
 (5.7)

exist in form of neutral eigenmodes. Similarly for the adjoined operator  $\mathcal{D}^{\dagger}(\bar{u};\tau)$ , the complementary Goldstone-mode is given by

$$\mathcal{G}_{x_i}^{\dagger}(x) = \begin{pmatrix} \frac{\partial}{\partial x_i} \bar{u}(x) \\ -\frac{\partial}{\partial x_i} \bar{u}(x) \end{pmatrix}$$
 (5.8)

and the complementary propagator mode is chosen to

$$\mathcal{P}_{x_i}^{\dagger}(\mathbf{x}) = \begin{pmatrix} \frac{1}{\kappa_3} \frac{\partial}{\partial x_i} \bar{u}(\mathbf{x}) \\ 0 \end{pmatrix}. \tag{5.9}$$

In order to model the dynamics in the vicinity of a supercritical drift-bifurcation at  $\tau_c = \frac{1}{\kappa_3}$ , a bifurcation parameter  $\hat{\tau}$  is introduced as

$$\varepsilon^2 \hat{\tau} = \tau - \tau_{\rm c} \tag{5.10}$$

where  $\varepsilon$  corresponds to the ratio of the diameter of a dissipative soliton and the distance between the interacting solitons. Additionally, it is assumed, that the spatially depending perturbation  $\hat{\kappa}_1$  scales as  $\varepsilon^2 \tilde{\kappa}_1$ .

By introducing time scales  $T_m = \varepsilon^m t$  with m = 1, 2, 3 the position  $p_i \in \mathbb{R}^n$  of the  $i^{\text{th}}$  dissipative soliton is given as  $p_i = p_i(T_1, T_2, T_3)$ . In this respect  $p_i$  is the displacement vector describing the shift of a stationary dissipative soliton from the origin to its position, such that the respective vector field is given as  $\bar{u}_i = \bar{u}(x - p_i)$ . Also for each dissipative soliton its n-dimensional propagator mode  $\mathcal{P}(x - p_i)$  and the respective propagator mode amplitude  $\alpha_i = \alpha_i(T_1, T_2) \in \mathbb{R}^n$  are taken into account:

$$u(x,t) = \bar{u}(x - p_1(T_1, T_2, T_3)) - \epsilon \kappa_3 \alpha_1(T_1, T_2) \mathcal{P}(x - p_1(T_1, T_2, T_3)) + \bar{u}(x - p_2(T_1, T_2, T_3)) - \epsilon \kappa_3 \alpha_2(T_1, T_2) \mathcal{P}(x - p_2(T_1, T_2, T_3)) + \epsilon^2 r(x, T_1) + \epsilon^3 R(x).$$
(5.11)

Here, the components of  $\mathcal{P}(\cdot)$  are given by (5.7) and corrections of order  $\mathcal{O}^2$  and  $\mathcal{O}^3$  are denoted  $r(x, T_1)$  and R(x), respectively. Note, that the factor  $\kappa_3$  has been introduced for historical reasons in order to match the perturbation ansatz presented in [5.14], which is revealed by inserting the propagator mode definition (5.7)

into (5.11), omitting the arguments on the right hand side of the equation and writing the components of vector field u separately:

$$u(x, T_1, T_2, T_3) = \bar{u}_1 + \bar{u}_2 + \varepsilon^2 r_u + \varepsilon^3 R_u, \tag{5.12a}$$

$$v(\mathbf{x}, T_1, T_2, T_3) = \bar{u}_1 + \bar{u}_2 + \varepsilon \boldsymbol{\alpha}_1 \nabla \bar{u}_1 + \varepsilon \boldsymbol{\alpha}_2 \nabla \bar{u}_2 + \varepsilon^2 r_v + \varepsilon^3 R_v. \tag{5.12b}$$

In order to derive dynamical equations for  $p_1$  and  $\alpha_1$  on a two-dimensional domain, ansatz (5.12) is inserted into field Eq. (5.5) and the resulting equations are projected onto eigenmodes  $\mathcal{G}_x^{\dagger}(x-p_1)$ ,  $\mathcal{G}_y^{\dagger}(x-p_1)$  (5.8) and  $\mathcal{P}_x^{\dagger}(x-p_1)$ ,  $\mathcal{P}_y^{\dagger}(x-p_1)$  (5.9). Similarly, equations for the second dissipative soliton are derived by projection onto eigenmodes  $\mathcal{G}_x^{\dagger}(x-p_2)$ ,  $\mathcal{G}_y^{\dagger}(x-p_2)$  and  $\mathcal{P}_x^{\dagger}(x-p_2)$ ,  $\mathcal{P}_y^{\dagger}(x-p_2)$ .

An important point for the evaluation of the substitution is the treatment of the nonlinear term

$$N(u(x, T_1, T_2, T_3)) = N(\bar{u}_1 + \bar{u}_2 + \varepsilon^2 r_u + \varepsilon^3 R_u). \tag{5.13}$$

Following an ansatz of Elphick et al. [5.5], the nonlinearity N(u) (4.49c) is expanded as polynomial

$$N(\bar{u}_1 + \bar{u}_2 + \varepsilon^2 r_u + \varepsilon^3 R_u) = \sum_{j=0}^{\infty} a_j (\bar{u}_1 + \bar{u}_2 + \varepsilon^2 r_u + \varepsilon^3 R_u)^j. \quad (5.14)$$

Note, that coefficients  $a_0$  and  $a_1$  vanish due to the nature of N(u) (4.49c). Therefore the projection of  $\mathcal{D}(\mathbf{u}, \tau_c)$  onto eigenmodes  $\mathcal{G}_{1,x_j}^{\dagger}$  (5.8) and  $\mathcal{P}_{1,x_j}^{\dagger}$  (5.9) basically leads to terms of type

$$\langle \frac{\partial}{\partial x_i} \bar{u}_1 | \bar{u}_1^n \bar{u}_2^m \rangle = \mathcal{O}(\varepsilon^{2\min\{n+1,m\}}). \tag{5.15}$$

Their order results from the fact, that the localized structures basically decay exponentially and are of order  $\mathcal{O}(\varepsilon^2)$  for  $|x| \geq |p_2 - p_1|$ . In this respect  $\varepsilon \to 0$  describes the limit of large distances between the interacting dissipative solitons. The evaluation of polynomial (5.15) and its rearranging concerning all terms up to third order leads to

$$N(\bar{u}_1 + \bar{u}_2 + \varepsilon^2 r_u + \varepsilon^3 R_u) = N(\bar{u}_1) + N(\bar{u}_2) + N'(\bar{u}_1)(\bar{u}_2 + \varepsilon^2 r_u + \varepsilon^3 R_u) + N'(\bar{u}_2)(\bar{u}_1 + \varepsilon^2 r_u + \varepsilon^3 R_u),$$
 (5.16)

which is referred to as *weak coupling* in quantum mechanics [5.16, S. 76f]. Note, that the first two terms of this expansion depend on the undisturbed stationary solution, while the interaction between the dissipative solitons is governed by the third and fourth term, which are of the same order as the inhomogeneity  $\tilde{\kappa}_1$ . Taking

all substitutions and expansions into account, system (5.5) will take the following form for the first dissipative soliton, if its terms are sorted with respect to their order in  $\varepsilon$  [5.14]:

 $\mathcal{O}(\varepsilon)$ :

$$0 = \left(\frac{\partial}{\partial T_1} \mathbf{p}_1 - \kappa_3 \mathbf{\alpha}_1\right) \cdot \nabla \bar{u}_1,\tag{5.17a}$$

$$0 = \left(\frac{\partial}{\partial T_1} \mathbf{p}_1 - \kappa_3 \mathbf{\alpha}_1\right) \cdot \nabla \bar{u}_1. \tag{5.17b}$$

 $\mathcal{O}(\varepsilon^2)$ :

$$(\mathcal{L} + N'(\bar{u}_1))r_u - \kappa_3 r_v = -\frac{N'(u_1)}{\varepsilon^2} \bar{u}_2 - \tilde{\kappa}_1 - \frac{\partial}{\partial T_2} \mathbf{p}_1 \cdot \nabla \bar{u}_1, \tag{5.17c}$$

$$\frac{r_u - r_v}{\tau_c} = \frac{\partial}{\partial T_1} \boldsymbol{\alpha}_1 \cdot \nabla \bar{u}_1 - \frac{\partial}{\partial T_2} \boldsymbol{p}_1 \cdot \nabla \bar{u}_1 - \boldsymbol{\alpha}_1 \cdot \left( H(\bar{u}_1) \frac{\partial}{\partial T_1} \boldsymbol{p}_1 \right). \tag{5.17d}$$

 $\mathcal{O}(\varepsilon^3)$ :

$$(\mathcal{L} + N'(\bar{u}_1))R_u - \kappa_3 R_v = \kappa_3 \boldsymbol{\alpha}_2 \cdot \nabla \bar{u}_2 - \frac{\partial}{\partial T_3} \boldsymbol{p}_1 \cdot \nabla \bar{u}_1 + \frac{\partial}{\partial T_1} r_u - \frac{\partial}{\partial T_2} \boldsymbol{p}_2 \cdot \nabla \bar{u}_2,$$

$$(5.17e)$$

$$\frac{R_{u} - R_{v}}{\tau_{c}} = \frac{\partial}{\partial T_{2}} \boldsymbol{\alpha}_{1} \cdot \nabla \bar{u}_{1} + \frac{\boldsymbol{\alpha}_{2}}{\tau_{c}} \cdot \nabla \bar{u}_{2} - \frac{\partial}{\partial T_{3}} \boldsymbol{p}_{1} \cdot \nabla \bar{u}_{1} 
+ \frac{\partial}{\partial T_{1}} \boldsymbol{r}_{v} - \boldsymbol{\alpha}_{1} \cdot \left( H(\bar{u}_{1}) \frac{\partial}{\partial T_{2}} \boldsymbol{p}_{1} \right) - \hat{\tau} \kappa_{3} \frac{\partial}{\partial T_{1}} \boldsymbol{p}_{1} \cdot \nabla \bar{u}_{1} 
- \frac{\partial}{\partial T_{1}} \boldsymbol{p}_{2} \cdot \nabla \bar{u}_{2}.$$
(5.17f)

Here,  $H(\bar{u})$  denotes the Hessian matrix

$$H(\bar{u}_i) = \begin{pmatrix} \frac{\partial^2}{\partial x^2} \bar{u}_i & \frac{\partial^2}{\partial x \partial y} \bar{u}_i \\ \frac{\partial^2}{\partial y \partial x} \bar{u}_i & \frac{\partial^2}{\partial y^2} \bar{u}_i \end{pmatrix}. \tag{5.18}$$

In spite of the fact, that the terms of order  $\mathcal{O}(\varepsilon^3)$  depend on the second order perturbation  $r_u$  and  $r_v$ , they need not be calculated explicitly. Instead the derivative of (5.17d) with respect to  $T_1$  is computed, resolved for  $r_u$  and substituted into (5.17e)–(5.17f). By projecting these equations onto eigenmodes  $\mathcal{G}_{1,x_j}^{\dagger}$  (5.8) and  $\mathcal{P}_{1,x_j}^{\dagger}$  (5.9) and returning to the original time scale t the following dynamics is derived:

$$\dot{p}_1 = \kappa_3 \alpha_1 - W_{DS}(d) + W_{\kappa_1}(p_1),$$
 (5.19a)

$$\dot{\boldsymbol{\alpha}}_1 = \kappa_3^2 \left( \tau - \frac{1}{\kappa_3} \right) \boldsymbol{\alpha}_1 - \kappa_3 Q \alpha_1^2 \boldsymbol{\alpha}_1 - \boldsymbol{W}_{DS}(\boldsymbol{d}) + \boldsymbol{W}_{\kappa_1}(\boldsymbol{p}_1). \tag{5.19b}$$

The dynamics of the second particle is computed in the same way to

$$\dot{\boldsymbol{p}}_2 = \kappa_3 \boldsymbol{\alpha}_2 + \boldsymbol{W}_{\mathrm{DS}}(\boldsymbol{d}) + \boldsymbol{W}_{\kappa_1}(\boldsymbol{p}_2), \tag{5.19c}$$

$$\dot{\boldsymbol{\alpha}}_2 = \kappa_3^2 \left( \tau - \frac{1}{\kappa_3} \right) \boldsymbol{\alpha}_2 - \kappa_3 Q \alpha_2^2 \boldsymbol{\alpha}_2 + \boldsymbol{W}_{DS}(\boldsymbol{d}) + \boldsymbol{W}_{\kappa_1}(\boldsymbol{p}_2)$$
 (5.19d)

with  $\alpha_i = |\alpha_i|$ . Here Q denotes a form factor as given by (4.45),  $W_{DS}(d)$  the interaction between the dissipative solitons separated by distance

$$d = |\mathbf{d}| = |\mathbf{p}_2 - \mathbf{p}_1|, \tag{5.19e}$$

and  $W_{\kappa_1}(p)$  the influence due to an inhomogeneity located at p. Just as the form factor Q, the interaction terms are computed from the activator  $\bar{u}$  of a stationary radial symmetric structure  $\bar{u}$ 

$$W_{\kappa_1}(\boldsymbol{p}_1) = -\frac{\left\langle \nabla \bar{u} | \hat{\kappa}_1 \right\rangle}{\left\langle \left(\frac{\partial}{\partial x} \bar{u}_1\right)^2 \right\rangle},\tag{5.19f}$$

$$W_{\rm DS}(\boldsymbol{d}) = \frac{\left\langle \nabla \bar{u}_1 | N'(\bar{u}_1) \bar{u}_2 \right\rangle}{\left\langle \left(\frac{\partial}{\partial x} \bar{u}\right)^2 \right\rangle} \frac{\boldsymbol{d}}{d} = F(d) \frac{\boldsymbol{d}}{d}. \tag{5.19g}$$

Due to the radial symmetry of the dissipative solitons the interaction F(d) can be interpreted as distance dependent central force which acts in direction of the displacement vector  $\mathbf{d}/d$  between the dissipative solitons.

In order to generalize the reduced dynamics (5.19) to several interacting dissipative solitons, the interaction field  $W_{DS}(d)$  (5.19g) describing the two-particle interaction has to be extended to a many-particle field  $W_i(p_1, \ldots, p_N)$ , such that for N interacting dissipative solitons the dynamics of the ith particle becomes

$$\dot{\boldsymbol{p}}_i = \kappa_3 \boldsymbol{\alpha}_i - \boldsymbol{W}_i(\boldsymbol{p}_1, \dots, \boldsymbol{p}_N) + \boldsymbol{W}_{\kappa_1}(\boldsymbol{p}_i), \tag{5.20a}$$

$$\dot{\boldsymbol{\alpha}}_{i} = \kappa_{3}^{2} \left( \tau - \frac{1}{\kappa_{3}} \right) \boldsymbol{\alpha}_{i} - \kappa_{3} Q \alpha_{i}^{2} \boldsymbol{\alpha}_{i} - \boldsymbol{W}_{i}(\boldsymbol{p}_{1}, \dots, \boldsymbol{p}_{N}) + \boldsymbol{W}_{\kappa_{1}}(\boldsymbol{p}_{i}). \tag{5.20b}$$

The many-particle interaction  $W_i(p_1, ..., p_N)$  can be approximated by superposition of the two-particle interaction as

$$W_{i}(p_{1},...,p_{N}) = \sum_{\substack{j=1\\j\neq i}}^{N} F(|p_{j}-p_{i}|) \frac{p_{j}-p_{i}}{|p_{j}-p_{i}|}$$
(5.20c)

[5.15, S. 70]. This many-particle interaction is the basis of Sects. 5.5 and 5.6 which discuss systems with more than two interacting dissipative solitons.

## 5.2.2 Inhomogeneous Systems

In many cases spatial inhomogeneities of reaction-diffusion systems can be modelled in terms of parameter inhomogeneities like the ones introduced in (5.3). In the context of the reduced dynamics the effect  $W_{\kappa_1}(p)$  of the inhomogeneities is determined by (5.19f) from the field representation  $\kappa_1(x)$  of the parameter inhomogeneity and the stationary dissipative soliton  $\bar{u}$ .

An application of this approach is the investigation of the influence of coarse spatial discretization on the dynamics of dissipative solitons observed in numerical solutions of the field Eq. (5.19). Modelling the spatial discretization as lattice of perturbations in terms of the reduced dynamics shows, that the direction of motion of the dissipative solitons is deflected towards the symmetry axes of the lattice [5.15, S. 106ff]. This phenomenon is frequently observed for numerical solutions computed on coarsely discretized domains. In addition Bode et al. have shown, that slowly propagating dissipative solitons are not only scattered at parameters inhomogeneities of Gaussian shape but also can be captured on circular paths [5.14, S. 57ff]. Also to mention is the work of Ward et al. [5.17] who derived a reduced dynamics for the description of pinning effects. Intensive investigations on the interaction of dissipative solitons with localized inhomogeneities have also been presented by Nishiura et al. [5.18–5.21].

In contrast to the aforementioned approaches we are going to neglect parameter inhomogeneities throughout the following sections of the book. Therefore we choose  $\hat{\kappa}_1 = 0$ , such that  $W_{\kappa_1}(p) \equiv 0$  follows from (5.19f).

#### 5.2.3 Interaction Law

Within the scope of the reduced dynamics (5.19), the distance dependent interaction of radially symmetric dissipative solitons is characterized by the central force F(d), which in turn is computed via (5.19g) from the stationary solution  $\bar{u}$  of the considered structure. Because the reduced dynamics (5.12) is only valid for sufficiently separated dissipative solitons, the interaction force F(d) is basically determined by the decay characteristics of the dissipative solitons against the homogeneous ground state, which surrounds the interacting structures.

In order to illustrate this behaviour Fig. 5.2 shows two typical dissipative solitons with monotonous (5.2a) and oscillatory (5.2b) decay characteristics. The respective interaction forces are plotted in Fig. 5.2c, d as solid curves. The force F(d), which corresponds to the monotonously decaying dissipative soliton, increases with decreasing distance d between two solitons and reflects purely repulsive interaction. This can be clarified on basis of the reduced dynamics (5.19b) if a one-dimensional domain hosting two approaching dissipative solitons is considered. We neglect inhomogeneities and assume that both dissipative solitons are significantly

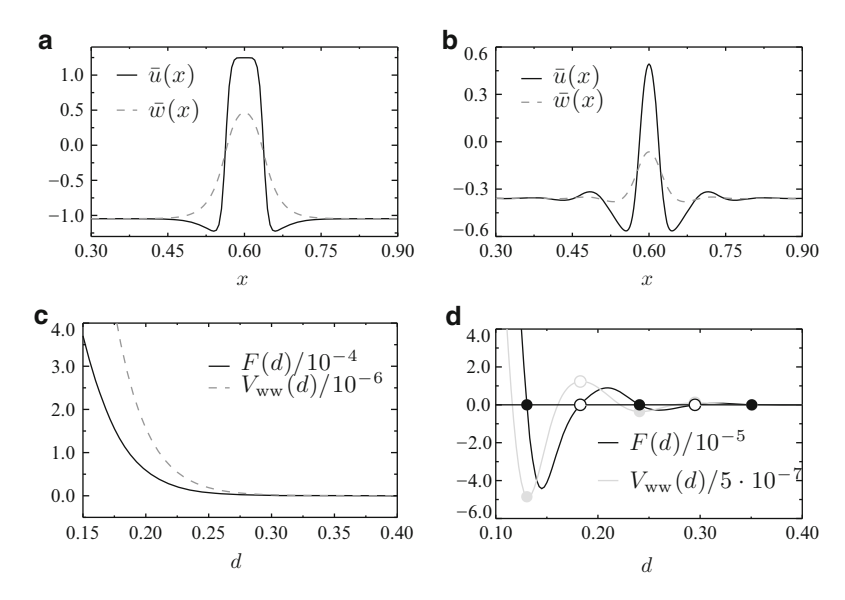


Fig. 5.2 Distance dependent interaction of dissipative solitons. (a) and (b) Stationary dissipative solitons as solutions of the three-component reaction-diffusion system (3.69). Due to the neglected diffusion of the slow inhibitor  $(D_v = 0)$  its distribution is identical with the distribution of the activator  $\bar{u}(x) = \bar{v}(x)$ . (c) and (d) Interaction force F(d) (black curves) and interaction potential  $V_{\rm ww}(d)$  (gray curves) according to (5.19g) and (5.24) of the dissipative solitons depicted in subfigures (a) and (b). Solid and open symbols indicate stable and unstable binding distances. Parameters (a) and (c):  $D_u = 8.0 \cdot 10^{-5}$ ,  $D_v = 0$ ,  $D_w = 10^{-3}$ ,  $\lambda = 3.0$ ,  $\kappa_1 = -0.1$ ,  $\kappa_3 = 1.0$ ,  $\kappa_4 = 1.0$ ,  $\Omega = [0, 1.2]$ , no-flux boundary condition,  $\Delta_x = 5 \cdot 10^{-3}$ . Parameters (b) and (d):  $D_u = 5.0 \cdot 10^{-5}$ ,  $D_v = 0$ ,  $D_w = 9.64 \cdot 10^{-3}$ ,  $\lambda = 1.71$ ,  $\kappa_1 = -0.15$ ,  $\kappa_3 = 1.0$ ,  $\kappa_4 = 1.0$ ,  $\Omega = [0, 1.2]$ , no-flux boundary condition,  $\Delta_x = 2.5 \cdot 10^{-3}$ 

separated and initially approach each other with their equilibrium propagation velocity  $\dot{p}_1(t_0) = \kappa_3 \bar{\alpha}$  and  $\dot{p}_2(t_0) = -\kappa_3 \bar{\alpha}$ , such that (5.19b) reduces to

$$\dot{\alpha}_1 = -W_{\rm DS}(d) = -F(d).$$
 (5.21)

In this situation a positive interaction F(d) decreases the propagator mode amplitude  $\alpha_1$  and the propagation velocity  $p_1$  (5.19a). The same holds for the second dissipative soliton such that both localized structures are decelerated due to their repulsive interaction.

One should be aware, that the interaction law and therefore the reduced dynamics become invalid if the distance d between the centers of the interacting dissipative decreases beyond a critical threshold such that the shape of the structures changes significantly. This would render the perturbation ansatz (5.12) invalid. Concerning dissipative solitons with monotonous decay characteristics this critical distance  $d_{\rm c}$  can be estimated from the distance  $d_{\rm min}$  between the center of the dissipative soliton and its first local minimum as

$$d_{\rm c} \approx \frac{3}{2} d_{\rm min}.\tag{5.22}$$

In most cases this estimation will also hold for dissipative solitons with oscillatory tails. However, if these tails are strongly pronounced it might be necessary to choose the second or third local minimum instead of the first one in order to prevent the replication of dissipative solitons (Sect. 7.3.1).

The dissipative soliton displayed in Fig. 5.2b represents a localized structure with weak pronounced oscillatory tails, such that the scope of application of the reduced dynamics can be estimated from (5.22) to  $d_{\rm c}\approx 0.1$ . The corresponding interaction force is plotted in Fig. 5.2d as black curve, which shows the characteristic oscillatory decay characteristics. Due to the alternating sign of the interaction F(d) its roots  $F(d)|_{d=\bar{d}}=0$  separate attractive (F(d)<0) and repulsive (F(d)>0) regions. At these distinguished distances  $d=\bar{d}$  the interaction between the dissipative solitons vanishes, which allows for the formation of bound states. The resulting elementary binding states are discussed in following section.

From the historical point of view, it might be noted that oscillatory interaction laws have already been discussed in the eighteenth century by Boscovich [5.1] in the context of first atomistic theories (cf. citation on p. 119). Although this theory was common to scientists in the nineteenth century it has fallen into oblivion due to the success of quantum mechanics [5.22].

#### 5.2.4 Bound States

Dissipative solitons with oscillatory tails which bind in distinguished distances  $d = \bar{d}$  due to  $F(d)|_{d=\bar{d}} = 0$  and do not change their relative position to each other can be regarded as elementary bound states of dissipative solitons (cf. Fig. 4.3). In contrast to rigid bound states there also exist dissipative soliton molecules with internal degrees of freedom, which are discussed in Sect. 5.5. However, the relative simple structure of the reduced dynamics (5.19) enables the discussion of the stability of dissipative soliton-molecules.

For this purpose the reduced dynamics (5.19) are simplified by comparing the order of magnitudes of the occurring terms [5.16, S. 106]. It follows, that the interaction term of (5.19b) determines the dynamics of the propagator mode  $\alpha$  significantly, while the dynamics of the position p (5.19a) is much less influenced by the interaction term. Therefore the reduced dynamics can be formulated in analogy to classical mechanics as dynamics of two point-like particles with unity mass:

$$\ddot{\mathbf{p}}_{1} = \kappa_{3}^{2} \left( \tau - \frac{1}{\kappa_{3}} \right) \dot{\mathbf{p}}_{1} - \frac{Q}{\kappa_{3}} \dot{p}_{1}^{2} \dot{\mathbf{p}}_{1} - \kappa_{3} F(d) \frac{d}{d}, \tag{5.23a}$$

$$\ddot{\mathbf{p}}_{2} = \kappa_{3}^{2} \left( \tau - \frac{1}{\kappa_{3}} \right) \dot{\mathbf{p}}_{2} - \frac{Q}{\kappa_{3}} \dot{p}_{2}^{2} \dot{\mathbf{p}}_{2} + \kappa_{3} F(d) \frac{d}{d}. \tag{5.23b}$$

Now the interaction can be formulated as potential

$$V_{\text{ww}}(d) = -\int_{d}^{\infty} -\kappa_3 F(d_{\text{h}}) \, dd_{\text{h}} = \kappa_3 \int_{d}^{\infty} F(d_{\text{h}}) \, dd_{\text{h}}. \tag{5.24}$$

The velocity dependent driving respectively friction term can be interpreted as kinetic energy

$$V_{v}(\dot{p}) = -\int_{0}^{\dot{p}} \left(\kappa_{3}^{2} \left(\tau - \frac{1}{\kappa_{3}}\right) p_{h} - \frac{Q}{\kappa_{3}} p_{h}^{3}\right) dp_{h}$$

$$= -\frac{\kappa_{3}^{2}}{2} \left(\tau - \frac{1}{\kappa_{3}}\right) \dot{p}^{2} + \frac{Q}{4\kappa_{3}} \dot{p}^{4}, \qquad (5.25)$$

which leads to the following representation of the dynamics:

$$\ddot{\mathbf{p}}_{1} = -\frac{\dot{p}_{1}}{\dot{p}_{1}}V_{v}'(\dot{p}_{1}) - \frac{d}{d}V_{ww}'(d), \tag{5.26a}$$

$$\ddot{\mathbf{p}}_{2} = -\frac{\dot{p}_{2}}{\dot{p}_{2}}V'_{v}(\dot{p}_{2}) + \frac{d}{d}V'_{ww}(d). \tag{5.26b}$$

In this notation, a prime denotes the first derivative with respect to the argument. Considering the system in close vicinity of the drift-bifurcation point  $(\tau \leq \frac{1}{\kappa_2})$  one finds that all terms of the kinetic energy  $V_{\rm v}(\dot{p})$  (5.25) are positive. In analogy to the pitchfork-bifurcation the resulting stationary solutions are determined by the parabolic potential, such that the only solution  $\dot{p} = 0$  is globally stable (Sect. 3.1). In this case the stability of the bound state is completely determined by the interaction potential  $V_{ww}(d)$  (5.24). Typical interaction potentials are plotted in Fig. 5.2c, d as gray curves. These considerations clarify, that dissipative solitons with monotonously decaying tails repel each other, because increasing their distance d by  $\delta d$  decreases their potential energy by  $(V_{\rm ww}(d+\delta d)-V_{\rm ww}(d))$  (Fig. 5.2c). On the other hand the interaction potential  $V_{\rm ww}(d)$  of oscillatory interaction is characterized by a series of less pronounced local extremes (Fig. 5.2d) each one determining a stationary binding distance. From the potential representation (5.26) follows, that a bound state, whose binding distance refers to a local maximum of  $V_{\rm ww}(d)$ , is unstable, while a binding distance corresponding to a local minimum of  $V_{\rm ww}(d)$  refers to a stable bound state.

This consideration also holds beyond the drift-bifurcation, which implies  $\tau > \frac{1}{\kappa_3}$ . Here, the stability of a bound state has to be given for interaction potential  $V_{\rm ww}(d)$  (5.24) as well as the kinetic energy  $V_{\rm v}(\dot{p})$  (5.25). Due to  $\tau > \frac{1}{\kappa_3}$  the kinetic energy (5.25) has a negative quadratic term and has become a double well potential , which has a local maximum at  $\dot{p}=0$  and two relative minima at  $\dot{p}=\pm \bar{c}_x$  (4.43). Therefore, a dissipative soliton travelling with its intrinsic velocity  $\bar{c}_x$  is stable, while its steady state is unstable. If the dissipative solitons of the bound state propagate in parallel directions  $\dot{p}_1 \parallel \dot{p}_2$ , the stability of stationary solutions of (5.26) are determined by the stability of each of the potentials  $V_{\rm ww}(d)$  and  $V_{\rm v}(\dot{p})$  (Fig. 5.3). Consequently, four different cases can be discriminated: The bound state is stationary ( $\dot{p}=0$ , upper row in Fig. 5.3), or propagates uniformly ( $\dot{p}=\pm \bar{c}_x$ , lower row of Fig. 5.3), its localized structures reside in an unstable binding state

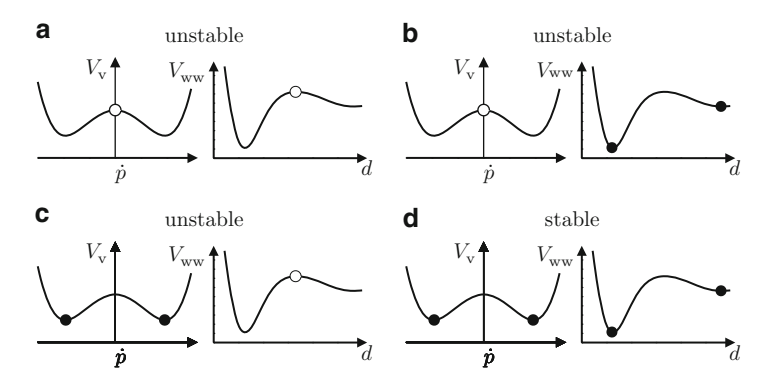


**Fig. 5.3** Qualitative stability considerations of dissipative solitons propagating in parallel. Each scenario is represented by the respective kinetic energy and interaction potential defined in Eqs. (5.25) and (5.24). The curves have been computed for the dissipative soliton shown in Fig. 5.2b. (a)  $\dot{p}=0, V_{\rm ww}''(\bar{d})>0$ . (b)  $\dot{p}=0, V_{\rm ww}''(\bar{d})<0$ . (c)  $\dot{p}=\pm\bar{c}_x, V_{\rm ww}''(\bar{d})>0$ . (d)  $\dot{p}=\pm\bar{c}_x, V_{\rm ww}''(\bar{d})<0$ 

 $V_{\rm ww}''(\bar{d}) > 0$  (left column of Fig. 5.3), or an stable binding state  $V_{\rm ww}''(\bar{d}) < 0$  (right column of Fig. 5.3). Consequently, the reduced dynamics of two dissipative solitons beyond the drift-bifurcation has stable solutions, which can be interpreted as uniformly propagating bound states. These are characterized by translational velocity  $\bar{c}_x$  (4.43) and binding distances  $\bar{d}_i$  with  $(F(\bar{d}_i) = 0) \land (F'(\bar{d}_i) < 0)$  (Fig. 5.3d).

The attentive reader will notice, that these bound states have already been discussed in Sect. 4.2, where also rotating bound states have been taken into account. The difference between translating and rotating bound states can also be explained with respect to the reduced dynamics: While for translating bound states, both the translational and the interaction terms of the reduced dynamics have to vanish separately, for rotating bound states these terms have to balance each other. Therefore, the binding distance depends on the intrinsic velocity of the involved dissipative solitons, which will be discussed in detail in Sect. 5.4.2.

Finally, it has to be remarked, that the reduced dynamics (5.19) of radial symmetric solutions does not take into account, that due to the broken rotational symmetry, the translational and rotational modes of a bound states are coupled. It can be shown, that only the motion in direction of the longitudinal axis of the bound state is stable, which can be shown by solutions of the field Eq. (3.69) [5.15, S. 93]. This effect can be reproduced by reduced dynamics, if the dissipative soliton molecule is regarded as rigid structure exhibiting an additional rotational degree of freedom [5.16,5.23,5.24]. While this ansatz gives reliable predictions in the vicinity of the drift-bifurcation, it shows significant deviations at larger intrinsic velocities due to the negligence of the internal degree of freedom (cf. Sect. 5.4.2).

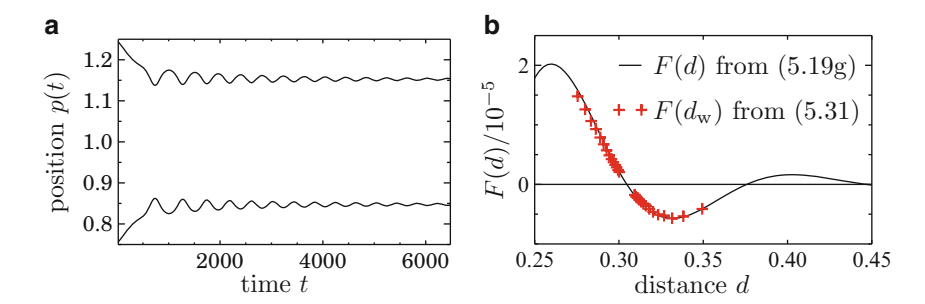


Fig. 5.4 Deriving the interaction of dissipative solitons from particle-particle interaction. (a) Position  $p(t) = p_x(t)$  of two dissipative solitons, which form a bound state due to a head-on collision similar to the one presented in Fig. 5.1. (b) Comparison of interaction F(d) (black curve), which has been computed from (5.19g) on basis of high resolution simulations of stationary dissipative solitons, and sampled interaction  $F(d_w)$  (red crosses), which has been computed from (5.31) on basis of the inflection points  $p(t_w)$  of the trajectories shown in subfigure (a). Parameters from (4.22) with  $\tau = 3.335$ ,  $\Omega = [0, 2]^2$ ,  $\Delta_x = 5 \cdot 10^{-3}$ ,  $\Delta_t = 0.01$ 

## 5.2.5 Checking the Reduced Dynamics

The distance dependent interaction F(d) of dissipative solitons is of vital importance for the validity of the reduced dynamics (5.19). Because this law is not directly derived from the parameters of the reaction diffusion system, but is computed from its stationary solutions according to (5.19g), inaccuracies e.g. due to insufficient spatial discretization have to be ruled out. Of course, the most elegant way is to compute the interaction law directly from simulations of the partial differential equations instead of comparing scattering trajectories.  $^{1}$ 

Starting point is a molecule formation process due to a head on collision similar to the one presented in Fig. 5.1. This scenario is replicated for the evaluation of interaction law (5.19g) (Fig. 5.7) by setting up the initial condition

$$\mathbf{p}_{1,0} = (-0.4, 0)^{\mathrm{T}}, \quad \boldsymbol{\alpha}_{1,0} = (\bar{c}_{x}(\tau)/\kappa_{3}, 0)^{\mathrm{T}}, \mathbf{p}_{2,0} = (0.4, 0)^{\mathrm{T}}, \quad \boldsymbol{\alpha}_{2,0} = (-\bar{c}_{x}(\tau)/\kappa_{3}, 0)^{\mathrm{T}}.$$
(5.27)

with  $\tau=3.335$  from stationary dissipative solitons. Figure 5.4a shows the solutions of the field equations as time series of the position of the dissipative solitons. Due to the small intrinsic velocity of the interaction dissipative solitons the equilibrium state of the bound state to be formed is the second closest configuration  $d_{0,\text{II}}=0.308$  to which the particles relax in an out of phase oscillation. Describing this

<sup>&</sup>lt;sup>1</sup>Historically, the presented method had been developed because the angular velocities (Sect. 5.4.2), which had been predicted by the interaction law published in [5.14, Eq. (28)], could not be confirmed by solutions of the full dynamics. The reason was a simple typo, which has been corrected in an erratum [5.25].

molecule formation in a center of mass coordinate system with respect to the reduced dynamics (5.19) and choosing the dissipative soliton at position  $p(t) = \frac{d}{2}$ , its propagator mode amplitude  $\alpha(t)$  is given from (5.19a) as

$$\alpha(t) = \frac{\dot{p}(t) - F(2p(t))}{\kappa_3}.\tag{5.28}$$

Inserting this equation into (5.19b) reveals the acceleration  $\ddot{p}(t)$  of the particle:

$$\ddot{p}(t) = \kappa_3 F(2p(t)) - \kappa_3^2 \left(\tau - \frac{1}{\kappa_3}\right) [F(2p(t)) - \dot{p}(t)] + \frac{Q}{\kappa_3} [F(2p(t)) - \dot{p}(t)]^3 + 2F'(2p(t)) \dot{p}(t).$$
 (5.29)

This analytical expression can be simplified by taking into account, that the dissipative solitons change their direction of motion recurrently, while relaxing to the stationary bound state. For each turning point  $t_{\rm w}$  the propagation velocity  $\dot{p}(t_{\rm w})$  vanishes ( $\dot{p}(t_{\rm w})=0$ ). Taking into account, that the distance  $d_{\rm w}$  of the dissipative solitons at the inflection point is given by  $d_{\rm w}=2\,p(t_{\rm w})$  Eq. (5.29) can be simplified to

$$\ddot{p}(t_{\rm w}) = \frac{Q}{\kappa_3} F(d_{\rm w})^3 - \kappa_3^2 \left(\tau - \frac{2}{\kappa_3}\right) F(d_{\rm w}). \tag{5.30}$$

Due to the fact, that the interaction F(d) appears as second order term in the course of deriving the reduced dynamics (5.17) the cubed interaction term  $F(d_w)^3$  of (5.30) can be neglected in comparison to the acceleration  $\ddot{p}$ , which is of first order. Therefore, one gets the following expression for the interaction of the dissipative solitons at the turning points:

$$F(d_{\mathbf{w}}) = \frac{\ddot{p}(t_{\mathbf{w}})}{\kappa_3^2(\frac{2}{\kappa_3} - \tau)}.$$
 (5.31)

Of course the turning points as well as the corresponding accelerations can be extracted from the trajectories of the interaction process, such that an estimation  $\{(d_{w,0}, F(d_{w,0})), \ldots, (d_{w,N}, F(d_{w,N}))\}$  of the interaction F(d) is computed from the set of turning points  $\{(t_{w,0}, \dot{p}(t_{w,0})), \ldots, (t_{w,N}, \dot{p}(t_{w,N}))\}$ .

Applying this analysis to the trajectories of the relaxation process depicted in Fig. 5.4a and comparing the resulting interaction  $F(d_{w,i})$  (red crosses in Fig. 5.4b) with the corresponding continuous interaction F(d) (5.19g) of the reduced dynamics (black curve in Fig. 5.4b), which has been computed from high-resolution simulations of stationary dissipative solitons, the correspondence between both interactions is found to be excellent. This example may be regarded as confirmation that the interaction law between dissipative solitons can be derived at least in parts from simulations of the field equations if the dissipative solitons are sufficiently slow and particle generation processes can be neglected.

5.3 Scattering 135

## 5.3 Scattering

The most often observed interaction between slowly propagating dissipative solitons is scattering. This is caused by the fact, that a major class of dissipative solitons does not exhibit oscillatory tails, and even dissipative solitons with pronounced oscillatory tails do need to approach each other with optimal impact condition in order to form bound states. This has been shown e.g. by Bode et al. [5.14, Fig. 4] and will be discussed extensively in the following section.

Here, we are going to compare the trajectories of two scattering dissipative solitons on behalf of simulations of the field equations and the reduced dynamics (5.19) for a three-dimensional setup. It is important to note, that the simulated field equations do not match the limit case of the reduced dynamics exactly, because the fast inhibitor stabilizes the activator with a small delay:

$$D_u = 4.67 \cdot 10^{-3}, \ D_v = 0, \ D_w = 10^{-2}, \ \lambda = 5.67, \ \kappa_1 = -1.126,$$
  
 $\kappa_3 = 1.0, \ \kappa_4 = 3.33, \ \tau = 1.03, \ \theta = 0.01, \ \Omega = [0, 2.25]^3,$   
no-flux boundary condition,  $\Delta_x = 2.8 \cdot 10^{-2}, \ \Delta_t = 10^{-3}.$  (5.32)

For these parameters the dissipative solitons exhibit only weak oscillatory tails. Therefore, they behave to most extent repulsively and are well suited for the investigation of scattering processes. In order to visualize results of the simulation, isosurfaces of the activator u(x) = -1.0 (red) and the slow inhibitor v(x) = -1.0 (green) are shown in Fig. 5.5a–c, while the isosurface of the fast inhibitor is omitted. The depicted isosurfaces are nearly spherical, such that each dissipative soliton looks like a two-coloured sphere. This is due to the missing diffusion of the slow inhibitor does not diffuse and the close vicinity of the drift-bifurcation point, which causes only a weak symmetry breaking of the localized structures. The isosurface of the fast inhibitor would be centered around the activator and would either be hidden by the isosurface of the activator or would shield it.

In the beginning of the simulation both dissipative solitons propagate to the center of the domain with one soliton moving parallel to the *y*-axis and one moving parallel to the *z*-axis (Fig. 5.5a). Additionally, both dissipative solitons are displaced with respect to the *x*-axis, such that they do not move in the same plane. In the course of the scattering the dissipative solitons reach a minimal distance at  $t \approx 64$  (Fig. 5.5b). Due to their repulsive behaviour they are deflected and continue their uniform propagation (Fig. 5.5c).

As mentioned before, the parameters of the field equation do not match the limit case of the reduced dynamics (5.5), because the time-scale parameter  $\theta$  of field w is not zero but is set to  $\theta = 0.01$  (5.32). Therefore, we are not dealing with a two-component reaction-diffusion system with local feedback, which is the limit case covered by the reduced dynamics, but with a three-component reaction-diffusion system also realizing a local feedback. Consequently, this simulation can be regarded as exemplary check to which extent reaction-diffusion systems, which

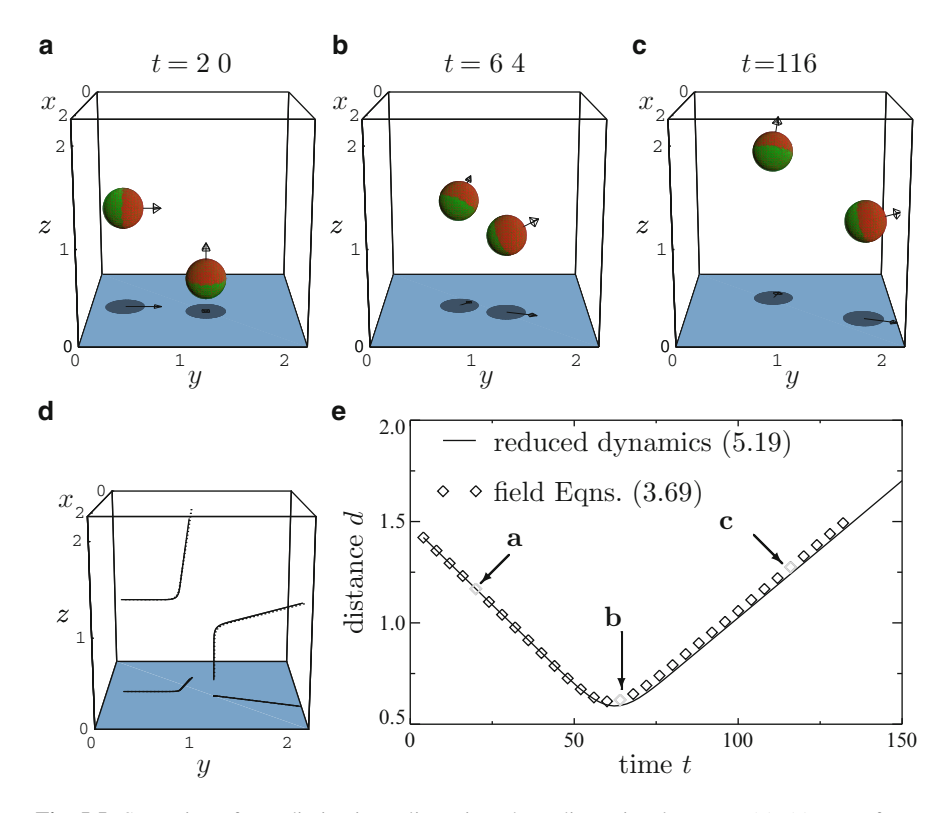


Fig. 5.5 Scattering of two dissipative solitons in a three-dimensional system. (a)–(c) Isosurfaces of activator u(x) = -1.0 (red) and slow inhibitor v(x) = -1.0 (green) for three snapshots of the simulation. Vectors point into the direction of motion. The projection of the isosurfaces onto the base of the domain enhances the spatial orientation. (d) Trajectories of the dissipative solitons computed from the activator distributions of the individual dissipative soliton and from the reduced dynamics. The curves cannot be discriminated with respect to the plotting accuracy. (e) Time series of the distance d(t) between the scattering structures from solution of the reduced dynamics and the field equations. Parameters of the reduced dynamics (5.19): Q = 235, F(d) as given by (5.33). Parameters of the field Eq. (3.69) as given by (5.32)

deviate from the limit case of the reduced dynamics in other parameters than the bifurcation parameter  $\tau$ , are still covered by the particle dynamics (5.19). In order to solve the reduced dynamics numerically, the interaction between the dissipative solitons has been computed by means of (5.19g) for a discrete set of distances  $\{d_i\}$  and the resulting set of distance-interaction tuples  $\{(d_i, F_i(d_i))\}$  has been approximated by the following function

$$F(d) = -\frac{5.33}{d}e^{-14.78d}\cos(6.77(d - 0.622)). \tag{5.33}$$

Furthermore the form factor Q (4.44) has been computed to Q = 235. Simulating the trajectories  $p_1(t)$  and  $p_2(t)$  of the dissipative solitons for the described scattering

process by means of the reduced dynamics and comparing them with the trajectories inferred from the solutions of the field equations shows no deviations with respect to the plotting accuracy (Fig. 5.5d). Only by comparing the time series d(t) of the distance between the dissipative solitons reveals a small deviation (Fig. 5.5e), which builds up with reaching the interaction region.

Because this deviation is quite small and can hardly be discriminated from numerical errors e.g. due to the spatial discretization of the domain, the discussed scenario of a fast reacting inhibitor field w ( $\theta = 0.01$ ) can be regarded as valid approximation to the limit case of the reduced dynamics ( $\theta \to 0$ ).

## **5.4 Rotating Bound States**

### 5.4.1 Formation of Rotating Bound States

It is know from experimental observations obtained in semiconductor-gas discharge systems, that dissipative solitons can form transient bound states (Fig. 2.17) due to soliton-soliton interaction. It is also observed, that dissipative solitons emerge as rotating bound states in the course of self-completion-scenarios (Sect. 2.2.5.3). While the dynamics of rotating bound states are discussed in Sect. 5.4.2, the following section investigates interaction processes leading to their formation in two-dimensional systems.

One thing is sure, if a reaction-diffusion system features slowly propagating dissipative solitons with oscillatory tails, rotating bound states will form under suitable initial conditions. This holds true even for weakly pronounced oscillatory tails. In this scenario only the propagation velocity has to be reduced significantly (Sect. 5.4.2). On the other hand, the formation of rotating bound states of dissipative solitons is much more likely, if the oscillatory character of their tails is pronounced. Therefore, we are investigating the formation of bound states on basis of parameter set (4.22), which already has been proven useful in the context of the rotational bifurcation (Sect. 4.2). For these parameters, the form factor Q (4.44) is computed from a single dissipative soliton (Fig. 4.4a) to Q = 1,950. The interaction  $F(d_i)$  (5.19g) is computed for a discrete set of distances  $\{d_i|1 < i \le N \land d_{i+1} = d_i + 10^{-2}\}$  with  $d_0 = 0$ . The resulting set of tuples  $\{(d_i, F(d_i))|1 < i \le N \land d_{i+1} = d_i + 10^{-2}\}$  is interpolated by

$$F(d) = -\frac{6.87 \cdot 10^{-4}}{\sqrt{d}} e^{-15.7 d} \cos(43.15(d - 0.199))$$
 (5.34)

[5.25]. This interaction holds for dissipative solitons like the one depicted in Fig. 4.4a. Note, that the interaction depends on the spatial discretization, but interpolation (5.34) has been proven sufficient for the following considerations (Sect. 5.2.5).

Two aspects have to be taken into account for the formation of bound states: The intrinsic velocity of the interacting particles and their initial position to each other. The intrinsic velocity can be regarded as a measure for the *power* of their intrinsic drive, which is mobilized for overcoming the repulsion of the interacting counterpart. Variations of the intrinsic velocity  $\bar{c}_x(\tau)$  (4.43) can be most easily achieved by changing the time scale parameter  $\tau$  (3.69) of the slow inhibitor, because the form factor Q (4.45) and the interaction law F(d) (5.19g) do not depend on  $\tau$  in the vicinity of the drift-bifurcation  $\tau \approx \tau_c$  (4.30) but on the stationary activator distribution  $\bar{u}$ .

For the following simulations the scattering parameter  $\xi$  is introduced, which quantifies the shift of two dissipative solitons approaching each other with antiparallel velocity vectors from a reasonable distance. This configuration is described by the following initial condition:

$$\mathbf{p}_{1,0} = (-0.4, \xi)^{\mathrm{T}}, \quad \boldsymbol{\alpha}_{1,0} = (\bar{c}_{x}(\tau)/\kappa_{3}, 0)^{\mathrm{T}},$$
  
$$\mathbf{p}_{2,0} = (0.4, -\xi)^{\mathrm{T}}, \quad \boldsymbol{\alpha}_{2,0} = (-\bar{c}_{x}(\tau)/\kappa_{3}, 0)^{\mathrm{T}}.$$
 (5.35)

The relatively large initial distance  $d \ge 0.8$  between the dissipative solitons ensures, that the particles do not interact at the beginning of simulation.

Solving the reduced dynamics (5.19) for the initial conditions (5.35) with  $\tau$  and  $\xi$  chosen from the two-dimensional parameter interval  $\tau \times \xi = [\tau_c, 3.51] \times [0, 0.2]$  leads to a set of trajectories, which are analyzed with respect to constant binding distances and non vanishing angular velocities. Both quantities indicate the formation of a rotating bound state, which is indicated in Fig. 5.6a by *gray* areas, while *white* areas refer to parameter sets for which scattering occurs. The formation of rotating bound states is observed for two parameter sets  $\mathbb{B}_{\rm I}$  and  $\mathbb{B}_{\rm II}$ . Note, that  $\mathbb{B}_{\rm I}$  does not touch the  $\xi = 0$ -axis, because this special case is a head-on collision, which leads to the formation of translating bound pairs (cf. Fig. 5.1).

In order to understand the difference between solutions of parameter sets  $\mathbb{B}_{I}$  and  $B_{II}$  a parameter tuple  $(\tau, \xi)$  has been chosen from both sets. For each tuple initial conditions for the field Eq. (3.69) have been created from a stationary dissipative soliton by applying the respective initial condition of the reduced dynamics (5.35)to ansatz (5.12) with  $\varepsilon = 1$ ,  $r_u \equiv 0$ ,  $r_v \equiv 0$ ,  $R_u \equiv 0$ , and  $R_v \equiv 0$ . The initial condition reflecting  $(\tau, \xi) = (3.35, 0.02)$  is depicted in Fig. 5.6b as gray scale image of the difference between the initial concentrations of activator u and slow inhibitor v. Dark areas indicate that the local activator concentration is larger than the respective concentration of the slow inhibitor, *light* areas reflect the opposite relation between both fields. The image visualizes not only the spatial arrangement of the dissipative solitons with respect to each other, but also the excitation of their propagator modes at the beginning of the simulation. Figure 5.6b is completed by two pairs of trajectories showing the paths of the interacting dissipative solitons, which have been extracted from solutions of the field Eq. (3.69). The pairs of trajectories correspond to initial conditions chosen from  $\mathbb{B}_{I}$  and  $\mathbb{B}_{II}$  and visualize the formation of two different types of rotating bound states: One bound state with binding distance  $d_{\rm I} = 0.164$  and one with  $d_{\rm II} = 0.320$ . These binding distances are slightly larger than the roots of interaction function F(d) (5.34) at  $d_{0,I} = 0.163$  and

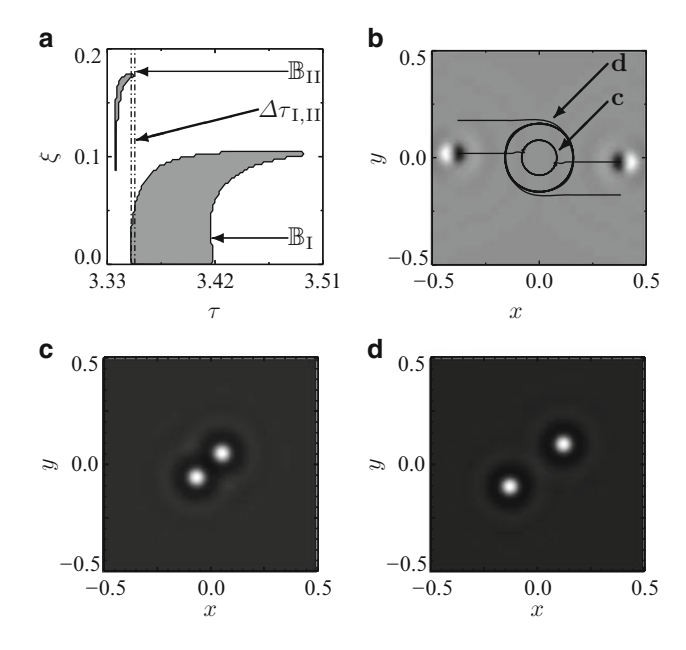
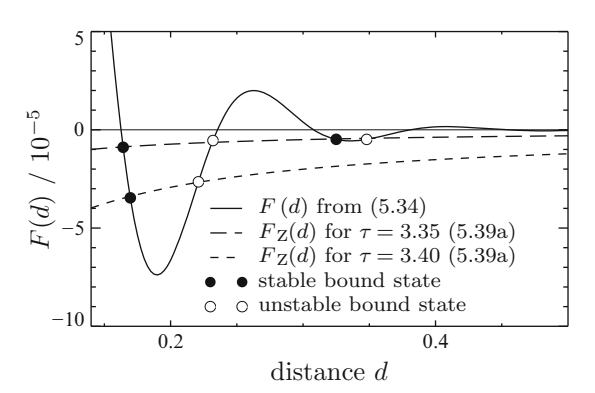


Fig. 5.6 Formation of rotating bound states in a two-dimensional reaction-diffusion system [5.26]. (a) Simulations of the reduced dynamics (5.19) with Q=1,950 and interaction F(d) given by (5.34) for varied parameters  $\tau$  and  $\xi$  (5.35). Gray areas indicate the formation of rotating bound states. (b) Initial conditions of the field Eq. (3.69) for  $(\tau, \xi) = (3.35, 0.02) \in \mathbb{B}_{\rm I}$  visualized as difference of activator and slow-inhibitor distribution. Dark and light areas indicate an activator concentration being higher and lower than the respective slow inhibitor concentration. The plotted pairs of trajectories are computed from solutions u(x,t) of the field Eq. (3.69) resulting into the bound states depicted in subfigures (c) and (d). (c) Activator distribution of a bound state with distance  $d_{\rm I}=0.164$  at  $t=4\cdot10^3$ . This bound state has formed from the initial condition depicted in subfigure (b) and rotates counterclockwise with a uniform angular velocity of  $\omega_{\rm I}=5.44\cdot10^{-3}$ . (d) Activator distribution of a bound state with distance  $d_{\rm II}=0.320$  shown at  $t=12\cdot10^3$ . The bound state has formed from initial condition  $(\tau,\xi)=(3.35,0.174)\in\mathbb{B}_{\rm II}$  and rotates counterclockwise with a uniform angular velocity of  $\omega_{\rm II}=2.90\cdot10^{-3}$ . Parameters according to (4.22) with  $\Omega=[-1,1]^2$ , no-flux boundary condition,  $\Delta_x=5\cdot10^{-3}$  and  $\Delta_t=0.1$ 

 $d_{0,\rm II}=0.308$  due to centrifugal forces, which are discussed in greater detail in the following section.

Snapshots of the activator distributions u(x,t), which correspond to the trajectory pairs depicted in Fig. 5.6b are shown in Fig. 5.6c, d as gray scale images. The bound state with smallest binding distance (Fig. 5.6c) has formed from the initial condition shown in Fig. 5.6b with  $(\tau, \xi) = (3.35, 0.02) \in \mathbb{B}_I$ . Bound states of this type can only form if the dissipative solitons are fast enough to overcome the repulsive interaction F(d) > 0 appearing at distances 0.235 < d < 0.308 (cf. Fig. 5.7). On the other hand the dissipative solitons must not propagate too fast  $(\tau > 3.494)$ , because the corresponding centrifugal forces cannot be compensated by the mutual attraction of the dissipative solitons. Note, that for the considered

Fig. 5.7 Force equilibrium of rotating dissipative soliton molecules. The graph shows the interaction F(d) and centrifugal forces for two different values of  $\tau$ . The case  $\tau=3.35$  refers to the molecule formation processed presented in Fig. 5.6b–d. Parameters from (4.22), F(d) from (5.34), Q=1,950



parameters (4.22) and  $\tau \gtrsim 3.41$  the validity of the reduced dynamics is limited. Its predictions are still qualitatively valid for interaction distances  $d \gtrsim 0.162$ , but in case of many-particle interactions, the conservation of the number of particles does not hold anymore for distances smaller than d < 0.162, which is discussed in Sect. 7.3.1.

The bound state shown in Fig. 5.6d is an example for dissipative solitons rotating with binding distance  $d_{\rm II}$ . The attraction between these dissipative solitons is much smaller than the attraction, experienced by dissipative solitons rotating with binding distance  $d_{\rm I}$ , because the oscillations of F(d) (5.34) decay exponentially. Therefore, the bound state of second type will only form if the dissipative soliton propagate slowly ( $\tau < 3.353$ ). The dissipative soliton molecule presented in Fig. 5.6d has been simulated with initial conditions (5.35) and ( $\tau, \xi$ ) = (3.35, 0.174)  $\in \mathbb{B}_{\rm II}$ . In this scenario the dissipative solitons are fast enough to overcome the repulsive interaction F(d) > 0 at 0.308 < d < 0.380 (Fig. 5.7) and slow enough to be captured by the mutual attraction F(d) > 0 at binding distance  $d_{\rm II}$ .

Figure 5.6a also reveals, that within a small parameter interval  $\tau \in \Delta \tau_{I,II} = [3.350, 3.352]$  the formation of both types of bound states is possible. This bistability is verified by simulations of the field Eq. (3.69), which have been carried out for  $\tau = 3.35$  and values of  $\xi$  according to  $\mathbb{B}_{I}$  and  $\mathbb{B}_{II}$  (Fig. 5.6b–d).

# 5.4.2 Dynamics of Rotating Bound States

The simulations performed in the context of investigating the formation of rotating bound states in two-dimensional systems on basis of the reduced dynamics (5.19) have shown (Fig. 5.6), that each binding type exhibits a certain upper limit for the intrinsic velocity  $\bar{c}_x$  of its dissipative solitons. Therefore, dissipative solitons propagating with an intrinsic velocity beyond this limit cannot form a rotating bound state. A similar scenario is observed in two-dimensional systems whose ground state is disturbed by a Gaussian-shaped parameter inhomogeneity [5.14]. Such inhomogeneities are also capable of capturing dissipative solitons and forcing them onto circular paths if the dissipative solitons are sufficiently slow, otherwise the

localized structure is simply scattered by the inhomogeneity. Both effects are caused by the propagation mechanism of dissipative solitons, which induces a certain *momentum* resulting from the shift between localized activator distribution and its counterpart of the slow inhibitor. In contrast to the inertia implied by Newtons first axiom [5.27] the velocity of the dissipative solitons cannot be tuned continuously, but has a well defined value, which is determined by the self-organized shift between activator and inhibitor distribution. However, in Newtons classical mechanics and the discussed dissipative system the direction of motion of the considered objects can only be changed by external influences. Concerning the simulations showing dissipative solitons propagating on a curved path the *directional inertia* implies, that the observed acceleration due to the continuous change of direction has to be caused by an attractive force, which in analogy to classical mechanics leads to the concept of centripetal and centrifugal forces. In the following paragraphs these concepts are deduced for the considered dissipative system on basis of the reduced dynamics (5.19).

For this purpose we are considering a two-dimensional reaction-diffusion system exhibiting a continuously rotating bound state (Fig. 5.6c). On basis of the reduced dynamics (5.19) such type of structure is described by eight dynamical equations consisting of two positions  $p_1$  and  $p_2$ , and two propagator mode amplitudes  $\alpha_1$  and  $\alpha_2$ . Each p,  $\alpha$ -pair describing the dynamics of one of the bound dissipative solitons. Due to the equilibrium velocity of dissipative solitons, the center  $p = \frac{1}{2}(p_1 + p_2)$  of the rotating bound state has to be stationary in a two-dimensional system. Therefore the dynamics are covered by the distance vector  $d = p_2 - p_1$  (5.19e), the sum of the propagator mode amplitudes  $\alpha_+ = \alpha_1 + \alpha_2$ , and the difference between them  $\alpha_- = \alpha_2 - \alpha_1$ , which leads to the following set of equations:

$$\dot{d} = \kappa_3 \alpha_- + 2F(d) \frac{d}{d},\tag{5.36a}$$

$$\dot{\boldsymbol{\alpha}}_{+} = \kappa_3^2 \left( \tau - \frac{1}{\kappa_3} \right) \boldsymbol{\alpha}_{+} - \frac{\kappa_3 Q}{4} \left( \alpha_+^2 + \alpha_-^2 \right) \boldsymbol{\alpha}_{+}, \tag{5.36b}$$

$$\dot{\boldsymbol{\alpha}}_{-} = \kappa_3^2 \left( \tau - \frac{1}{\kappa_3} \right) \boldsymbol{\alpha}_{-} - \frac{\kappa_3 Q}{4} \left( \alpha_+^2 + \alpha_-^2 \right) \boldsymbol{\alpha}_{-} + 2F(d) \frac{d}{d}. \tag{5.36c}$$

Note, that these equations are based on the assumptions, that the dissipative solitons cannot be distinguished and the symmetry of the bound states implies that the length of the propagator mode amplitudes is identical  $\alpha_1 = \alpha_2$ . Note, that the assumption of indistinguishability prevents stability considerations, which need a more complicated set of equations as discussed in [5.16, 5.23, 5.24].

The relevant degrees of freedom can be reduced even further by introducing the variables  $q_1 = d^2$ ,  $q_2 = \alpha_+^2$ ,  $q_3 = \alpha_-^2$ ,  $q_4 = d\alpha_-$ , and  $\phi(q_1) = F(d)$  which leads to the following set of equations:

$$\dot{q}_1 = 2\kappa_3 q_4 + 4\phi(q_1)q_1,\tag{5.37a}$$

$$\dot{q}_2 = 2\kappa_3^2 \left(\tau - \frac{1}{\kappa_3}\right) q_2 - \frac{\kappa_3 Q}{2} \left(q_2 + q_3\right) q_2,\tag{5.37b}$$

$$\dot{q}_3 = 2\kappa_3^2 \left(\tau - \frac{1}{\kappa_3}\right) q_3 - \frac{\kappa_3 Q}{2} \left(q_2 + q_3\right) q_3 + 4\phi(q_1) q_4, \tag{5.37c}$$

$$\dot{q}_4 = \kappa_3 q_3 + 2\phi(q_1)q_1 +$$

$$\kappa_3^2 \left( \tau - \frac{1}{\kappa_3} \right) q_4 - \frac{\kappa_3 Q}{4} \left( q_2 + q_3 \right) q_4 + 2\phi(q_1) q_4.$$
(5.37d)

Bound states are stationary solutions  $\dot{q} = (\dot{q}_1, \dots, \dot{q}_4)^T = \mathbf{0}$  of (5.37). Here, one has to consider two scenarios  $\phi(q_1) = F(d) = 0$  and  $\phi(q_1) = F(d) \neq 0$ . While the first case leads to moving bound states characterized by

$$d_0|_{F(d_0)=0}$$
,  $\alpha_+^2 = \frac{4}{Q}\kappa_3\left(\tau - \frac{1}{\kappa_3}\right)$ ,  $\alpha_-^2 = 0$ , and  $d_0\alpha_- = 0$ , (5.38)

the second case leads to rotating bound states

$$d_{\rm r}|_{F(d_r)=F_{\rm Z}(d_{\rm r})} \text{ with } F_{\rm Z}(d_{\rm r}) = -\frac{2\kappa_3^2(\tau - \frac{1}{\kappa_3})}{Q\,d_{\rm r} + \frac{4}{d_{\rm r}}},$$
 (5.39a)

$$\alpha_{-}^{2} = d_{\rm r}\alpha_{-} = -\frac{2}{\kappa_{3}}F(d_{\rm r})d_{\rm r},$$
 (5.39b)

$$\alpha_{+}^{2} = 0.$$
 (5.39c)

Note, that the moving bound state has parallel propagator mode amplitudes  $\alpha_+^2 = 4\bar{\alpha}^2$  with each dissipative soliton driven by its equilibrium propagator mode amplitude  $\bar{\alpha}$  (4.84). Furthermore, the relative position of the dissipative solitons to each other is arbitrary as long as their distance qualifies for vanishing interaction and their propagator mode amplitudes are parallel. However, simulations show, that the only stable configuration is given by the *wave-train* configuration, meaning one particle follows the other. In contrast to the moving bound state, the rotating bound state exhibits antiparallel propagator mode amplitudes (5.39c) and a well defined angle between the axis d of the bound state and anti-parallel propagator modes  $\alpha_-$  (5.39b). The angle depends on the diameter  $d_r$  of the circle on which the dissipative solitons propagate, which is defined by the equilibrium given in (5.39a). In analogy to classical mechanics, a centrifugal force  $F_Z(d)$  resulting from the curved path of propagation has to be compensated by a centripetal force F(d), which is the mere interaction F(d) between the dissipative solitons.

An example for the graphical solution of (5.39a) is depicted in Fig. 5.7, where the centrifugal force  $F_Z$  is plotted for two different values of  $\tau$ . Intersections of interaction F(d) and centrifugal force  $F_Z(d)$  denote *force* equilibria and are solutions of (5.39a), defining the distance  $d_\tau$  between the rotating dissipative solitons for the respective time-scale parameter  $\tau$ . Note, that decreasing the time-scale parameter  $\tau$  close to the limit of the drift-bifurcation point  $\tau_c$  (4.30) flattens the curve of the centrifugal force  $F_Z(d)$  (5.39a), such that the number of possible bound states increases due to successive saddle-node bifurcations. On the other hand, there

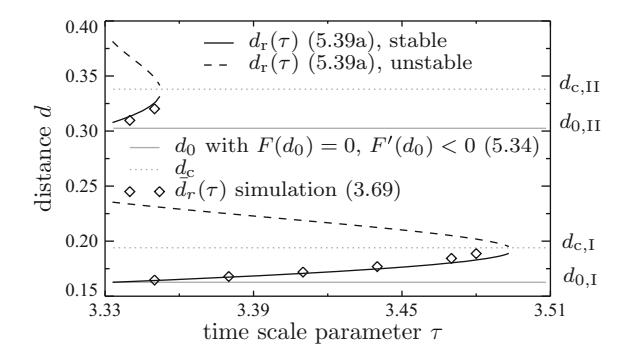


Fig. 5.8 Binding distances of rotational bound state. Black curves are predictions of the reduced dynamics (5.39a). Diamonds indicate mean binding distances derived from simulations of the field equations (Table 5.1). Gray horizontal lines reference the binding distance of stationary bound states and the maximal possible rotating state. Parameters from (4.22) with  $\Omega = [0, 1]^2$ ,  $1.25 \cdot 10^{-3} \le \Delta_x \le 5.00 \cdot 10^{-3}$ ,  $\Delta_t = 0.1$ 

do not exist any rotating bound states composed of fast dissipative solitons, which are characterized by comparatively large values of  $\tau$ . In these cases the attractive interaction cannot compensate the centrifugal force.

The stability of rotating bound states with rotational distance  $d_{\rm r}$  (5.39a) follows from the consideration, that small deviations  $|d_{\epsilon}| \ll 1$  leading to smaller distances  $d^{<} = d_{\rm r} - d_{\epsilon}$  have to be compensated by an increasing centrifugal force

$$F(d^{<}) > F_{\mathbf{Z}}(d^{<}), \tag{5.40a}$$

in order to increase the rotational distance. For deviations leading to larger rotational distances  $d^>=d_{\rm r}+d_{\rm e}$  the attractive interaction has to increase in order to decrease the distance

$$F_{\rm Z}(d^{>}) > F(d^{>}).$$
 (5.40b)

If these conditions are not fulfilled, the rotating bound state is unstable and small deviations will not decay but increase even further.

The evaluation of the equilibrium (5.39a) for varying time scale parameters  $\tau$  reveals all potential binding distances  $d_r$  of rotating dissipative solitons. In Fig. 5.8 the binding distances of the two smallest configurations 0.1627  $< d_r < 0.194 =$ :  $d_{c,I}$  (cf. Fig. 5.6c) and 0.3025  $< d_r < 0.332 =$ :  $d_{c,II}$  (cf. Fig. 5.6d) are plotted as function of  $\tau$ . In this diagram *black curves* denote binding distances  $d_r$  deduced from the force equilibrium (5.39a) with *solid* and *dashed curves* indicating stable and unstable configurations (5.40). Furthermore horizontal *gray lines* have been drawn referencing the binding distances of stable stationary states  $d_{0,I}$  and  $d_{0,II}$  (*solid lines*) and largest rotating states  $d_{c,I}$  and  $d_{c,II}$  (*dotted* lines). *Dashed curves* 

**Table 5.1** Influence of the spatial discretization  $\Delta_x$  on the binding distance  $d_r$  and the angular velocity  $\omega$  of two-dimensional rotating dissipative soliton-molecules in smallest possible configuration. The simulations have been performed for  $\tau = 3.38$ . While increasing the spatial discretization due to decreasing the discretization length  $\Delta_x$  from  $5 \cdot 10^{-3}$  to  $1.25 \cdot 10^{-3}$  changes the mean binding distance  $d_r$  and the mean angular velocity  $\omega$  only slightly, while the amplitude of the observed oscillations decreases by a factor of 6.5 concerning the binding distance and 3.5 concerning the angular velocity. Note, that discretization induced oscillations are also observed for the formation of rotating bound states documented in Fig. 5.10b. Parameters from Fig. 5.8

$\Delta_{x}$	$ar{d}_{ m r}$	$\hat{d}_{ m r}/ar{d}_{ m r}$	ω	$\hat{\omega}/\omega$
$5.00 \cdot 10^{-3}$	$1.679 \cdot 10^{-1}$	$9.1 \cdot 10^{-5}$	$8.97 \cdot 10^{-3}$	$7.5 \cdot 10^{-4}$
$2.50 \cdot 10^{-3}$	$1.680 \cdot 10^{-1}$	$2.4 \cdot 10^{-5}$	$8.99 \cdot 10^{-3}$	$1.8 \cdot 10^{-4}$
$1.25 \cdot 10^{-3}$	$1.680 \cdot 10^{-1}$	$1.4 \cdot 10^{-5}$	$8.99 \cdot 10^{-3}$	$2.1 \cdot 10^{-4}$

indicate unstable solutions. The plot is accomplished by binding distances extracted from numerical solutions of the field Eq. (3.69), which are indicated by *diamonds*.

Due to a relatively strong interaction in the vicinity of  $d_{0,\rm I}$ , the rotational distance  $d_{\rm I}$  deviates only slightly from the rotational distance of the stationary bound state for  $\tau \lesssim 3.36$ . Simulations of the second rotational state  $d_{\rm II}$  show significant larger binding distances compared to the stationary state. This tendency culminates in a backwards saddle-node-bifurcation for the critical binding distance  $d_{\rm c,II} = 0.352$  at which the bound state vanishes. The reason is the comparatively weak interaction in the vicinity of the second stationary binding distance  $d_{\rm 0,II}$  (Fig. 5.7). On the other hand the strong interaction stabilizing the first rotational state allows for significant deviations from  $d_{\rm 0,I}$  only for  $\tau \gtrsim 3.36$  and ensures the existence of this rotational state for a large range of time scale parameters  $\frac{10}{3} < \tau \lesssim 3.48$ , which has been verified on basis of field simulations.

Comparing the binding distances of rotating bound states derived from solutions of the field equations (*diamonds* in Fig. 5.8) with predictions of the reduced dynamics (*curves* in Fig. 5.8) shows an excellent agreement in the vicinity of the drift bifurcation, which does not depend on the spatial discretization of the field equations (Table 5.1). Significant deviations are visible for  $\tau \gtrsim 3.47$  for which rotational distances obtained from field solutions tend to reach the critical rotational binding distance  $d_{\rm c,I}$  for smaller values of  $\tau$  than predicted by the reduced dynamics on basis of equilibrium (5.39a).

The angular velocity  $\omega$  of a rotating bound state follows from Eqs. (5.36a) and (5.39) to

$$\omega(\tau) = \frac{|\mathbf{d}_{r}(\tau)|}{d_{r}(\tau)} = \frac{2\kappa_{3}^{2}(\tau - \frac{1}{\kappa_{3}})}{Qd_{r}^{2}(\tau) + 4}\sqrt{\frac{Qd_{r}^{2}(\tau) + 4}{\kappa_{3}(\tau - \frac{1}{\kappa_{3}})} - 4}$$
(5.41)

with  $d_r(\tau)$  given by (5.39a). This relation is visualized in Fig. 5.9 for the scenario presented in Fig. 5.8. The graph shows the angular velocity (5.41) deduced from the two-particle ansatz (5.36) as *black curves* with *solid* and *dashed lines* referring to

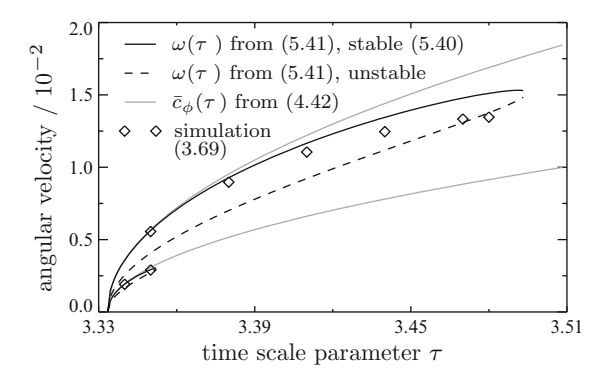


Fig. 5.9 Angular velocity of rotating bound states composed from two dissipative solitons. *Gray curves*: Angular velocity  $\bar{c}_{\phi}$  (4.42) of the one-particle approach deduced in the context of the rotational bifurcation. *Solid black curves*: Angular velocity  $\omega$  (5.41) of the stable states (5.40). *Dashed black curves*: Angular velocity (5.41) of the unstable configuration. *Diamonds*: Angular velocity obtained from solutions of the field Eq. (3.69). Parameters from Fig. 5.8

stable and unstable solutions, respectively. In retrospect to the rotational bifurcation (Sect. 4.2.5), the plot also includes the angular velocities  $\bar{c}_{\phi}$  (4.42) deduced from the related one-particle ansatz as *gray curves*. *Diamonds* refer to solutions of the three-component reaction-diffusion system (3.69).

According to the considerations of the rotational binding distances (Fig. 5.9) the angular velocities are plotted for the first and second bound state. Bound states of the second kind exhibit much smaller angular velocities compared to bound states of the first kind, which is obvious, because the same intrinsic velocity induces a longer time of circulation if the circumference is extended. This bound state does only exist for relatively slow dissipative solitons, which is in agreement with Fig. 5.8. Consequently, a rotating bound state of the second kind will break up if the time scale parameter  $\tau$  is increased about  $\tau > 3.352$ . While this effect is well covered by the two particle ansatz (5.36), it is not reflected by the one-particle approach (Sect. 4.2.5), which considers the bound state as rigid object. Concerning the rotating bound state of the first kind the prediction of angular velocities of the one-particle approach according to (4.42) agrees for a larger interval of time scale parameters ( $\frac{10}{3} < \tau \lesssim 3.39$ ) with the two-particle approach and the solutions of the field equations. This coincides with the parameter range observed for approximately constant binding distances in Fig. 5.8.

With increasing distance to the drift-bifurcation point  $\tau_c$  (4.30), the angular velocity  $\omega$  of rotating bound states obtained from simulations of the field equations deviates considerably from the square-root trend predicted by the one-particle approach (4.42). In parts, this effect is reproduced by the two-particle approach (5.41) of the reduced dynamics (5.36), which also shows significant deviations for larger values of  $\tau$ . In this parameter region the reduced dynamics fail, because the assumption of a point-to-point interaction does not hold anymore. Interestingly, the maximal possible angular velocity of the rotating bound state as

obtained from the field equations (*diamonds*) coincides approximately with the unstable branch of the angular velocity obtained from the two-particle approach (*dashed curve*). To what extent this observation is a particularity of the investigated parameter set (4.22) and agrees with reaching the maximal rotational distance at  $\tau = 3.493$  (Fig. 5.8) has to be clarified by further investigations.

## 5.4.3 Formation of Spiralling Bound States

In three-dimensional systems, bound states of dissipative solitons exhibit a much more complex dynamics than *wave train*-like solutions (Sect. 5.1) or rotating bound states (Sect. 5.4.2) observed in two-dimensional reaction-diffusion systems. Therefore, we are going to discuss a three-dimensional reaction-diffusion system with dissipative solitons, which do not move within the same plane.

The three-component reaction-diffusion system is solved for parameters, which have been successfully applied for the investigation of the formation of bound states in two-dimensional systems (cf. Fig. 5.6). Solving the reaction-diffusion equations for the parameter set (4.22) leads to localized solutions with form factor Q=1,375 and an oscillatory interaction, which is well approximated by the following function

$$F(d) = -3.865 \cdot 10^{-3} e^{-21.38d} \cos(45.81(d - 0.2180)). \tag{5.42}$$

Note, that the time scale parameter  $\tau$  of the slow inhibitor is chosen to  $\tau=3.36$  for the construction of the initial condition as well as for the simulation. The initial condition consists of two dissipative solitons approaching each other with intrinsic velocity  $\bar{c}_x = \kappa_3 \bar{\alpha}$ . The first dissipative soliton propagates to the center of the domain starting from distance  $\frac{\delta}{2}$ . The second dissipative soliton would pass the center of the domain in distance  $\xi$ , if interaction could be neglected. Additionally, its direction of motion is shifted by angle  $\varphi$  with respect to the direction of motion of the first dissipative soliton. If the first dissipative soliton propagates along the x-axis and the second one parallel to the x-y-plane, the following initial condition is constructed:

$$\begin{aligned} \boldsymbol{p}_{1,0} &= (-\frac{\delta}{2}, 0, 0), & \boldsymbol{\alpha}_{1,0} &= (\frac{\bar{c}_x}{\kappa_3}, 0, 0), \\ \boldsymbol{p}_{2,0} &= (-\frac{\delta}{2}\cos\varphi, -\frac{\delta}{2}\sin\varphi, -\xi), & \boldsymbol{\alpha}_{2,0} &= (\frac{\bar{c}_x}{\kappa_3}\cos\varphi, \frac{\bar{c}_x}{\kappa_3}\sin\varphi, 0). \end{aligned}$$
(5.43)

The geometrical relation of interaction parameters  $\varphi = \frac{5}{6}\pi$  and  $\xi = 0.208$  as well as the respective isosurfaces of activator u for u(x) = -0.1 are shown in Fig. 5.10a. For this scenario parameter  $\xi$  has been chosen such that two dissipative solitons being separated by  $d = \xi$  would experience maximal attraction with respect to (5.42) without violating the scope the reduced dynamics.

Solving the three-component reaction-diffusion system (3.69) for the initial condition depicted in Fig. 5.10a leads to a rotating bound state of two dissipative solitons, which are spiralling in a screw like motion across the cyclically continued

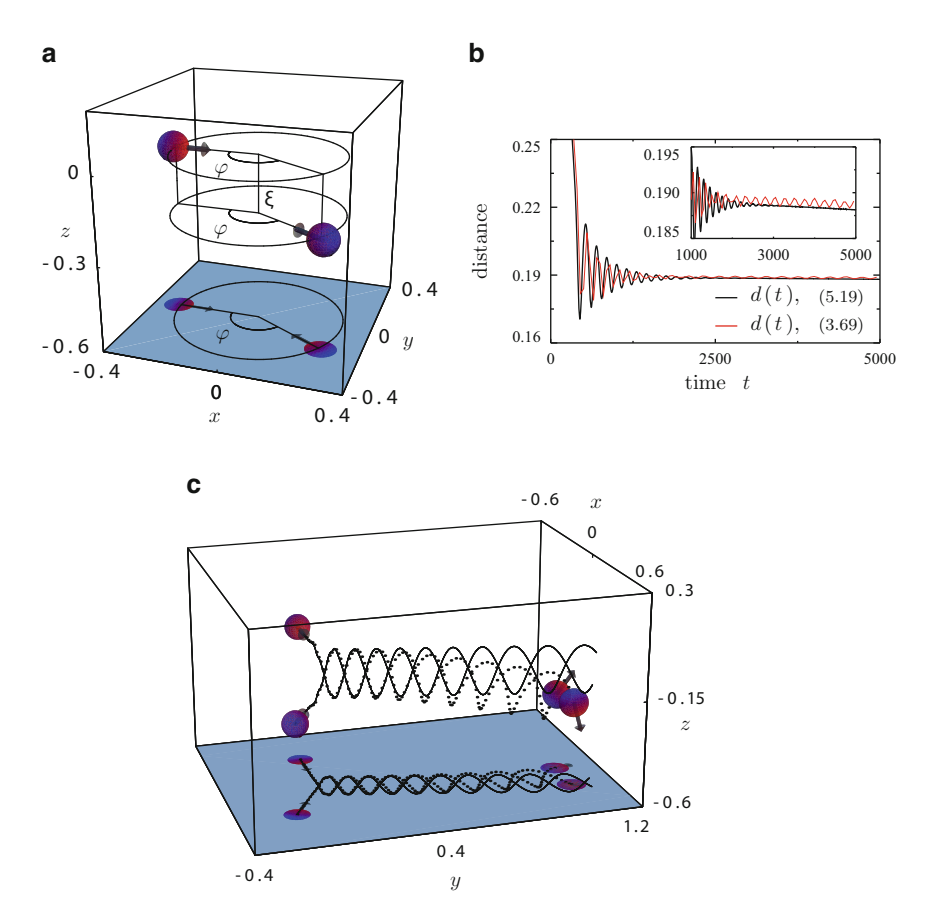


Fig. 5.10 Formation of a spiralling bound state. The activator isosurfaces depicted in (a) and (c) have been computed for u(x) = -0.1 and are coloured with respect to the local concentrations of the slow inhibitor v. Red and blue indicate low and high inhibitor concentrations, respectively. Arrows point into the direction of the propagator mode amplitudes. (a) Initial conditions defined by (5.43) for  $\delta = 0.6$ ,  $\varphi = \frac{5}{6}\pi$ ,  $\xi = 0.208$ . (b) Evolution of particle distance d(t). Black curves refer to solutions of the reduced dynamics (5.19), while red curves have been computed from solutions of the field Eq. (3.69). (c) Initial and final state of the system presented on the cyclically continued domain. Also shown are the trajectories of the centers of the dissipative solitons. Black curves and dots denote solutions of the reduced and field equations, respectively. Parameters from (4.22) with  $\tau = 3.36$ ,  $\Omega = [-0.6, 0.6]^3$ , cyclic boundary condition,  $\Delta_x = 0.01$ ,  $\Delta_t = 1.0$ , Q = 1,375, F(d) from (5.42)

domain. The distance between the dissipative solitons is nearly constant, although the distance computed from the activator centers of the field solution exhibits an oscillation of small amplitude (*red curve* in Fig. 5.10b), which is caused by the spatial discretization of the system. The amplitude of the distance oscillation is approximately one order of magnitude smaller than the discretization length  $\Delta_x$ .

The influence of the spatial discretization on the amplitude of the observed distance oscillations is discussed in Table 5.1 on page 144 in greater detail.

The dynamics of the formation process and the following spiralling propagation is visualized in Fig. 5.10c. The graph shows isosurfaces of the activator distribution for u(x) = -0.1 rendered for the initial condition (Fig. 5.10c, left hand side) and after 5,000 time steps (Fig. 5.10c, right hand side). Additionally, the trajectories of the centers of the dissipative solitons are plotted. While dotted curves correspond to solutions of the field equations with each dot representing a snapshot, the black curves result from the positions  $p_1(t)$  and  $p_2(t)$  as given by the solutions of the reduced dynamics. The trajectories show that the dissipative solitons propagate perpendicular to the plane of rotation, such that the trajectories form a double helix. While the trajectories resulting from the field Eq. (3.69) and the particle dynamics (5.19) agree very well at the beginning, the small deviations accumulate in the course of the simulation. It occurs, that the trajectories referring to the localized solutions of the field equations are bended into the direction of smaller x- and z-coordinates, while the direction of the angular momentum does not change in the particle model (5.19). This difference is accounted to the spatial discretization of the domain.

The projection of the double helix onto the bottom of the domain shows that the width of the slopes extends slightly in the course of the motion (Fig. 5.10c). This effect is caused by a small but continuous acceleration of the molecule center. Continuing the simulation on basis of the reduced dynamics (5.19) up to  $t=10^6$  reveals that the velocity of the center of the bound state relaxes to the intrinsic velocity  $\bar{c}_x$ , while the angular velocity is declining. The result is a bound state propagating perpendicular to its molecule axis d. From simulations of two-dimensional systems it is known, that this type of motion is not stable [5.15, S. 95], which has been confirmed in [5.16, 5.23, 5.24], where the dynamics of rigid bound states is discussed by means of its translational and rotational degrees of freedom. Transferring this ansatz to rigid bound states in three-dimensional systems will clarify the stability of the dynamical state described in this subsection.

# 5.5 Complex Bound States

Already in two-dimensional systems, bound states composed of three or more dissipative solitons show complex dynamics, which depend sensitively on the system parameters. The most simple example in this context is given by a bound state of three dissipative solitons. The stationary state of this system has been investigated by Schenk et al. [5.28, Fig. 5c], who showed that the dissipative solitons form a bended chain. It is characterized by an obtuse angle of  $160^{\circ} = \angle p_1 p_0 p_2$  between the outer particle at  $p_1$  and  $p_2$  and the central one being located at  $p_0$ .

Considering the parameter limit of the reduced dynamics such kind of bound states can be destabilized due to a rotational bifurcation occurring at  $\tau = \tau_c$  (4.30). For weakly excited propagator mode amplitudes the rotation is uniform, such that

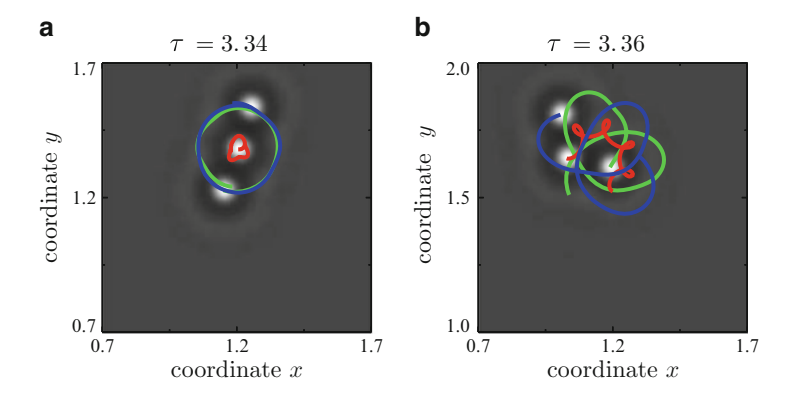


Fig. 5.11 Example for the complex dynamics of a bound state composed of three dissipative solitons as observed as solution of the field Eq. (3.69). *Red curves* represent trajectories of the central dissipative solitons, *green* and *blue curves* correspond to the outer dissipative solitons. (a) Activator concentration at t = 3,500 and trajectories for  $t \in [0,3500]$ . (b) Activator concentration at t = 3,000 and trajectories for  $t \in [0,3000]$ . Parameters from (4.22) with  $\Omega = [0,2] \times [0,2]$ , cyclic boundary condition,  $\Delta_x = 5 \cdot 10^{-3}$ ,  $\Delta_t = 0.1$ 

the outer particle propagates on a nearly circular path around the geometric center  $p_g = \frac{1}{3}(p_0 + p_1 + p_2)$  of the bound state. Due to the angled configuration of the bound state the geometric center is not identical with the position  $p_0$  of the central dissipative soliton  $p_0 \neq p_g$ . Therefore, the central particle also propagates on a circular path. This scenario is visualized in Fig. 5.11a as solution of the three-component reaction diffusion system (3.69) simulated for parameter set (4.22). Note, that the trajectory of the central dissipative soliton  $p_0(t)$  (red curve in Fig. 5.11a) is significantly influenced by the spatial discretization of the domain.

Increasing the time scale parameter slightly from  $\tau = 3.34$  (Fig. 5.11a) to  $\tau = 3.36$  (Fig. 5.11b) changes the equilibrium dynamics of the bound states qualitatively. This is surprising, because from the two-particle bound state one would anticipate a correspondingly small increase of the angular velocity (Fig. 4.6). But now the trajectory  $p_0(t)$  of the central dissipative soliton describes a looped trochoid or hypotrochoid:

A hypotrochoid is the curve traced out by a point either within or without the circumference of a circle which rolls without sliding on a fixed circle in the same plane, the rolling circle touching the inside of the fixed circle. [5.29, p. 93]

This definition hits the mark, but have a look at Fig. 5.12 which visualizes the construction. First of all, we have got two circles, a large one with diameter  $R_{\rm K}$  and a small one with diameter  $r_{\rm K}$ . In Fig. 5.12 the small circle rolls inside the larger one with angular velocity  $\omega$ . The trochoid itself is traced by point P, which in our example is fixed in distance  $a = \overline{CP}$  to the center C of the small circle. Denoting the difference between the circle radii as parameter  $b = R_{\rm K} - r_{\rm K}$  the hypotrochoid  $P(t) = (P_x(t), P_y(t))^{\rm T}$  can be parameterized by

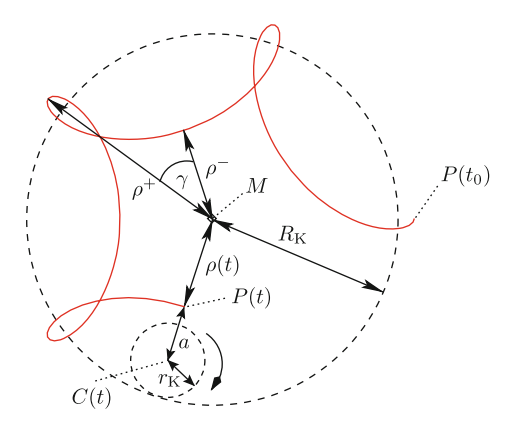


Fig. 5.12 Construction of a trochoid [5.31]. A trochoid is a plane curve P(t), which e.g. can be constructed by tracing out point P being attached to the center C of a circle, while the same circle rolls without sliding within a larger one being centered at point M. Note, that the same trochoid can be constructed by a circle rolling outside the larger one. However, the characteristic looped form of the displayed trochoid is caused by choosing parameter a to  $a = \frac{3}{2}r_{\rm K} > r_{\rm K}$ . This type of trochoid is also called hypotrochoid. Observing a hypotrochoid as curve P(t), its distance  $\rho(t)$  to the center M of the large circle is an important measure for estimating the parameters of the curve on basis of its extremes  $\rho_-$  and  $\rho_+$ 

$$P_x(t) = b\cos(\omega \cdot (t - t_0)) + a\cos\left(\frac{b}{r_K}\omega \cdot (t - t_0)\right) + M_x, \tag{5.44a}$$

$$P_{y}(t) = b\sin(\omega \cdot (t - t_0)) - a\sin\left(\frac{b}{r_{K}}\omega \cdot (t - t_0)\right) + M_{y}$$
 (5.44b)

with  $M = (M_x, M_y)^{\mathrm{T}}$  representing the center of the larger circle [5.30, S.319].

In the scenario described before (Fig. 5.11) not the complete hypotrochoid P(t) but a sample of snapshots  $p(t_0), \ldots, p(t_N)$  with  $t_{i+1} = t_i + \Delta_t$  is observed. From this time series, the current distance  $\rho(t_i)$  to the center M of the large circle can be computed by

$$\rho(t_i) = \sqrt{\left(\boldsymbol{p}(t_i) - \hat{\boldsymbol{M}}\right)^2}.$$
 (5.45)

Here,  $\hat{M}$  is an estimation of the larger circle's position

$$\hat{\mathbf{M}} = \langle \mathbf{M} \rangle = \frac{1}{N} \sum_{i=1}^{N} \mathbf{p}(t_i), \tag{5.46}$$

which can be averaged from recorded positions  $p(t_i)$  if their number N is sufficiently large. Now, the minimal distance  $\rho^- = b - a$  and the maximal distance  $\rho^+ = b + a$  can be estimated as arithmetic means:

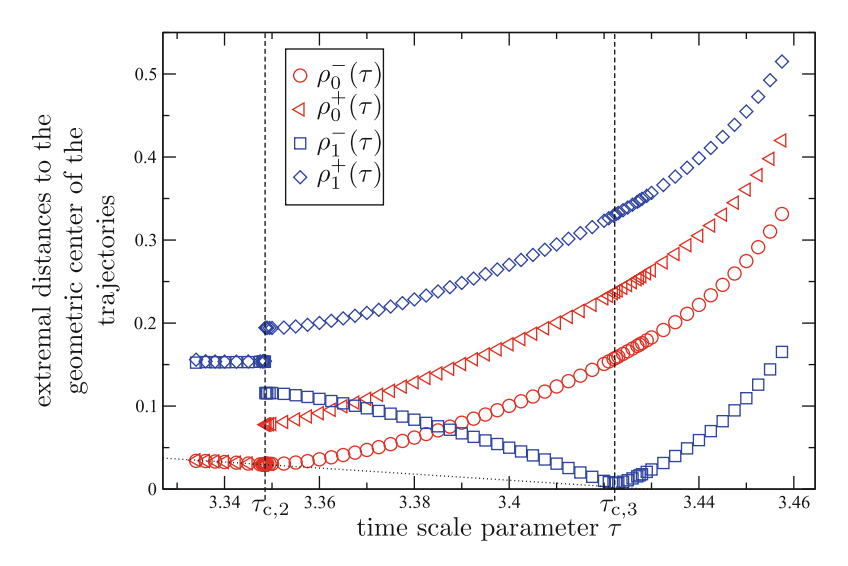


Fig. 5.13 Successive bifurcations of a complex bound state due to variations of time scale parameter  $\tau$  [5.31]. The diagrams shows fingerprints  $\rho_j^-(\tau)$  and  $\rho_j^+(\tau)$  (5.45) of the trajectories described by the central dissipative soliton (j=0, red symbols) and one of the outer dissipative solitons (j=1, blue symbols). The discontinuities of the curves and their derivatives indicate secondary and tertiary bifurcation points occurring at  $\tau_{c_2} \approx 3.349$  and  $\tau_{c_3} \approx 3.422$ . For  $\tau_c < \tau < \tau_{c,2}$  the measures  $\rho^+$  and  $\rho^-$  cannot be distinguished due to the uniform rotation of the bound state. Parameters from (4.22) with F(d) given by (5.34), Q=1,950, and  $\Delta_I=0.05$ 

$$\rho^{\pm} = \langle \rho(t_i) | \rho(t_i) \geqslant \rho(t_{i+1}) \wedge \rho(t_i) \geqslant \rho(t_{i-1}) \wedge t_i > T_0 \rangle \tag{5.47}$$

if the bound state is relaxed for  $t > T_0$ . Obviously, the quantities  $\rho^+$  and  $\rho^-$  allow for the characterization of observed or simulated hypotrochoids, because parameters  $a, b, \omega, r_K$ , and  $R_K$  of (5.44) can be estimated from these quantities [5.31].

Simulating the discussed bound state on basis of the reduced dynamics (5.19) and fingerprinting the observed trajectories by the discussed measures  $\rho^{\pm}$  reveals, that the drift-rotational bifurcation occurring at  $\tau=\tau_c=3.\bar{3}$  is followed by a secondary and a tertiary bifurcation occurring at  $\tau_{c_2}\approx 3.349$  and  $\tau_{c_3}\approx 3.422$ , which are indicated by discontinuities of  $\rho_{0,1}^{\pm}(\tau)$  and  $\frac{d}{d\tau}\rho_1^-(\tau)$  (Fig. 5.13).

After the rotational and before the secondary bifurcation the bound state rotates uniformly, such that the quantities  $\rho^+$  and  $\rho^-$  cannot be distinguished either for the central nor the outer particles ( $\tau_c < \tau < \tau_{c_2}$  in Fig. 5.13). The circular trajectories of the uniform rotation are exemplary depicted in Fig. 5.14a for  $\tau = 3.34$ . Consequently, the amplitude of the propagator modes of the rotating dissipative solitons are constant (Fig. 5.15a). Note, that the propagator mode amplitudes of the outer particles are close to their equilibrium state  $\bar{\alpha}$ , while the propagator mode amplitude of the central particle is only slightly excited, because this particle propagates on a much smaller orbit than its neighbours. However, the propagator mode amplitudes of the outer dissipative solitons are not exactly excited to their

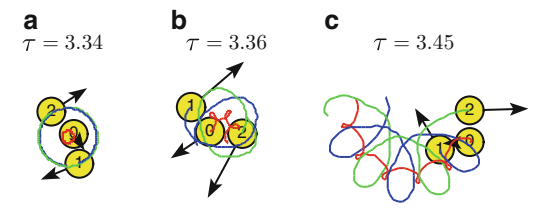


**Fig. 5.14** Trajectories of a complex bound state composed of three dissipative solitons based on simulations of the reduced dynamics [5.31]. The subfigures show the positions of the dissipative solitons at the end of the time interval for which the trajectories have been plotted. Vectors are proportional to the respective propagator mode amplitudes. (a) Circular trajectories plotted for 2,800 time steps. (b), (c) Trochoidal trajectories plotted for 1,875 time steps. Note, that the trochoids described by the outer particles in subfigure (a) have changed to hypotrochoids in subfigure (c). Parameters from Fig. 5.13

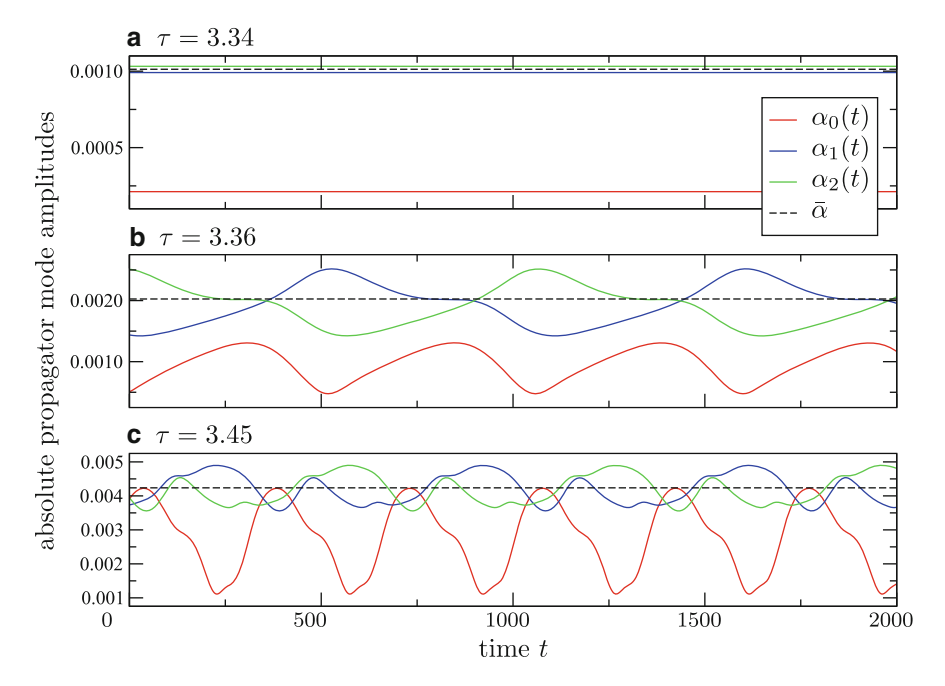
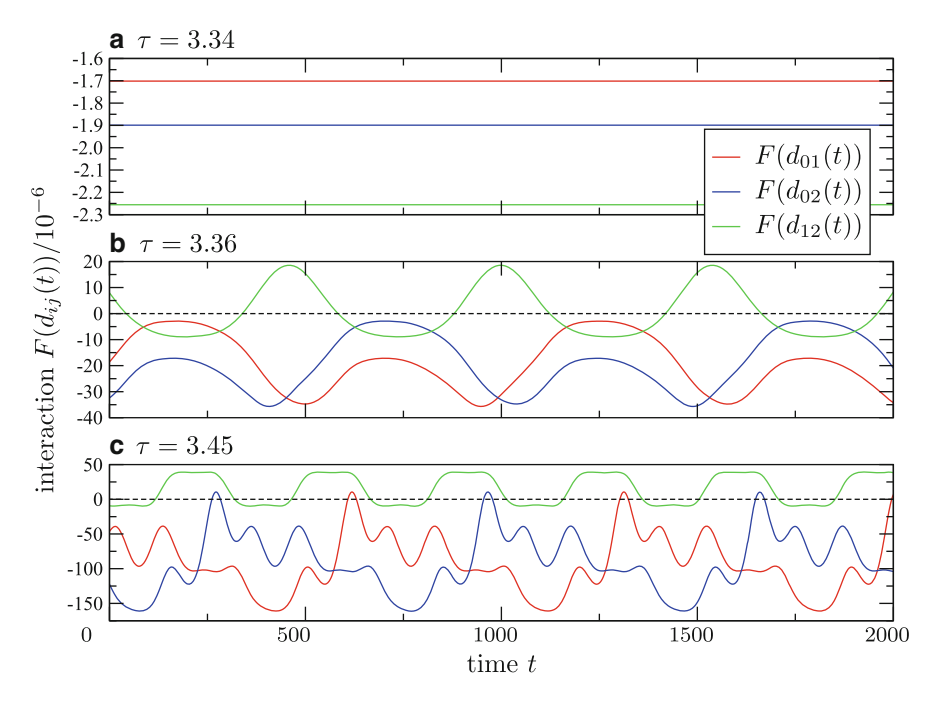


Fig. 5.15 Time series of the absolute propagator mode amplitudes for the dissipative solitons depicted in Fig. 5.14 [5.31]

equilibrium state, but particle No. 2 is slightly excited above the equilibrium level, while particle No. 1 is slightly less excited (Fig. 5.15a). This corresponds to the observation that particle No. 2 experiences a slightly larger acceleration towards the central dissipative soliton than particle No. 1 does (Fig. 5.16a).

After the secondary bifurcation, the propagator mode amplitudes oscillate inharmoniously with the outer dissipative solitons being opposite in phase with respect to



**Fig. 5.16** Time series of interaction  $F(|p_j(t)-p_i(t)|) = F(d_{ij}(t))$  between the three dissipative solitons building the bound state depicted in Fig. 5.14 [5.31]

the equilibrium propagator mode amplitude  $\bar{\alpha}$  (Fig. 5.15b). In this parameter regime between the secondary and the tertiary destabilization  $\tau_{c_2} < \tau < \tau_{c_3}$  the propagator mode amplitudes of the outer dissipative solitons are excited either too much or too little compared to  $\bar{\alpha}$ . Fig. 5.15b shows, that the overexcited state relaxes much quicker, than the under excited state of the other outer particle. Consequently, the outer dissipative soliton which has already relaxed to its equilibrium state is much faster than the other one. The latter is pushed from behind and accelerates while the pushing dissipative soliton decelerates. In Fig. 5.15b the exchange of propagator mode excitation happens at  $\alpha_1 = \alpha_2 \approx \bar{\alpha}$ . Due to the cyclic dynamics of the outer dissipative solitons the propagator mode amplitude of the inner particle oscillates twice as much as the outer ones. Its propagator mode amplitudes maximizes, if one of the outer dissipative solitons has relaxed to its equilibrium propagator mode amplitude.

After the tertiary destabilization  $\tau > \tau_{c_3}$  (Fig. 5.14c), all dissipative solitons of the bound state still show cyclic dynamics. Furthermore, the frequency of the central particle is still twice as large as the frequency of the outer particles, which retain their phase shift of one half cycle. Note, that one cycle of the outer particles can be discriminated into four phases: A long phase exhibiting a strongly excited propagator mode amplitude  $\alpha_i > \bar{\alpha}$  (i = 1, 2), two successive short phases with weak  $\alpha_i < \bar{\alpha}$  (i = 1, 2) and strong propagator mode excitation, and a long phase of

weak excitation. The absolute propagator mode amplitude of the central particle reaches its maximum  $\bar{\alpha}$ , when the propagator modes of both outer particles are weakly excited ( $\alpha_{1,2} < \bar{\alpha}$ ) at the same time. This relatively strong excitation of the central dissipative soliton's propagator mode amplitude is the reason for the qualitative difference of the dynamics beyond and before the tertiary bifurcation, which leads to the different types of hypotrochoids described by the positions of the dissipative solitons (Fig. 5.14b, c).

The described secondary bifurcation is also observed for spirals. In these systems it is the tips of the spirals which bifurcate from circular propagation to meandering paths [5.32, 5.33]. Barcley explains this transition on basis of a Hopf-bifurcation [5.34], whose modes interact with the eigenmodes of the euclidean symmetry. In case of the bound state, the bifurcation occurs at  $\tau \approx \tau_{c_2} \approx 3.3458$ . For this value of control parameter  $\tau$  we know from investigations of two-particle bound states (Fig. 5.8 and 5.9), that two interacting dissipative solitons cannot bound with second closest binding distance, due to their large intrinsic velocity, which cannot be compensated by the attractive interaction. Concerning the bound states of three dissipative solitons, this means, that the outer particles do not propagate anymore in a monotonic radial symmetric interaction field centered around the molecules geometric center (cf. Fig. 5.16a, b). They rather propagate within the relatively strong attraction of the central dissipative soliton, while the sign of their mutual interaction changes with their spatial orientation to each other. The frequency of this alternation corresponds to the amplitude of a Hopf-mode, whose interaction with the Goldstone-modes of the euclidean symmetry leads to the meandering of the central dissipative soliton.

This consideration also clarifies, why an ongoing increase of time-scale parameter  $\tau$  results into a tertiary bifurcation. Apparently, the propagator mode amplitudes of the outer dissipative solitons can be excited so much, that they enter a region of repulsion concerning the central dissipative soliton. E.g. the local maximum of absolute propagator mode amplitude  $\alpha_1(t)$  in Fig. 5.15c coincides with each second relative maximum of  $F(d_{01}(t))$  in Fig. 5.16c. The resulting push between outer and central particle is the reason of the qualitative difference between the molecule dynamics before and after the tertiary bifurcation.

# 5.6 Many-Particle Dynamics

In the semiconductor-gas-discharge system, one frequently observes configurations with many interacting dissipative solitons. One of the most interesting scenarios in this context is the observation of *phase equilibria* between a cluster of dissipative solitons and free dissipative solitons (Sect. 2.2.5.4). If the number of dissipative solitons in such scenarios is preserved, the generalized reduced dynamics (5.20) can be applied for investigating the underlying mechanisms, which has extensively been done by Röttger [5.31] and Bödeker [5.35]. Due to its complexity, this topic deserves a book on its own and only the most remarkable results are summarized.

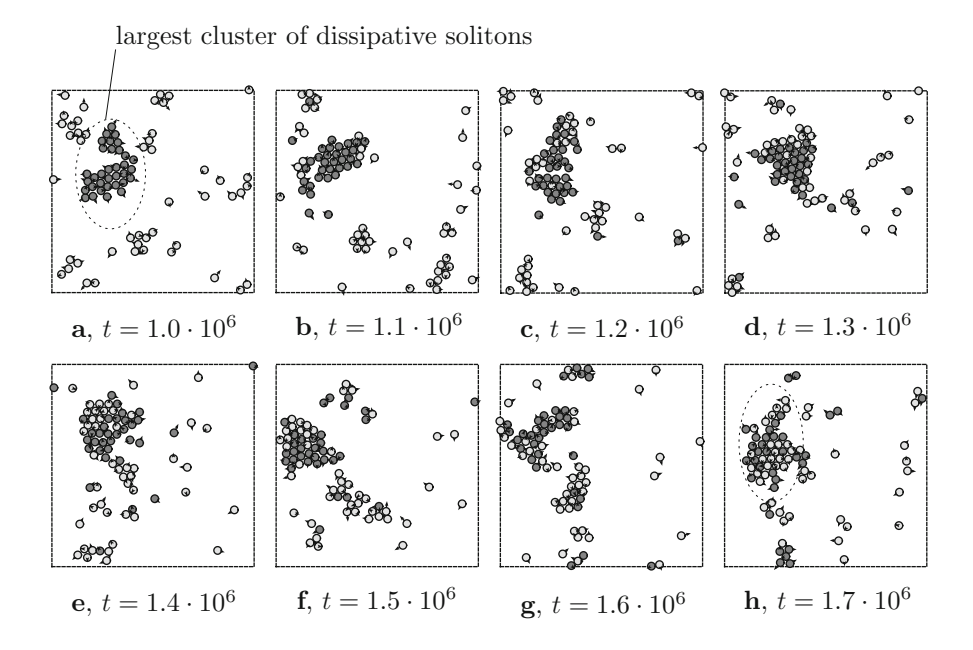


Fig. 5.17 Simulation of many-particle system under the influence of noise [5.31]. The subfigures show snapshots of system (5.48). Circles indicate the positions  $p_i(t)$  of the dissipative solitons while the attached vectors indicate the direction of the respective propagator mode amplitudes  $\alpha_i(t)$ . In subfigure (a) the dissipative solitons of the largest cluster are shaded in *dark gray*, while the remaining dissipative solitons are shaded in *light gray*. The shading is held fixed for subfigures (b)-h, such that the time series shows an ongoing mixing of the dissipative solitons. Parameters:  $\tau = 3.34$ , Q = 1,950, F(d) according to (5.34), N = 81,  $\Omega = [-2,2]^2$ , periodic boundary condition,  $\Delta_t = 0.1$ ,  $R = 2.2 \cdot 10^{-4}$ 

In order to account for the influence of noise the equations of propagator mode (5.20b) of the generalized reduced dynamics (5.20) are extended by an additive noise term  $R\Gamma$ :

$$\dot{\boldsymbol{p}}_{i} = \kappa_{3}\boldsymbol{\alpha}_{i} - \boldsymbol{W}_{i}(\boldsymbol{p}_{1}, \dots, \boldsymbol{p}_{N}) + \boldsymbol{W}_{\kappa_{1}}(\boldsymbol{p}_{i}), \tag{5.48a}$$

$$\dot{\boldsymbol{\alpha}}_{i} = \kappa_{3}^{2} \left(\tau - \frac{1}{\kappa_{3}}\right)\boldsymbol{\alpha}_{i} - \kappa_{3}Q\boldsymbol{\alpha}_{i}^{2}\boldsymbol{\alpha}_{i} - \boldsymbol{W}_{i}(\boldsymbol{p}_{1}, \dots, \boldsymbol{p}_{N}) + \boldsymbol{W}_{\kappa_{1}}(\boldsymbol{p}_{i}) + R\boldsymbol{\Gamma} \tag{5.48b}$$

with  $W_i(p_1, ..., p_N)$  given by (5.20c), while R and  $\Gamma$  denoting a noise amplitude and Langevin-force, respectively (Sect. 6.1). The numerical solver for these equations is described in Sect. 6.3.

The simulation series starts with a cluster of 81 dissipative solitons which are arranged in a hexagonal grid and the resulting 324 ordinary differential Eq. (5.48) are solved with respect to parameter set (4.22) leading to the two-particle interaction F(d) according to (5.34) and form factor Q = 1,950. The noise amplitude has

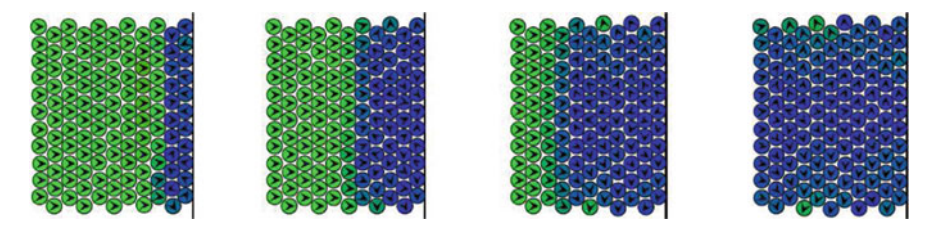


Fig. 5.18 Compression wave in bulk of dissipative solitons [5.31]. The bulk is subject to a headon collision with the domain boundary, where it sticks due to the no-flux boundary condition. The snapshots were taken with 500 time steps in between. The dissipative solitons are colored with respect to their propagator mode amplitude, with *green* indicating the equilibrium state and blue referring to small propagator mode amplitudes. Parameters:  $\tau = 3.36$ , Q = 1,950, F(d) according to (5.34), N = 121,  $\Omega = [-2, 2]^2$ ,  $\Delta_t = 0.1$ 

been chosen to  $R=2.2\cdot 10^{-4}$ . Time scale parameter  $\tau$  is set to 3.34. The result of the simulation is shown in Fig. 5.17. After a relaxation time of  $10^6$  some of the dissipative solitons are dissolved from the cluster (Fig. 5.17a) and propagate in small clusters or as unbounded particles through the surrounding area. The largest remaining cluster consists of 34 dissipative solitons, which have been marked by dark shading in Fig. 5.17a. The following snapshots have been taken with  $10^6$  time steps in between, while the dark shading of the dissipative solitons marked in Fig. 5.17a has been held fixed. The time series shows, that the size of the largest cluster is approximately preserved, while light shaded dissipative solitons continuously integrate into the large cluster and dark shaded dissipative solitons dissolve into the surrounding area (Fig. 5.17b–h). These processes obviously have reached some kind of equilibrium which is similar to the experimental observation discussed in Sect. 2.2.5.4.

A cluster of dissipative solitons, which does only change slightly for small noise amplitudes, dissolves completely due to an increase of the noise amplitude [5.31]. For large noise amplitudes the system still exhibits small clusters of dissipative solitons. This short-range order associates a liquid state, which is clearly distinguishable from the hexagonally ordered solid state of large clusters. Therefore, the noise induced transition reported by Röttger can be interpreted as phase transition and the example discussed in Fig. 5.17 represents a phase equilibrium of a solid and a liquid phase.

Another example for many particle interaction is shown in Fig. 5.18. Here a bulk of 121 hexagonally ordered dissipative solitons has collided with the domain boundary, where it sticks due to the no-flux boundary condition. A compression wave is propagating through the cluster of dissipative solitons switching the dissipative solitons from equilibrium propagator mode amplitude (*green*) to vanishing propagator mode excitation (*blue*). The wave propagates approximately one order of magnitude faster than the individual dissipative soliton and the cluster of dissipative soliton as a whole could propagate [5.31].

References 157

#### References

5.1. P.R.J. Boscovich, *Theoria philosophiae naturalis. Redacta ad unicam legem virium in natura existentium* (Remondiniana, Venedig, 1763)

- R.J. Boscovich, A Theory of Natural Philosophy. English Edition From the Text of the First Venetian Edition Published Under the Personal Superintendence of The Author in 1763 (MIT, Cambridge, 1966)
- 5.3. M.C. Cross, P.C. Hohenberg, Rev. Mod. Phys. **65**(3), 851 (1993)
- 5.4. C. Elphick, E. Meron, E.A. Spiegel, Phys. Rev. Lett. **61** (1988)
- 5.5. C. Elphick, E. Meron, E.A. Spiegel, SIAM J. Appl. Math. **50**(2), 490 (1990)
- 5.6. C. Elphick, G.R. Ierley, O. Regev, E.A. Spiegel, Phys. Rev. A 44(2), 1110 (1991)
- 5.7. D. Barkley, Phys. D 49(1-2), 61 (1991)
- 5.8. M. Or-Guil, I.G. Kevrekidis, M. Bär, Phys. D 135, 154 (2000)
- 5.9. T. Ohta, J. Kiyose, M. Mimura, J. Phys. Soc. Jpn. **66**(5), 1551 (1997)
- 5.10. T. Ohta, Physica D **151**(1), 61 (2001)
- 5.11. S.I. Ei, M. Mimura, M. Nagayama, Phys. D 165(3–4), 176 (2002). doi: 10.1016/ S0167-2789(02)00379-2
- 5.12. T. Teramoto, K.I. Ueda, Y. Nishiura, Phys. Rev. E 69(056224), 1 (2004)
- 5.13. M. Bode, Physica D **106**(3–4), 270 (1997)
- 5.14. M. Bode, A.W. Liehr, C.P. Schenk, H.-G. Purwins, Phys. D **161**(1–2), 45 (2002)
- 5.15. C.P. Schenk, Numerische und analytische Untersuchung solitärer Strukturen in zwei- und dreikomponentigen Reaktions-Diffusions-Systemen. Dissertation, Institut für Angewandte Physik, Westfälische Wilhelms-Universität Münster (1999)
- 5.16. A. Moskalenko, Dynamische gebundene Zustände und Drift-Rotations-Dynamik von dissipativen Solitonen. Master's thesis, Institut für Angewandte Physik, Westfälische Wilhelms-Universität Münster (2002)
- M.J. Ward, D. McInerney, P. Houston, D. Gavaghan, P. Maini, SIAM J. Appl. Math. 62(4), 1297 (2002)
- Y. Nishiura, T. Teramoto, X. Yuan, K.I. Ueda, Chaos 17(037104), 1 (2007). doi: 10.1063/1. 2778553
- 5.19. X. Yuan, T. Teramoto, Y. Nishiura, Phys. Rev. E **75**(036220), 1 (2007)
- 5.20. T. Teramoto, X. Yuan, M. Bär, Y. Nishiura, Phys. Rev. E 79(046205), 1 (2009). doi: 10.1103/ PhysRevE.79.046205
- 5.21. Y. Nishiura, T. Teramoto, X. Yuan, Commun. Pure Appl. Anal **11**(1), 307 (2012). doi: 10. 3934/cpaa.2012.11.307
- 5.22. L.L. Whyte, in *Roger Joseph Boscovich, S.J., F.R.S., 1711–1787, Studies of His Life and Work on The 250th Anniversary of his Birth*, ed. by L.L. Whyte (Fordham University Press, New York, 1961), pp. 102–126
- 5.23. A. Moskalenko, A.W. Liehr, M. Bode, H.-G. Purwins, in *International Conference on Theoretical Physics*, July 22–27, 2002, Paris (2002), p. 321
- 5.24. A. Moskalenko, A.W. Liehr, M.C. Röttger, M. Bode, H.-G. Purwins, in *Verhandl. DPG (VI)*, vol. 37 (Deutsche Physikalische Gesellschaft e. V., 2002), vol. 37, p. 125. Frühjahrstagung des Arbeitskreises Festkörperphysik bei der DPG, Regensburg vom 11. bis 15.03.2002
- 5.25. M. Bode, A.W. Liehr, C.P. Schenk, H.-G. Purwins, Phys. D 165(1-2), 127 (2002)
- 5.26. A.W. Liehr, A.S. Moskalenko, Yu.A. Astrov, M. Bode, H.-G. Purwins, Eur. Phys. J. B 37, 199 (2004). Figures published with kind permission of EDP Sciences
- 5.27. I. Newton, Philosophiæ naturalis principia mathematica (Innys, London, 1726). http://resolver.sub.uni-goettingen.de/purl?PPN512261393
- 5.28. C.P. Schenk, P. Schütz, M. Bode, H.-G. Purwins, Phys. Rev. E **57**(6), 6480 (1998)
- 5.29. R.A. Proctor, A Treatise on the Cycloid and all Forms of Cycloidal Curves and on the Use of Such Curves Dealing With Motions of Planets, Comets, and of Matter Projected From the Sun (Longmans, Green and Co., London, 1879). http://historical.library.cornell.edu/cgi-bin/cul.math/docviewer?did=02260001&seq=9

- 5.30. H. Stöcker (ed.), *Taschenbuch mathematischer Formeln und moderner Verfahren*, 3rd edn. (Verlag Harri Deutsch, Thun und Frankfurt am Main, 1995)
- 5.31. M.C. Röttger, Numerische Untersuchungen zur reduzierten Dynamik dissipativer Solitonen in einem dreikomponentigen Reaktions-Diffusions-System. Master's thesis, Institut für Angewandte Physik, Westfälische Wilhelms-Universität Münster (2003). Figures published with kind permission of the author.
- 5.32. D. Barkley, M. Kness, L.S. Tuckerman, Phys. Rev. A **42**(4), 2489 (1990)
- 5.33. A.T. Winfree, Chaos **1**(3), 303 (1991)
- 5.34. D. Barkley, Phys. Rev. Lett. **72**(1), 164 (1994)
- 5.35. H.U. Bödeker, Universal properties of self-organized localized structures. Dissertation, Institut für Angewandte Physik, Westfälische Wilhelms-Universität Münster (2007). http://nbn-resolving.de/urn/resolver.pl?urn=urn:nbn:de:hbz:6-68579565596

# **Chapter 6 Dynamics and Interaction of Experimental Dissipative Solitons**

We now know that science cannot grow out of empiricism alone, that in the construction of science we need to use free invention which only a posteriori can be confronted with experience as to its usefulness.

Albert Einstein, 1932 [6.1], translation cited from [6.2, p. 14].

**Abstract** Encouraged by the successful description of the dynamics and interaction of dissipative solitons by means of the particle approach, the concept is applied to experimentally observed dissipative solitons. Because the deterministic dynamics of dissipative solitons is superimposed by stochastic processes, a stochastic time series analysis is discussed, which enables not only the measurement of the drift-bifurcation but also the interaction between dissipative solitons.

## 6.1 Stochastic Time Series Analysis

Motivated by the particle description of dissipative solitons on basis of the reduced dynamics (5.19), the question arises if the dynamics (Fig. 2.15) and particle-preserving interaction (Figs. 2.16 and 2.17) of dissipative solitons observed in the semiconductor-gas-discharge experiment also can be described in the scope of a particle approach. Because the dynamics of experimentally observed dissipative solitons is perturbed by strong fluctuations, this section discusses a method of stochastic time series analysis, which has been introduced by Friedrich et al. for separating the observed dynamics into its deterministic and its stochastic part [6.3, 6.4]. This method is adapted towards the analysis of two-dimensional particle trajectories by means of a projection technique (Sect. 6.2). The data analysis is checked on basis of simulated particle trajectories and is applied to trajectories of experimentally observed dissipative solitons (Sect. 6.3). The investigations show,

that the dynamics of experimentally observed dissipative solitons can always be categorized to two qualitatively different types of propagation: Purely noise driven dissipative solitons with over-damped intrinsic dynamics (Brownian motion) and active Brownian motion, which is characterized by a finite equilibrium velocity of the dissipative solitons being superimposed by noise. The transition between both states can be observed due to variation of suitable control parameters and, according to theoretical considerations (Sect. 4.2), is identified as drift-bifurcation (Sect. 6.4). Furthermore, the stochastic data analysis method is extended towards the measurement of the interaction of experimentally observed dissipative solitons. These investigations reveal a distance dependent interaction law with alternating sign (Sect. 6.5), which can be attributed to the oscillating tails of the dissipative solitons in agreement with the theoretical considerations (Sect. 5.2.3).

An important class of stochastic systems consists of continuous n-dimensional Markov-Systems, which are described by Langevin-equations:

$$\dot{q}_i(t) = h_i(q, t) + R_{ii}(q(t), t)\Gamma_i(t), \quad i = 1, \dots, n.$$
 (6.1)

The dynamics of the n time-dependent quantities  $(q_1(t), \ldots, q_n(t))^T = \boldsymbol{q}(t)$  is determined by a deterministic and a stochastic part. The deterministic part is modelled by function  $\boldsymbol{h} = (h_1, \ldots, h_n)^T$ , while the stochastic part is given as product of noise amplitude matrix  $\underline{\boldsymbol{R}}(\boldsymbol{q},t)$  and fluctuating Langevin-force  $\boldsymbol{\Gamma}$ . In most cases, the latter is assumed to be  $\delta$ -correlated Gaussian noise with vanishing mean:

$$\langle \Gamma_i(t) \rangle = 0,$$
  $i = 1, \dots, n,$  (6.2a)

$$\langle \Gamma_i(t)\Gamma_j(t')\rangle = 2\delta_{ij}\delta(t-t'), \qquad i,j=1,\ldots,n.$$
 (6.2b)

Here  $\langle \cdot \rangle$  denotes the ensemble mean, while (6.2b) characterizes the fluctuations as Gaussian white noise. Starting from this ansatz and having in mind the definition of Stratonovich concerning stochastic integrals [6.5], the following relations can be deduced for solution  $\hat{q}(t)$  of (6.1) [6.6, 6.7]:

$$h_i(\boldsymbol{q}) + R_{kj}(\boldsymbol{q}) \frac{\partial}{\partial q_k} R_{ij}(\boldsymbol{q}) = \lim_{\Delta_t \to 0} \frac{1}{\Delta_t} \left\langle \dot{q}_i(t + \Delta_t) - \dot{q}_i(t) \right\rangle \Big|_{\dot{\boldsymbol{q}}(t) = \boldsymbol{q}}, \tag{6.3}$$

$$R_{ik}(\boldsymbol{q})R_{jk}(\boldsymbol{q}) = \frac{1}{2} \lim_{\Delta_t \to 0} \frac{1}{\Delta_t} \left\langle \left( \dot{q}_i(t + \Delta_t) - \dot{q}_i(t) \right) \cdot \left( \dot{q}_j(t + \Delta_t) - \dot{q}_j(t) \right)^T \right\rangle \Big|_{\dot{\boldsymbol{q}}(t) = \boldsymbol{q}}.$$
(6.4)

For practical reasons, it can be assumed, that Eqs. (6.3) and (6.4) are also valid for finite  $\Delta_t$ , if  $\Delta_t$  is smaller than the characteristic time-scale of the investigated system [6.3,6.4] and greater than the correlation time of the noise [6.8]. In this case the ensemble mean is replaced by the mean of  $\hat{q}(t_i) \approx q$  of all observations at  $t_i = 1$ 

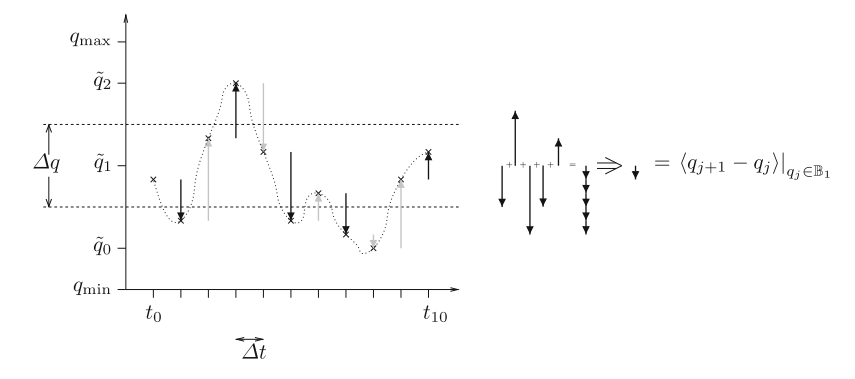


Fig. 6.1 Illustration of the stochastic data analysis in one dimension [6.10]. The graph shows the evolution of signal q(t) which is determined by deterministic and stochastic dynamics. Signal q(t) is sampled to time series  $q_i = q(t_i)$ . The differences  $\Delta q_j = (q_{j+1} - q_j)$  between successive samples  $q_j$  and  $q_{j+1}$  are shown as vectors with length  $\Delta q_j$ . In order to estimate the deterministic part of the dynamics, the interval  $[q_{\min}, q_{\max}]$  is partitioned into three bins  $\mathbb{B}_i$ , i = 1, 2, 3 of width  $\Delta_q$ , which are centered around  $\tilde{q}_i$ . In the illustrated example, the averaging is shown for bin  $\mathbb{B}_1$  as summation of all differences  $\Delta q_j$  with  $q_j \in \mathbb{B}_1$  (black vectors) and subsequent division by the number  $N_1 = 5$  of summands. Dividing the result by  $\Delta_t$  gives an estimation of the deterministic dynamics  $h(\tilde{q}_1)$ 

 $t_0+i\Delta_t$ . Note, that the second term on the left hand side of (6.3) vanishes for additive noise. The same holds for the interpretation of the Langevin-equation (6.2) in terms of Itô's theory, which can be shown by considering generalized Stratonovich-integrals [6.9].

In order to illustrate the practical application of this analysis technique Fig. 6.1 shows the evolution of signal

$$q(t) \in [q_{min}, q_{max}] \subset \mathbb{R}. \tag{6.5}$$

In the course of a simulated measurement, signal q(t) is sampled at  $t_j = t_0 + j\Delta_t$  with  $j = 0, \ldots, 10$  leading to time series  $q_j := q(t_j)$ . Because the series has to be discretized for the analysis, interval  $[q_{min}, q_{max}]$  is partitioned into three non-overlapping subsets  $\mathbb{B}_i = \left[\tilde{q}_i - \frac{\Delta_q}{2}, \tilde{q}_i + \frac{\Delta_q}{2}\right]$  for i = 0, 1 and  $\mathbb{B}_2 = \left[\tilde{q}_2 - \frac{\Delta_q}{2}, \tilde{q}_2 + \frac{\Delta_q}{2}\right]$ . Each subset is centered around  $\tilde{q}_i$  and has width  $\Delta_q$ . In the course of the discussion these subsets  $\mathbb{B}_i$  are called bins.

The algorithm of the analysis consists of the following steps: First of all scalar  $\hat{q}_i = 0$  and counter  $N_i = 0$  are initialized for each bin  $\mathbb{B}_i$ . Each sample  $q_j$  is assigned to the corresponding bin  $q_j \in \mathbb{B}_i$ , the respective counter  $N_i$  is increased by one, and scalar  $\hat{q}_i$  is increased by the difference  $(q_{j+1}-q_j)$ . After assigning all elements of the time series to a bin, their mean  $\langle q_{j+1}-q_j\rangle\big|_{q_j\in\mathbb{B}_i}$  is the quotient of scalar  $\hat{q}_i$  and counter  $N_i$ . The algorithm is visualized in Fig. 6.1 by drawing vectors of length  $(q_{j+1}-q_j)$  for each sample  $q_i$ . In this example black vectors mark samples belonging to bin  $\mathbb{B}_1$ . The average  $\langle q_{j+1}-q_j\rangle\big|_{q_j\in\mathbb{B}_1}$  is the sum of all vectors belonging to bin  $\mathbb{B}_1$  divided by the number  $N_1$  of accounted vectors.

Assuming that the noise amplitude does not depend on q, the number of samples is sufficiently large, and the discretization length  $\Delta_q$  is small compared to the time scale of the deterministic dynamics  $h(\bar{q}_i)$ , the latter can be computed from (6.3) by evaluating

$$h(\tilde{q}_i) \approx \frac{\langle q_{j+1} - q_j \rangle \Big|_{q_j \in \mathbb{B}_i}}{\Delta_t}.$$
 (6.6)

The statistical error of the estimation is proportional to  $(N\Delta_t)^{-\frac{1}{2}}$  [6.11].

### 6.2 Adaption to Two-Dimensional Trajectories

In order to model the motion of a particle in a two-dimensional system, one would choose the position  $p(t) = (p_x, p_y)^T$  of its center of mass. In a conservative system, its dynamics are modelled by the following equation of motion:

$$\ddot{\mathbf{p}}(t) = \mathbf{f}(\mathbf{p}(t)). \tag{6.7}$$

Due to the fact, that the investigated semiconductor-gas discharge system is dissipative, additional terms modelling dissipation and fluctuation have to be taken into account:

$$\ddot{\boldsymbol{p}}(t) = \boldsymbol{f}(\boldsymbol{p}(t)) + \boldsymbol{h}(\boldsymbol{p}(t), \dot{\boldsymbol{p}}(t)) + \underline{\boldsymbol{R}}(\boldsymbol{p}(t), \dot{\boldsymbol{p}}(t)) \boldsymbol{\Gamma}(\boldsymbol{p}(t), t). \tag{6.8}$$

Here, quantity h models the acceleration due to friction and internal degrees of freedom, while  $\underline{R}\Gamma$  covers fluctuations being characterized by noise amplitude matrix  $\underline{R}$ . Due to the homogeneity of the investigated experimental system, term f vanishes and the quantities h,  $\underline{R}$ , and  $\Gamma$  do not depend on position p. Therefore, (6.8) simplifies to

$$\ddot{\mathbf{p}} = \dot{\mathbf{v}} = \mathbf{h}(\mathbf{v}) + \underline{\mathbf{R}}(\mathbf{v}(t)) \mathbf{\Gamma}(t). \tag{6.9}$$

In order to apply the analysis technique described in the foregoing section, (6.2) has to be fulfilled. Of course, (6.2a) can always be fulfilled by taking an offset of h into account. Furthermore, the validity of (6.2b) is approximately given, if the correlation of the noise decays on a smaller time scale than the characteristic time scale of the investigated dynamics [6.8].

At least for some experimental configurations, the measurement of the noise amplitude matrix  $\underline{\mathbf{R}}$  on basis of (6.4) shows, that the noise amplitudes do not depend on the velocity of the dissipative solitons [6.10]:

$$\mathbf{R}(\mathbf{v}) = R = \text{const.} \tag{6.10}$$

In these cases, the deterministic dynamics h(v) can be estimated on basis of (6.3). Otherwise, if the experimental system is found to exhibit multiplicative noise, the Langevin-equation (6.2) has to be interpreted by Itô's calculus, which requires a different approach for deducing the following results [6.12] but does not alter the resulting projection method.

For the following considerations, the final size of the experimental system is neglected. Following from the O(2) symmetry of the system, the rotational symmetry of h(v) is taken into account, such that (6.9) transforms to

$$\dot{\boldsymbol{v}} = h_{\boldsymbol{v}}(\boldsymbol{v})\,\boldsymbol{e}_{\boldsymbol{v}} + R\,\boldsymbol{\Gamma}(t) \tag{6.11}$$

for  $h(v) = h_v(e)e_v$  with  $e_v = \frac{v}{v}$ . The analysis of two-dimensional particle trajectories on basis of (6.11) demands a large number of sampling points, in order to gain a sufficiently accurate estimation of the deterministic dynamics. Therefore, it is important to enhance the statistics by reducing the degrees of freedom of the system by explicitly taking the radial symmetry of h(v) into account. Consequently, (6.11) is considered in polar coordinates

$$\begin{pmatrix} \dot{v} \\ \dot{\varphi} \end{pmatrix} = \begin{pmatrix} h_v(v) \\ 0 \end{pmatrix} + \begin{pmatrix} R \cos \varphi & R \sin \varphi \\ -\frac{R}{v} \sin \varphi & \frac{R}{v} \cos \varphi \end{pmatrix} \begin{pmatrix} \Gamma_x \\ \Gamma_y \end{pmatrix}$$
(6.12)

with  $\Gamma = (\Gamma_x, \Gamma_y)$  while having Stratonovich's interpretation in mind. Starting from this ansatz, it can be shown that a solution  $\dot{v}(t)$  of (6.12) approximately fulfills the following relation

$$h_v(v) + \frac{R^2(v)}{v} \approx \frac{1}{\Delta_t} \langle \acute{v}(t + \Delta_t) - \acute{v}(t) \rangle|_{\acute{v}(t) \approx v}$$
 (6.13)

[6.10]. Alternatively the deterministic dynamics  $h_v(v)$  can be estimated from  $\acute{v}(t)$  by using projection

$$h_{v}(v) \approx \frac{1}{\Delta_{t}} \left| \frac{(\acute{\boldsymbol{v}}(t + \Delta_{t}) - \acute{\boldsymbol{v}}(t)) \cdot \acute{\boldsymbol{v}}(t)}{\acute{\boldsymbol{v}}(t)} \right|_{\acute{\boldsymbol{p}}(t) \approx v}. \tag{6.14}$$

Due to this projection, the bins, which have been introduced in the foregoing section, transform to rings of middle radius  $\tilde{q}_i$  and width  $\Delta_q$ .

#### **6.3** Brownian and Active Brownian Motion

Although Eqs. (6.13)–(6.14) have been deduced mathematically, it is not clear how efficient the algorithm works for finite numbers of sampling points. Therefore, it is important to test the suggested analysis technique on basis of a suitable Langevin-equation, whose solution can be analyzed in turn with respect to (6.14).

The comparison of the deterministic dynamics of the numerically solved Langevinequation and the result of the stochastic data analysis can be regarded as adequate test of the method.

Starting point for constructing a Langevin-equation is the reduced dynamics of single dissipative soliton (4.83) to which an additional noise term fulfilling (6.2) is added:

$$\ddot{\boldsymbol{p}} = \kappa_3^2 \left( \tau - \frac{1}{\kappa_3} \right) \dot{\boldsymbol{p}} - \frac{Q}{\kappa_3} \dot{p}^2 \dot{\boldsymbol{p}} + R \boldsymbol{\Gamma}. \tag{6.15}$$

Note, that the deterministic part of this equation exhibits the assumed rotational symmetry (6.11) with respect to  $\dot{p} = v$ , such that (6.14) can be applied. In order to solve (6.15) numerically, the algorithm discussed by Risken is used [6.7, S. 60ff]. It basically consists of Euler-steps

$$\boldsymbol{v}_{n+1} = \boldsymbol{v}_n + \Delta_t \left[ \kappa_3^2 \left( \tau - \frac{1}{\kappa_3} \right) \boldsymbol{v}_n - \frac{Q}{\kappa_3} v_n^2 \boldsymbol{v}_n \right] + R \sqrt{\Delta_t} \boldsymbol{\gamma}_n, \tag{6.16}$$

with  $\Delta_t$  denoting the step size. Vector  $\boldsymbol{\gamma}_n = (\gamma_{n,x}, \gamma_{n,y})^{\mathrm{T}}$  contains Gaussian random numbers with  $\langle \gamma_{n,i} \rangle = 0$  and  $\langle \gamma_{n,i} \gamma_{n',j} \rangle = 2\delta_{ij}\delta_{nn'}$  for i,j=x,y. The random numbers are computed from a uniformly distributed pseudo random number  $\hat{\gamma}_v$  with  $0 \le \hat{\gamma}_v < 1$  and  $\langle \hat{\gamma}_v \rangle = \frac{1}{2}$  by applying

$$\gamma_{n,i} = \sqrt{\frac{24}{M}} \sum_{\nu=1}^{M} \left( \hat{\gamma}_{\nu} - \frac{1}{2} \right). \tag{6.17}$$

Here variable M denotes a large integer, which has been chosen to M=20 for the following simulations. Solutions of (6.15) are computed with parameter set (4.22), which already has been used in the foregoing sections for the investigation on the dynamics and interaction of dissipative solitons. From these investigations it is known, that form factor Q (4.45) is Q=1,950, while the transition from stationary to intrinsically driven dissipative solitons occurs at  $\tau_c=3.\overline{3}$  (4.30). In order to give an impression of the influence of noise on the dynamics of dissipative solitons Fig. 6.2a, b show trajectories for parameters beyond and before the drift-bifurcation point, respectively. Due to the noise and the significant deviation of parameter  $\tau$  from the drift-bifurcation point, the simulations cannot be compared with solutions of the reaction-diffusion system (3.69). Nevertheless, the trajectories show a significant qualitative similarity to the experimentally observed trajectories of dissipative solitons shown in Sect. 2.2.4.

In order to test the stochastic time series analysis, the simulated trajectories are regarded as primary data, from which the corresponding velocities are computed with first order accuracy. In a second step the deterministic dynamics is estimated on basis of (6.14). The results are shown in Figs. 6.3a and 6.4a. In these diagrams, *symbols* represent the deterministic dynamics  $h_v(v)$  as function of velocity v,

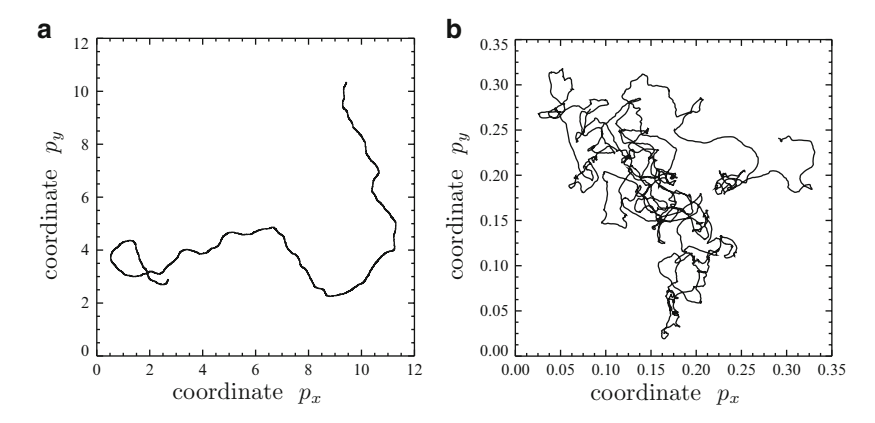


**Fig. 6.2** Trajectories of dissipative solitons simulated on basis of the Langevin-equation (6.15) [6.10]. (a) Active Brownian motion of a dissipative soliton beyond the drift-bifurcation point  $\tau = 3.8 > \tau_c = 3.\overline{3}$ . (b) Brownian motion of a dissipative soliton before the drift-bifurcation point  $\tau = 2.87 < \tau_c = 3.\overline{3}$ . Parameters from (4.22) with Q = 1,950,  $R = 3 \cdot 10^{-4} \kappa_3$ ,  $\Delta_t = 0.05$ . Each trajectory comprises  $2 \cdot 10^5$  time steps

while *dotted curves* denote the counting rate  $N_i$  of the corresponding bins. Note, that the distribution of the counting rates is not equivalent to the solution  $P_{\rm st}$  of the corresponding Fokker-Planck-equation. The difference can be regarded to the nonlinear transformation of infinitesimal area elements from Cartesian to polar coordinates

$$\iint dv_x dv_y = \iint v \, dv d\phi = 2\pi \int v \, dv, \tag{6.18}$$

which has to be taken into account for the calculation of  $P_{\rm st}$ .

Figures 6.3a and 6.4a also show the deterministic terms of (6.15) as *solid lines*. Comparing these curves with the deterministic dynamics estimated from the trajectories (*crosses*) clarifies, that the stochastic time series analysis estimates the deterministic dynamics very well. The estimation is the better the higher the counting rates of the respective bins are. As a rule of thumb, at least 10–20 events have to be recorded for each bin to get an acceptable estimation.

The most important information to be extracted from the estimated deterministic dynamics are the fixed points, which are easily identified as intersections of the *solid lines* with the abscissae. These fixed points determine the equilibrium velocity  $\bar{c}_x$  of the dissipative solitons for the respective set of system parameters. Because the tested time series analysis estimates these fixed points in both examples (Figs. 6.3a and 6.4a) with high precision, one can conclude, that the proposed algorithm is qualified for the analysis of experimentally observed trajectories of non-interacting dissipative solitons.

Due to the qualitative similarity of the simulated trajectories (Fig. 6.2) to the recorded trajectories of dissipative solitons, which have been observed in the

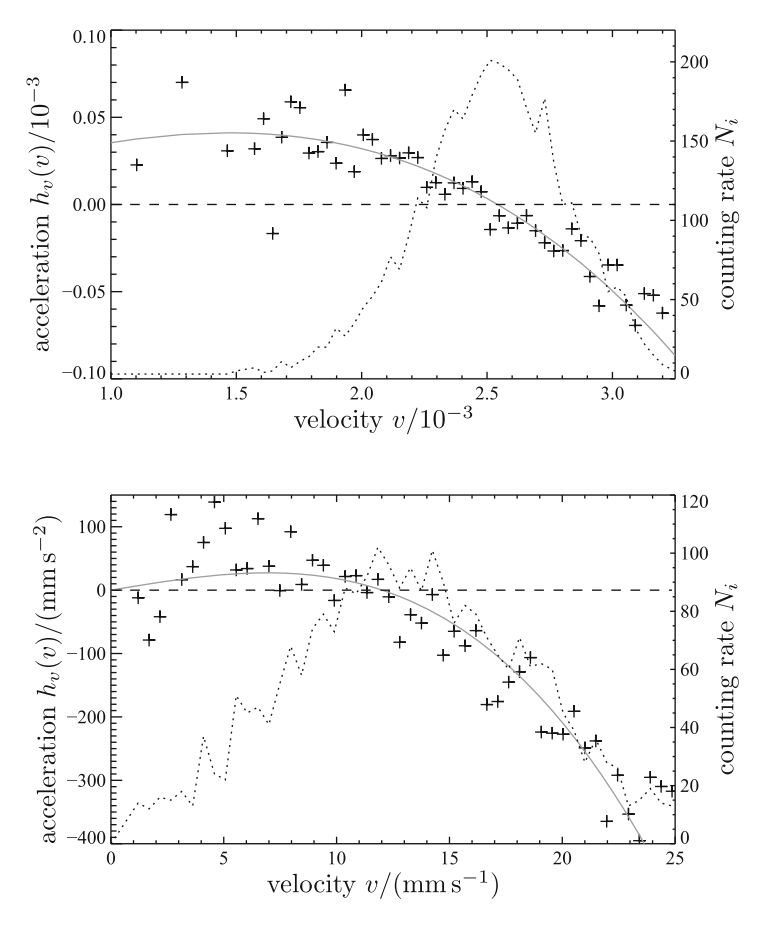


Fig. 6.3 Results of the stochastic time series analysis for trajectories reflecting active Brownian motion [6.10]. Crosses indicate the estimated deterministic part  $h_v(v)$  of the dynamics (6.14). Dotted curves show the counting rates of the evaluated system states per bin. (a) Analysis of the simulated trajectories depicted in Fig. 6.2a for  $\Delta_v = 3.6 \cdot 10^{-5}$ . The solid line shows the deterministic part of the dynamics as defined by (6.15). The intersection of this curve with the abscissa reflects the equilibrium velocity  $v_0 = \bar{c}_x$  (4.43) of the dissipative soliton. (b) Analysis of the experimentally observed trajectory depicted in Fig. 2.15a for  $\Delta_v = 0.5 \, \mathrm{mm \, s^{-1}}$ . Here, the solid line is the cubic polynomial defined in (6.15), whose parameters have been estimated by the method of least squares from the estimated deterministic dynamics. For this fit only bins containing more than ten samples have been taken into account. From this analysis follows that the observed dissipative solitons exhibits an intrinsic velocity of  $\bar{c}_x \approx 11 \, \mathrm{mm \, s^{-1}}$ 

semiconductor-gas discharge system (Fig. 2.15), the latter are optimal observations for applying the stochastic time series analysis to experimental data.

The first experiment to be analyzed is the one depicted in Fig. 2.15b, which has been recorded for 62 s with a sampling rate of 50 frames per second. Computing the velocity from the observed trajectory and applying the described analysis algorithm

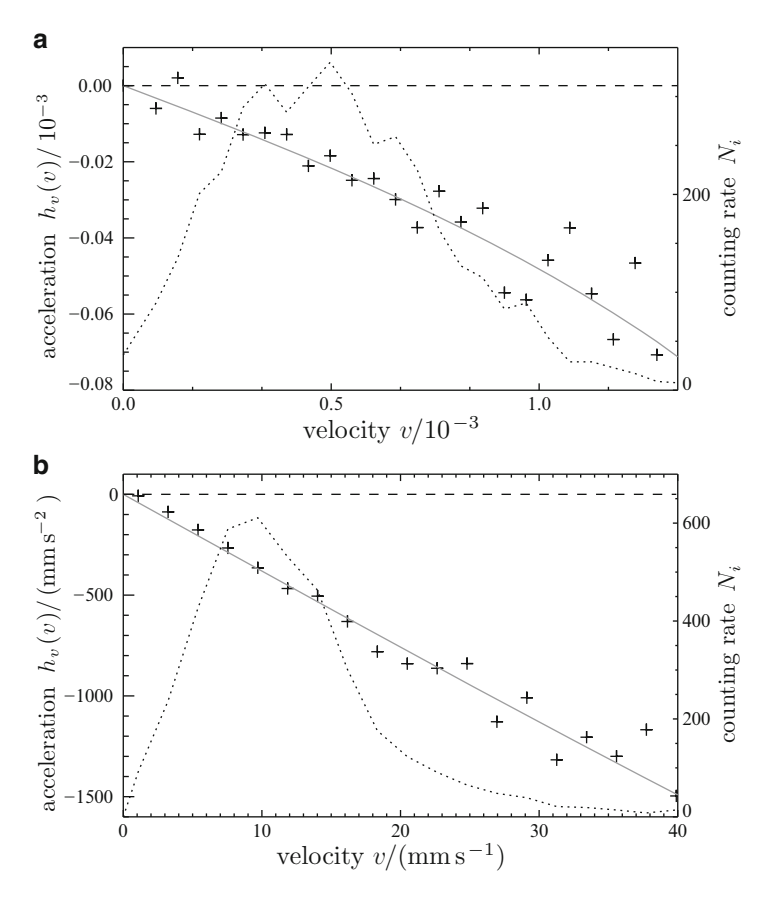


Fig. 6.4 Results of the stochastic time series analysis for trajectories reflecting Brownian motion [6.10]. Crosses indicate the estimated deterministic part  $h_v(v)$  of the dynamics (6.14). Dotted curves show the counting rates of evaluated system states per bin. The vanishing intrinsic velocity of both cases characterize the trajectories as Brownian motion. (a) Analysis of the simulated trajectories depicted in Fig. 6.2b for  $\Delta_v = 5.3 \cdot 10^{-5}$ . The solid line visualizes the deterministic part of the dynamics as defined by (6.15). (b) Analysis of the experimentally observed trajectory depicted in Fig. 2.15b for  $\Delta_v = 2 \text{ mm s}^{-1}$ . Here, the solid line is the cubic polynomial defined in (6.15), whose parameters have been estimated by the method of least squares from the estimated deterministic dynamics. For this fit only bins containing more than ten samples have been taken into account. From this analysis follows that the observed dissipative solitons exhibits a vanishing intrinsic velocity of  $\bar{c}_x \approx 0 \text{ mm s}^{-1}$ 

with 50 bins of width  $\Delta_v = 0.5 \, \mathrm{mm \, s^{-1}}$  to the time series reveals the deterministic dynamics of the dissipative soliton (*symbols* in Fig. 6.3b). The counting rate of the respective bins is shown as *dotted curve*. Motivated by the theoretically deduced dynamics (4.83) of dissipative solitons, a cubic function has been fitted by the method of least squares to the extracted deterministic dynamics whereby only bins with sufficient large counting rates ( $N_i > 10$ ) have been taken into account.

The resulting polynomial is plotted as *solid line* in Fig. 6.3b. The intersection of this curve with the abscissa at  $v_0 \approx 11 \, \mathrm{mm \, s^{-1}}$  is the equilibrium velocity of the observed dissipative soliton. The maximum of the counting rate distribution is located close to this intersection, which is similar to the simulated scenario (Fig. 6.3a) and indicates that the dissipative solitons propagates most of the time with its equilibrium velocity (active Brownian motion). Without noise and in an infinite system the dissipative soliton would propagate with finite constant velocity  $v_0$  for all times.

Quite different deterministic dynamics are expected to be revealed for the measured trajectories shown in Fig. 2.15a, because the dissipative soliton is located in a much smaller area of the experimental system although the trajectory has been recorded for 72 s, which is significantly longer than the recording interval of the trajectory discussed before (Figs. 2.15b and 6.3b). This assumption is confirmed by applying the analysis algorithm for 20 bins of width  $\Delta_v = 2 \text{ mm s}^{-1}$  to the observed trajectory, which is documented in Fig. 6.4b. In this scenario, the acceleration of the dissipative soliton is approximately proportional to its velocity and the constant of proportionality is found to be negative. Therefore, the deterministic part of the dynamics is purely damped (Brownian motion), which is qualitatively different to the scenario discussed before (Fig. 2.15a). Concerning the dynamics depicted in Fig. 6.4b the damping constant can be estimated to  $\zeta = (37.6 \pm 1.5) \,\mathrm{s}^{-1}$ . It follows that the dissipative soliton does not exhibit an intrinsic velocity and would stay stationary for all times without the driving fluctuations. These trajectories represent an Ornstein-Uhlenbeck-process, which is confirmed by computing the stationary solution  $P_{\rm st}$  of the corresponding Fokker-Planck-equation from the counting rate distribution, because  $P_{\rm st}$  is found to be a Gauss distribution with a central second moment of 19.1 mm s $^{-1}$ . Note, that the corresponding simulated scenario (Fig. 6.4b) also corresponds to an Ornstein-Uhlenbeck-process.

Having in mind that the basis of the stochastic time series analysis (6.11) has only been deduced from symmetry arguments, the qualitative similarities between simulated and observed trajectories of dissipative solitons indicate that the deterministic dynamics of both cases is given by the same fundamental law.

#### 6.4 Drift-Bifurcation

Further investigations on the dynamics of single dissipative solitons for different experimental setups reveal, that the deterministic dynamics can always be categorized as Brownian or active Brownian motion. Therefore, the question arises, whether a transition between these qualitatively different dynamics corresponding to the theoretically predicted drift-bifurcation (Sect. 4.2) can be observed experimentally.

Systematic investigations show that the drift-bifurcation can be observed experimentally, if the specific resistance  $\rho_{SC}$  of the semiconductor is used as control parameter. For this purpose, the experimental settings documented in Fig. 6.5 are

6.4 Drift-Bifurcation 169

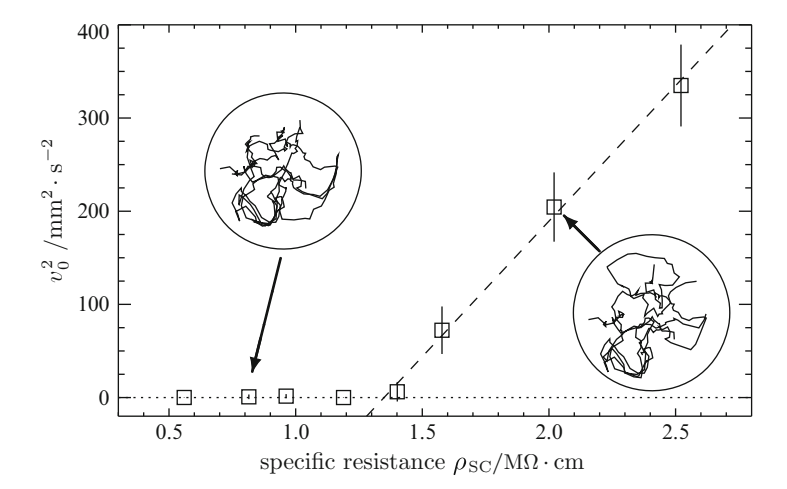


**Fig. 6.5** Drift-bifurcation measured in the semiconductor gas-discharge system [6.13]. The diagram shows the squared intrinsic velocity against bifurcation parameter  $\rho_{SC}$ . The intersection of the linearly increasing part of the diagram with the abscissa reveals the drift-bifurcation point, which is located at  $\rho_{SC,c}=1.3\,\mathrm{M}\Omega\mathrm{cm}$ . The inlays show exemplary trajectories of dissipative solitons on the active area for parameters before and beyond the drift-bifurcation point. Parameters:  $U_0=3,700\,\mathrm{V},~R_0=10\,\mathrm{M}\Omega,~p=286\,\mathrm{mbar},~T_{SC}=105\,\mathrm{K},~d=750\,\mathrm{\mu m},~t_{\rm exp}=0.02\,\mathrm{s},~I=107\,\mathrm{\mu A}$ 

chosen and trajectories of dissipative solitons have been recorded for each value of control parameter  $\rho_{SC}$ . From each trajectory the intrinsic velocity  $v_0$  has been estimated by means of the stochastic time series analysis. Following the convention of the theoretically deduced drift-bifurcation (Fig. 4.6) the square of the intrinsic velocity has been plotted as function of control parameter  $\rho_{SC}$  in Fig. 6.5. It shows a supercritical drift-bifurcation occurring at  $\rho_{SC,c}=1.3\,\mathrm{M}\Omega\mathrm{cm}$ , which is characterized by vanishing intrinsic velocity before the bifurcation point and quadratic intrinsic velocity respectively linearly increasing squared intrinsic velocity beyond the bifurcation point. Note, that the qualitative change of the deterministic part of the dynamics cannot be seen by naked eye from the trajectories (inlays of Fig. 6.5).

Because this transition has been predicted by the three-component reaction-diffusion system (3.69) for variations of time scale parameter  $\tau$  (Sect. 4.2), the question arises how the specific resistance  $\rho_{SC}$  is related to the time scale parameter of the field equations. The answer to this question is found in the modelling of the experiment by means of the equivalent circuit (Sect. 3.4.3). This phenomenological model predicts a linear dependency (3.74) of the normalized time scale constants  $\tau$  and  $\theta$  on the resistors  $R_G$  and  $R_H$ , which belong to the linear layers of the equivalent circuit and are directly related to the specific resistivity. These resistors also influence other parameters of the reaction-diffusion system. For example parameters  $\tau$ ,  $D_v$ ,  $\kappa_1$  and  $\kappa_3$  of the three-component reaction-diffusion system depend on the resistor  $R_G$ . Therefore, the transition from Brownian to active Brownian motion

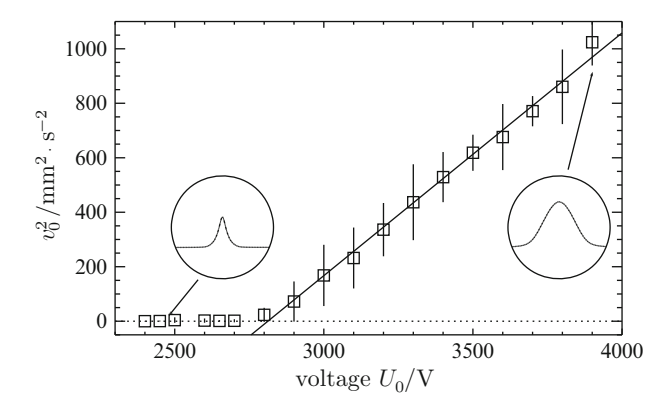


**Fig. 6.6** Experimentally measured drift bifurcation due to a change of shape [6.15]. The externally applied voltage  $U_0$  has been used as control parameter. Inlays show intersections of the averaged luminance of the dissipative solitons. Parameters: resistivity of the semiconductor  $\rho_{SC} = 1.83 \cdot 10^6 \,\Omega \cdot \text{cm}$ , series resistor  $R_0 = 10 \,\text{M}\Omega$ , pressure  $p = 280 \,\text{hPa}$ , temperature  $T = 100 \,\text{K}$ , width of the discharge gap  $d = 500 \,\mu\text{m}$ , exposure time  $t_{exp} = 0.02 \,\text{s}$ 

due to a change of the specific resistivity of the semiconductor corresponds to a four-dimensional path in the parameter space of the reaction-diffusion system. This consideration indicates, that other drift-bifurcation scenarios are possible.

Systematic experimental investigations have shown, that a drift-bifurcation can be accompanied by a change of the shape of the dissipative soliton (Fig. 6.6). Or, from the theoretical point of view, are caused by the change of shape [6.14, 6.15], because the change of shape shifts the bifurcation point according to (4.29), which results in a variation of the intrinsic velocity according to (4.43). Despite of the different mechanisms enabling the drift-bifurcation, it is notably that the square of the intrinsic velocity  $v_0^2$  always depends linearly on the bifurcation parameter in the vicinity of the bifurcation point.

#### 6.5 Interaction

Motivated by the measurement of the theoretically predicted drift-bifurcation, the stochastic time series analysis is enhanced in order to investigate the interaction of dissipative solitons for which the number of dissipative solitons is preserved, e.g. scattering (Fig. 2.16) and molecule formation (2.17). Having the particle description (5.19) of the model system (3.69) in mind, the following assumptions are taken:

- 1. Only mutual interaction is taken into account.
- 2. The interaction between experimentally observed dissipative solitons is modelled by means of generalized central forces acting on their connecting line (cf. Sect. 5.2.3).

6.5 Interaction 171

3. The influence of the interaction on the velocity of the dissipative solitons is weak and can be neglected (cf. Sect. 5.2.4).

Starting from this assumptions (6.11) can be extended to the following form:

$$\dot{\boldsymbol{v}}_i = h_v(v_i) \cdot \boldsymbol{e}_{\boldsymbol{v}_i} - F_{\mathrm{e}}(|\boldsymbol{p}_j - \boldsymbol{p}_i|) \frac{\boldsymbol{p}_j - \boldsymbol{p}_i}{|\boldsymbol{p}_i - \boldsymbol{p}_i|} + R\boldsymbol{\Gamma}_i(t), \tag{6.19}$$

with indices  $i, j = 1, 2, i \neq j$  denoting different dissipative solitons. Starting from (6.19) a new acceleration  $\dot{v}_{i,n}$  can be introduced

$$\dot{\boldsymbol{v}}_{i,n} := \dot{\boldsymbol{v}}_i - h_v(v_i)\boldsymbol{e}_{v_i} = -F_e(|\boldsymbol{p}_j - \boldsymbol{p}_i|) \frac{\boldsymbol{p}_j - \boldsymbol{p}_i}{|\boldsymbol{p}_j - \boldsymbol{p}_i|} + R\boldsymbol{\Gamma}_i(t), \tag{6.20}$$

if the deterministic acceleration  $h_v(v)$  is known for a certain system configuration. Assuming, that (6.2) is valid for each type of noise source  $\Gamma_i$ , the interaction law  $F_e(d)$  can be estimated using

$$F_{e}(d) = -\left| \left\langle \dot{\boldsymbol{v}}_{i,n} \frac{\boldsymbol{p}_{j} - \boldsymbol{p}_{i}}{|\boldsymbol{p}_{j} - \boldsymbol{p}_{i}|} \right\rangle \right|_{|\boldsymbol{p}_{j} - \boldsymbol{p}_{i}| = d}.$$
(6.21)

This equation can be simplified for practical applications to

$$F_{e}(d) \approx -\left| \left[ \boldsymbol{v}_{i}(t + \Delta_{t}) - \boldsymbol{v}_{i}(t) - \Delta_{t} h_{v}(v_{i}) \boldsymbol{e}_{v_{i}} \right] \cdot \frac{\boldsymbol{p}_{j} - \boldsymbol{p}_{i}}{|\boldsymbol{p}_{j} - \boldsymbol{p}_{i}|^{2}} \right|_{|\boldsymbol{p}_{i} - \boldsymbol{p}_{i}| \approx d}$$
(6.22)

with  $v_i$  denoting the measured velocity of the *i*th dissipative soliton [6.12].

In order to measure the intrinsic dynamics  $h_v(v)$  of dissipative solitons and their interaction  $F_e(d)$  for more than one dissipative soliton simultaneously, the following algorithm can be applied: For a zeroth approximation of the intrinsic dynamics  $h_{v,0}(v)$  the interaction is neglected and the trajectories are analyzed on basis of (6.14) for the complete time interval  $\mathbb{T}_0$  for which the trajectories have been recorded. Having an estimate for the intrinsic dynamics at hand, the zeroth estimation of the interaction  $F_{e,0}(d)$  on basis of (6.22) can be performed. From this interaction follows a critical interaction distance  $d_{C,0}$ , separating the regions of negligible and considerable interaction  $F_{e,0}(d(t))$ . Now the interaction  $F_e(d)$  can be estimated iteratively with variable k denoting the iteration step:

1. Starting from the interaction  $F_{e,k-1}(d(t))$  and the corresponding critical distance  $d_{C,k-1}$  of the last iteration (k-1), the set  $\mathbb{T}_k$  of all time intervals is determined for which the interaction between the dissipative solitons can be neglected:

$$\mathbb{T}_{i} = \left\{ \int \left\{ t : F_{e,k-1}(d(t)) \approx 0 \land d(t) > d_{C,k-1} \right\}.$$
 (6.23a)

2. The intrinsic dynamics  $h_{v,k}(v)$  is estimated from velocities  $\mathbf{v}_i(t)$  and  $\mathbf{v}_i(t+\Delta_t)$  with  $\{t,(t+\Delta_t)\}\subset \mathbb{T}_k$  on basis of (6.14).

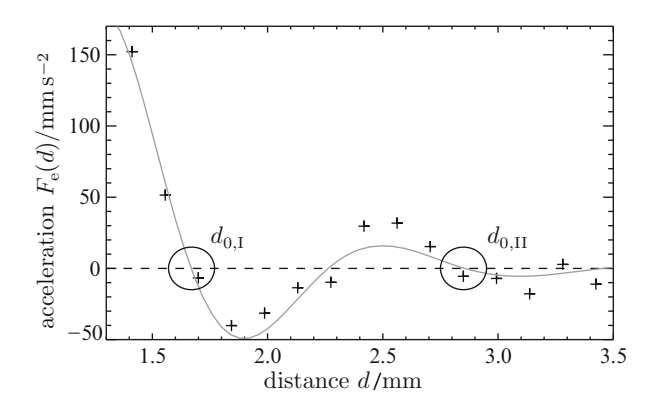


**Fig. 6.7** Interaction of dissipative solitons observed in the semiconductor-gas discharge experiment [6.12]. The result of the stochastic data analysis are plotted as *crosses*, while the *curve* represents the fitted function (6.25). The roots of the fitted curve are denoted with  $d_{0,\rm I}$  and  $d_{0,\rm II}$  and define stable binding distances, which are observed as transient bound states due to the influence of noise. Parameters: Number of evaluated samples 4,500,  $U_0 = 4.6\,\rm kV$ ,  $R_0 = 4.4\,\rm M\Omega$ ,  $p = 283\,\rm mbar$ ,  $T_{\rm SC} = 100\,\rm K$ ,  $d = 500\,\mu m$ ,  $t_{\rm exp} = 0.02\,\rm s$ ,  $I = 235\,\mu A$ .

- 3. A new estimate of the interaction  $F_{e,k}(d(t))$  is performed on basis of (6.22).
- 4. From the estimated interaction  $F_{e,k}(d(t))$  follows a critical distance  $d_{C,k}$ , such that the interaction between the dissipative solitons can be neglected for  $d(t) > d_{C,k}$ :

$$d_{C,k} = \min_{t} \left\{ d(t) \left| F_{e,k}(d(t)) \approx 0 \land d(t) > d_{C,k-1} \right\}.$$
 (6.23b)

5. The iteration converges if the critical distance  $d_{C,k}$  does not change significantly compared to the last iteration.

A typical distance dependent interaction  $F_{\rm e}(d)$  for experimentally observed dissipative solitons showing the formation of transient bound states is shown in Fig. 6.7. In this diagram *crosses* denote the results of the data analysis. Like the interaction of the model system (Fig. 5.7) the estimated interaction function exhibits an alternating sign. Estimating the continuous representation

$$F(d, \mathbf{a}) = -\frac{a_1}{\sqrt{d}} e^{-a_2 d} \cos(a_3 (d - a_4))$$
(6.24)

to the experimental data gives the following interaction law

$$F_{\rm e}(d) = -\frac{1387 \,\mathrm{mm}^{\frac{3}{2}} \,\mathrm{s}^{-2}}{\sqrt{d}} e^{-1.217 \,\mathrm{mm}^{-1} \cdot d} \cos \left(5.28 \,\mathrm{mm}^{-1} \cdot (d - 1.604 \,\mathrm{mm})\right),\tag{6.25}$$

which has been plotted as gray curve in Fig. 6.7.

References 173

In analogy to the considerations of Sect. 5.2.3 regions with  $F_{\rm e}(d) > 0$  and  $F_{\rm e}(d) < 0$  correspond to repulsive and attractive interaction, respectively. Therefore, bound states exhibit binding distances  $d_0$  with  $F_{\rm e}(d_0) = 0 \land F'_{\rm e}(d_0) < 0$ , which are observed as transient states due to the influence of noise. For the discussed experiment the binding distances are  $d_{0,\rm I} \approx 1.65$  mm and  $d_{0,\rm II} \approx 2.85$  mm with the latter being the preferred binding distance. The statistical analysis of the trajectories also shows that the minimal scattering distance typically undershoots  $d_{0,\rm II}$  and  $d_{0,\rm II}$  slightly, which is caused by the repulsive interaction affecting the dissipative solitons for distances being slightly smaller than  $d_{0,\rm II}$  or  $d_{0,\rm II}$ . Experiments show that the binding distances of experimentally observed dissipative solitons are determined by the relative maxima of their oscillating tails [6.12], which is in agreement with the model system (cf. Fig. 5.2b, d).

#### References

- 6.1. A. Einstein, in Contributions to the Medical Sciences in Honor of Emanuel Libman by his Pupils, Friends and Colleagues, vol. 1, ed. by E. Libman (International Press, New York, 1932), pp. 363–364
- 6.2. A. Pais, Subtle is the Lord . . . . The Science and the Life of Albert Einstein (Oxford University Press, New York, 1982)
- 6.3. S. Siegert, R. Friedrich, J. Peinke, Phys. Lett. A 243, 275 (1998)
- 6.4. R. Friedrich, S. Siegert, S. Lück, M. Siefert, M. Lindemann, J. Raethjen, G. Deutschl, G. Pfister, Phys. Lett. A 271, 217 (2000)
- 6.5. R.L. Stratonovich, Conditional Markov Processes and Their Application to the Theory of Optimal Control (Elsevier, New York, 1968)
- 6.6. A. Kolmogoroff, Math. Ann. 104, 415 (1931)
- 6.7. H. Risken, *The Fokker-Planck-Equation. Methods of Solution and Applications*, 2nd edn. (Springer, Berlin, 1996)
- 6.8. S. Siefert, A. Kittel, R. Friedrich, J. Peinke, Eur. Lett. 61, 466 (2003)
- 6.9. P. Hänggi, Helv. Phys. Acta **51**, 183 (1978)
- 6.10. H. Bödeker, M.C. Röttger, A.W. Liehr, T. Frank, R. Friedrich, H.-G. Purwins, Phys. Rev. E 67(056220), 1 (2003). doi:10.1103/PhysRevE.67.056220
- 6.11. D. Kleinhans, R. Friedrich, in *Wind Energy*, ed. by J. Peinke, P. Schaumann, S. Barth (Springer Berlin/Heidelberg, 2007), pp. 129–133. doi:10.1007/978-3-540-33866-6\_23
- 6.12. H. Bödeker, A.W. Liehr, T.D. Frank, R. Friedrich, H.-G. Purwins, New J. Phys. 6(62), 1 (2004). Published with kind permission of IOP
- 6.13. A.W. Liehr, H.U. Bödeker, M.C. Röttger, T.D. Frank, R. Friedrich, H.-G. Purwins, New J. Phys. 5(89), 1 (2003). http://stacks.iop.org/1367-2630/5/89. Published with kind permission of IOP
- 6.14. S.V. Gurevich, H.U. Bödeker, A.S. Moskalenko, A.W. Liehr, H.-G. Purwins, in *Physics and Control (PhysCon). International Conference*, August 20–22, 2003, Saint Petersburg, ed. by A.L. Fradkov, A.N. Churilov (IEEE, Piscataway, 2003), pp. 601–606
- 6.15. S.V. Gurevich, H.U. Bödeker, A.S. Moskalenko, A.W. Liehr, H.-G. Purwins, Phys. D 199(1–2), 115 (2004). doi:10.1016/j.physd.2004.08.020. Reprinted with permission from Elsevier

# **Chapter 7 Generation and Annihilation**

Most of an organism, most of the time, is developing from one pattern into another, rather than from homogeneity into a pattern. One would like to be able to follow this more general process mathematically also. The difficulties are, however, such that one cannot hope to have any very embracing theory of such process, beyond the statement of the equations. It might be possible, however, to treat a few particular cases in detail with the aid of a digital computer. This method has the advantage that it is not necessary to make simplifying assumptions as it is when doing a more theoretical paper analysis. [...] The essential disadvantage of the method is that one only gets results for particular cases.

A.M. Turing, 1952 [7.1, 71pp].

Abstract On basis of an exemplary simulation campaign the transition from particle conserving interaction to generation and annihilation phenomena is demonstrated. The transition is controlled by the intrinsic velocity of the dissipative solitons, which is adjusted by varying the time scale constant of the driving inhibitor. The formation of bound states is observed for slow dissipative solitons. With increasing propagator mode amplitude, the interaction processes are complemented by generation through self-completion and finally by annihilation through fading. These observations are the starting point for discussing the mechanisms of generation and annihilation phenomena. Concerning annihilation processes the mechanisms of fading and merging are introduced. The generation of dissipative solitons occurs due to the formation of complex intermediate states, the division of dissipative solitons (self-replication), Turing-destabilization of homogeneous systems, destabilization of single dissipative solitons (self-completion), and interaction of two and more dissipative solitons (replication). Finally, the phenomena of selfcompletion and replication are related to the superposition of oscillating tails which leads to the formation of a critical nucleus.

### 7.1 Controlling Generation and Annihilation

## 7.1.1 Controlling the Propagation Velocity

The theoretical investigations on interaction processes of dissipative solitons in reactions-diffusion systems have shown that processes with and without conservation of the number of particles are commonly found [7.2–7.9]. The same holds for experimental systems (Chap. 2). Therefore, the question arises if the transition between these qualitatively different interaction regimes can be controlled by changing a characteristic property of the system. In this context, it is known from the semiconductor-gas discharge experiments of Astrov and Purwins [7.10] that the transition between both interaction regimes is controlled by the specific resistivity of the semiconductor (Sect. 2.2.3.1). In Chap. 4 it has been shown that this parameter is related to the time-scale constant of the driving inhibitor triggering the driftbifurcation in three-component reaction diffusion systems. Therefore, the time scale parameter  $\tau$  of model (3.69) has been chosen as control parameter for investigating the transition between particle conserving interaction and generation-annihilationphenomena. For this purpose, the control parameter is increased significantly beyond the vicinity of the drift-bifurcation which is in contrast to the simulations discussed in Chap. 5.

Starting point is parameter set (4.22) for which the model system (3.69) exhibits dissipative solitons with oscillating tails. The initial condition is constructed on basis of ansatz (5.12) from a stationary dissipative soliton solution  $\bar{u}$ : Two dissipative solitons are placed close to the center of the domain  $(\frac{1}{2},\frac{1}{2})^T\in\Omega=[0,1]^2$  such that the distance  $\delta=0.1$  of their localized activator distributions is smaller than the distance of the first binding state  $d_{0,1}=0.163$  expected for a bound state. Additionally, the respective distributions of the driving inhibitor are shifted by  $\alpha_0=5\cdot 10^{-3}$  with respect to the localized activator distributions such that the dissipative solitons initially propagate perpendicular to the connecting line d of the localized activator distributions in opposite direction. Choosing the axis d parallel to the x-axis of the coordinate system and taking an additional shift of a half discretization length  $\Delta_x/2$  into account, the following non-equilibrium initial condition is constructed:

$$u(\mathbf{x},0) = \bar{u} \left( \mathbf{x} - \left( \frac{1 - \delta - \Delta_x}{2}, \frac{1 - \Delta_x}{2} \right)^{\mathrm{T}} \right)$$

$$+ \bar{u} \left( \mathbf{x} - \left( \frac{1 + \delta - \Delta_x}{2}, \frac{1 - \Delta_x}{2} \right)^{\mathrm{T}} \right) - u_0,$$

$$v(\mathbf{x},0) = \bar{u} \left( \mathbf{x} - \left( \frac{1 - \delta - \Delta_x}{2}, \frac{1 - \Delta_x}{2} + \alpha_0 \right)^{\mathrm{T}} \right)$$

$$+ \bar{u} \left( \mathbf{x} - \left( \frac{1 + \delta - \Delta_x}{2}, \frac{1 - \Delta_x}{2} - \alpha_0 \right)^{\mathrm{T}} \right) - u_0.$$

$$(7.1)$$

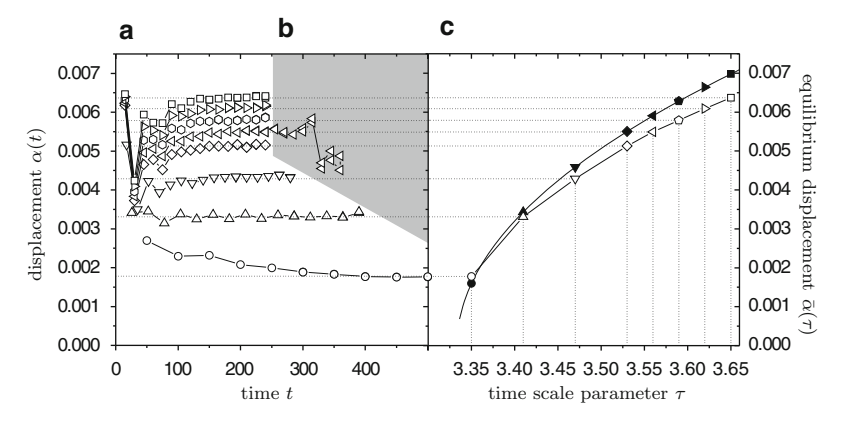


Fig. 7.1 Displacement  $\alpha(t)$  between localized activator and (driving) inhibitor distribution for varied time scale parameter  $\tau$ . (a) Relaxation of displacement  $\alpha(t)$  while the dissipative solitons approach the domain boundaries from the initial configuration (7.1). For each time series the displacement of both dissipative solitons is shown but cannot be discriminated with respected to plotting accuracy. (b) The gray area shows the displacements  $\alpha_1(t)$  and  $\alpha_2(t)$  for  $\tau=3.56$  while the dissipative solitons interact with the domain boundary. (c) Equilibrium displacement  $\bar{\alpha}(\tau)$  as obtained from simulation (open symbols) and from reduced dynamics (filled symbols). Parameters from Fig. 4.3 with  $\Omega=[0,1]^2$ ,  $\Delta_x=5\cdot 10^{-3}$ ,  $\Delta_t=0.1$ , no-flux boundary condition

Here  $u_0 = v_0$  and  $\bar{u} = \bar{v}$  denote the stationary solutions of the homogeneous and the solitary state for parameter set (4.22), respectively. The initial condition for the second inhibitor w is not specified, because this component acts as local feedback field due to  $\theta = 0$  and can be directly computed by inverting Eq. (3.69c). Note, that shifting the initial configuration of the dissipative solitons by  $\Delta_x/2$  against the center of the domain breaks the rotational symmetry of the system. Consequently, the dissipative solitons will approach the no-flux boundaries of the domain under different angles and trigger different interaction scenarios while colliding with their mirror particles.

Due to the small distance between the dissipative solitons the latter are repelling each other  $F(d) > 0|_{\delta \leq d < d_{0.1}}$  (cf. Fig. 5.7), such that solving the field equations (3.69) with initial conditions (7.1) and varied time scale constants  $\tau$  leads to a rapid increase of the propagator mode amplitude  $\alpha$ . Its evolution is visualized in Fig. 7.1a by estimating  $\alpha$  as distance between the centers of localized activator and localized (driving) inhibitor distributions according to the ansatz of the reduced dynamics (5.12). Due to this increase the dissipative solitons do not form a stable bound state but depart from each other while their propagator mode amplitudes relax to the respective equilibrium state  $\bar{\alpha}(\tau)$  (Fig. 7.1a, t > 25). In the vicinity of the drift-bifurcation ( $\tau \lesssim 3.42$ ) the equilibrium propagator mode amplitude reproduces the results of the reduced dynamics  $\bar{\alpha} = \frac{1}{\kappa_3} \bar{c}_x$  very well (Fig. 7.1c). For  $\tau > 3.42$  the distance  $\bar{\alpha}$  between localized activator and localized (driving) inhibitor distribution is significantly smaller than the value predicted by the reduced dynamics. Therefore this parameter regime can be characterized as *far beyond from* 

*drift-bifurcation* such that the reduced dynamics of the dissipative solitons (5.19) can only give a qualitative description of the particle dynamics.

Because the dissipative solitons propagate due to relaxed activator-inhibitor displacements  $\bar{\alpha}(\tau)$  their collision with the domain boundary occurs with equilibrium velocity  $\bar{c}_x(\tau)$ . Therefore, these interactions can be regarded as characteristic for the respective parameter set. In Fig. 7.2 six characteristic simulations are summarized as space-time-trajectories of the localized activator distributions. In these diagrams colours *red* and *blue* indicate the initial dissipative solitons, while the positions of generated particles are indicated with *green* symbols.

In the vicinity of the drift-bifurcation (e.g.  $\tau=3.35$ ) the dissipative solitons propagate slowly and cannot cross the repulsive interaction region of their mirror particles. Therefore, only scattering is observed for the chosen configuration (Fig. 7.2a). In Sect. 5.4.1 it has been shown that for the same parameter set but different scattering geometries the formation of bound states is possible. However, for the chosen scattering geometry (7.1) the dissipative solitons have to propagate with an increased equilibrium velocity  $\bar{c}_x$  in order to form bound states. This is demonstrated in Fig. 7.2b for an increased time scale parameter  $\tau$ . Here, four dissipative solitons (4-DS) form a bound state which consist of three mirror particles and one of the initial dissipative solitons. Due to the boundary condition these bound states are stationary. Without these restrictions a rotating bound state would form.

Increasing the time scale parameter up to  $\tau=3.47$  enables the generation of dissipative solitons (Fig. 7.2c). In this scenario, the oscillating tails of the *red* dissipative soliton superimpose in the corner of the domain with the oscillating tails of its mirror particles, which leads to the ignition of an additional dissipative soliton (*green*). This particle is located in the  $(0,0)^T$ -corner of the domain such that only one quarter of it extends into the domain. Consequently, the quarter particle is stationary. After the generation, the initial dissipative solitons forms a propagating bound state (2-DS) with one of its mirror particles and moves into the direction of the  $(0,1)^T$ -corner where it forms a stationary bound state consisting of four dissipative solitons. Rotational symmetric to these trajectories are the trajectories of the *blue* particle and its product, which are not shown in Fig. 7.2c. Note, that this generation is also observed for unbound dissipative solitons (Fig. 7.10).

In contrast to the simulations shown in Fig. 7.2b, c exhibiting stationary 4-DS bound states, the latter are unstable for  $\tau > 3.47$  (Fig. 7.2d). The reason is a supercritical Hopf-bifurcation occurring at  $\tau_{Hopf} \approx 3.47$  [7.11, S. 84ff]. Therefore, the 4-DS bound state starts to oscillate. For  $\tau = 3.53$  the amplitude of these oscillations increases such that the dissipative soliton is driven out off the attractive interaction region and enters the repulsive interaction region of its neighbours and the bound state breaks apart. Due to the boundary condition the break-up happens synchronously with one of its mirror particles such that both dissipative solitons form a bound state propagating along the edge of the domain towards the next domain corner. Here the cycle of 4-DS formation and break-up continues.

For  $\tau \leq 3.53$  the trajectories of the dissipative solitons are approximately rotational symmetric with respect to the center of the domain due to the initial condition (7.1). For  $\tau \geq 3.56$  this point symmetry is not observed anymore.

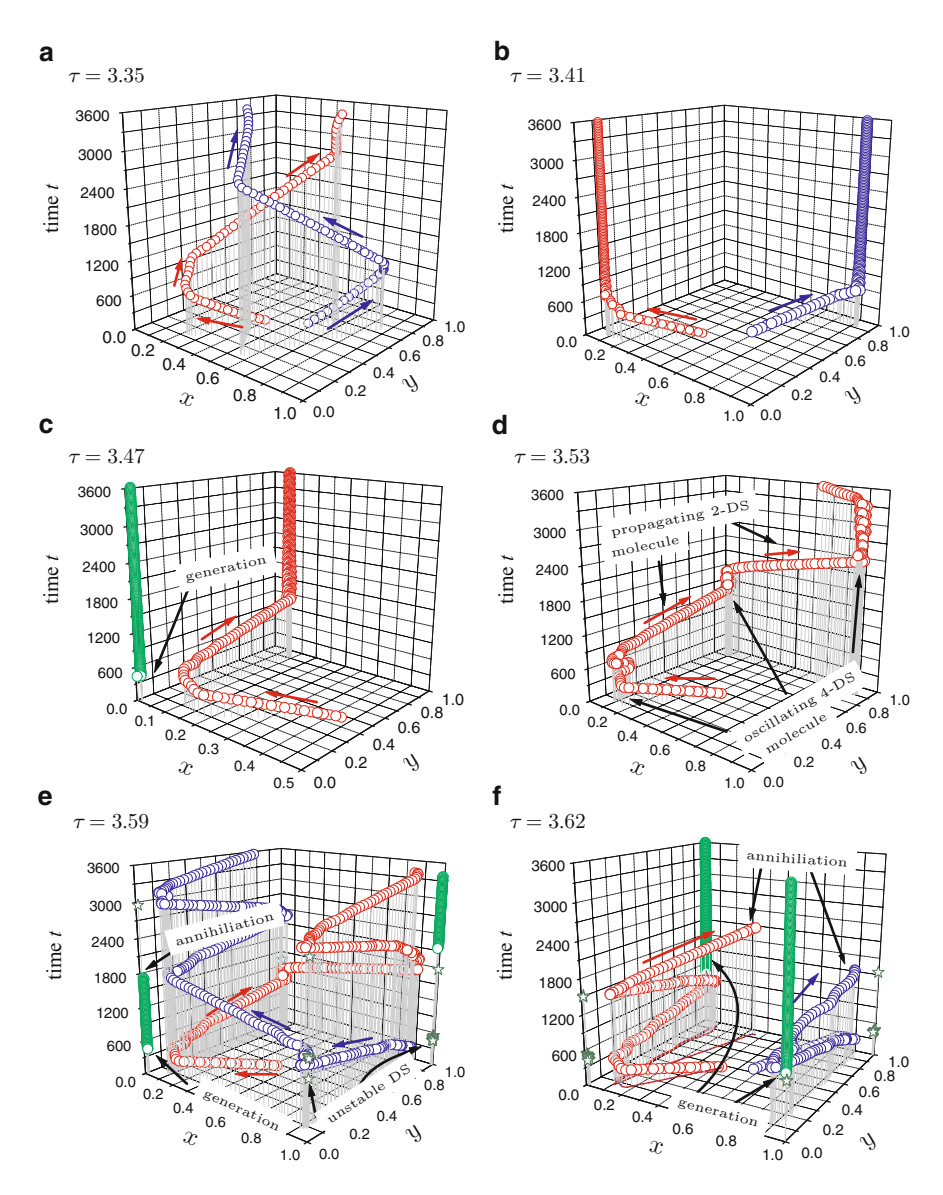


**Fig. 7.2** Transition from interaction with conservation of the number of dissipative solitons to generation and annihilation. The plots show the trajectories of the dissipative solitons in spacetime. *Red* and *blue symbols* indicate the initial dissipative solitons (7.1). *Red* and *blue arrows* point into their direction of motion. Generated particles are indicated by *green symbols*. Plots (**c**) and (**d**) show only the trajectory of one dissipative solitons for reasons of clarity. Parameters from Fig. 7.1

For example in case of  $\tau=3.56$  one dissipative soliton is trapped momentarily at the  $(0,0)^T$ -domain corner while the other particle is reflected at the opposite corner. This deviation is reflected in Fig. 7.1b by the deviating evolution of the propagator mode amplitudes  $\alpha_i(t)$ . Taking a close look at the trajectories reveals

that both dissipative solitons pass the corner of the domain in a distance with nearly vanishing interaction. One dissipative soliton passes the corner of the domain in the attractive interaction region, while the opposite dissipative soliton passes the respective corner in the repulsive interaction region. This difference is caused by a shift of  $-\frac{1}{2}(\Delta_x, \Delta_x)^T$  breaking the rotational symmetry of the initial condition with respect to the domain center. Consequently, the dissipative solitons are either attracted or repelled by their mirror particles.

Increasing the time scale parameter even further leads to a new interaction phenomena: The annihilation of dissipative solitons (Fig. 7.2e). In this simulation the dissipative solitons ignite a quarter particle while passing the domain corner, which is either unstable and vanishes in the course of the interaction (*green* stars in Fig. 7.2e) or evolves to a quarter particle, which is indicated as *green* cylinders appearing in the domain corners. The space-time trajectories show that a quarter particle can be annihilated due to the collision with a 2-DS molecule propagating along the domain boundary. In this case the quarter particle is literally quenched between two 2-DS molecules approaching from opposite directions. However, for larger propagation velocities one also observes the annihilation of dissipative solitons in two particle processes at the domain boundary (Fig. 7.2f). In such a process both the dissipative soliton and its mirror particle are annihilated. For  $\tau=3.65$  one observes that the interaction geometry leading to the annihilation of a quarter particle (Fig. 7.2e) favours the annihilation of all incorporated dissipative solitons.

The simulation campaign visualized in Figs. 7.1 and 7.2 demonstrates that the transition from interaction phenomena with conservation of the number of particles to generation and annihilation of dissipative solitons can be realized by increasing their propagation velocity. The simulations indicate that the transition is closely related to the displacement of activator and driving inhibitor distributions, which is discussed in detail in Sects. 7.2 and 7.3.

## 7.1.2 Generating Clusters from Scratch

In Sect. 3.3.2 the Turing instability has been introduced, which explains the spontaneous formation of periodical structures in a continuously driven, homogeneous system. Under certain conditions these patterns are hexagonally ordered grids covering the domain completely. Inspired by the experimental observation reporting the generation of clustered current density filaments in the course of a controlled Turing-destabilization (Sect. 2.2.3.1) this section is devoted to the theoretical investigation of this phenomenon. In this context the system is controlled on two different levels. First of all, there is the control of an experimental parameter triggering the structure formation process and there is an inherent control due to the global resistor, which restricts the overall current and therefore suppresses the ignition of additional filaments.

Therefore a two-component reaction-diffusion-system with global feedback (3.57) is investigated with the following parameters:

$$D_u = 6 \cdot 10^{-5}, \ D_v = 6 \cdot 10^{-4}, \ \lambda = 0.8, \ \kappa_1 = -1.575,$$
  
 $\kappa_2 = 5, \ \kappa_3 = 1, \ \tau = 1.0, \ \Omega = [0, 1]^2, \ \Delta_x = 0.01, \ \Delta_t = 0.05,$  (7.2)  
no-flux boundary condition,  $u(\mathbf{x}, 0) = v(\mathbf{x}, 0) = 0.5.$ 

For these parameters, the homogeneous state  $u(x) = v(x) = u_0 = v_0 = -0.2978$  is unstable against perturbations of wavelength  $\bar{v}_c = [0.0996, 0.1101]$  due to a Turing-bifurcation occurring at  $\kappa_{1,c} = -1.580$ . At the bifurcation point the critical wavelength is  $v_c = \frac{2\pi}{k_c} = 0.1047$ . Because the homogeneous state is still a solution of the system for  $\kappa_1 > \kappa_{1,c}$ , perturbations of amplitude  $R_u = 10^{-6}$  and  $R_v = 10^{-7}$  are applied to activator u and inhibitor v after each time-step.

A cluster of dissipative solitons is formed via a controlled Turing-instability in four elementary steps, which are presented in Fig. 7.3. First of all, activator u and inhibitor v evolve a regular structure of small amplitude which exhibits a characteristic wavelength of  $v \approx 0.1$  (Fig. 7.3b). The second phase starts with the ignition of a localized structure, which is embedded into a hexagonal pattern of small perturbations (Fig. 7.3e). These perturbations trigger the ignition of additional spots in rapid sequence (3rd phase, Fig. 7.3h) leading to a significant increase of the activator integral (Fig. 7.3g). Consequently, the effective driving parameter  $\kappa_{1,\text{eff}}$  (3.28) of the activator equation (3.57a) is decreased and the ignition of further spots is stopped (Fig. 7.3j). Finally, the cluster of dissipative solitons expands (4th phase, Fig. 7.3k) because the particles arrange themselves due to the laws of reduced dynamics (Sect. 5.2.3).

To some extent, this mechanism allows for the controlled generation of dissipative solitons, which is show in Fig. 7.4. In order to obtain this series, the simulation presented in Fig. 7.3 has been repeated with varied control parameter  $\kappa_1 > \kappa_{1,c} = -1.580$ . The value of activator integral  $\frac{1}{\|\Omega\|} \int_{\Omega} u(t) d\Omega$  as well as the number of generated dissipative solitons have been recorded after relaxation [7.13]. An increase of control parameter  $\kappa_1$  is compensated by a proportional increase  $(0.1925 \pm 0.0019)\kappa_1$  of the activator integral (Fig. 7.4a). In the vicinity of the Turing-bifurcation point  $\kappa_{1,c} \leq \kappa_1 = -1.5$  this increase is caused by the generation of new dissipative solitons (Fig. 7.4b). The process saturates, because the domain fills up completely with dissipative solitons, which form a hexagonal pattern and cannot be regarded as individual dissipative solitons anymore. In this situation an additional increase of the control parameter is compensated by an increase of the amplitude of the pattern holding the linear relation between control parameter  $\kappa_1$  and activator integral  $\frac{1}{\|\Omega\|} \int_{\Omega} u(t) d\Omega$ . Consequently, the system stabilizes approximately at the same effective driving parameter  $\kappa_{1,\rm eff}^{\rm clus} = -0.1067 \pm 6.1 \,\%$ . Note, that its value is significantly smaller than the effective driving parameter  $\kappa_{1,\text{eff}}^{\text{hom}} = (\kappa_{1,\text{c}} - \kappa_2 u_0) = -0.091 \ (3.28)$  of the homogeneous system at the Turingbifurcation point  $\kappa_{1,c}$ . From this observation follows that clusters of dissipative

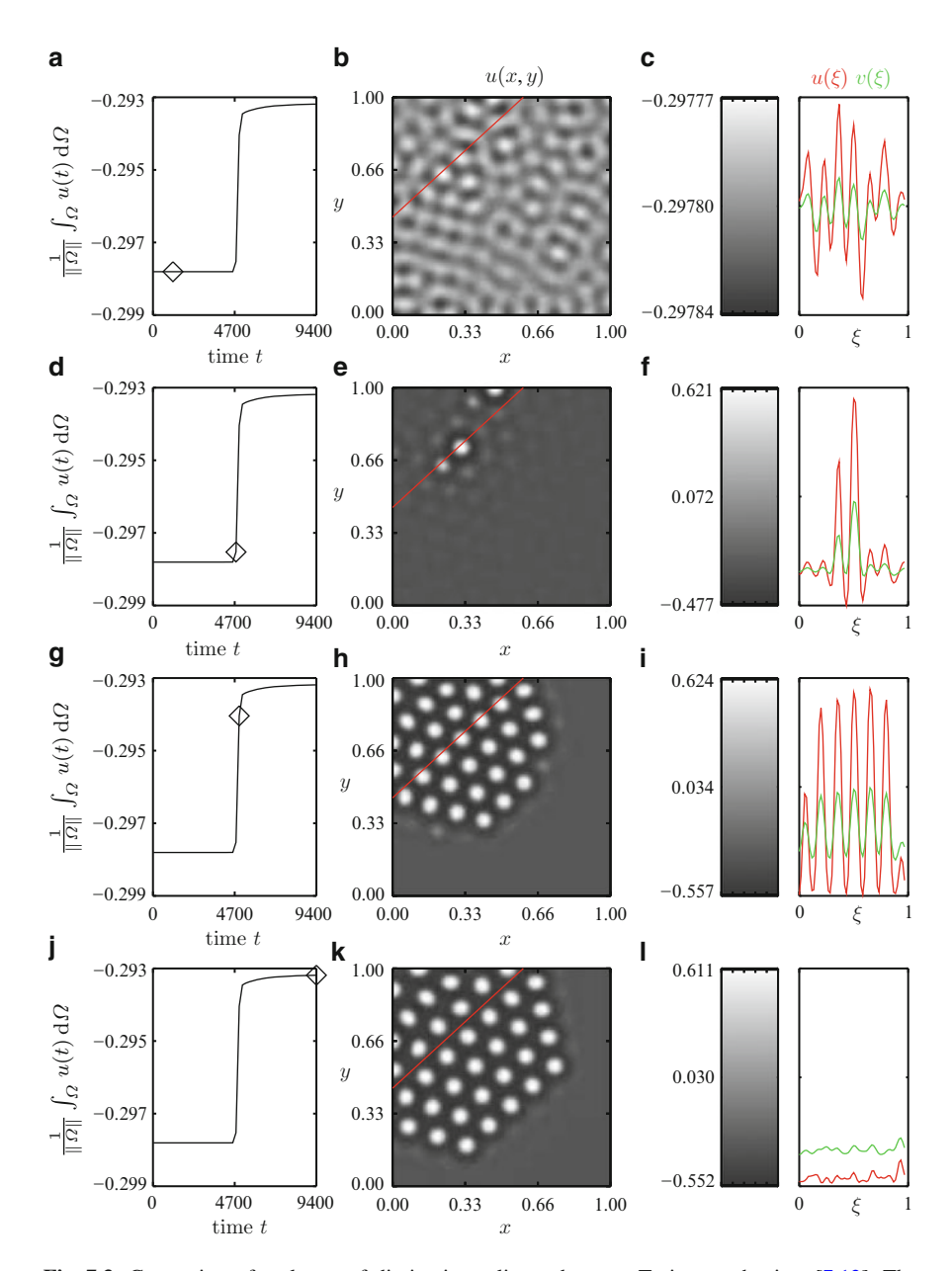


**Fig. 7.3** Generation of a cluster of dissipative solitons due to a Turing-mechanism [7.12]. The *left column* shows time series of activator integral  $\frac{1}{\|\Omega\|} \int_{\Omega} u(t) d\Omega$  with *diamonds* referring to the snapshots of activator u(x, y) (*middle column*) and intersections (*right column*) shown in each *row*. The intersections  $u(\xi)$  (*red curves*) and  $v(\xi)$  (*green curves*) are parameterized along the *red line* shown in the activator snapshots. The legend maps the activator amplitudes to the respective shades of *gray* given in the snapshots. Parameters from (7.2)

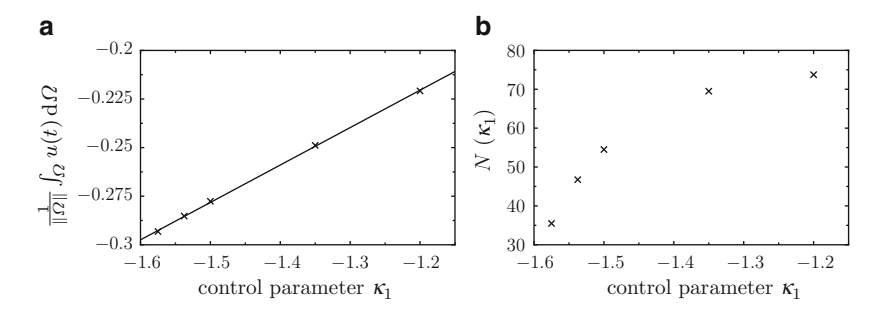


Fig. 7.4 Controlling the generation of dissipative solitons by global feedback. *Symbols* refer to simulations. The leftmost symbol references the simulation shown in Fig. 7.3. (a) Activator integral compensating the control parameter  $\kappa_1$ . For the investigated parameter set the integral depends linearly on the control parameter, such that the systems stabilizes at  $\kappa_{1,\text{eff}}^{\text{clus}} = -0.1067 \pm 6.1 \%$ . (b) Dependency of the number  $N(\kappa_1)$  of generated dissipative solitons on the control parameter  $\kappa_1$ . For  $\kappa_1 > -1.4$  the domain is covered by a hexagonal pattern of dissipative solitons. Parameters from (7.2), data published in Full-Metadata Format [7.13, 7.14]

solitons exhibit an instability in the vicinity of the Turing-bifurcation point, which vanishes for  $\kappa_{1,\rm eff} < \kappa_{1,\rm eff}^{\rm clus} < \kappa_{1,\rm eff}^{\rm hom}$ . In the following section this observation is related to the self-completion mechanism and the underlying mechanism is identified in Sect. 7.4.2 as the nonlinear superposition of oscillating tails.

The presented mechanism cannot generate single dissipative solitons from scratch but only clusters of dissipative solitons. This is due to the fact, that the Turing-mechanism renders a homogeneous state unstable against a hexagonal triad of wave vectors [7.15, 104pp]. If a localized structure ignites due to external noise (Fig. 7.3e) the coupling of these wave vectors leads to an increase of the pattern, too. This perturbation leads to the ignition of additional dissipative solitons at the oscillating tails of the initial one. The successive ignition of dissipative solitons continues until the global feedback has decreased the effective control parameter  $\kappa_{1,\text{eff}}$  (3.28) beyond the critical parameter  $\kappa_{1,\text{eff}}^{\text{clus}}$  such that the cluster becomes a stable solution of the reaction-diffusion system.

## 7.1.3 Self-completion

The generation of dissipative solitons in the direct neighbourhood of existing ones is called self-completion and has been reported for the first time in 1974 by Meinhardt and Gierer for simulations of morphogenesis [7.16]. Experimentally, the phenomenon of self-completion has been observed in a semiconductor-gas discharge system (Sect. 2.2.3). In order to understand the underlying mechanism a two-component reaction-diffusion system with global feedback (3.57) is investigated on a two-dimensional domain [7.12]. Parameters have been taken from the previous section (7.2) but feedback has been increased ( $\kappa_2 = 45.0$ ). The initial condition

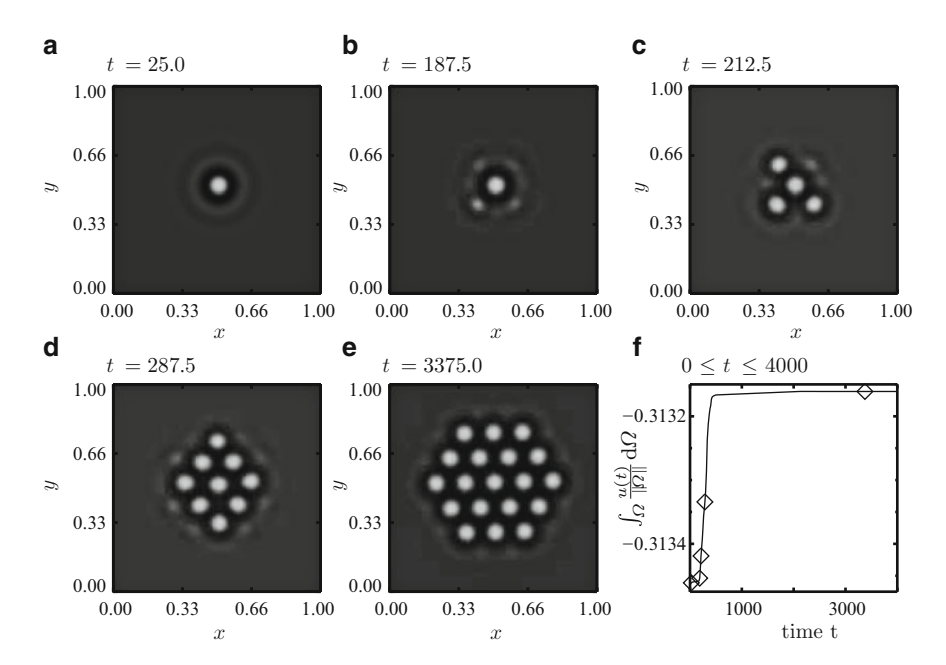


**Fig. 7.5** Self-completion in a two-component reaction-diffusion system with global feedback [7.12]. Subfigures (**a**)–(**e**) show grayscale images of the activator distribution u(x, y) with light and dark shades of gray refer to high and low activator concentrations, respectively. (**f**) Time series of feedback integral  $\frac{1}{\|\Omega\|} \int_{\Omega} u \, d\Omega$  with diamonds indicating the snapshots (**a**)–(**e**). Parameters from (7.2) with  $\kappa_1 = -14.4$  and  $\kappa_2 = 45.0$ 

has been realized as single dissipative soliton and the driving parameter has been adapted to  $\kappa_1 = -14.4$  such that the homogeneous system is stable ( $\kappa_{1,eff} < \kappa_{1,eff}^0$ ) but the a single dissipative soliton is unstable ( $\kappa_{1,eff} > \kappa_{1,eff}^{ds} = -0.0973$ ).

Snapshots of the simulation are shown in Fig. 7.5 as grayscale images of the activator distribution u(x, y) with *light* and *dark* shades of gray referring to high and low activator concentrations, respectively. In Fig. 7.5a the pronounced oscillating tail of the initial soliton is visible as ring surrounding the activator peak. In the course of the simulation this ring is modulated periodically (Fig. 7.5b). These perturbations act as nuclei for the ignition of three new dissipative solitons (Fig. 7.5c), which is accompanied by an increase of the feedback integral (Fig. 7.5f). The new dissipative solitons exhibit oscillating tails, which superimpose in a nonlinear way leading to the ignition of further dissipative solitons (Fig. 7.5d). This repeating process is stopped by the feedback integral which stabilizes the system at  $\kappa_{1,\text{eff}}^{\text{clus}'} = -0.1078$  and establishes a cluster of 19 dissipative solitons surrounding the initial one (Fig. 7.5e).

Note, that the wavelength characterizing the distance between the clustered dissipative solitons does not change in the course of the formation. This is in contrast to the process discussed in the previous section showing the formation of

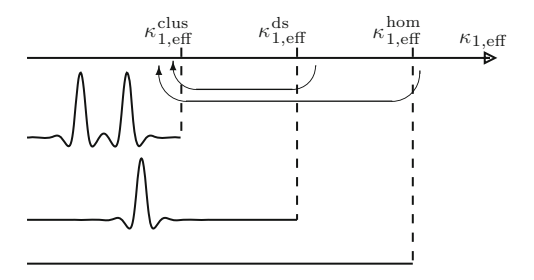


**Fig. 7.6** Hierarchy of bifurcation points in the vicinity of the Turing-bifurcation [7.17]. While a cluster of dissipative solitons becomes unstable for  $\kappa_{1,\text{eff}} > \kappa_{1,\text{eff}}^{\text{clus}}$  the stability of a single dissipative soliton and a homogeneous system is given for  $\kappa_{1,\text{eff}} < \kappa_{1,\text{eff}}^{\text{ds}}$  and  $\kappa_{1,\text{eff}} < \kappa_{1,\text{eff}}^{\text{hom}}$ , respectively

dissipative solitons from scratch. In the latter scenario the Turing-wavelength of the perturbation pattern determines the initial distance, which later on evolves to the relaxation wavelength of the oscillating tails.

#### 7.1.4 Feedback Control

The preceding sections have shown that a destabilized system can stabilize itself due to the generation of dissipative solitons if a feedback control with respect to the average activator concentration is applied. Although parameters and initial conditions of the investigated systems differ, they both stabilize at the same effective driving constant  $\kappa_{1,\text{eff}}^{\text{clus}} \approx \kappa_{1,\text{eff}}^{\text{clus}'}$  with  $\kappa_{1,\text{eff}}^{\text{clus}} - \kappa_{1,\text{eff}}^{\text{clus}'} = 1.1 \cdot 10^{-3}$ .

In the vicinity of the Turing-bifurcation, a hierarchy of bifurcation points with

$$\kappa_{1,\text{eff}}^{\text{clus}} < \kappa_{1,\text{eff}}^{\text{ds}} < \kappa_{1,\text{eff}}^{\text{hom}}$$
(7.3)

exists and dominates the dynamics (Fig. 7.6) of homogeneous systems such that the destabilization of a single dissipative soliton ( $\kappa_{1,\rm eff} > \kappa_{1,\rm eff}^{\rm ds}$ ) or a homogeneous state ( $\kappa_{1,\rm eff} > \kappa_{1,\rm eff}^{\rm hom}$ ) always leads to the generation of a cluster of dissipative solitons. In both scenarios the initially generated dissipative soliton changes the solution qualitatively, such that the next lower bifurcation point becomes relevant and renders the new structure unstable. Consequently, several dissipative solitons are generated until the feedback integral (3.28) stabilizes the system.

Although the hierarchy of bifurcation points has been demonstrated in a special reaction-diffusion system, several aspects have also been observed in other systems. For example Astrov and Logvin have simulated the self-completion of a dissipative soliton in a semi-phenomenological reaction-diffusion system modelling the structure formation of semiconductor gas-discharge systems [7.18]. Coulett et al. discuss the stability of a single dissipative soliton in the context of cluster instabilities [7.19]. It follows, that all reaction-diffusion systems, which show the formation

of hexagonal pattern due to a Turing destabilization of homogeneous states, also exhibit single dissipative solitons and clusters of dissipative solitons in adjacent parameter intervals.

## 7.2 Annihilation of Dissipative Solitons

## 7.2.1 Strong Repulsion

In the course of increasing the intrinsic velocity of dissipative solitons we have already observed some annihilation processes (Sect. 7.1.1). These are characterized by the fact that the cores of the interacting particles do not merge but simply fade away. In order to understand the underlying mechanism, the head-on collision of two fast dissipative solitons is simulated in a three-dimensional system (Fig. 7.7). The initial condition (5.1) is constructed from a dissipative soliton  $\vec{u}$  propagating with equilibrium velocity along the *y*-coordinate. Starting from a uniformly propagating dissipative soliton, which is located into the center of a co-moving coordinate system, the initial condition can be constructed as

$$\boldsymbol{u}(\boldsymbol{x},t)|_{t=0} = \widehat{\bar{\boldsymbol{u}}}\left(x, y - \frac{\ell_y - \delta}{2}, z\right) + \widehat{\bar{\boldsymbol{u}}}\left(x, \frac{\ell_y + \delta}{2} - y, z\right) - u_0, \tag{7.4}$$

with  $\delta=1.2$  specifying the initial distance between the interacting particles and  $\ell_{\nu}=2.08$  denoting the edge length of the system in y-direction.

The resulting annihilation is visualized in Fig. 7.7a as space-time plot of activator intersection u(x(y), t) along the symmetry axis  $x(y) = (0, y, 0)^T$ . In this image the paths of the dissipative solitons appear as *dark* stripes surrounded by *white* borders indicating the undershooting of the oscillating tails. *Gray areas* correspond to the homogeneous background state. In the beginning of the simulation the dissipative solitons propagate with equilibrium velocity  $\bar{c} = \frac{\Delta y}{\Delta t} = \pm 1.693 \cdot 10^{-3}$  with  $\Delta y/\Delta t$  denoting the reciprocal slope of the (*black*) activator stripes. Note, that the dissipative solitons propagate twice as fast as the particles depicted in Fig. 5.1a, where a similar configuration leads to the formation of a bound state. A snapshot of the approaching dissipative solitons is shown in Fig. 7.7b as activator iso-surface for u = -0.1 at t = 128. The shading of the iso-surface reflects the local concentration of the driving inhibitor with *blue* and *red* indicating high and low concentrations, respectively. Of course the dissipative solitons propagate into the direction of the lowest inhibitor concentration, which is indicated by *arrows*.

At t = 280 the dissipative solitons collide and their propagation is stopped immediately (Fig. 7.7a). Therefore, the activator peaks cannot escape their pushing inhibitor peaks anymore and the displacement between localized activator and inhibitor distributions diminishes. This is reflected in Fig. 7.7c by the dominating bluish shading of the activator iso-surface and the decreased volume enclosed by

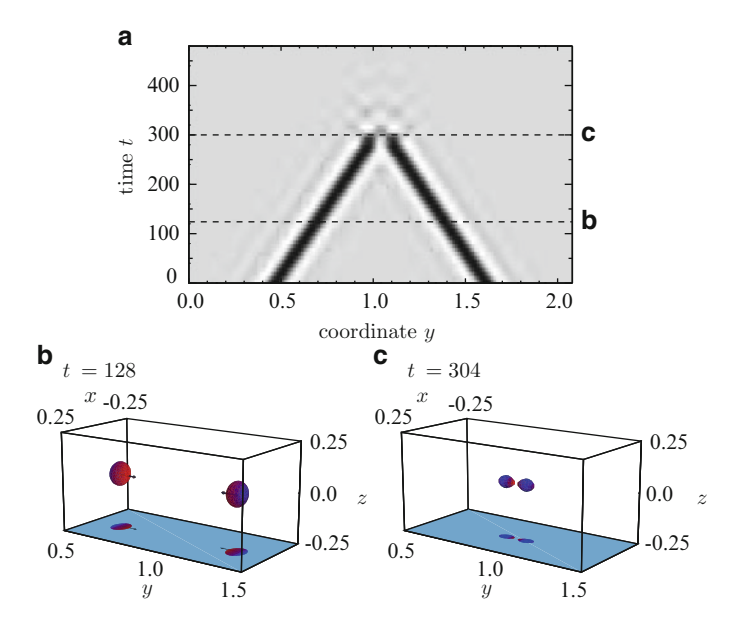


Fig. 7.7 Annihilation of two dissipative solitons by fading. (a) Space-time diagram of activator intersection u(x(y), t) with x(y) = (0, y, 0). Dark and light colours indicate large and low activator concentrations, respectively. The homogeneous background state is represented by a light gray shading, while the dissipative solitons are black stripes with white borders. Subfigures (b) and (c) show snapshots of the activator iso-surface for u(x) = -0.1 which is coloured with respect to the local concentration of the driving inhibitor. Blue and red indicate a large and low concentration of the driving inhibitor, respectively. Arrows indicate the direction of motion. In order to promote spatial orientation, shadows of all objects are projected onto the base of the domain. Parameters from (5.2) with  $\tau = 4.35$ 

the iso-surface. At the same time, the activator peaks visible in the space-time plot have turned gray, which indicates the shrinking of the activator peaks (Fig. 7.7a). This processes continues to such an extent that for a short period of time the activator peaks become inverted and the local activator concentration decreases beyond the homogeneous background state. Finally, the system relaxes completely to the homogeneous state.

## 7.2.2 Weak Repulsion

A completely different type of annihilation is observed for dissipative solitons exhibiting weak repulsion. In order to illustrate this scenario the three-component reaction-diffusion system (3.69) has been solved on a three-dimensional domain with the following parameter set [7.5]:

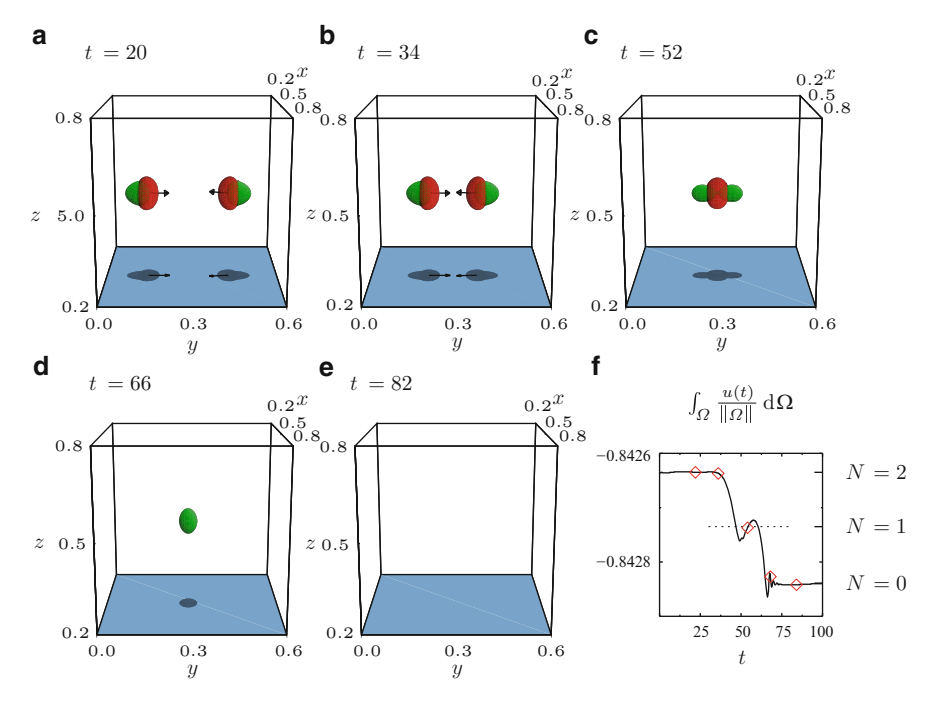


Fig. 7.8 Annihilation of two dissipative solitons caused by weak repulsion [7.5]. Subfigures (a)–(e) show iso-surfaces of activator u(x)=-0.5 and driving inhibitor v(x)=-0.5 with *red* and *green* faces, respectively. *Arrows* indicate the direction of motion. In order to promote spatial orientation shadows of all objects are charted onto the base of the domain. Subfigure (f) shows the evolution of activator integral  $\frac{1}{\|\Omega\|} \int_{\Omega} u \ d\Omega$  with *diamonds* indicating snapshots (a)–(e). Parameters from (7.5)

$$D_u = 1.5 \cdot 10^{-4}, \ D_v = 1.86 \cdot 10^{-4}, \ D_w = 9.6 \cdot 10^{-3}, \ \lambda = 2.0,$$
  

$$\kappa_1 = -6.92, \ \kappa_2 = 0, \ \kappa_3 = 1.0, \ \kappa_4 = 8.5, \ \tau = 25.0, \ \theta = 1.0,$$
  

$$\Omega = [0, 0.8]^3, \ \Delta_x = 0.085, \ \Delta_t = 0.02.$$
(7.5)

Localized solutions of this system are characterized by a strongly diffusing stabilizing inhibitor w and an extreme separation of time-scales concerning activator u and driving inhibitor v. This leads to dissipative solitons exhibiting acorn-like iso-surfaces (Fig. 7.8a) which are in contrast to the radial-symmetric iso-surfaces observed in systems without extreme time-scale separation (Fig. 7.7).

The flat peak of the stabilizing inhibitor and the pronounced displacement between the peaks of activator and driving inhibitor causes a weak repulsive interaction between the approaching dissipative solitons. They are slightly decelerated in their head-on collision but are not stopped while approaching each other. Therefore, the activator peaks of the dissipative solitons merge (Fig. 7.8c) and are enclosed by the following peaks of the driving inhibitor (Fig. 7.8d). This configuration

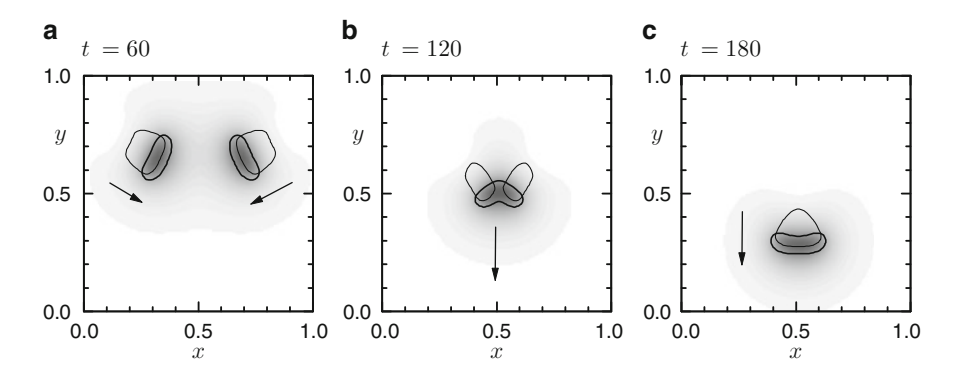


Fig. 7.9 Partial annihilation due to weak repulsion [7.23, p. 97]. The subfigures show contour plots of activator u and driving inhibitor v for the respective half-values as *thick* and *thin solid lines*, respectively. Gray scale images visualize the distribution of the stabilizing inhibitor w, arrows indicate directions of motion. Parameters from (7.6)

is unstable due to the local excess of inhibitor and the merged structure fades completely (Fig. 7.8e). Note, that the activator of the merged state approximately has the same size of a single dissipative soliton (Fig. 7.8f) and therefore can be considered as unstable dissipative soliton.

A completely different interaction is observed if dissipative solitons with weak repulsion do not collide head-on. In this state it is likely that the dissipative solitons merge to an unstable state, which evolves to a single dissipative soliton. This case is visualized on basis of a simulation of the three-component system (3.69) and parameter set

$$D_u = 1.55 \cdot 10^{-4}, \ D_v = 1.93 \cdot 10^{-4}, \ D_w = 5.0 \cdot 10^{-2}, \ \lambda = 2.0,$$
  

$$\kappa_1 = -8.72, \ \kappa_2 = 0, \ \kappa_3 = 8.45, \ \kappa_4 = 1.0, \ \tau = 48.0, \ \theta = 0.0,$$
  

$$\Omega = [1.3, 1.3]^2, \ \Delta_x = 0.01, \ \Delta_t = 1.0.$$
(7.6)

from [7.11, p. 97]. Figure 7.9 shows gray-scale images of the stabilizing inhibitor, which is complemented by half-value contour plots of the activator (*thick lines*) and driving inhibitor (*thin lines*). Note, that the evolving dissipative solitons has the same size than the initial ones. This is in contrast to the observations of Krischer and Mikhailov [7.21], who stabilized the dissipative solitons not by an additional component but by global feedback. In this case the dissipative soliton evolving from a merged state has twice the size than a initial particle. Nishiura et al. investigate the merging of dissipative solitons in a three-component variant of the Gray-Scottmodel and relate the annihilation to a so-called peanut scattor, which is an unstable solution of the reaction-diffusion-system [7.22].

In higher dimensional systems partial annihilation by merging could also lead to the generation of new dissipative solitons, which is discussed in Sect. 7.3.2.

### 7.3 Generation of Dissipative Solitons

## 7.3.1 Strong Repulsion

Motivated by the experimental observation of current density filaments generating a single dissipative soliton in the course of interaction (Fig. 2.13) a similar scenario is simulated on basis of the three-component reaction-diffusion system (3.69). For this purpose the interacting dissipative solitons have to propagate with large intrinsic velocity (Fig. 7.2c). Furthermore, they have to exhibit pronounced oscillating tails in order to feature self-completion (Sect. 7.1.3). However, because no global feedback is considered and the investigated systems hold  $\kappa_{1,eff} = \kappa_1 < \kappa_{1,eff}^{clus}$  (Fig. 7.6), two or more dissipative solitons need to interact directly in order to generate further dissipative solitons in a process called *replication* [7.24].

#### 7.3.1.1 Replication in Two-Dimensional Systems

The following simulation demonstrates the replication of a dissipative soliton on a two-dimensional domain for parameter set (4.22) with  $\tau=3.47$ . After each time step the solutions of activator u and driving inhibitor v are perturbed with spatiotemporal uncorrelated noise of amplitude  $R_u=10^{-9}$  and  $R_v=0.5\cdot10^{-9}$ . The noise amplitude has a uniform probability density distribution in order to accelerate transients of unstable states.

The simulation is depicted in Fig. 7.10 by means of four subsequent snapshots (middle column of Fig. 7.10) visualizing the activator distribution u(r,t) as grayscale images with *arrows* indicating the velocity vectors of the dissipative solitons. The snapshots are supplemented by intersections of activator u and stabilizing inhibitor w along the symmetry axis x = 0.5 (right column of Fig. 7.10). This symmetry axis is indicated within the grayscale images of the middle column as *broken* line. The intersections of the right column are combined with legends mapping the grayscale of the middle column to the activator concentration of the right column. The left column of Fig. 7.10 shows the evolution of quantity  $\hat{u}(t)$ , which indicates the conservation, annihilation and generation of dissipative solitons, such that an increase of  $\hat{u}(t)$  by  $\hat{u}(t) = 0$ 0 indicates the generation of an additional dissipative soliton, if  $N_0$  is the number of initially existing dissipative solitons. Therefore,  $\hat{u}(t) \approx 1$  refers to the conservation of the number  $N_0$  of initially existing particles. The indicator  $\hat{u}(t)$  is computed by:

$$\hat{u}(t) = \frac{\int_{\Omega} (u(\boldsymbol{r}, t) - u_0)^2 d\boldsymbol{r}}{\int_{\Omega} (u(\boldsymbol{r}, 0) - u_0)^2 d\boldsymbol{r}}$$
(7.7)

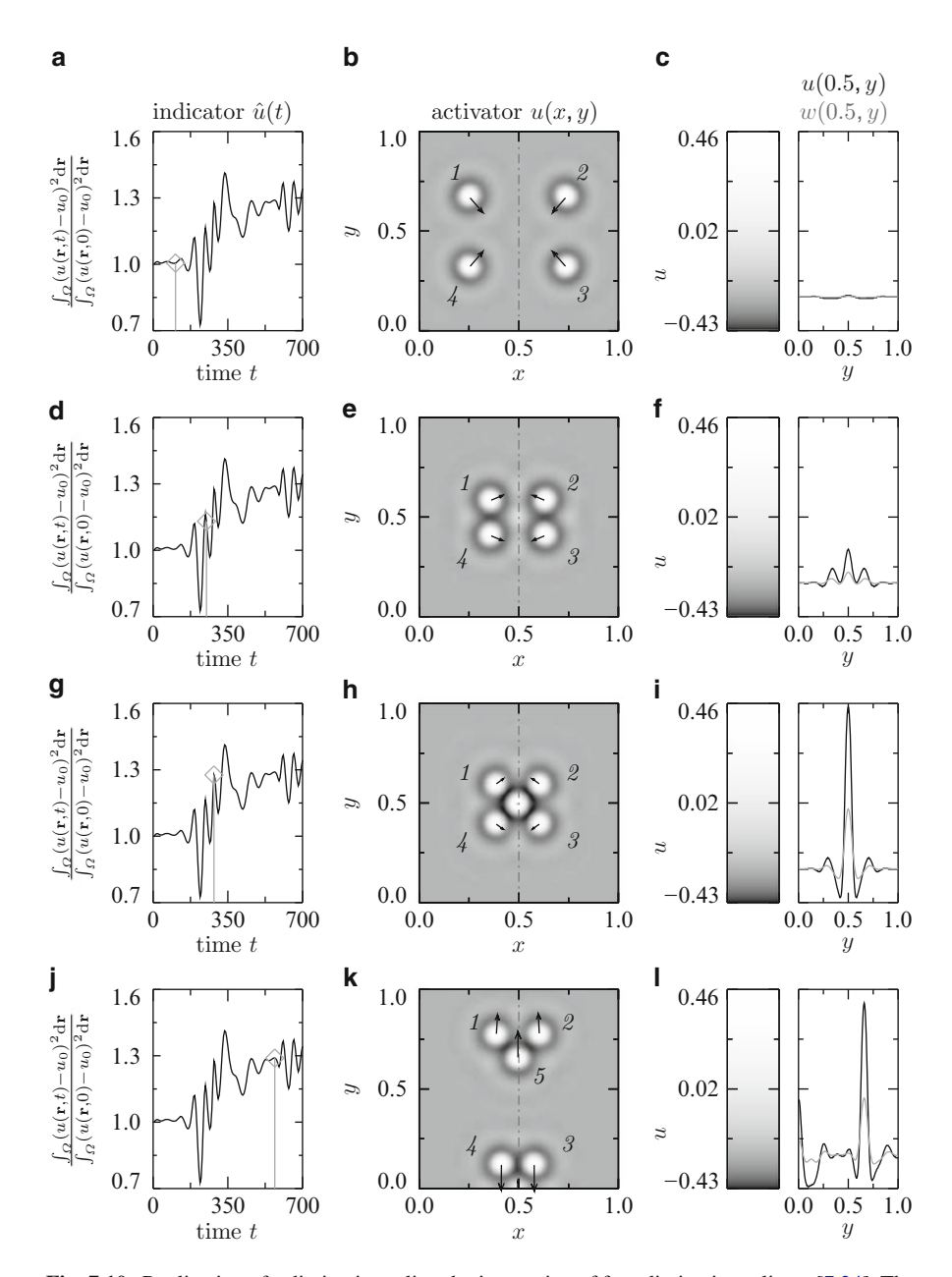


Fig. 7.10 Replication of a dissipative soliton by interaction of four dissipative solitons [7.24]. The resulting 5-soliton-cluster decays under symmetry breaking into a 2-soliton bound state and a 3-soliton bound state. The figure shows four snapshots of the simulation (*rows*). Columns from left to *right*: Evolution of indicator  $\hat{u}(t)$  (7.7), activator distribution, grayscale legend, and intersections of activator u and fast inhibitor w at x = 0.5. Diamonds in the indicator diagram reference the snapshot. Arrows overlaying the activator distribution indicate the direction of motion. Parameters from (4.22) with  $\tau = 3.47$ 

with  $u_0$  corresponding to the homogeneous background state. Within these diagrams a *diamond* indicates the time t of snapshot  $u(\mathbf{r},t)$  and intersections u(0.5, y, t), w(0.5, y, t) depicted in the same row.

The simulation starts with four dissipative solitons being positioned symmetrically to the central axes of the domain, which are defined by x = 0.5 and y = 0.5. The dissipative solitons denoted with 1 and 3 propagate towards collision point  $P_{1,3} = (0.4, 0.5)$ , and dissipative solitons denoted with 2 and 4 move towards collision point  $P_{2.4} = (0.6, 0.5)$ , such that close to  $P_{1.3}$  and  $P_{2.4}$  the interacting particle form bound states (Fig. 7.10e). Both bound states head for the center of the domain where their tales overlap. The intersection in Fig. 7.10f shows the superposing oscillatory tails in detail. In the center of the domain a local activator maximum is formed due to the influence of four dissipative solitons. Additionally, two smaller maxima are created due to the superposition of the tails of two dissipative solitons. This local increase of activator concentration causes a deflection of initial dissipative solitons (Fig. 7.10e) and the ignition of a fifth dissipative soliton (Fig. 7.10h), which is accompanied by an increase of indicator  $\hat{u}(t)$  (Fig. 7.10g). The generated particle also exhibits oscillatory tails (Fig. 7.10i) which interact with the neighbouring particles without the ignition of additional dissipative solitons.

Finally, the symmetry with regard to the y=0.5-axis is broken, which is shown in Fig. 7.10k. Here the 5-soliton-bound state has decayed into a bound state consisting of two dissipative solitons propagating towards the lower domain boundary and a bound state consisting of three dissipative solitons propagating towards the upper domain boundary. At the depicted snapshot the two-soliton bound state has already reached the lower domain boundary, where due to the no-flux boundary condition another replication occurs. In the same time the bound state consisting of particles 1, 2, and 5 has only reached the middle of the upper domain half.

In order to investigate the symmetry breaking and the velocity difference of the two-soliton and the three-soliton bound state, we will take a closer look at the dynamics. Therefore, in Fig. 7.11 the evolution of two characteristic variables of the dynamics are plotted for each dissipative soliton. One is the absolute value of shift  $\alpha(t)$  between the center of the activator peaks and corresponding peaks of the driving inhibitor distribution v. The other is the angle  $\phi(t)$  of the direction of motion, which is estimated from shift  $\alpha(t) = (\alpha_x(t), \alpha_v(t))$  such that

$$\cos \phi(t) = \frac{\alpha_x(t)}{\alpha(t)} \wedge \sin \phi(t) = \frac{\alpha_y(t)}{\alpha(t)}.$$
 (7.8)

Additionally, Fig. 7.11a shows a grayscale image of the activator distribution u(x, y) at t = 437.5 with the interacting dissipative solitons being numbered. The image also shows contour lines of the activator u(x, y) = -0.2 at t = 17.5. Arrows indicate the direction of motion.

In the beginning, dissipative soliton 1 propagates with an angle of  $-\frac{\pi}{3}$  from the upper left quarter of the domain towards its collision point close to the middle of the

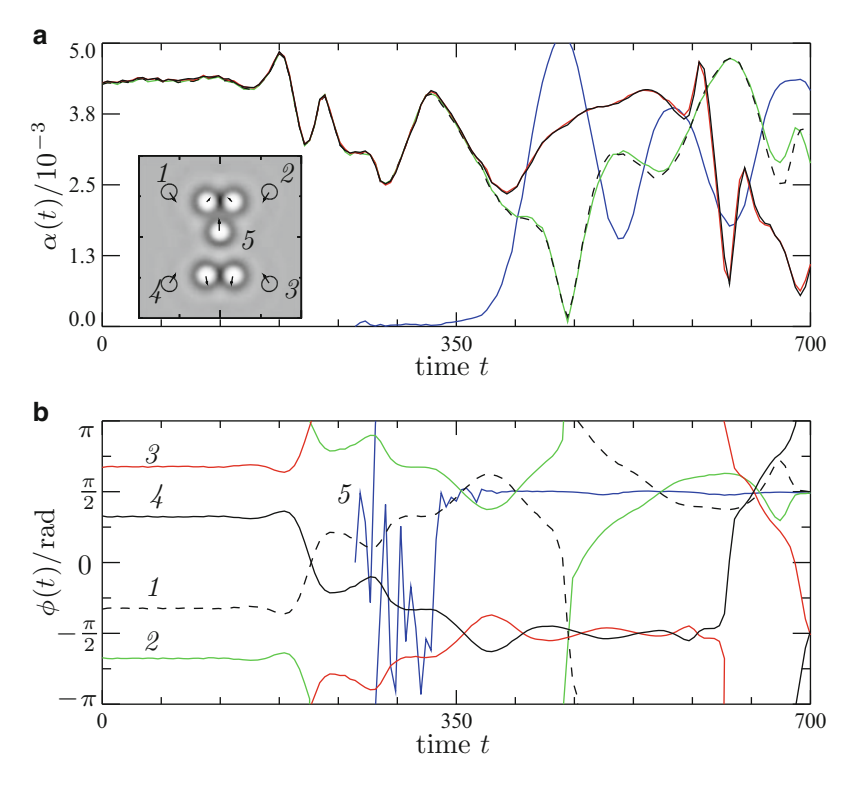


Fig. 7.11 Dynamics of the interacting dissipative solitons presented in Fig. 7.10 [7.24]. (a) Time evolution of the absolute value of shift  $\alpha(t)$  between the centers of activator peaks and corresponding peaks of driving inhibitor distribution. The inlay of subfigure (a) shows the activator distribution u at t=437.5 and contour lines of the activator u(x,y)=-0.2 at t=17.5. Arrows denote directions of motion and numbers identify the individual dissipative solitons. (b) Evolution of the angle  $\phi(t)$  of the direction of motion (7.8). The numbers within the grayscale image of (a) and the numbered curves of (b) refer to the same dissipative solitons. That applies also to the line styles of (a) and (b). Curves vanishing at the top (bottom) and reemerging at the bottom (top) reflect the periodicity of the inverse function used for the calculation of  $\phi(t)$ 

domain. Dissipative solitons 2, 3, and 4 exhibit angles of  $-\frac{2\pi}{3}, \frac{2\pi}{3}$ , and  $\frac{\pi}{3}$ , respectively (Fig. 7.11b,  $t \in [0, 100]$ ). The symmetry of the initial condition is reflected in Fig. 7.11a by the identity of  $|\alpha(t)|$  for  $t \in [0, 100]$ . This symmetric behaviour persists even while dissipative solitons 1-4 are deflected by the replicated fifth dissipative soliton such that their angles of propagation change signs (Fig. 7.11a, b,  $t \in [100, 340]$ ).

After its generation, dissipative soliton 5 is stationary and therefore is an unstable solution of system. Its propagator amplitude  $\alpha(t)$  is just slightly excited and its direction of motion changes rapidly (Fig. 7.11b,  $t \in [250, 350]$ ) until it relaxes at  $t \approx 340$  to an angle of  $\frac{\pi}{2}$ . At this time the symmetry of the solution with regard to the y = 0.5 axis is broken, such that the curves of  $|\alpha(t)|$  for the 1,2-bound state and

the 3,4-bound state branch off. This process is caused by the noise being applied to the system.

While the excitation of propagator mode  $\alpha_5$  (blue curve in Fig. 7.11a) and the excitations of propagator modes  $\alpha_3$  and  $\alpha_4$  (solid red and overlaid broken black curves) increase, dissipative solitons 1 and 2 are slowed down and the amplitudes of their propagator modes decrease (solid green and overlaid broken black curves). Obviously, the new dissipative soliton is located within a repulsive region regarding particles 3 and 4, and within an attractive region concerning particles 1 and 2. The repulsive interaction leads to a mutual acceleration of dissipative solitons 3, 4, and 5 which is even increased by the attractive interaction between dissipative solitons 1,2, and 5. At the same time, dissipative solitons 1 and 2 are slowed down in the course of pulling the fifth particle. The velocity vectors indicated in the grayscale image of Fig. 7.11a show an extreme case of this configuration at t = 437.5, for which the propagator mode amplitudes of the 1,2-bound state are close to zero, while the propagator mode of dissipative soliton 5 is strongly excited and, on the other hand, pushes 1 and 2. It follows an alternating acceleration and deceleration of dissipative solitons 1, 2, and 5, which leads to a smaller average velocity of the 3-soliton-cluster compared to the 2-soliton bound state.

The described scenario is very similar to the experimental observations reported by Astrov and Purwins in 2001 (Fig. 2.13), where three dissipative solitons approach each other and replicate a fourth one. This generation mechanism can be understood in the context of the presented simulation, which explains the replication as a result of the nonlinear superposition of oscillating tails. Experimental evidence for oscillating tails of dissipative solitons has also been given in the d.c. gas-discharge system (Fig. 2.8b).

#### 7.3.1.2 Replication in Three-Dimensional Systems

In order to simulate the replication of dissipative solitons in three dimensions, the following parameters have been chosen, which lead to solitary solutions with oscillating tails:

$$D_u = 1.1 \cdot 1.3 \cdot 10^{-4}, \ D_v = 0, \ D_w = 9.64 \cdot 10^{-3}, \ \lambda = 0.95,$$
  
 $\kappa_1 = -0.08, \ \kappa_3 = 0.25, \ \kappa_4 = 1, \ \tau = 4.5, \ \theta = 0,$  (7.9)  
 $\Omega = [0, 1.4]^3, \ \Delta x = 0.011, \ \Delta t = 1.0, \text{ periodic boundary condition.}$ 

Note, that the time scale constant  $\tau$  of the driving inhibitor exceeds the critical value of  $\tau_c=4.0~(4.30)$  significantly, such that the limit case of particle conservation is not given anymore. The initial conditions have been set up from radial symmetric stationary dissipative soliton solutions of parameters (7.9) such that three particles are starting from the vertexes of an equilateral triangle with sides of length 0.8 (Fig. 7.12a). The peaks of the driving inhibitor for each dissipative soliton have been shifted with respect to the respective activator peaks by  $8.2 \cdot 10^{-4}$  length units such

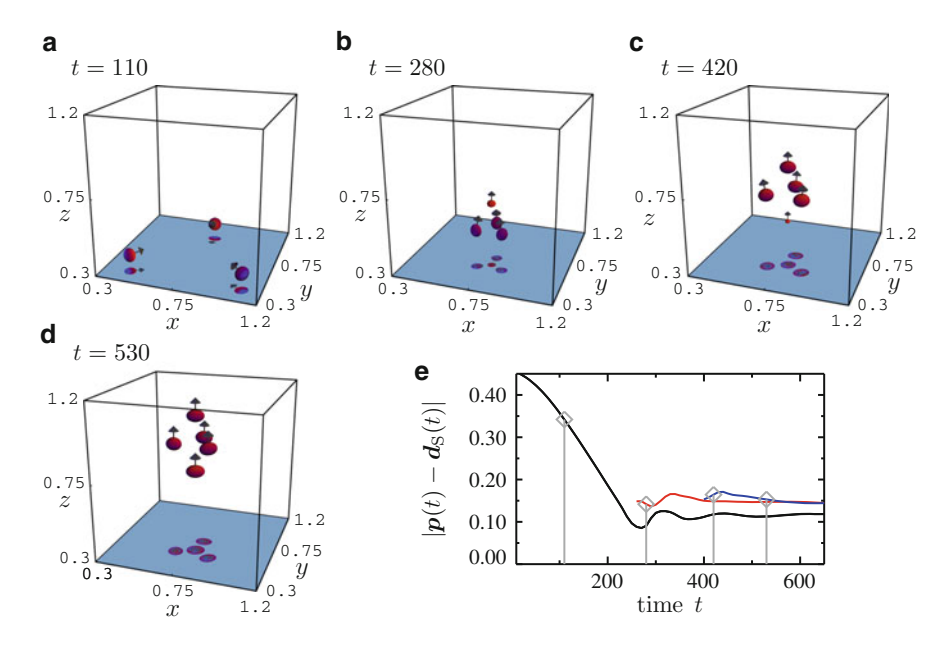


Fig. 7.12 Replication of dissipative solitons in a three-dimensional reaction-diffusion system [7.25]. Subfigures (a)–(d) show iso-surfaces of activator u(x, y, z) = 0.0, which are coloured with respective to the local concentration of the driving inhibitor. A large (small) inhibitor concentration is indicated by blue(red). Vectors denote the direction of motion of the dissipative solitons, which is approximated by the shift of the slow inhibitor v with respect to the activator u of the individual dissipative soliton. Subfigure (e) shows the evolution of distance to the center of the initial particles. The black curve refers to the initial dissipative solitons, the red and blue curve to the fourth and fifth dissipative solitons, respectively. Parameters from (7.9)

that the motion of each dissipative soliton is directed towards collision point  $P_c = (0.75, 0.58, 0.51)^T$ . The peaks of the stabilizing inhibitors are centered around the activator peaks.

In order to visualize the evolution of the field equations (3.69), Fig. 7.12 shows four subsequent snapshots of activator iso-surfaces u(x, y, z) = 0.0, which are coloured with respect to the concentration of the driving inhibitor concentration. Here red (blue) indicates a high (low) inhibitor concentration, respectively. Arrows indicate the direction of motion of the dissipative solitons. An overview of the dynamics is given in Fig. 7.12e showing the distance  $d(t) = |p(t) - d_S(t)|$  between the individual dissipative solitons and their center

$$d_{S}(t) = \frac{1}{3}(p_{1}(t) + p_{2}(t) + p_{3}(t)). \tag{7.10}$$

*Black* curves refer to the initial dissipative solitons, which coincide due to the choice of the center  $d_S(t)$ , whereas the dynamics of the generated particles is plotted with *red* and *blue* curves.

While relaxing to their equilibrium velocity, the dissipative solitons reach their closest distance  $d_{\min} = 0.088$  at t = 280 to their center  $d_{\rm S}(t)$  and a fourth dissipative solitons ignites at a distance of d = 0.146 to  $d_{\rm S}(t = 280)$  (Fig. 7.12b). This event turns the direction of motion of the initial dissipative solitons parallel to the z-axis. The distance between the particles relaxes in an oscillatory manner to a steady state corresponding to minimal interaction (Fig. 7.12e). During this process the initial dissipative solitons come close together for another time (d = 0.110) and a fifth particle ignites at a distance of d = 0.153 to center  $d_{\rm S}(t)$  (Fig. 7.12e). The double pyramid cluster of five dissipative solitons continues to propagate parallel to the z-axis and the particles relax towards an equilibrium distance of d = 0.118, while the distance of the ahead and behind running dissipative solitons to the center reaches an equilibrium distance of d = 0.145.

The simulation shows that several individual dissipative solitons can generate a limited number of new dissipative solitons. The mechanism seems to be related to the distance between the structures, because the replication mechanism only occurs if the initial dissipative solitons come close to each other and overcome a critical distance. If they form a bound state and relax to a steady configuration, which is observed for t > 400 in the presented simulation, no replication phenomena occur.

#### 7.3.2 Weak Repulsion

The partial annihilation of dissipative solitons due to weak repulsion (Fig. 7.9) offers a natural way for generating dissipative solitons in higher dimensional systems if the driving inhibitor v is too slow to prevent the bursting of the activator u into the additional dimensions. This scenario is discussed on basis of a simulation, which demonstrates the merging of two dissipative solitons to an intermediate state and the emerging of two new dissipative solitons propagating perpendicularly to the original plane of motion [7.5, 7.20]. The respective parameter set is derived from (7.5) by increasing the time scale constant of the driving inhibitor to  $\tau = 48.0$ . This leads to a pronounced spreading of the driving inhibitor, which can be seen in Fig. 3.20 on basis of an intersection and in Fig. 7.13a on basis of the iso-surfaces of the activator (red) and the driving inhibitor (green). The iso-surface of the stabilizing inhibitor is not shown, because it is centered around the localized activator distribution (Fig. 3.20).

Due to the pronounced displacement between activator u and driving inhibitor v the repulsion between the dissipative solitons is weak and they merge in the course of a head-on collision (Fig. 7.8b). Perpendicular to the original plane of motion two new activator peaks emerge (Fig. 7.8c) and evolve to independent particles (Fig. 7.8d) exhibiting approximately the same shape as the original ones (Fig. 7.8e).

(Fig. 7.8d) exhibiting approximately the same shape as the original ones (Fig. 7.8e). The evolution of the normalized activator integral  $\int_{\Omega} \frac{u(t)}{\|\Omega\|} d\Omega$  is shown in Fig. 7.13f. Its initial value characterizes the two-particle state. In the course of merging the normalized activator integral oscillates around the value being characteristic for a system hosting one dissipative soliton. After the emerging of two new particles

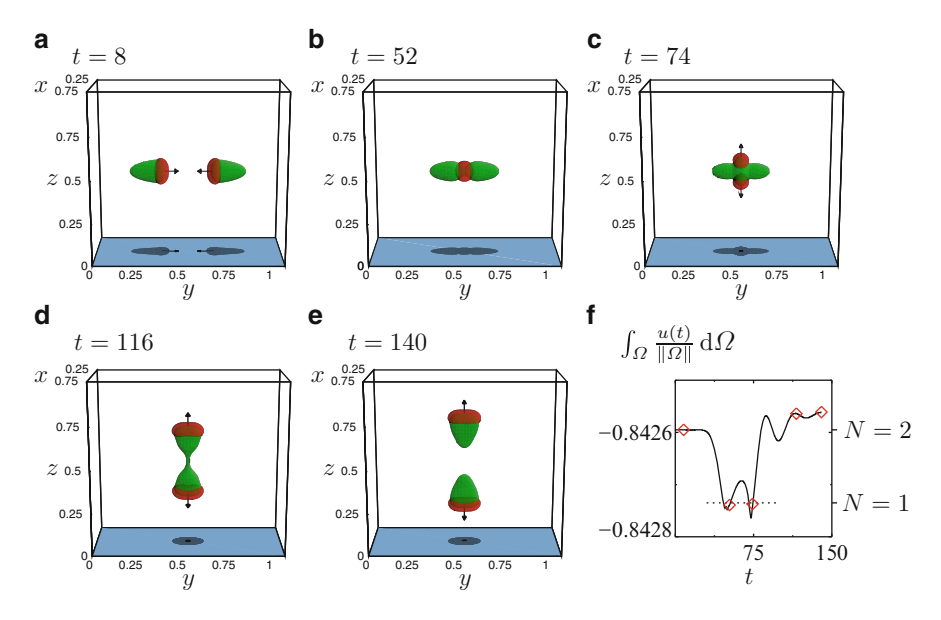


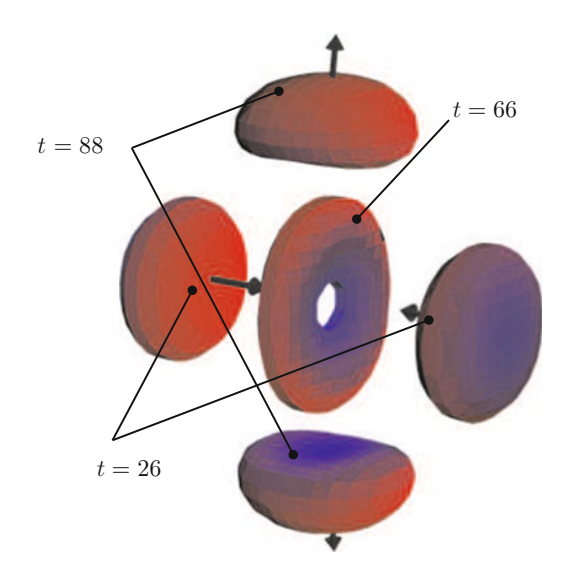
Fig. 7.13 Formation of complex intermediate states due to weak repulsion [7.5]. (a)–(e) Isosurfaces of activator u(x) = -0.5 (red) and driving inhibitor v(x) = -0.5 (green). Arrows indicate the direction of motion. In order to promote spatial orientation shadows of all objects are projected onto the base of the domain. Subfigure (f) shows the evolution of activator integral  $\frac{1}{|\Omega|} \int_{\Omega} u \ d\Omega$  with diamonds indicating snapshots (a)–(e). Parameters from (7.5) mit  $\tau = 48$ ,  $\Omega = [0,1] \times [0,1.33] \times [0,1]$ 

the measure starts to relax to the original value. Note, that the relaxation is not finished at t=150, because the trailing tails of the localized activator distributions still have not evolved their original form, which can be seen from comparing the respective intersections [7.25, p. 54].

A more detailed view on the merged state is given in Fig. 7.14, which shows the iso-surfaces of activator u(x,t) = 0.8 for  $t \in \{26, 66, 88\}$ . The surfaces are shaded with respect to the local concentration of the driving inhibitor with *red* and *blue* indicating low and high concentrations, respectively. The shading illustrates that the structures propagate against the gradient of the driving inhibitor field. In this figure the merged state appears as torus from which the new dissipative solitons evolve.

Similar phenomena of transient merging processes are also observed for other types of self-organized solitary structures such like Hopf solitons. Concerning a  $\phi^4$ -model with stabilizing Skyrme-term two-dimensional simulations of head on collisions between two solitons show the merging and reemerging perpendicular to the original direction of motions [7.26]. This might lead to the conclusion that the described process is generic for self-organized solitary structures under the precondition of weak repulsion.

Fig. 7.14 Transient activator torus [7.12]. Iso-surfaces u(x) = 0.8 for the simulation presented in Fig. 7.13 are coloured with respect to the local concentration of the driving inhibitor with *red* and *blue* indicating low and high concentrations, respectively



## 7.3.3 Self-replication

The most frequently investigated generation mechanism of dissipative solitons in reaction-diffusion systems is the so-called self-replication. It is characterized by the splitting of a dissipative soliton into two independent structures, eventually undergoing further division processes. Experimentally, self-replication has been observed for one- and two-dimensional semiconductor-gas discharge systems [7.27, 7.28] and for concentration drops in the ferrocyanide-iodie-sulphite reaction (Sect. 2.1.5). From the theoretical point of view this phenomenon has been investigated for reaction-diffusion systems with cubic nonlinearity and additional drift term [7.29, 7.30] and for two-dimensional Gray-Scott systems [7.31]. Bode analyses the self-replication of dissipative solitons on basis of division rules for one-dimensional front-pairs [7.32, S. 105ff], while Nishiura and Ueyama explain the self-replication mechanism by means of a hierarchic arrangement of saddle-node-bifurcations in the vicinity of a Bogdanov-Takens-Turing bifurcation point [7.33]. The self-replication of dissipative solitons triggered by a parameter inhomogeneity is discussed in the following paragraphs.

For this purpose the homogeneous state of a three-component reaction-diffusion system (3.69) has been overlaid by an inhomogeneity of Gaussian shape:

$$\kappa_1(\mathbf{x}) = -12.34 + 0.8 \exp\left(\frac{-\ln(2)\left(\mathbf{x} - \left(\frac{1}{2}, \frac{1}{2}\right)^{\mathrm{T}}\right)^2}{1.932 \cdot 10^{-2}}\right). \tag{7.11}$$

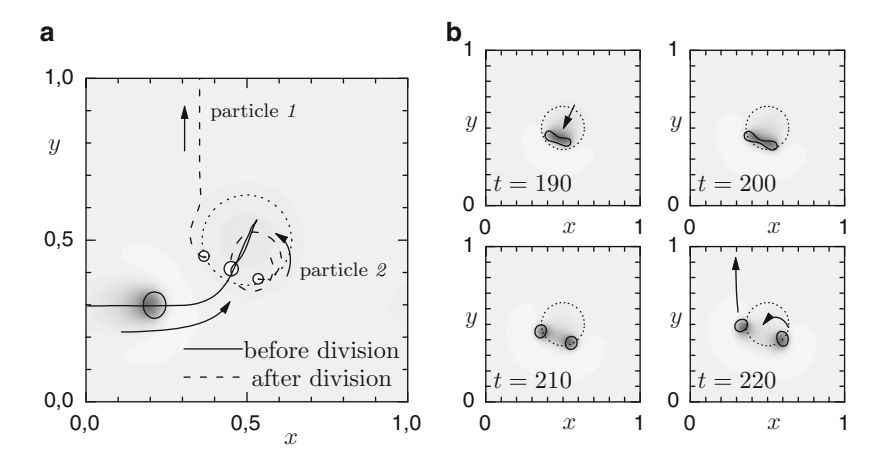


Fig. 7.15 Self-replication of dissipative solitons triggered by a spatial inhomogeneity [7.20]. (a) Initial condition of driving inhibitor v, trajectories of dissipative solitons before and after self-replication (solid and broken curves), and the half width of the inhomogeneity (7.11) (dotted circle). (b) Snapshots of the first self-replication. Parameters:  $D_u = 1.21 \cdot 10^{-4}4$ ,  $D_v = 1.7 \cdot 10^{-3}$ ,  $D_w = 1.46 \cdot 10^{-2}$ ,  $\lambda = 4.3$ ,  $\kappa_1$  from (7.11),  $\kappa_2 = 0$ ,  $\kappa_3 = 1.0$ ,  $\kappa_4 = 8.0$ ,  $\tau = 60.0$ ,  $\theta = 0.0$ ,  $\Omega = [0, 1.0]^2$ ,  $\Delta_x = 7.14 \cdot 10^{-3}$ ,  $\Delta_t = 0.1$ , periodic boundary condition

The inhomogeneity is located in the center of the domain and its half-width is indicated in Fig. 7.15a as a *dotted circle*. The figure also shows the distribution of the driving inhibitor as gray-scale image and the half-width contour line of the activator. The trajectories indicate that the dissipative soliton is attracted by the inhomogeneity and is drawn into its center. It crosses the maximum of the inhomogeneity, reverses its direction of motion and crosses the maximum again. At the same time the dissipative soliton starts to stretch perpendicular to its direction of motion, until it separates into two independent particles. (Fig. 7.15b). The dissipative soliton indicated with *1* leaves the inhomogeneity (*broken* curve in Fig. 7.15a), while the second dissipative soliton stays within the inhomogeneity and undergoes three more self-replications, until all particles leave the inhomogeneity.

The ability to create a number of dissipative solitons successively can be interpreted as prototype of a particle generator, which might become important in view of particle based arithmetic [7.34]. In this context an important building part is a particle generator, which has been realized in [7.35] by means of an inhomogeneity.

## 7.4 Mechanisms of Strong Interaction

#### 7.4.1 Annihilation

From the investigations on the formation of bound states it is known, that a headon collision of dissipative solitons does not lead to annihilation in the vicinity of

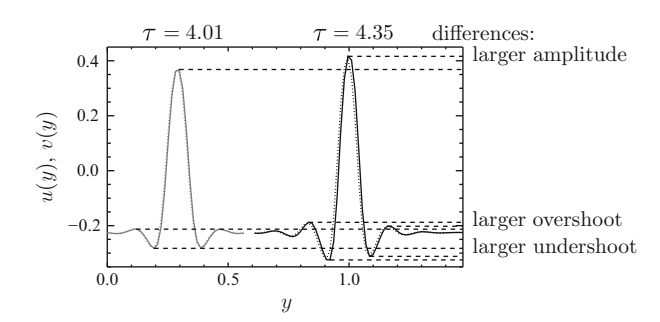


Fig. 7.16 Comparison of slow and fast dissipative solitons. The plot shows intersections of the activator (*solid curves*) and inhibitor peaks (*dotted curves*) for a slow dissipative soliton (*left hand side*) and a fast one (*right hand side*). In the vicinity of the drift-bifurcation the distributions of activator u and driving inhibitor v can hardly be discriminated. The chart indicates, that a dissipative soliton grows with increasing distance to the drift-bifurcation. Parameters from (5.2)

the drift-bifurcation (Fig. 5.1). The most obvious difference to the system discussed in this chapter is the equilibrium propagation velocity which is twice as large for  $\tau = 4.35$  (Fig. 7.8) compared to  $\tau = 4.01$  (Fig. 5.1). In order to understand how this parameter change influences the shape of the dissipative solitons the intersections u(y) and v(y) of a slow and a fast dissipative soliton along their symmetry axis y are shown in Fig. 7.16. Because the slow dissipative soliton has been obtained in the vicinity of the drift-bifurcation the ansatz of the reduced dynamics (5.12) holds and the distributions of activator and driving inhibitor can hardly be discriminated from each other. The structure differs from a stationary solution only by the propagator mode amplitude, which is hardly visible in the left hand side of Fig. 7.16 as small displacement  $\alpha = \alpha_{\nu} e_{\nu}$  between the peaks of activator and driving inhibitor. For the fast dissipative soliton the displacement is clearly visible and obviously has led to significantly increased amplitudes of the activator and inhibitor peaks (right hand side of Fig. 7.16). Therefore, also the amplitude of the oscillating tails is increased and causes stronger attractive and repulsive interaction between the dissipative solitons.

Due to their large velocity the dissipative solitons enter the strongly repulsive interaction region of their collision partners very quickly and the activator peaks are stopped nearly immediately. The driving inhibitor catches up and destabilizes the structure because the large inhibitor peak diminishes locally much more activator than the latter is able to produce. Due to the large time scale constant the inhibitor adapts only slowly to the reduced activator concentration, which accelerates the fading of the dissipative solitons even more.

This disequilibrium between self-activation and self-inhibition does not occur for slowly propagating dissipative solitons in the vicinity of the drift-bifurcation, because the shape of the pulses differs only negligibly from the stationary state, which on the one hand is the prerequisite for the reduced dynamics and on the other hand ensures the conservation of the number of particles.

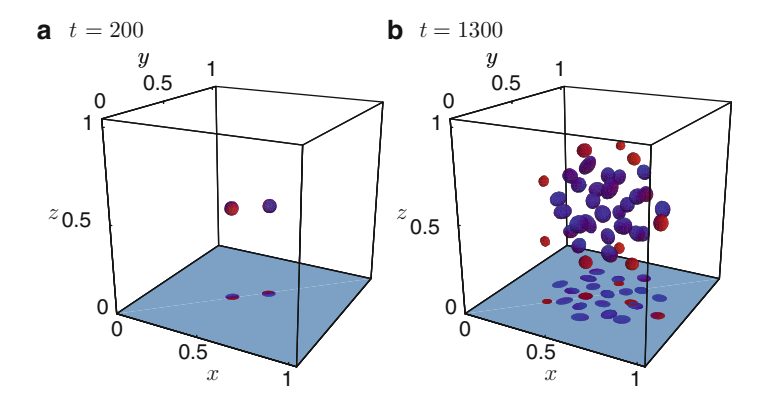


Fig. 7.17 Unstable rotating bound state of two dissipative solitons, which fills the domain with generated dissipative solitons due to self-completion. The figures show iso-surfaces of activator u(x,t)=0 which are shaded with respect to the local concentration of the driving inhibitor. Blue and red indicate a large and low concentration, respectively. Parameters from (7.12) with  $\kappa_1=-0.071$ 

#### 7.4.2 Generation

The previous sections on self-completion (Sect. 7.1.3) and on replication (Sect. 7.3.1) have shown that clusters of dissipative solitons can be destabilized in the vicinity of the Turing-bifurcation, while single dissipative solitons still remain stable (Fig. 7.6). Concerning the strong interaction between dissipative solitons it has been shown, that there is a critical distance between dissipative solitons. If dissipative solitons undercut this critical distance, the generation of new dissipative solitons will be triggered (Fig. 7.12). These generation processes have in common that the involved dissipative solitons exhibit pronounced oscillating tails. Therefore the question arises whether the oscillating tails are directly related to the underlying generation mechanism?

In order to investigate this question the three-component reaction-diffusion system (3.69) is solved on a three-dimensional domain for the following set of parameters:

$$D_u = 1.3 \cdot 10^{-4}, \ D_v = 0, \ D_w = 9.64 \cdot 10^{-3}, \ \lambda = 0.95,$$
  
 $\kappa_1 \in [-0.08; -0.07], \ \kappa_3 = 0.25, \ \kappa_4 = 1, \ \tau = 4.01$   
 $\theta = 0.01, \ \Omega = [0, 1]^3, \text{ no-flux boundary condition,}$   
 $\Delta_x = 1.49 \cdot 10^{-2}, \ \Delta_t = 0.05.$  (7.12)

For these parameters dissipative solitons exist as stable solutions of the investigated reaction-diffusion system, while rotating bound states of dissipative solitons become unstable e.g. for  $\kappa_1 = -0.071$ . In this case the domain is filled with dissipative solitons due to a self-completion process (Fig. 7.17). The border between the

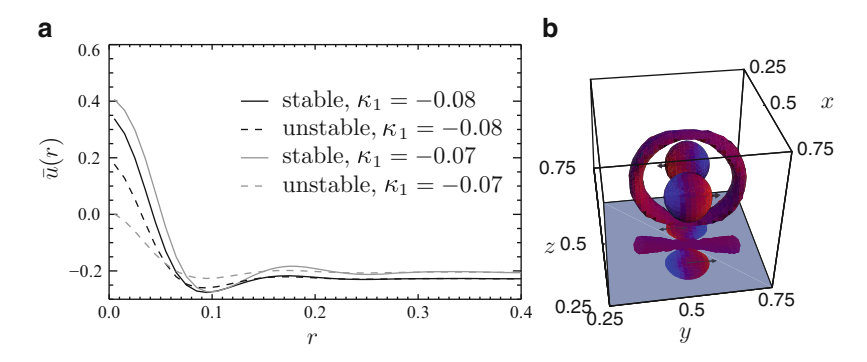
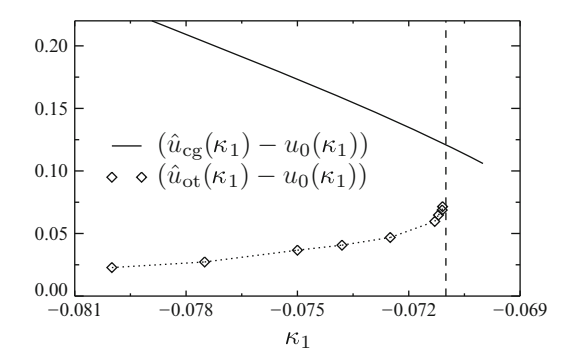


Fig. 7.18 Three-dimensional dissipative solitons with pronounced oscillating tails. (a) Stationary, radial-symmetric solutions of activator  $\bar{u}(r)$  for parameter set (7.12) with  $\Delta_x = 0.01$ . Stable and unstable solutions are plotted with *solid* and *broken lines*, respectively. *Black* and *gray curves* show solutions obtained for  $\kappa_1 = -0.8$  and  $\kappa_1 = -0.7$ , respectively. The horizontal shift of these solutions is caused from the dependency of the homogeneous state  $u_0$  on  $\kappa_1$ . (b) Iso-surface of activator  $u(x,t)|_{t=0} = -0.177$  for the initial condition of the simulation campaign summarized in Fig. 7.19. The surface is coloured with respect to the local concentration of the driving inhibitor v with *red* and *blue* denoting low and high concentrations, respectively. The torus results from the superposition of oscillating tails. Parameters from (7.12) with  $\kappa_1 = -0.071$ ,  $\tau = 4.01$ 

structured part of the domain and the homogeneous part can be modelled as three-dimensional front, which does not propagate continuously like in Fig. 3.7 but stepwise for every ignition of a new spherical shell of dissipative solitons. In Fig. 7.17b the latest dissipative solitons exhibit purely red shaded iso-surfaces, because the respective activator peaks have formed but the inhibitor peaks have not formed, yet. Note, that the front propagation is not stopped like the one visualized in Fig. 3.9 because the simulations discussed in this section do not take global feedback into account.

In order to investigate the difference between stable and unstable bound states in relation to the respective stationary dissipative soliton solutions intersections of activator u(r) have been plotted both for  $\kappa_1 = -0.8$  (black curves) and  $\kappa_1 = -0.7$ (gray curves) in Fig. 7.18a. For both parameter sets the stable stationary solution (solid curves) and the unstable stationary solutions (broken curves) the so-called critical nuclei are shown. The figure demonstrates in analogy to Fig. 3.19 that the amplitude of the stable stationary solutions increases with increasing driving parameter  $\kappa_1$ , while the amplitude of the critical nucleus decreases for increasing driving parameter. Therefore, the difference in size between the stable stationary solution and the respective unstable stationary solution increases for increasing driving parameter. Furthermore, Fig. 7.18a indicates, that the difference between the amplitude of the unstable stationary solution and the amplitude of the oscillating tails of the stable stationary solution decreases for increasing driving parameter. Having in mind that the critical nucleus is a separatrix in state space between the homogeneous state and the dissipative soliton solution (Sect. 3.3.6), one can conclude that the superposition of oscillating tails can more easily trigger the generation of dissipative solitons if the amplitude of the respective critical nucleus is small.

References 203



**Fig. 7.19** Comparing the amplitudes of critical nuclei  $\hat{u}_{cg}(\kappa_1)$  and superimposing oscillating tails  $\hat{u}_{ot}(\kappa_1)$  for varied driving parameter  $\kappa_1$ . Both amplitudes have been reduced by the respective value of the homogeneous ground state  $u_0(\kappa_1)$ . The initial condition for the simulation campaign is depicted in Fig. 7.18b. On the *left hand side* of the *vertical line* the bound state is a stable solution of the reaction-diffusion system. On the *right hand side* the bound state is unstable with respect to self-completion. Parameters from (7.12)

In order to prove this assumption, a simulation campaign on basis of a rotating bound state is undertaken for varied driving parameter  $\kappa_1$ . For such kind of structure the largest superposition of oscillating tails occurs in the plane being perpendicular to the axis of the compound. For a three-dimensional bound state this superposition is a torus of increased activator concentration (Fig. 7.18b). In Fig. 7.19 the maximum activator concentration  $\hat{u}_{\text{ot}}$  of this torus is compared to the amplitude  $\hat{u}_{\text{cg}}$  of the critical nucleus for varied control parameter  $\kappa_1$ . The parameter scan shows, that the amplitude of the critical nucleus decreases for increasing control parameter, while the amplitude of the activator torus increases for increasing control parameter, until generation by self-completion is initiated for  $\kappa_1 > -0.0711$ .

This parameter scan clarifies, that the superposition of oscillating tails can trigger the generation of dissipative solitons, if the superposition grows up to the magnitude of an unstable stationary dissipative soliton, the so-called critical nucleus. In case of the replication scenario (Sect. 7.3.1) this condition is met by the superposition of the oscillating tails of several dissipative solitons, if the interacting particles fall below a critical distance. Otherwise the respective clusters are stable solutions. In case of the self-completion scenario (Sect. 7.1.3) already the superposition of the oscillating tails of two dissipative solitons triggers the generation process. Other possibilities for meeting the critical nucleus criterion are given by localized perturbations due to spatial inhomogeneities or instabilities of individual dissipative solitons.

#### References

- 7.1. A.M. Turing, Phil. Trans. R. Soc. B 237, 37 (1952)
- 7.2. C.P. Schenk, M. Or-Guil, M. Bode, H.-G. Purwins, Phys. Rev. Lett. 78, 3781 (1997)

- 7.3. T. Ohta, J. Kiyose, M. Mimura, J. Phys. Soc. Jpn. **66**(5), 1551 (1997)
- 7.4. S. Kawaguchi, M. Mimura, SIAM J. Appl. Math. **59**(3), 920 (1998)
- 7.5. C.P. Schenk, A.W. Liehr, M. Bode, H.-G. Purwins, in High Performance Computing in Science and Engineering '99. Transactions of the High Performance Computing Center, Stuttgart 1999, ed. by E. Krause, W. Jäger (Springer, Berlin, 2000), pp. 354–364. http://www.uni-muenster.de/Physik/AP/Purwins/struktur/Literatur/hlrs1999-e.html
- 7.6. T. Ohta, Phys. D **151**(1), 61 (2001)
- 7.7. Y. Nishiura, T. Teramoto, K.I. Ueda, Chaos **13**(3), 962 (2003)
- 7.8. Y. Nishiura, T. Teramoto, K.I. Ueda, Phys. Rev. E **67**(056210) (2003)
- 7.9. S. Kawaguchi, M. Mimura, Phys. Rev. E **77**(046201), 1 (2008). doi:10.1103/PhysRevE.77. 046201
- 7.10. Yu.A. Astrov, H.-G. Purwins, Phys. Lett. A **283**, 349 (2001). doi:10.1016/S0375-9601(01) 00257-2
- 7.11. C.P. Schenk, Numerische und analytische Untersuchung solitärer Strukturen in zwei- und dreikomponentigen Reaktions–Diffusions–Systemen. Dissertation, Institut für Angewandte Physik, Westfälische Wilhelms-Universität Münster, 1999
- 7.12. A.W. Liehr, M. Bode, H.-G. Purwins, in *High Performance Computing in Science and Engineering 2000. Transactions of the High Performance Computing Center, Stuttgart (HLRS) 2000*, ed. by E. Krause, W. Jäger (Springer, Berlin, 2001), pp. 425–439
- 7.13. A.W. Liehr, Generation of dissipative solitons on basis of controlled turing destabilization. Scientific Information 20090624a, Freiburg Materials Research Center, 2009. doi:10.1594/fmf.SI20090624a
- 7.14. M.K. Riede, K.O. Sylvester-Hvid, M. Kühne, M.C. Röttger, K. Zimmermann, A.W. Liehr, Comput. Phys. Commun. 181(3), 651 (2010). doi:10.1016/j.cpc.2009.11.014
- 7.15. P. Schütz, Strukturen mit großen Amplituden in Reaktions–Diffusions–Systemen vom Aktivator–Inhibitor–Typ. Dissertation, Institut für Angewandte Physik, Westfälische Wilhelms–Universität Münster, 1995
- 7.16. H. Meinhardt, A. Gierer, J. Cell Sci. 15, 321 (1974)
- 7.17. A.W. Liehr, Dissipative Solitonen in Reaktions-Diffusions-Systemen. Dissertation, Institut für Angewandte Physik, Westfälische Wilhelms-Universität Münster, 2003
- 7.18. Yu.A. Astrov, Yu.A. Logvin, Phys. Rev. Lett. **79**(16), 2983 (1997)
- 7.19. P. Coullet, C. Riera, C. Tresser, Phys. Rev. Lett. **84**(14), 3069 (2000)
- 7.20. M. Bode, A.W. Liehr, C.P. Schenk, H.-G. Purwins, Phys. D **161**(1–2), 45 (2002). Reprinted with permission from Elsevier.
- 7.21. K. Krischer, A. Mikhailov, Phys. Rev. Lett. **73**(23), 3165 (1994)
- 7.22. Y. Nishiura, T. Teramoto, K.I. Ueda, Chaos **15**(047509), 1 (2005)
- 7.23. C.P. Schenk, Numerische und analytische Untersuchung solitärer Strukturen in zwei- und dreikomponentigen Reaktions-Diffusions-Systemen. Dissertation, Institut für Angewandte Physik, Westfälische Wilhelms-Universität Münster, 1999. Figures published with kind permission of the author
- 7.24. A.W. Liehr, A.S. Moskalenko, M.C. Röttger, J. Berkemeier, H.-G. Purwins, in *High Performance Computing in Science and Engineering '02. Transactions of the High Performance Computing Center Stuttgart (HLRS) 2002*, ed. by E. Krause, W. Jäger (Springer, Berlin, 2003), pp. 48–61
- 7.25. A.W. Liehr, Dissipative Quasiteilchen in dreikomponentigen Reaktions-Diffusions-Systemen. Master's thesis, Institut für Angewandte Physik, Westfälische Wilhelms-Universität Münster, 1999
- 7.26. R.S. Ward, Phys. Lett. A 208, 203 (1995)
- 7.27. H. Willebrand, F.-J. Niedernostheide, E. Ammelt, R. Dohmen, H.-G. Purwins, Phys. Lett. A 153(8), 437 (1991)
- 7.28. C. Strümpel, H.-G. Purwins, Yu.A. Astrov, Phys. Rev. E **63**(2), 026409/1 (2001)
- 7.29. R. Dohmen, Entwicklung von Modellgleichungen zur Beschreibung nichtlinearer Systeme und Untersuchung der Lösungsvielfalt mit analytischen und numerischen Mitteln. Dissertation, Institut für Angewandte Physik, Westfälische Wilhelms-Universität Münster (1991)

References 205

- 7.30. C. Elphick, A. Hagberg, E. Meron, Phys. Rev. E **51**(4), 3052 (1995)
- 7.31. J.E. Pearson, Science **261**(9), 189 (1993). doi:10.1126/science.261.5118.189
- 7.32. M. Bode, Beschreibung strukturbildender Prozesse in eindimensionalen Reaktions– Diffusions–Systemen durch Reduktion auf Amplitudengleichungen und Elementarstrukturen. Dissertation, Institut für Angewandte Physik, Westfälische Wilhelms-Universität Münster (1993)
- 7.33. Y. Nishiura, D. Ueyama, Phys. D **130**, 73 (1999)
- 7.34. A. Adamatzky, Computing in Nonlinear Media and Automata Collectives (Institute of Physics Publishing, Bristol, 2001)
- 7.35. X. Yuan, T. Teramoto, Y. Nishiura, Phys. Rev. E **75**(036220), 1 (2007)

# Chapter 8 Summary

Nature uses only the longest thread to weave her patterns, so each small piece of her fabric reveals the organization of the entire tapestry.

Richard Feynman [8.1]

**Abstract** Dissipative solitons in reaction-diffusion systems are self-organized localized structures with particle-like properties: They are generated or annihilated as entities, propagate with a well-defined stabilized velocity and are able to form bound states with qualitative different properties compared to their constituents.

The following statements order the most important findings on dissipative solitons with respect to this monograph:

Structure Formation: Self-organization is evident in animate and inanimate nature on nearly every spatio-temporal scale. Reaction-diffusion systems are a prominent example of self-organized systems, because they exhibit all important types of structure: Patterns, spirals and solitary structures, so-called dissipative solitons (Chap. 1).

Experiment: Dissipative solitons in experimental systems show complex dynamics including: propagation, formation of bound states, merging and splitting, generation, annihilation, spatio-temporal chaos and certain phenomena of condensed phases (Chap. 2).

Modelling: The scale of spatial coupling basically determines the size of localized structures. The nonlinear dynamics of neighboured local states fosters structure formation. Feedback control stabilizes solitary structures in dissipative systems. Delayed feedback introduces uniform motion or oscillation (Chap. 3).

208 8 Summary

Propagation: The transition between stationary and propagating dissipative solitons is called drift-bifurcation. Bound states of dissipative solitons exhibit qualitatively different dynamics compared to its separated constituents (Chap. 4). The drift-bifurcation is evident in experimental systems as transition from Brownian to active Brownian motion (Chap. 6).

Particle Conservation: Slow dissipative solitons interact by scattering or the formation of bound states. The latter is caused by alternating regions of attraction and repulsion surrounding the dissipative solitons (Chaps. 5 and 6). The complexity of their dynamics increases with the number of dissipative solitons involved and the number of spatial dimensions of the system.

Far From Equilibrium Dynamics: The generation and annihilation of dissipative solitons is induced by global or local changes of system parameters, such that the system or its self-organized structures become unstable. Concerning dissipative solitons, the instability might be subliminal and becomes evident only in the course of interaction processes with other dissipative solitons (Chap. 7).

Dissipative solitons are local excitations of nonlinear continuous systems. By itself they are also continuous entities, but their localization makes them distinguishable and allows for the modelling of their dynamics and interaction by means of a particle approach. Large ensembles of dissipative solitons may be described by field equations modelling the evolution of the mean local particle density and the mean local velocity. And here, the next level of localization occurs, e.g. trigger waves propagating through the system.

From this point of view, we are exhibiting a hierarchy of modelling paradigms for dissipative systems:

- The flux of matter or energy fosters the self-organized formation of structure, which is modelled by field equations.
- Structure implicates the concept of localization and the dynamics of localized entities, which is modelled by ordinary differential equations.
- Ensembles of localized entities are modelled by field equations, which again may exhibit self-organization, such that the hierarchy is continued to the next abstraction level.

#### Reference

8.1. R.P. Feynman, *The Character of Physical Law* (British Broadcasting Corporation, London, 1965)

Activator, 62	pitchfork
Activator-inhibitor-system, 62	disturbed, 50
Akhmediev, 6	point, 2, 46
Albedo, 55	co-dimension-2, 51
Alfimov, 49	saddle-node, 51, 75, 142, 198
Ammelt, 29	backwards, 144
Amoeba, 3	supercritical pitchfork, 46
Ankiewicz, 6	Bin, 161
AOT, 20	Bistability, 23, 43, 52, 66
ARTS, xi	formation of bound states, 140
Astrov, 23, 27–30, 38, 176, 185	Bistable, 45
Asymptotically stable, 44	Bloch, 66
Attractor, 43	Bode, 7, 54, 60, 65, 108, 120, 128, 135, 198
Austin, 22, 23	Bödeker, 31, 32
Autosoliton, 5	Boedeker, 154
Axis longitudinal, 132	Bogdanov-Takens-Turing, 198
	Bordeaux, 23
	Boscovich, 130
Ball, 5	Bound state, rotating, 138
Bantu, 2	Brandeis, 16
Barcley, 154	Breathing, 91
Barkley, 120	Bromothymol blue, 22
Barkley-model, 120	Brownian, 160, 165-169, 208
Basuto, 2	
Baumann, 47	
Bechana, 2	cAMP, 4
Becker, 29	Cells, olfactory, 44
Belousov, 3, 4, 17	Central force, 127
Belousov-Zhabotinsky, 16, 17	CFUR, 19
Belousov-Zhabotinsky reaction, 3	Chaos, spatio-temporal, 23, 27
Bérnard, 2, 93	Characteristic, 27
Bifurcation, 45	Chemotaxis, 4
Bogdanov-Takens-Turing, 198	CIMA, 15, 20
drift, 96, 116, 176	Circular waves, segmented, 22
drift-pitchfork, 107	Co-dimension-2-bifurcation, 50
Hopf, 154, 178	Control, 180
Ising-Bloch, 66	Coulett, 185

Coupling weak, 125	Fixed points, 44, 65
Cray T3E, xi	FIZ, 70
Critical nucleus, 202	Fluctuations, thermal, 25
Cross, 5	FMF, xi
CSTR, 22	Focus, 56, 65
Curvature, 55	Fokker-Planck, 165, 168
Cusp catastrophe, 52	Force
Cyclic adenosine monophosphate, 4	centrifugal, 139, 141
	centripetal, 141
	Form factor, 106, 127
Dash waves, 22	Fréchet, xviii, 95
de Kepper, 15, 20, 22	Fréchet-derivative, 95
Denardo, B., 46	Fredholm, 113
Determinant criterion, 69, 78	Friedrich, 159
DFG, xi	Fronts, 48, 54
Dictyostelium discoideum, 3	of bubbles, 22
Dielectric, 28	pairs, 71, 198
Dirac, 61	propagation velocity, 69
	triple, 72
Dirichlet, 55	Fruiting body, 4
Discharge	Full-Metadata Format, 183
gap, 24	,
noise, 25	
Dissipative soliton	Gas-discharge system, ac, 93
pronounced oscillatory tails, 137	Gauss, 168
Dominance rule, 66, 70	Gaussian, 128, 140, 160, 164
Double well potential, 131	Gaussian white noise, 160
Drift	Generator, 199
bifurcation, 96, 116	Gierer, 28, 183
pitchfork-bifurcation, 107	Goldstone, xviii, 73, 94–98, 100–102, 105,
Dynamics, reduced, 120	110, 112, 123, 124
	boson, 95
	mode, 94, 110, 123
Ei, 120	complementary, 97, 105
Eigenbasis, 96	eigenmode, 95
Eigenmode	Gray-Scott, 189, 198
generalized, 96	Green, 61, 78, 109, 123
Goldstone-mode, 95	function, 78, 123
Electrode, planar, 24	Gurevich, 25
Elphick, 120, 125	Guievicii, 23
Entire solution, 55	
Epstein, 20	Haken, 5
Euclidean, 154	
Euler, 164	Hamilton, 65
	Hassan, 55
	Heaviside, 61
F 1 25	Hempel, 107
Faraday, 25	Herero, 2
Ferroin, 17	Hessian, 126
Fife, 5	Heteroclinic orbit, 57, 67
FilaCount, 33	HLRS, xi
FilaTrace, 33	Hodgkin, 7
FitzHugh, 7	Hohenberg, 5
FitzHugh-Nagumo-model, 107	Homoclinic, 53, 57

Homoclinic orbit, 67 Hopf, 69 bifurcation, 154	Monostable, 45, 68 Morphogens, 2 Multi-stability, 27, 43
supercritical, 178 oscillations, 69	
Hoyle, 5	Nagumo, 7
Huxley, 7	Nearest neighbor problem, 71
Hysteresis, 27	Nerve pulse, 4, 70
	Neutral curve, 64
	Newton, 141
Ignition voltage, 25	Nishiura, 5, 61, 120, 128, 189, 198
Indium tin oxide (ITO), 24	Nitrogen, 24
Inhibition, delayed, 76 Inhibitor, 62	Noise amplitude matrix, 160, 162
fast, 79	discharge, 25
slow, 69, 79	Nonlinearity, cubic, 44
Inhomogeneity, spatial, 38	Nucleus, critical, 203
Instability	Nullcline, 50, 65
breathing, 79	
Turing, 69, 78	
wave, 78	Ohta, 120
Integral, elliptic, 47	Operator, unity, 96
Interaction	Orbit
many-particle, 127	heteroclinic, 57, 67
oscillatory, 130 Ising, 66	homoclinic, 53, 57, 67 Oregonator, 3, 20
Isosurface, 135	Oregonator-model, 3
Itô, 161, 163	Or-Guil, 83, 120
ITO. See Indium tin oxide (ITO)	Ornstein-Uhlenbeck, 168
	Oscillating tail, 29
	Oscillator, torsional, 44, 46
Krischer, 189	Oscillatory tails, 98
	Osipov, 107
Langevin, xix, 155, 160, 161, 163–165	
Laplace, 85	Pair effect, 108
Laplacian, 67	Particle generator, 199
Liquid-like state, 27	Phase space portrait, 44
Logvin, 28, 29, 38, 185	Photo effect, 25
Luminance distribution, 25	Pitchfork bifurcation
	disturbed, 50
Madam 100	supercritical, 46
Markov, 160	Poly(acrylamide) gel, 22 Poly(acrylate), 22
Markstein, 55 McKean, 7	Potential, 44
Meinhardt, 28, 183	double well, 131
Microemulsion, 20	Printer's instability, 93
Mikhailov, 189	Propagation, 91
Mode, propagator, 96	Propagation velocity, front, 69
Model	Propagator mode, 96, 110, 124
$\phi^4$ , 197	amplitude, 177
Barkley, 120	Puls, 5, 77
Monostability, 52	Purwins, 6, 23, 27, 30, 176

Radical, 20	breaking, 2
Rayleigh, 2, 93	cylindrical, 121
Rayleigh-Bérnard	radial, 107
convection, 93	rotational, 101
experiment, 2	Synergetics, 2
Replication, 190, 203	Szalai, 22
Resistivity, specific, 176	
Rinzel-Keller-model, 107	
Risken, 164	Tank reactor, continuously stirred, 22
Rotermund, 16	Tessellation, 71
Röttger, 154, 156	Thermal fluctuations, 25
$Ru(bipy)_3^{2+}, 17$	Thyristor, 64
114(01)7/3 , 17	Time-scale, slow, 68
	Torsional oscillators, 46
Saddle-node bifurcation, 51, 75, 142, 198	Tortoise, 1
Sc, 4	Trace criterion, 69, 78
Scattor, 189	Trigger front, 54
Schenk, 98, 148	Turing, 9, 15, 19–22, 25–29, 43, 62–65, 69, 75,
Schlögl, 50, 52, 55–57	77, 78, 81, 98, 175, 180–183, 185,
Schmeling, 83	186, 201
Schrödinger equation, nonlinear, 5	bifurcation, 98
Self-completion, 28, 36, 38, 183, 190, 201, 203	
Self-replication, 22, 29	
Separatrix, 45	Ueyama, 198
Shadow system, 61	•
Shangaan, 2	
Sine-Gordon equation, 5	Vanag, 20
Skew gradient systems, 65	Voronoi, 43, 70, 71, 74
Skyrme, 197	
Slime mould, 3	
Smoller, 5	Ward, 128
Soliton, 5	Waves, accelerating, 20
Spatial tessellation, 71	Wave-trains, 120, 122, 142
Spirals, 3, 22	Weak coupling, 125
Spot, 5	
Stable, asymptotically, 44	
Starch, 20	Xhosa, 2
Stationary, 44	
Stochastic resonance, 19	
Stratonovich, 160, 161, 163	Zanette, 55
Strümpel, 29	Zebra, 2
Surface waves, 5	Zhabotinsky, 3, 4, 17
Symmetry, 95	Zulu, 2